IMPROVED ANALYTICAL METHODS FOR ASSESSMENT OF HYPERSONIC DRAG-MODULATION TRAJECTORY CONTROL

A Thesis
Presented to
The Academic Faculty

by

Zachary R. Putnam

In Partial Fulfillment
of the Requirements for the Degree
Doctor of Philosophy in the
Daniel Guggenheim School of Aerospace Engineering

Georgia Institute of Technology
March 2015

IMPROVED ANALYTICAL METHODS FOR ASSESSMENT OF HYPERSONIC DRAG-MODULATION TRAJECTORY CONTROL

Approved by:

Dr. Robert D. Braun, Advisor
Daniel Guggenheim School of Aerospace Engineering
Georgia Institute of Technology

Dr. Mark Costello
Daniel Guggenheim School of Aerospace Engineering
Georgia Institute of Technology

Dr. Marcus J. Holzinger
Daniel Guggenheim School of Aerospace Engineering
Georgia Institute of Technology

Dr. Michael J. Grant
School of Aeronautics and Astronautics
Purdue University

Mr. Gregg H. Barton
Mission Design Group, Algorithms and Software Division
Charles Stark Draper Laboratory

Mr. Christopher J. Cerimele
Aerosciences and Flight Mechanics Division, Johnson Space Center
National Aeronautics and Space Administration

Date Approved: March 5, 2015

ACKNOWLEDGEMENTS

This work was supported by a NASA Space Technology Research Fellowship.

TABLE OF CONTENTS

ACKNOWLEDGEMENTS . . . . . **iii**

LIST OF TABLES . . . . . **viii**

LIST OF FIGURES . . . . . **ix**

NOMENCLATURE . . . . . **xv**

SUMMARY . . . . . **xix**

I INTRODUCTION **1**

1.1 Planetary Aeroassist Systems 1

1.1.1 Aeroassist Maneuvers 1

1.1.2 Deployable Decelerators 5

1.2 Aeroassist Flight Dynamics 8

1.2.1 The Equations of Motion 8

1.2.2 Trajectory Control Options 11

1.2.3 Aerodynamic Force Parameterization 18

1.2.4 Planetary Entry Corridors 20

1.2.5 Flight Performance Evaluation 21

1.3 Contributions of Thesis 26

II SURVEY OF ANALYTICAL SOLUTIONS FOR PLANETARY ENTRY TRAJECTORIES **29**

2.1 Approximating Trajectory Solutions for Planetary Entry 30

2.2 Analytical Approximate Solutions 31

2.2.1 Ballistic Entry 33

2.2.2 Lifting Entry 41

2.2.3 General Methods 51

2.3 Hybrid Analytical-Numerical Approximate Solutions 57

2.3.1 Chapman and Vinh 57

2.3.2 Yaroshevskiy 58

2.3.3 Matched Asymptotic Solutions 59
2.4 Numerical Approximate Solutions and Machine Computation 60
2.5 Summary 61

III ENHANCEMENT OF THE ALLEN-EGGERS SOLUTION . . . 62

3.1 Methods and Assumptions 64
3.2 Review of the Allen-Eggers Solution 66
3.2.1 Altitude-Velocity Profile 66
3.2.2 Acceleration Magnitude 67
3.2.3 Convective Heat Rate 68
3.2.4 Simplified Expressions 69
3.2.5 Application to Example Trajectories 70
3.3 Enhancement of the Allen-Eggers Solution 74
3.3.1 Determining the Constant Flight-Path Angle 74
3.3.2 Bounding the Domain of Applicability 77
3.3.3 Closed-Form Expressions for Range 83
3.3.4 Trajectory States as a Function of Time 89
3.4 Assessment of Approximation Error and Applicability 95
3.4.1 The Extended and Enhanced Allen-Eggers Approximation . . 95
3.4.2 Applicability to Other Initial Conditions 98
3.5 Summary 103

IV ANALYTICAL ASSESSMENT OF DISCRETE-EVENT DRAG-MODULATION SYSTEMS 105

4.1 Application of the Enhanced Allen-Eggers Solution 105
4.2 Range Control Authority 107
4.3 Minimizing Peak Deceleration for Single-Stage Systems 110
4.4 Minimizing Stagnation-Point Heat Rate 115
4.5 Summary 117

V APPLICATION OF DRAG-MODULATION TRAJECTORY CONTROL TO AEROASSIST SYSTEMS: NUMERICAL FEASIBILITY . . . 118

5.1 Precision Landing at Mars Using Discrete-Event Drag-Modulation . 118

5.1.1 System Concept . . . 120

5.1.2 Numerical Analysis Methods and Assumptions . . . 126

5.1.3 Corridor Definition and Divert Capability . . . 130

5.1.4 Entry, Descent, and Landing Flight Performance . . . 135

5.1.5 Summary . . . 141

5.2 Drag-Modulation System Options for Planetary Aerocapture . . . 146

5.2.1 Drag Modulation Flight Control Concepts . . . 147

5.2.2 Real-time Guidance . . . 150

5.2.3 Methodology . . . 152

5.2.4 Corridor and Feasibility . . . 154

5.2.5 Case Study: Aerocapture at Mars . . . 160

5.2.6 Summary . . . 166

5.3 Conclusions . . . 166

VI COMPARISON OF LIFT AND DRAG-MODULATION SYSTEMS USING NONLINEAR VARIATIONAL METHODS . . . 168

6.1 Introduction . . . 168

6.2 Nonlinear Variational Methods . . . 169

6.3 Application to Ballistic Entry Using the Allen-Eggers Solution . . . 171

6.3.1 Robustness to Atmospheric Parameters . . . 172

6.4 Comparison of Lift and Drag-Modulation Systems for Steep Entry Trajectories . . . 182

6.4.1 Atmospheric Parameters . . . 182

6.4.2 Initial State Parameters . . . 183

6.4.3 Vehicle Aerodynamic Parameters . . . 183

6.5 Integrated Results . . . 189

6.6 Conclusions . . . 190

VII CONCLUSIONS AND FUTURE WORK 192

7.1 Research Contributions 192

7.2 Future Work 193

REFERENCES 196

LIST OF TABLES

1 Approximations in Selected Flight Dynamics Texts 30

2 Closed-form Ballistic Entry Solutions and Assumptions 34

3 Parameters for example trajectories at Earth 66

4 Vehicle states at peak acceleration 72

5 Vehicle states at peak heat rate 72

6 Nominal Parameters for Example Trajectory 107

7 Mars Properties 127

8 Monte Carlo Simulation Uncertainty Models and Parameters 131

9 Nominal Trajectory Parameters 136

10 Monte Carlo Simulation Results 142

11 Planetary Model Parameters 152

12 Monte Carlo Simulation Input for Mars Trajectories 153

13 Monte Carlo Simulation Results for Single-stage System at Mars . . . 162

14 Monte Carlo Simulation Results for Two-stage System at Mars 163

15 Monte Carlo Simulation Results for Continuously-variable System at Mars 164

16 Parameters in the Allen-Eggers Solution 170

17 Ballistic Entry Trajectory Parameters 174

18 MSL-Class Vehicle Entry Trajectory Parameters 188

19 Lift Versus Drag Modulation for an MSL-Class Vehicle 190

LIST OF FIGURES

1 Example planetary aeroassist trajectories: a) entry and b) aerocapture. 1

2 Example Earth entry trajectory: lunar return with $V_0 = 11$ km/s, $\gamma_0 = -8$ deg, $L/D = 0$, $\beta = 315$ kg/m^2, $r_N = 3.0$ m. 3

3 Deployable hypersonic aerodynamic decelerator concepts: a) IRVE-3, b) ADEPT, c) trailing ballute. 8

4 Coordinate systems and free-body diagram for planar entry trajectories. 11

5 Bank-angle steering for blunt body entry vehicle. 15

6 Bank reversal, wind-relative velocity vector is directed out of the page. 15

7 Required L/D to achieve a particular limit on peak deceleration during planetary entry at several velocities. 16

8 Example lift-modulation entry trajectory using bank-angle steering. . 16

9 Options for parameterizing the aerodynamic force. 19

10 Planetary entry corridor. 21

11 Notional corridor-bounding entry trajectories for a lift-modulation entry system. 22

12 Applicability of various first-order approximations of the equations of motion. 23

13 Comparison of the applicability of select first-order methods. 32

14 H. Julian Allen with his blunt body theory. 35

15 Sänger's and Bredt's rocket bomber. 42

16 Gazley's lifting entry corridor. 44

17 Comparison of analytical and numerical spherical planet solutions with analytical flat planet solutions. 49

18 Loh's second-order solution applied to an oscillatory endoatmospheric trajectory ($R/H = 900$). 53

19 Comparison of Allen-Eggers, Citron-Meir, Loh, and numerical integration ($R/H = 900$). 55

20 Comparison of Citron-Meir, Loh, and numerical integration for lifting entry: a) altitude and b) flight-path angle versus normalized velocity ($R/H = 900$). 56

21 Comparison of Citron-Meir, Loh, and numerical integration for ballistic entry: a) altitude and b) flight-path angle versus normalized velocity ($R/H = 900$). 56

22 Comparison of solution methods to the matched asymptotic solution. 60

23 Example application of the Allen-Eggers solution (solid) compared to numerical integration (dashed): a) altitude, b) acceleration, c) flight-path angle, and d) heat rate versus velocity. 72

24 Allen-Eggers approximation error for a) altitude, b) acceleration, c) flight-path angle, and d) heat rate versus velocity. 73

25 Three methods for computing the Allen-Eggers constant flight-path angle, γ^*, for the sample-return example entering with three different values of γ_0. 76

26 Comparison of the approximation error with $\gamma^* = \gamma_0$ (dashed) and the proposed method for computing γ^* (solid): a) altitude, b) acceleration, c) flight-path angle, and d) heat rate versus velocity. 77

27 Vehicle state approximation error at peak conditions for $\gamma^* = \gamma_0$ and the proposed method for computing γ^*. 78

28 Allen-Eggers approximation error in altitude-velocity profile a) early and b) late in the trajectories. 79

29 Example bounds on the Allen-Eggers domain of applicability for the sample-return example case. 81

30 Allen-Eggers approximation error versus a) the initial dynamic pressure stand-off factor and b) the final velocity stand-off factor for the sample-return example case. 81

31 Comparison of the approximation error for bounded (solid, $\delta_V = 0.05$, $\delta_q = 2$) and unbounded (dashed) domains: a) altitude, b) acceleration, c) flight-path angle, and d) heat rate versus velocity. 84

32 Allen-Eggers approximation error of vehicle states at peak conditions for bounded ($\delta_V = 0.05$, $\delta_q = 2$) and unbounded domains. 84

33 Planetary entry range and range angle. 86

34 Comparison of numerical integration (dashed) and estimates (solid) of a) range and b) range-to-go. 89

35 Comparison of range estimation error for Eq. (97) (solid) and Kornreich's expression (dashed) a) percent error with respect to total range and b) absolute error. 89

36 Range-to-go estimation error: a) percent error with respect to total range and b) absolute error. 90

37 Comparison of states from the time-dependent Allen-Eggers solution (solid) with numerical integration (dashed): a) velocity, b) altitude, c) flight-path angle, and d) range angle versus time. 94

38 Comparison of states from the time-dependent Allen-Eggers solution (solid) with numerical integration (dashed): a) acceleration and b) heat rate versus time. 94

39 Absolute error in trajectory time estimates for Eq. (102c) (solid) and Kumagai's solution (dashed). 95

40 Comparison of the extended and enhanced Allen-Eggers solution (solid), the original Allen-Eggers solution (gray), and numerical integration (dashed): a) altitude, b) acceleration, c) flight-path angle, and d) heat rate versus velocity. 96

41 Comparison of approximation error for the extended and enhanced Allen-Eggers solution (solid) and the original Allen-Eggers solution (dashed): a) altitude, b) acceleration, c) flight-path angle, and d) heat rate versus velocity. 97

42 Approximation error for the original and extended and enhanced Allen-Eggers solutions. 97

43 Improvements to the domain of applicability of the Allen-Eggers (Gazley) solution [1]. 98

44 Normalized integrated error in acceleration, heat rate, and range-to-go over a range of initial conditions for the sample-return example vehicle ($\beta = 60$ kg/m^2). 101

45 Normalized integrated error in acceleration, heat rate, and range-to-go over a range of initial conditions for the strategic example vehicle ($\beta = 10000$ kg/m^2). 102

46 Normalized integrated error in acceleration, heat rate, and range-to-go over a range of initial conditions for the LEO-return example vehicle ($\beta = 450$ kg/m^2). 102

47 Percent error in a) peak acceleration and b) peak heat rate estimates. 103

48 Example application of the Allen-Eggers solution. 106

49 Range profiles for several V_J. 108

50 Divert capability over a range of ballistic coefficients. 109

51 Acceleration profiles for several V_J. 111

52 Jettison velocity for minimum a_{max} as a function of (β_1, β_2). 113

53 Minimum a_{max} as a function of (β_1, β_2). 113

54 Jettison velocity for minimum a_{max} as a function of ballistic coefficient ratio. 114

55 Minimum a_{max} as a function of ballistic coefficient ratio. 115

56 Heat rate as a function of velocity for several V_J. 116

57 Discrete-event drag-modulation vehicle concept. 122

58 Discrete-event drag-modulation trajectory control concept EDL sequence. 122

59 Guidance and targeting modes. 123

60 Example corridor-bounding entry trajectories for a drag-modulation trajectory control system at Mars. 133

61 Total entry range as a function of a) drag skirt jettison time and b) planet-relative velocity at jettison. 134

62 Change in total entry range and nominal g-load as a function of drag skirt jettison time. 134

63 Altitude versus downrange for corridor-bounding trajectories over three different density profiles. 135

64 Nominal entry trajectory for guidance mode 1. 137

65 Dispersed entry trajectories for guidance mode 1. 141

66 Post-jettison drag skirt segment trajectories for guidance mode 1. . . 143

67 Terminal a) downrange, b) crossrange, and c) total range error for all three guidance modes. 144

68 Parachute deploy conditions for a) pre-set velocity trigger and b) range-based trigger. 145

69 Single-stage jettison drag modulation aerocapture system. 148

70 Two-stage jettison drag modulation aerocapture system. 149

71 Continuously-variable drag modulation aerocapture system. 149

72 Example bounding trajectories for aerocapture aerodynamic corridor at Mars: a) altitude, b) flight-path angle, and c) sensed deceleration versus planet-relative velocity. 155

73 Aerocapture corridor bounding AI flight-path angles versus AI velocity for several β at Mars. 156

74 Aerodynamic corridor width as a function of β for several AI velocities at Mars. 157

75 Aerodynamic corridor width as a function of β_1 for several β-ratios at Mars for AI velocity of 6 km/s. 158

76 Aerocapture aerodynamic corridor widths at a) Mars, b) Titan, and c) Venus for two values of β_1 and several β-ratios. 159

77 Peak stagnation-point convective heat rates for several β. 160

78 Monte Carlo results for single-stage system at Mars: a) apoapsis error versus jettison time and b) periapsis raise ΔV and c) apoapsis correction ΔV versus apoapsis error. 162

79 Monte Carlo results for two-stage system at Mars: a) stage 2 versus stage 1 jettison time and b) periapsis raise ΔV and c) apoapsis correction ΔV versus apoapsis error. 163

80 Monte Carlo results for CV system at Mars: a) area command versus time (black curve denotes nominal) and b) periapsis raise ΔV and c) apoapsis correction ΔV versus apoapsis error. 164

81 Comparison of drag modulation aerocapture system options for Mars: a) apoapse error and b) total ΔV. 165

82 Closed form solution for $\partial s_f/\partial \rho_{ref}$ using the Allen-Eggers solution. . 173

83 Effect of reference density perturbations on final range. 174

84 Change in final range for various β values, analytical solution. 175

85 Change in final range for various β values, numerical root-finding computation. 175

86 Effect of reference density perturbations on range divert capability. . 177

87 Effect of scale height perturbations on final range. 178

88 Change in final range with respect to changes in scale height for various β values, analytical solution. 179

89 Change in final range with respect to changes in scale height for various β values, numerical solution with analytical solution superimposed in blue. 179

90 First-order change in final range in km for various β with respect to perturbations in H and ρ_{ref}. 180

91 Combined first and second-order change in final range in km for various β with respect to perturbations in H and ρ_{ref}. 181

92 Comparison of perturbations in final range relative to atmospheric parameter perturbations for lift and drag-modulation systems. 184

93 Comparison of perturbations in final range relative to initial state perturbations for lift and drag-modulation systems. 185

94 Comparison of perturbations in final range relative to vehicle parameter perturbations for lift and drag-modulation systems. 186

95 Change in final range in km due to perturbations in β and L/D for ballistic systems (red) and lifting systems (blue, $L/D = 0.1$) at Earth. 187

96 Change in final range in km due to perturbations in β and L/D for ballistic systems (red) and lifting systems (blue, $L/D \approx 0.24$). Black box shows approximate uncertainty in MSL aerodynamics. 188

NOMENCLATURE

Abbreviations

ADEPT	Adaptive Deployable Entry and Placement Technology
AI	Atmospheric interface
c.g.	Center of gravity
DGB	Disk-Gap-Band
DHD	Deployable Hypersonic Decelerator
EDL	Entry, Descent, and Landing
EI	Entry Interface
GNC	Guidance, Navigation, and Control
HIAD	Hypersonic Inflatable Aerodynamic Decelerator
ICBM	Intercontinental Ballistic Missile
IRBM	Intermediate Range Ballistic Missile
IRVE	Inflatable Re-entry Vehicle Experiment
MER	Mars Exploration Rover
MSL	Mars Science Laboratory
NPC	Numerical Predictor-Corrector
RCS	Reaction Control System
SLE	Steep lifting entry

TPS	Thermal Protection System

Subscripts

0	Initial condition
f	Final condition
I	Inertial frame
i	Index
L	Local horizontal frame
W	Wind frame
rel	Planet-relative frame

Symbols

α	Angle of attack, rad
β	Ballistic coefficient, kg/m^2
Δt	Time between measurements, s
ΔV	Change in velocity, m/s
$\dot{Q}$	Stagnation-point heat rate, W/cm^2
η	Noise magnitude
γ	Flight-path angle, rad
$\mathbf{a}$	Acceleration vector, m/s^2
$\mathbf{D}$	Drag vector, N
$\mathbf{e}$	Error vector

$\mathbf{L}$	Lift vector, N
$\mathbf{P}_{SS}$	Steady-state covariance matrix
$\mathbf{r}$	Position vector, m
$\mathbf{V}$	Velocity vector, m/s
$\mathbf{W}$	Weight vector, N
$\mathbf{x}$	Markov-process random variable vector
ϕ	Longitude, rad
ψ	Latitude, rad
ρ	Atmospheric density, kg/m^3
ρ_{ref}	Reference density, kg/m^3
σ	Bank angle, rad
σ	Standard deviation
τ	Time constant, s
θ	Range angle, rad
a	Acceleration magnitude, m/s^2
C_D	Drag coefficient
C_L	Lift coefficient
D	Drag magnitude, N
g	Acceleration due to gravity, m/s^2
H	Atmospheric scale height, m

h	Altitude, m
h_{ref}	Reference altitude, m
J_2	Gravity perturbation
L	Lift magnitude, N
L/D	Lift-to-drag ratio
m	Mass, kg
q	Dynamic pressure, N/m^2
R	Planetary radius, m
r	Radius vector magnitude, m
s	Range, m
S_{ref}	Aerodynamic reference area, m^2
t	Time, s
V	Velocity magnitude, m/s
V_C	Circular velocity, m/s
W	Weight magnitude, N
x	Markov-process random variable

SUMMARY

During planetary entry, a vehicle uses drag generated from flight through the planetary atmosphere to decelerate from hyperbolic or orbital velocity. To date, all guided entry systems have utilized lift-modulation trajectory control. Deployable aerodynamic devices enable drag-modulation trajectory control, where a vehicle controls its energy and range during entry by varying drag area. Implementation of conventional lift-modulation systems is challenging for deployable systems. In contrast, drag-modulation trajectory control may be simpler and lower-cost than current state-of-the-art lift-modulation systems.

In this investigation, a survey of analytical methods for computing planetary entry trajectories is presented and the approximate analytical solution to the entry equations of motion originally developed by Allen and Eggers is extended to enable flight performance evaluation of drag-modulation trajectory control systems. Results indicate that significant range control authority is available for vehicles with modestly sized decelerators. The extended Allen-Eggers solution is closed-form and enables rapid evaluation of nonlifting entry trajectories. The solution is utilized to develop analytical relationships for discrete-event drag-modulation systems. These relationships have direct application to onboard guidance and targeting systems.

Numerical techniques were used to evaluate drag-modulation trajectory control for precision landing and planetary aerocapture missions, including development of prototype real-time guidance and targeting algorithms. Results show that simple, discrete-event drag-modulation trajectory control systems can provide landed accuracies competitive with the current state of the art and a more benign aerothermal

environment during entry for robotic-scale exploration missions. For aerocapture, drag-modulation trajectory control is shown to be feasible for missions to Mars and Titan and the required ΔV for periapsis raise is insensitive to the particular method of drag modulation. Overall, results indicate that drag-modulation trajectory control is feasible for a subset of planetary entry and aerocapture missions.

To facilitate intelligent system selection, a method is proposed for comparing lift and drag-modulation trajectory control schemes. This method applies nonlinear variational techniques to closed-form analytical solutions of the equations of motion, generating closed-form expressions for variations of arbitrary order. This comparative method is quantitative, performance-based, addresses robustness, and applicable early in the design process. This method is applied to steep planetary entry trajectories and shows that, in general, lift and drag-modulation systems exhibit similar responses to perturbations in environmental and initial state perturbations. However, significant differences are present for aerodynamic perturbations and results demonstrate that drag systems may be more robust to uncertainty in aerodynamic parameters.

Finally, the results of these contributions are combined to build a set of guidelines for selecting lift or drag-modulation for a Mars Science Laboratory-class planetary entry mission.

CHAPTER I

INTRODUCTION

1.1 Planetary Aeroassist Systems

1.1.1 Aeroassist Maneuvers

Spacecraft traveling near planetary bodies with atmospheres may use the planetary atmosphere to change their trajectory with aerodynamic forces. Termed aeroassist, these maneuvers may be used to reduce vehicle energy, change the direction of a vehicle's trajectory, or both, while using only a small amount of propellant, often providing a significant mass savings over equivalent fully-propulsive maneuvers. Figure 1 shows two types of aeroassist maneuvers: a) entry and b) aerocapture.

During entry, a vehicle uses drag generated from flight through the planetary atmosphere to decelerate from hyperbolic or orbital velocity. The vehicle state at the top of the atmosphere, commonly referred to as entry interface (EI), is typically considered to be the initial condition for entry trajectories. EI is defined at a specific altitude at which atmospheric density, and therefore aerodynamic force, is negligible.

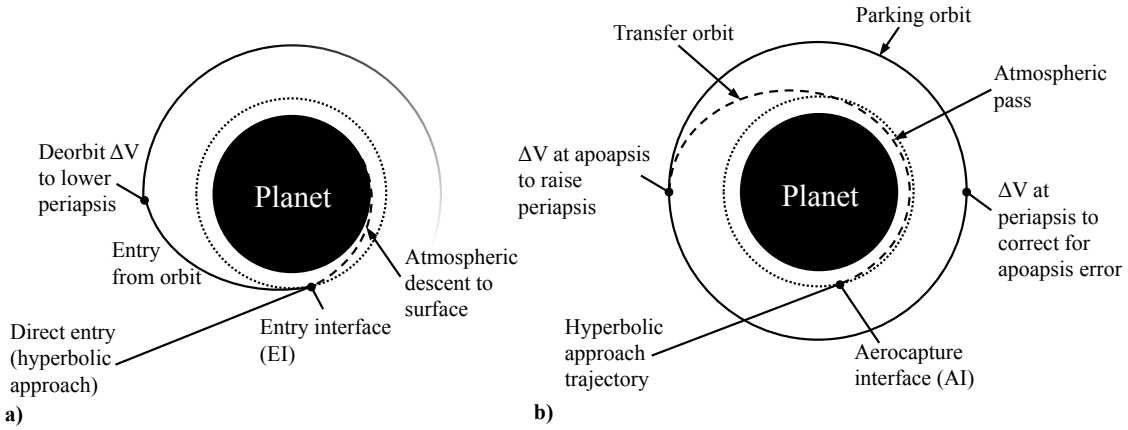

Figure 1: Example planetary aeroassist trajectories: a) entry and b) aerocapture.

After an entry vehicle passes through EI, hypersonic aerodynamic forces begin to build on the vehicle until they dominate its motion as shown in the example entry trajectory in Fig. 2. As atmospheric density increases with decreasing altitude, deceleration magnitude builds to a peak value (Fig. 2b). Aerodynamic heating from the high-speed flow peaks just before deceleration (Fig. 2c); integrated heat load continues to build throughout entry (Fig. 2d). The majority of the deceleration and heat pulses occur in a relatively narrow altitude band (Fig. 2a). Entry vehicles must be designed to accommodate both the high loads and high heat fluxes experienced during hypersonic flight through the atmosphere. For this reason, and to increase drag, entry vehicles utilize blunted aerodynamic surfaces; the flow field surrounding blunted surfaces carries away most of the thermal energy associated with the vehicle's decrease in kinetic energy [2]. Even so, a substantial thermal protection system (TPS) is required to protect the vehicle and its payload from the aerothermal environment. Once sufficient deceleration has occurred, planetary entry vehicles either deploy a terminal descent system, such as a parachute, or glide to a runway landing as the Space Shuttle did. Planetary entry maneuvers are accomplished solely through the dissipation of kinetic energy through aerodynamic control; to do so propulsively would require a deceleration system mass fraction on the order of that required for launch (near 90% at Earth). Such a vehicle would have to be launched itself and generally represents an infeasible scenario.

During aerocapture (see Fig. 1b), a vehicle performs a single pass through the atmosphere and returns to space, using drag to reduce energy to transition from a higher-energy orbit to a lower-energy orbit. For identical initial conditions, aerocapture trajectories typically exhibit lower peak deceleration and heat flux values relative to entry trajectories, because they deplete less energy. The challenges and benefits inherent in aerocapture are similar to that of entry, including exposure to a severe

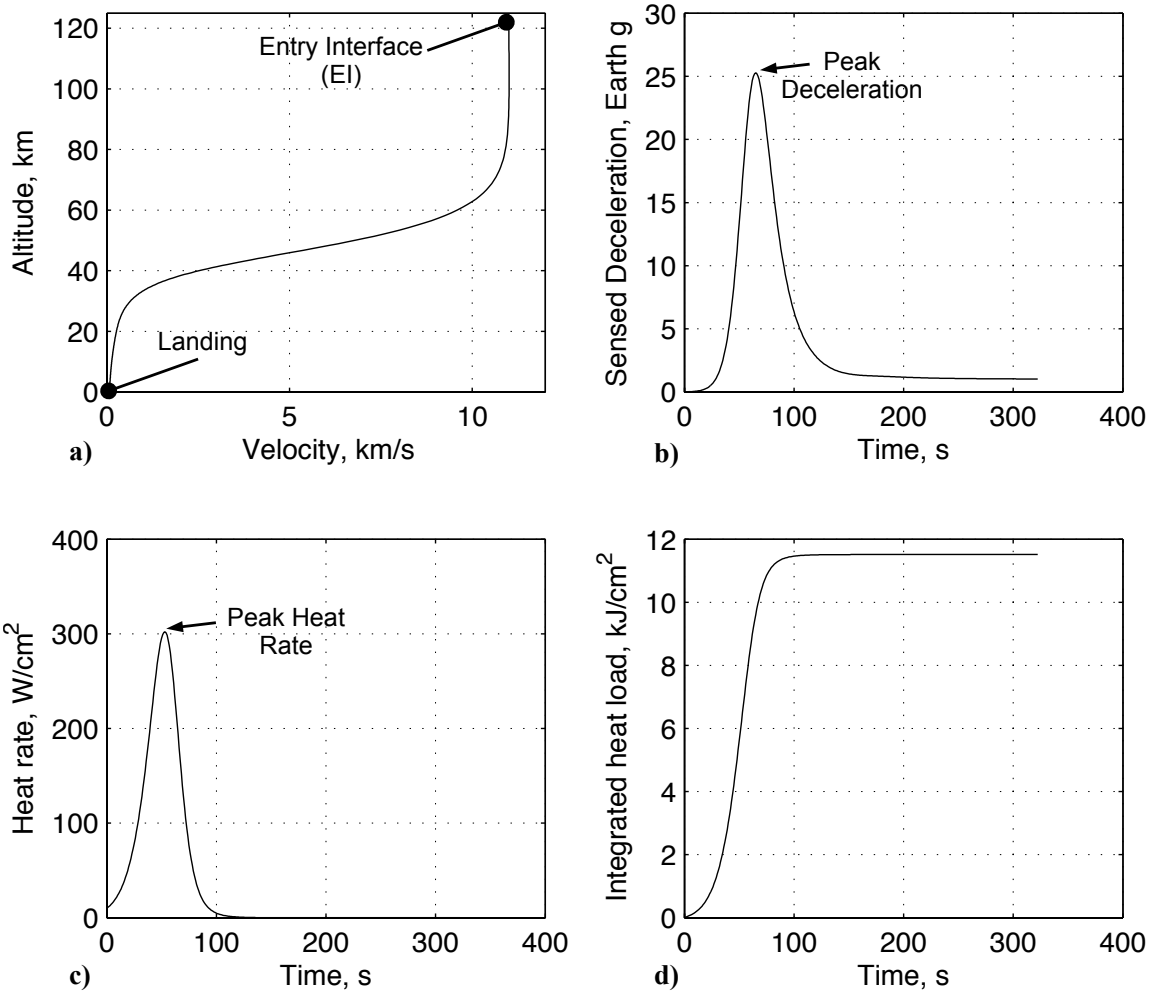

Figure 2: Example Earth entry trajectory: lunar return with $V_0 = 11$ km/s, $\gamma_0 = -8$ deg, $L/D = 0$, $\beta = 315$ kg/m^2, $r_N = 3.0$ m.

aerothermal environment and significant mass savings relative to full-propulsive options. Aerocapture typically requires two small propulsive changes in velocity (ΔV) after the atmospheric pass: one at the apoapsis of the transfer orbit to raise periapsis out of the atmosphere and one at periapsis to correct for any apoapse error. Relative to propulsive orbit insertion, the reduced propellant mass required for aerocapture may result in vehicle mass savings of 15% to nearly 300%, depending on mission and destination [3]. Plane changes are also possible during entry and aerocapture if out-of-plane control is available.

Atmospheric entry has been performed by numerous vehicle systems since the dawn of the space age. Early robotic systems, such as that used by the Corona program, utilized an entry vehicle to return film containing orbital reconnaissance imagery to the surface of Earth [4]. Atmospheric entry has also been a major part of every human spaceflight system, from Vostok to the Space Shuttle [5]. Recently developed entry systems include NASA's Mars Science Laboratory [6] and Orion Multipurpose Crew Vehicle [7] and Space Exploration Technologies' Dragon capsule [8]. While numerous test flights for aerocapture have been proposed, such as the Aeroassist Flight Experiment [9] and ST7 [10], aerocapture has never been demonstrated. However, aerocapture was a flight option for the Apollo Command Module [11] and has been the subject of extensive study. Because aerocapture utilizes nearly identical technology and flight systems as atmospheric entry, it is considered to be nearly flight-ready with current technology [12].

Atmospheric entry missions to date have relied on technology developed in the 1960s and 70s. While incorporating skip entry as a flight option, the current Project Orion largely uses Apollo-era entry technology developed in the 1960s [7]; the Space Shuttle entry system was developed in the 1970s [13]. Current Mars missions, capable of landed masses of approximately 1 metric ton, are near the performance limit of their Viking-era entry technology, also developed in the 1960s and 1970s [14]. Future

missions of interest at Earth, Mars, Venus, Titan, and the outer planets will require a significant improvement in the performance capabilities of planetary entry systems to accommodate the more massive payloads necessary to complete more ambitious mission goals while limiting launch costs [15]. This increase in capability may be achieved through the development of new technologies for planetary entry.

1.1.2 Deployable Decelerators

Future planetary entry systems must be able to provide more accurate delivery of more massive payloads than current systems to support the next generation of exploration missions. This performance improvement and increase in delivered payload mass may be achieved by reducing or eliminating the diameter and shape constraints placed on the entry system by the launch vehicle payload fairing, allowing the entry vehicle to assume an aerodynamic form that best facilitates mission success. Current launch vehicle fairings restrict maximum payload diameter to about 5 m. Deployable aerodynamic devices, both rigid and inflatable, have the potential to enable a broad spectrum of next-generation missions by mitigating launch vehicle payload fairing shape and size constraints on aeroassist vehicles and potentially providing an in-flight reconfiguration capability. While deployable decelerators have long been used for low-speed systems (e.g. parachutes for descent, projectile control via deployable fences), only recently has technology matured sufficiently to make deployable decelerators attractive for hypersonic applications.

The NASA draft Entry, Descent, and Landing Space Technology Roadmap released in November of 2010 lists Deployable hypersonic decelerators (DHDs) as a key recommended technology development area, stating "deployed rigid or flexible drag devices for both the entry and descent phases" and "improved entry and descent control authority through higher L/D, control surfaces, c.g. modulation, and controllable descent decelerators" [15] are enabling for the next generation of planetary

exploration missions. DHDs may be used to decrease a vehicle's ballistic coefficient, increase trajectory control authority, and provide additional robustness during entry. Ballistic coefficient (β) is defined by:

$$\beta = \frac{m}{C_D S_{ref}} \tag{1}$$

and may be thought of as the ratio of inertial to drag forces for a particular vehicle configuration of mass m, aerodynamic reference area S_{ref}, and hypersonic drag coefficient C_D. The Space Technology Roadmap identifies "low ballistic coefficient deployable decelerators" as a"key push technology" for missions to "all [planetary] destinations" [15]. DHDs are an enabling technology for low ballistic coefficient vehicles. A lower ballistic coefficient allows the vehicle to decelerate higher in the atmosphere, preserving altitude and timeline margin while reducing the severity of the aerothermodynamic environment. This reduces stress on the TPS and vehicle structure and reduces the criticality of the terminal descent timeline.

DHDs are frequently classified by their structure, which range from hypersonic inflatable aerodynamic decelerators (HIADs) to semi-rigid systems, where rigid spars support a flexible drag area, to fully rigid systems. Several examples are shown in Fig. 3: a) the Inflatable Re-entry Vehicle Experiment (IRVE-3) flight-test vehicle [16], b) the Adaptive Deployable Entry and Placement Technology (ADEPT) semi-rigid concept [17], and c) a trailing toroidal ballute concept for aerocapture missions [18]. These vehicles all provide deployable, lightweight drag areas that are compatible with current launch vehicle maximum diameter constraints.

Ref. [19] provides a summary of inflatable deployable decelerator development through 2005, conducted by both NASA and the Department of Defense. Since then, NASA has continued to mature HIAD technology through the IRVE sub-scale flight-test program [16] and wind-tunnel testing of larger-diameter concepts [20]. IRVE-3, the latest flight of the IRVE program, demonstrated lifting flight of a 3-m-diameter HIAD for the first time; lift was generated using a c.g. offset mechanism, but no

active control of the lift was attempted [21]. HIAD-based entry system architecture options were also featured prominently in NASAs Entry, Descent, and Landing Systems Analysis Study where they were used to decelerate large payloads in the thin Mars atmosphere [22, 23].

While significant development work has been completed for HIADs, little work has been completed for semi-rigid and rigid deployables. NASA's Space Technology Roadmap identifies the development of rigid deployable systems as an "immediate action," calling for investigation into "deployable entry systems that would be an alternative to inflatable approaches (currently being investigated) in order not to depend on a single path"[15]. Semi-rigid and rigid deployables may provide several advantages over HIADs, including reduced sensitivity to fluid-structure interaction effects, better micrometeoroid damage tolerance, and possible reconfigurabilty that may be used for steering [24]. The only significant development effort being conducted for these types of vehicles is the umbrella-like ADEPT semi-rigid concept [17]. Currently, ADEPT development is focused on a potential planetary entry mission at Venus, where its relatively large drag area will be used primarily to reduce the severity of the aerothermal environment [25].

Regardless of their structural class, only limited work has been completed to date in the area of guidance and control for DHDs, making current assessments of DHD flight performance suspect, despite their promise. The NASA Space Technology Roadmap notes that "advanced guidance and navigation systems adapted to deployable system controllers" will be required [15]. Initial feasibility studies have outlined the potential benefits of DHDs, particularly HIADs, but have made numerous simplifying assumptions regarding vehicle guidance and flight control systems [26, 22, 23, 17, 27, 28]. In general, these studies have assumed that DHD vehicles may be steered in the much the same way as more traditional entry systems and fail to take into account the potential complexities and limitations of effectors required

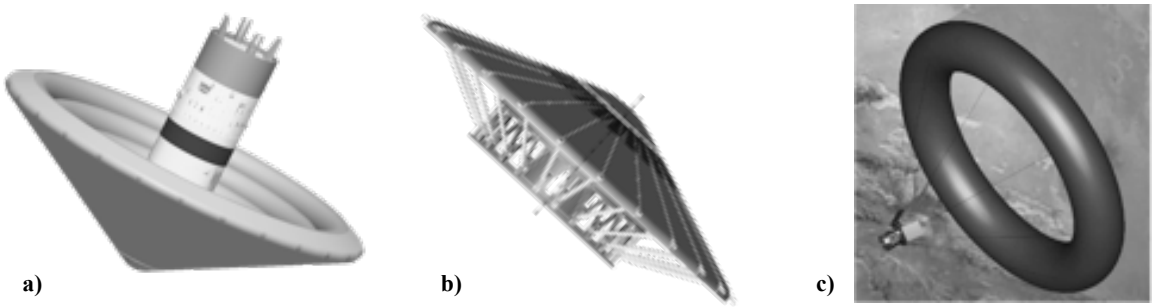

Figure 3: Deployable hypersonic aerodynamic decelerator concepts: a) IRVE-3, b) ADEPT, c) trailing ballute.

for large, and potentially flexible, vehicles. Future work must build on these early studies by increasing the level of detail, reevaluating assumptions, and investigating additional flight control methods and vehicle configurations.

1.2 Aeroassist Flight Dynamics

1.2.1 The Equations of Motion

The equations of motion for aeroassist systems are well-documented in the literature. For example, the full six-degree-of-freedom equations of motion are presented by Platus in [29]. This thesis focuses on translational motion and neglects rotational motion of the vehicle, allowing use of the two and three-degree-of-freedom formulations of the equations of motion.

The hypersonic phase of an aeroassist (aerocapture or planetary entry) maneuver is typically unpowered, in the sense that thrust is used only for attitude control. The small amount of thrust required for attitude control results in a nearly constant vehicle mass. Using Newton's Second Law, the three-degree-of-freedom translational equation of motion for a general entry vehicle with constant mass m is:

$$\sum \mathbf{F}_{ext} = \mathbf{L} + \mathbf{D} + \mathbf{W} = m\frac{d\mathbf{V}}{dt} \tag{2}$$

In scalar form, the three-degree-of-freedom equations of motion for a nonrotating spherical planet are given by [30]:

$$\frac{dV}{dt} = -\frac{D}{m} - g\sin\gamma \tag{3a}$$

$$V\frac{d\gamma}{dt} = \frac{L}{m}\cos\sigma - g\cos\gamma + \frac{V^2}{r}\cos\gamma \tag{3b}$$

$$V\frac{d\psi}{dt} = \frac{L}{m}\frac{\sin\sigma}{\cos\gamma} - \frac{V^2}{r}\cos\gamma\cos\psi\tan\phi \tag{3c}$$

$$\frac{dr}{dt} = V\sin\gamma \tag{3d}$$

$$\frac{d\theta}{dt} = \frac{V\cos\gamma\cos\psi}{r\cos\phi} \tag{3e}$$

$$\frac{d\phi}{dt} = \frac{V\cos\gamma\sin\psi}{r} \tag{3f}$$

where

$$L = \frac{1}{2}\rho V^2 S_{ref} C_L \tag{4a}$$

$$D = \frac{1}{2}\rho V^2 S_{ref} C_D \tag{4b}$$

$$h = r - R \tag{4c}$$

where ρ is the atmospheric density, S_{ref} is the aerodynamic reference area, and C_L and C_D are the hypersonic aerodynamic lift and drag coefficients, respectively. Lees and Hartwig, and Cohen provide a good justification for assuming a non-rotating planet and atmosphere, resulting in the inertial and planet-relative velocities being equal [31].

The two-degree-of-freedom equations of motion restrict the three-degree-of-freedom equations to the plane defined by $\mathbf{r}_0$ and $\mathbf{V}_0$ (see Fig. 4). The scalar, planar equations of motion may be derived for a non-rotating planet (in a similar manner as Ch. 7 of Ref. [32]) by considering the coordinate systems and free-body diagram for a planar entry trajectory shown in Fig. 4. The coordinate frames are the planet-centered inertial frame (X_I, Z_I), the local horizontal frame (X_L, Z_L), and the wind frame (X_W, Z_W). Expressing the vectors in Eq. (2) in the wind frame, one obtains

two scalar equations of motion:

$$\frac{dV}{dt} = -\frac{D}{m} - g\sin(\gamma) \tag{5a}$$

$$\frac{d\gamma}{dt} = \frac{d\theta}{dt} + \frac{1}{V}\frac{L}{m} - \frac{g}{V}\cos(\gamma) \tag{5b}$$

where the range angle, θ, is the angle between the X_I and X_L directions and the flight-path angle, γ, is the angle between X_L and X_W directions and is defined to be positive above the local horizontal. From kinematics, two more equations may be written for altitude above the planetary surface, h, and range angle, assuming a spherical planet:

$$\frac{dh}{dt} = V\sin\gamma \tag{6a}$$

$$\frac{d\theta}{dt} = \frac{V\cos(\gamma)}{h + R_E} \tag{6b}$$

Combining Eqs. (5), (6), (4a), and (1); recognizing that $C_L/C_D = L/D$; and rearranging terms, the planar equations of motion for an aeroassist vehicle may be written as:

$$\frac{dV}{dt} = -\left(\frac{\rho}{2\beta}\right)V^2 - g\sin(\gamma) \tag{7a}$$

$$\frac{d\gamma}{dt} = \frac{V\cos\gamma}{R_E + h} + \left(\frac{\rho}{2\beta}\right)\left(\frac{L}{D}\right)V - \frac{g}{V}\cos(\gamma) \tag{7b}$$

$$\frac{dh}{dt} = V\sin(\gamma) \tag{7c}$$

$$\frac{d\theta}{dt} = \frac{V\cos\gamma}{R_E + h} \tag{7d}$$

The acceleration due to gravity changes little during entry, as altitude changes are typically in the 10s of km compared to planetary radii in the 1000s of km. Therefore, g is assumed to be constant during entry. Atmospheric density is assumed to vary exponentially with altitude according to:

$$\rho = \rho_{ref}\exp\left[\frac{h_{ref} - h}{H}\right] \tag{8}$$

where H is the scale height and ρ_{ref} is the reference density at a reference altitude, h_{ref}. While the scale height varies with altitude in a real atmosphere, peak deceleration, peak heating, and most interesting aspects of planetary entry occur in a

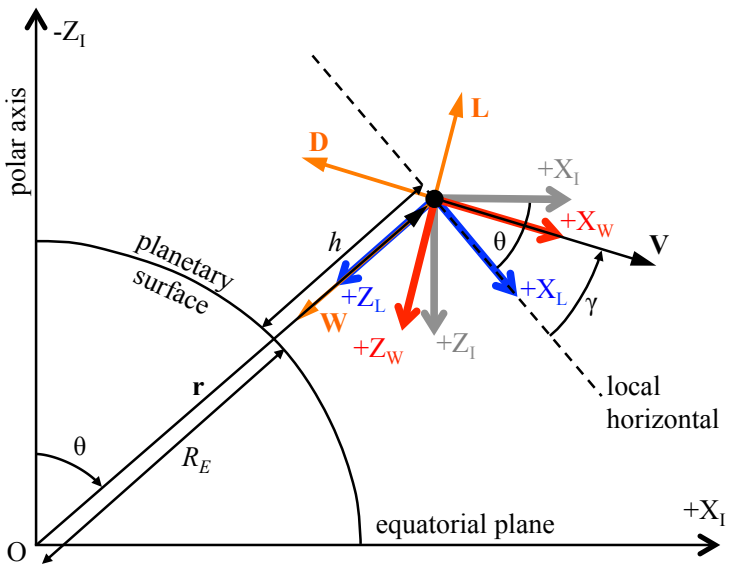

Figure 4: Coordinate systems and free-body diagram for planar entry trajectories.

relatively narrow altitude band, making the assumption of constant H reasonable. This assumption is consistent with an isothermal atmosphere in that altitude band. The reference density need not be selected as the zero-altitude density. Due to the variation in scale height, choosing a reference density and scale height base on a higher altitude may produce a more accurate representation of the true atmospheric density profile over the altitude range in which entry occurs.

The equations of motion may be further simplified by assuming constant values for the aerodynamic coefficients, C_L and C_D, and thus for β and L/D. While these parameters generally vary with Mach number and angle-of-attack to first order, Mach-number independence in the hypersonic flight regime (Mach numbers above about 5) and the lack of angle-of-attack control on most entry vehicles make constant aerodynamic coefficients a good assumption for entry trajectories [33].

1.2.2 Trajectory Control Options

Exerting a measure of control over an entry trajectory during flight is important for many missions, whether it is used to limit peak deceleration, perform precision

landing, or accomplish another objective. Mission designers typically choose initial conditions (γ_0, V_0) for a particular trajectory to ensure favorable flight performance. However, even the most perfectly selected initial conditions do not eliminate the need to steer out error during entry caused by uncertainty in vehicle properties, onboard state estimation, and the planetary environment, as well as delivery error. The planar equations of motion (Eq.(7)) show that only two vehicle parameters are available to control the vehicle trajectory during flight: lift-to-drag ratio (L/D) and ballistic coefficient (β). All other parameters are either states or environmental parameters over which no direct control is possible. While hypersonic trajectory control may be achieved by varying one or both of these parameters, atmospheric entry systems to date have used control of L/D exclusively. In this thesis, trajectory control achieved through changes in L/D will be termed lift modulation; trajectory control achieved through changes in β will be termed drag modulation.

1.2.2.1 Lift-Modulation Trajectory Control

To date, all guided hypersonic systems have utilized lift modulation for trajectory control. Specifically, all guided entry systems have utilized a bank-angle (σ) steering scheme where only the direction of the lift is modulated for trajectory control. Notable bank-to-steer entry vehicles include the Apollo Command Module [11], the Soyuz Descent Module [34], the Mars Science Laboratory [35], and the forthcoming Orion Crew Module [36]. Existing and proposed planetary entry systems have also utilized angle-of-attack (α) control during entry, but this capability has been reserved to maintain a specific angle-of-attack profile to reduce uncertainty in aerodynamic properties, not to control the vehicle trajectory directly. Examples of entry vehicles that utilize angle-of-attack control coupled with bank-angle steering include the Space Shuttle Orbiter [37], NASA's HL-20 [38], and the Sierra Nevada Corporation's Dream Chaser [39].

Figure 5 shows an example bank-angle steering maneuver for a blunt body vehicle: changing the bank angle, σ, rotates the lift vector ($\mathbf{L}$) about the vehicle's wind-relative velocity vector ($\mathbf{V}_W$). Bank angle does not appear explicitly in Eqs. (7); rather it is implicitly included in the value of L/D. Because Eqs. (7) are two-dimensional, the L/D in Eq. (7b) is the in-plane L/D, were L is the amount of lift in the in-plane direction. The in-plane L/D is related to the bank angle and the total L/D by:

$$\frac{L}{D} = \cos\sigma \left(\frac{L}{D}\right)_{total} \tag{9}$$

While bank maneuvers have no direct effect on the drag vector ($\mathbf{D}$), they do change the amount of lift pointed in the vertical direction. A more lift-up orientation causes the vehicle to decelerate at a higher altitude and lower atmospheric density, reducing the magnitude of the drag vector; a more lift-down orientation causes the vehicle to decelerate at a lower altitude and higher atmospheric density, increasing the magnitude of the drag vector. In this manner, a vehicle may use bank-angle steering to control its flight path and energy depletion rate, allowing it to satisfy a variety of trajectory constraints on range, peak deceleration, and heating. However, because the vehicle has no control over its lift magnitude, bank angles other than 0 deg and 180 deg result in an out-of-plane component of lift that causes the vehicle to turn. This out-of-plane component may be used for crossrange control but must be continuously managed through bank reversals to maintain the desired heading. A bank reversal (see Fig. 6) is a maneuver in which the vehicle changes the sign of its out-of-plane component of lift while maintaining the same in-plane, or vertical, lift magnitude, e.g. changing the bank angle from 60 deg to -60 deg. Periodic bank reversals maintain heading but cause disturbances to the in-plane lift due to their finite nature: bank slew maneuvers may require a significant amount of time to complete, during which the in-plane lift is not at its prescribed value.

Bank-angle steering is particularly well suited to blunt-body capsules. Blunt-body capsules are typically axisymmetric; lift is generated by offsetting the c.g. from the

centerline, causing the vehicle to fly at a nonzero angle-of-attack (as shown in Fig. 5). While capsule-type vehicles have simpler TPS and exhibit excellent packaging efficiency, they do not possess the ability to control the magnitude of their lift: the restoring aerodynamic pitch moment is generally too large to be overcome by the onboard reaction control system (RCS) jets. However, winged and lifting body vehicles that possess aerodynamic control surfaces capable of countering the aerodynamic pitch moment still use bank-angle steering as the primary means of trajectory control in the hypersonic regime. For example, while the Space Shuttle's body flap could control the magnitude of the lift vector, the body flap was instead used to maintain a prescribed angle-of-attack (and therefore L/D) profile to reduce aerodynamic uncertainty while bank-angle steering was used to control energy and range [37].

For lift-modulation trajectory control systems, hypersonic L/D is the control authority metric. Higher values of L/D imply a greater ability to control a given trajectory, while lower values of L/D imply a lesser ability. An example of this is the ability of higher L/D vehicles to limit peak deceleration during entry, as shown in Fig. 7.

Figure 8 shows an example trajectory for a bank-to-steer lift-modulation system: Orion return from low-Earth orbit [40]. The vehicle in this trajectory has a modest L/D of 0.25 at Mach 25. As the vehicle decelerates, it maintains a relatively constant flight-path angle; the presence of lift also allows it to limit deceleration to less than 4 g while accurately targeting a landing site (see Fig. 8c). The on-board guidance algorithm varies the bank angle (Fig. 8d) to reach the desired landing site. The magnitude of the bank angle is commanded to manage vehicle energy and downrange, while the sign of the bank angle is commanded to limit out-of-plane error. Bank reversals are commanded when out-of-plane errors exceed a pre-set deadband (Fig. 8e). However, control lag when performing bank reversals results in command tracking errors (Fig. 8d); these errors require additional control authority to steer out during

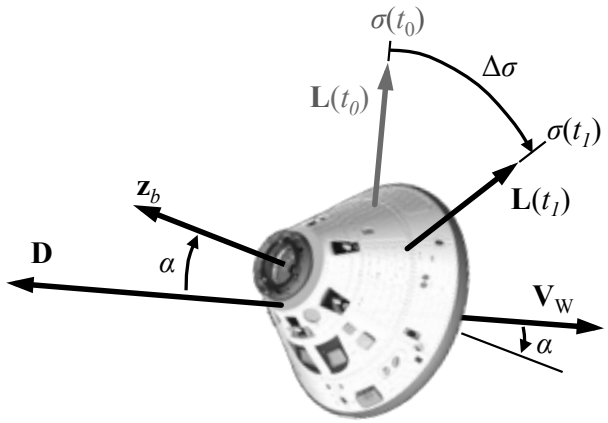

Figure 5: Bank-angle steering for blunt body entry vehicle.

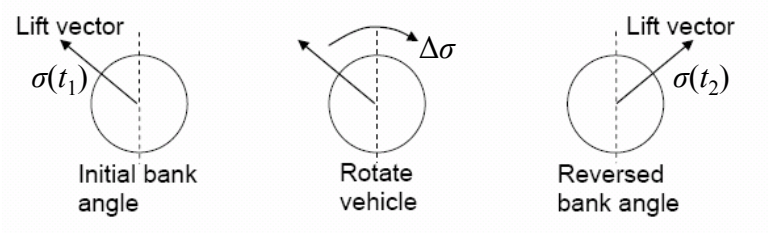

Figure 6: Bank reversal, wind-relative velocity vector is directed out of the page.

entry. This trajectory performs four bank reversals, introducing significant error.

1.2.2.2 Drag-Modulation Trajectory Control

DHDs enable new options for trajectory control during atmospheric flight. One such option is drag-modulation trajectory control. Consider the ballistic coefficient defined in Eq. (1). The ballistic coefficient may be thought of as the ratio of inertial to drag forces; decreasing the ballistic coefficient increases the influence of drag forces relative to inertial forces, increasing the rate of energy depletion during atmospheric flight. Increasing the ballistic coefficient has the opposite effect. Therefore, an entry vehicle that can vary its ballistic coefficient is capable of controlling its energy or range in a manner similar to that of a lift-modulation vehicle. Operationally, changing vehicle mass by a significant amount is difficult and undesirable. For an entry vehicle of constant mass m, drag-modulation trajectory control is accomplished by changing

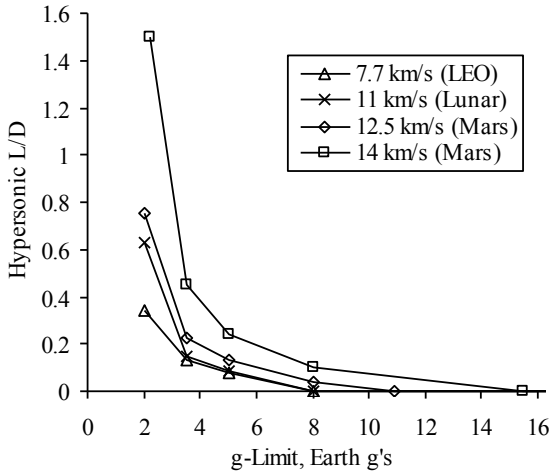

Figure 7: Required L/D to achieve a particular limit on peak deceleration during planetary entry at several velocities [41].

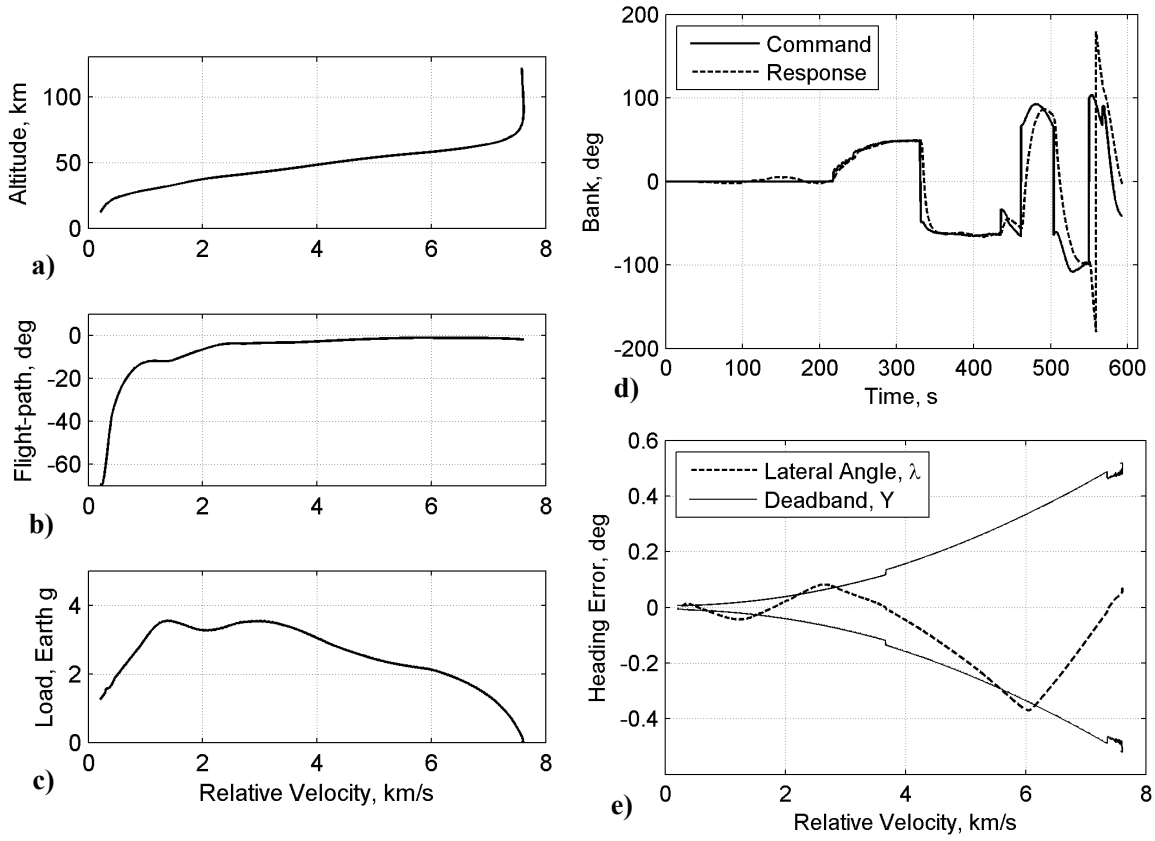

Figure 8: Example lift-modulation entry trajectory using bank-angle steering [40].

the drag area ($C_D S_{ref}$) to change ballistic coefficient and adjust the magnitude of the drag force.

Drag-modulation trajectory control is a prime candidate for use with large, flexible heatshields, such as those envisioned by NASA's HIAD program. While NASA's HIAD development program will lead to mature inflatable devices suitable for drag-modulation trajectory control applications, studies to date have not considered drag modulation as a trajectory control option [22, 23]. Instead, they have assumed that lift-modulation trajectory control is possible for these types of vehicles, either through bank-angle or angle-of-attack modulation. However, effector requirements for large inflatable vehicles may make lift modulation infeasible or undesirable. For these types of vehicles, or for missions in which a simpler system is enabling in terms of cost and risk, drag-modulation trajectory control presents a solution that does not require complex effectors or asymmetric flight conditions. The ability to fly at zero angle of attack reduces the criticality of vehicle aerodynamic properties at asymmetric flight conditions; the absence of an RCS eliminates concerns about effector latency and jet interaction with a flexible structure and complex wake flow field; the absence of propellant tanks, propellant, and ejectable ballast masses (for c.g. control) greatly simplifies packaging, system integration, and operational complexity.

Only a small number of studies on drag modulation for aeroassist missions is available in the literature. In the 1960s, Levy determined a closed-form solution using drag modulation to limit the rate of increase of deceleration during entry [42], Rose and Hayes evaluated drag modulation as means for orbit phasing and entry targeting [43], and Warden developed analytical solutions for entry with varying ballistic coefficients to describe trajectories with significant TPS mass loss through ablation [44]. More recently, Vinh et al. proposed an explicit analytical guidance algorithm for aeroassisted orbit transfer [45] and Kuo et al. examined the use of drag modulation to track reference trajectories for ballistic missiles [46]. These studies all assumed drag could

be controlled continuously within a given interval.

Discrete-event drag modulation has been studied for planetary aerocapture mission applications at the conceptual level. McRonald conducted several studies addressing discrete-event drag modulation options for aerocapture at several planetary bodies of interest [47, 48, 49]. Hall and Le identified common trajectory properties for discrete-event drag-modulation systems across different vehicles, missions, and atmospheric compositions [50]. Westhelle and Masciarelli performed a more detailed study of a discrete-event system for use at Titan [51]. Only two studies in the current literature attempt to address real-time trajectory control issues for discrete-event systems, beyond identifying that jettison timing is critical: Miller et al. present a real-time predictive algorithm for single-stage jettison aerocapture at Titan using a trailing toroidal ballute but provide only limited information on flight performance [18]; Johnson and Lyons use a computationally simple heuristic trigger based on curve fits of the aerocapture vehicle dynamics to perform single-stage jettison aerocapture at Titan, but results show that this technique results in a relatively high failure rate in the presence of expected uncertainty [52].

Overall, the feasibility of using drag-modulation trajectory control for aerocapture has not been conclusively addressed in the literature; the feasibility of using drag-modulation trajectory control for planetary entry is not addressed at all in the current literature. Specifically, no studies have comprehensively addressed the costs and benefits of continuous versus discrete-event drag-modulation systems, determined whether real-time targeting is feasible, or investigated flight performance for drag-modulation systems for planetary entry.

1.2.3 Aerodynamic Force Parameterization

It is perhaps important to note that the common decomposition and parameterization of aerodynamic forces into lift and drag components is inherently arbitrary.

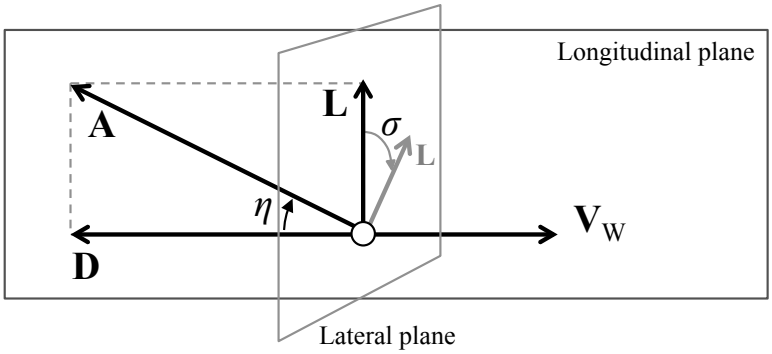

Figure 9: Options for parameterizing the aerodynamic force.

Although convenient, the lift and drag forces are merely one realization of the total aerodynamic force acting on an atmospheric flight vehicle. For example, in two dimensions, one could just as easily parameterize the total aerodynamic force **A** in terms of its magnitude A and an angle η, as shown in Figure 9.

This inherent arbitrariness raises the question of whether there is a fundamental difference between lift and drag-modulation systems, since the basis for their separate designation is arbitrary. For example, a lift-modulation vehicle that controls its L/D through angle-of-attack modulation changes not only its lift but also its drag when changing angle of attack. For the purposes of this work, lift and drag modulation will be defined in the following manner. Lift-modulation trajectory control is that which utilizes changes in lift to directly modify the trajectory in the desired manner; drag-modulation trajectory control is that which utilizes changes in drag to directly modify the trajectory. Hybrid systems which specify changes in lift and drag to achieve trajectory objectives are also possible. Under these definitions, the Space Shuttle Orbiter is a pure lift-modulation system in the hypersonic regime. While angle-of-attack modulation is available and used, indicating some level of drag-modulation capability, it is only used in an open-loop sense to maintain a particular angle-of-attack profile, with the primary goal of reducing aerodynamic uncertainty during hypersonic flight. Range, deceleration, and heating constraints are all met through the use of lift modulation through bank-angle steering.

1.2.4 Planetary Entry Corridors

A central goal of trajectory analyses for planetary entry systems is the definition of the entry corridor for a specific mission and entry vehicle. For a given inertial velocity at entry interface, there are many possible trajectories that satisfy a given set of trajectory constraints. The entry corridor is the locus of initial states at the top of the atmosphere for which the vehicle can achieve its mission objectives, including satisfying relevant trajectory and terminal constraints. The entry corridor is illustrated in Fig. 10: an undershoot trajectory results from trajectories below the corridor, overshoot trajectories result from trajectories above the corridor. The entry corridor is frequently defined in terms of the range of acceptable EI flight-path angles. For entry, if the initial flight-path angle is too shallow, the vehicle will skip out of the atmosphere. If the initial flight-path angle is too steep, the vehicle will not dissipate enough energy before it reaches the surface of the planet. The steep, or undershoot, and shallow, or overshoot, trajectories bound the aerodynamic corridor.

Additional requirements may be imposed on entry trajectories that define an operational corridor. Such constraints may include limits on the peak heat rate, total integrated heat load, or on the peak deceleration. Peak heat rate and peak deceleration typically limit the undershoot boundary, whereas limits on the integrated heat load will limit the overshoot boundary [53].

Entry vehicles that possess a means of trajectory control, either through lift or drag modulation, may use their control authority to widen the corridor. Figure 11 shows example aerodynamic and operational corridor-bounding trajectories for a bank-to-steer lift-modulation system. The lift vector is used to allow the vehicle to enter the atmosphere at a wider range of EI flight-path angles. The overshoot boundary is achieved with a lift-down orientation, followed by constant altitude flight to reduce peak deceleration. The aerodynamic undershoot boundary is achieved with a lift-up orientation and a 90-deg flight-path angle; this trajectory reaches a peak declaration

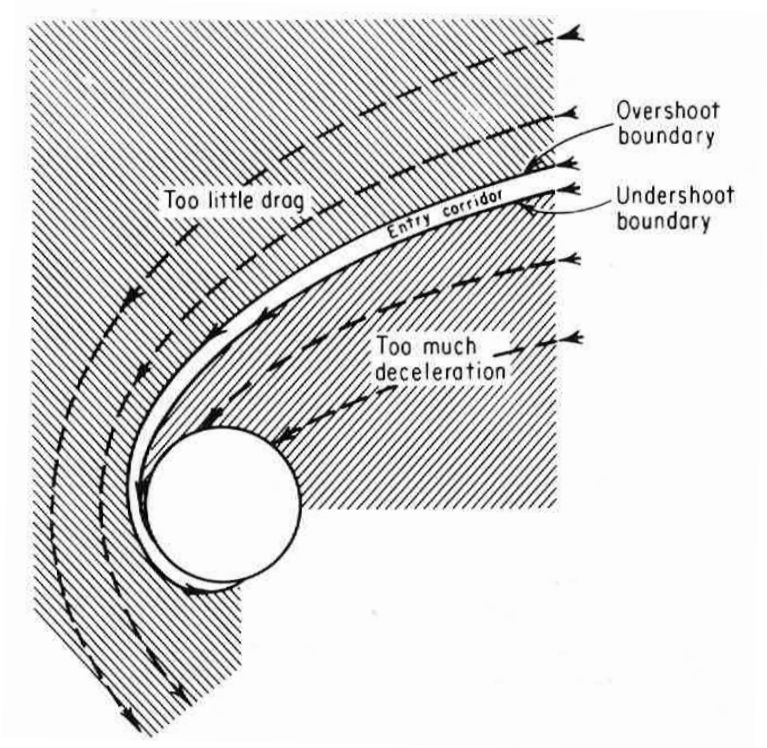

Figure 10: Planetary entry corridor and bounding entry trajectories [53].

in excess of 360 g and represents a vertical dive. The operational undershoot boundary is achieved with a lift-up orientation and constant deceleration flight to limit peak deceleration to 5 g.

1.2.5 Flight Performance Evaluation

The equations of motion for planetary entry flight dynamics are a set of coupled, first-order, nonlinear, ordinary differential equations. While these equations are not complex, they are highly nonlinear due to the presence of the planetary atmosphere and defy analytical solution unless simplifying assumptions are applied. When planetary entry flight performance was first studied in the 1950s and 60s, analytical approximations were developed to enable vehicle and mission designers to evaluate vehicle performance without or with minimal computer usage. New approximations continued to be developed into the 1970s. However, advances in computing eventually made high-accuracy numerical integration of the equations of motion feasible for most

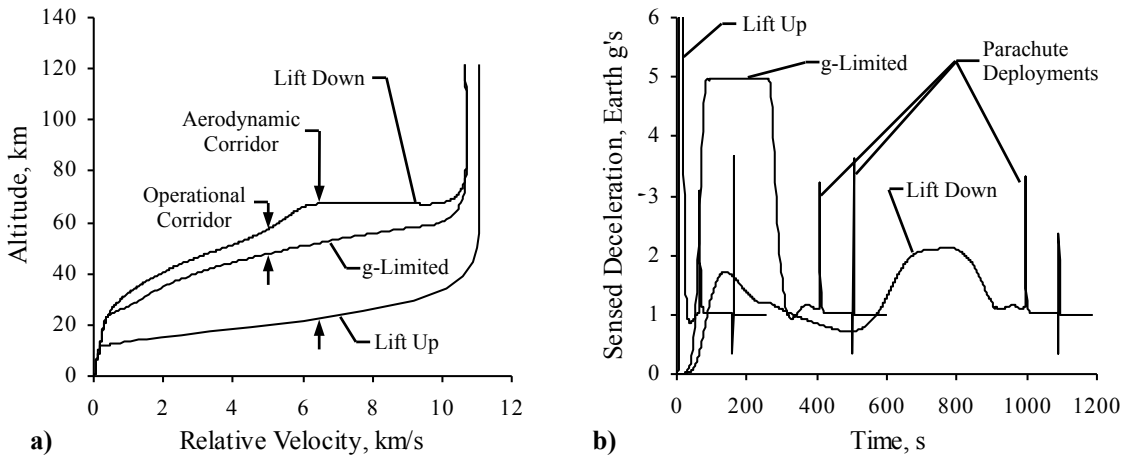

Figure 11: Notional corridor-bounding entry trajectories for a lift-modulation entry system [41].

applications. Today, vehicle and missions designers have significant computational resources available, enabling rapid, low-cost assessments of entry trajectories.

Early approximations by Sänger [54], Allen and Eggers [55, 56], Lees [31], Ting [57], Loh [58], Arthur [59], Kornreich [60], and others from the middle 1940s to the early 1960s addressed specific classes of aeroassist trajectories and vehicles. Figure 12 shows how these early, first-order approximations each addressed only a small area of the entry trajectory space of interest to the community (in Fig. 12, EI flight-path angle is denoted by θ_f, with positive values below the local horizontal). For example, Loh's solution is only valid for L/D less than zero and small initial flight-path angles; positive values of L/D require the use of a totally different approximate solution. This limited applicability made these early first-order approximations difficult to use: determining the boundaries of applicability was difficult when numerical solutions were not generally available for comparison and evaluation purposes.

The limited applicability of most first-order approximations led to the development of more generally applicable second-order approximations. In 1962, Loh proposed a second-order method for a wide range of entry conditions [61], with later extensions to skipping entry and other more complex trajectories [62, 63]. Loh's

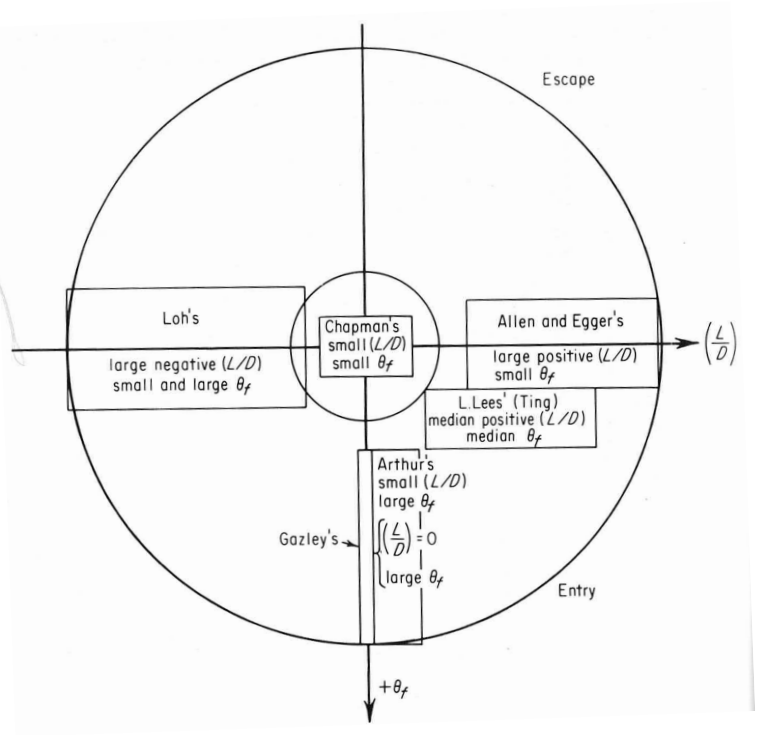

Figure 12: Applicability of various first-order approximations of the equations of motion [1].

method utilizes insights gained from the development of first-order solutions. Specifically, he found that combinations of certain terms were insensitive to integration over trajectory states, allowing analytical integration of a specific form of the equations of motion. This results in two coupled, transcendental equations that relate flight-path angle, atmospheric density, and velocity. Solutions are obtained by choosing a state for a domain, typically velocity, then iteratively solving the system of two equations and two unknowns for the other two states over the domain.

In 1965, Citron and Meir published a second-order approximation that assumes density variation can be approximated by a power series of a velocity-like parameter [64] . By neglecting powers higher than two, Citron and Meir were able to develop explicit expressions for density and flight-path angle as functions of velocity. This approximation is generally superior to Loh's in accuracy. Citron and Meir also show how Low's solution can be derived using their method when powers above one are

neglected; the authors point out that this is equivalent to "neglecting the gravity and centrifugal forces compared to the inertia and drag forces for a ballistic vehicle."

These second-order approximations trade better accuracy for ease of evaluation. Loh's approximation requires iterative solution of two transcendental equations at each point on the trajectory; the Citron-Meir approximation requires evaluation of the exponential integral at each point. The level of complexity required to utilize either of these approximations is comparable to that required to numerically integrate the equations of motion on a modern computer. However, such analytical solutions provide additional information beyond trajectory data: analytical solutions may be used to provide information on partial derivatives, sensitivities, and other insights into a particular trajectory.

Using a different approximation paradigm, hybrid numerical-analytical solutions to the equations of motion were developed that were more accurate than the analytical approximations developed in the 1960s. These hybrid approximations required numerical integration, but sought to limit computational resource requirements. The first of these was the approximation developed by Chapman in 1959 [65]. Chapman was able to collapse the equations of motion into a single second-order ordinary differential equation by performing a carefully orchestrated change of variables. This differential equation only needed to be solved once numerically; other trajectories could then be found through arithmetic manipulations of the single trajectory. Vinh and his students at the University of Michigan revised, enhanced, and extended Chapman's method to all aeroassist trajectory types, including orbit decay, to additional degrees of freedom, to exact solutions, and phugoid modes [66, 30, 67]. Ferreira contributed further refinements to this body of work as late as 2000 [68]. However, similar to the second-order solutions, these solutions trade reduced computational requirements for increased mathematical complexity.

As computers became both powerful and ubiquitous, engineers began to approximate entry trajectory solutions by integrating the equations of motion directly using numerical techniques instead of using the previously developed analytical and hybrid approximate techniques. Numerical integration of the equations of motion allows one to determine trajectory and performance parameters of interest for a particular entry system configuration. Complex computer programs, typically described as simulations, have been developed to handle a wide variety of systems and environments, such as the Program to Optimize Simulated Trajectories (POST) [69], the Dynamic Simulator for ENtry Descent and Surface landing (DSENDS) [70], and the Advanced NASA Technology Architecture for Exploration Studies (ANTARES) [71]. These simulations include a range of environment and vehicle models of varying fidelity and can accommodate complex nonlinearities, such as vehicle configuration changes at parachute deploy.

These complex simulations require significant effort to set up for a particular analysis and a relatively large quantity of information to model a given aeroassist vehicle and its mission. Early in the design phase, using a complex simulation typically requires one to either wait until the design matures to evaluate its performance or make a large number of assumptions about yet-to-be-determined vehicle parameters. Making assumptions about unknown vehicle parameters may lead to misleading results and create design inertia based on an arbitrary choice that is difficult to change later in the design process. These issues can be exacerbated by the widely-held misconception that high-fidelity numerical simulations always produce accurate results. For these reasons, the power of high-fidelity numerical simulation and readily available inexpensive computational resources have limited exploration of both vehicle and mission designs and understanding of those designs early in the design phase when exploration and understanding may have the largest positive impact on the final design.

1.3 Contributions of Thesis

The body of work presented in this thesis advances the state of the art in several areas of interest to the aeroassist and design methods communities. Specific contributions are listed below and are discussed in detail in subsequent chapters.

- *Extended the Allen-Eggers ballistic entry trajectory solution.*

  The closed-form analytical solution to the equations of motion for ballistic entry developed by Allen and Eggers is enhanced and extended. Specifically, a method of choosing an appropriate constant flight-path angle is identified, a closed-form expression for range to go is developed, and limits based on the equations of motion and acceptable approximation error are proposed to bound the domain of applicability of the Allen-Eggers solution. These extensions address key weaknesses in the original solution and a gap in the current literature: existing analytical solutions for ballistic entry do not provide closed-form expressions for flight range. These new relations are placed in the proper context through completion of a comprehensive survey of analytical methods for the solution of planetary entry trajectories.

- *Developed closed-form analytical relationships for discrete-event drag modulation systems.*

  The extended and enhanced Allen-Eggers approximate solution is used to evaluate discrete-event drag-modulation trajectory control systems for planetary entry. Closed-form, analytical boundaries on jettison conditions are developed to limit peak deceleration and peak heating. The ratio of the maximum to minimum ballistic coefficient is shown analytically to be the control authority metric for drag-modulation systems, analogous to L/D for lift-modulation systems.

- *Demonstrated feasibility of drag-modulation trajectory control for planetary entry and aerocapture missions.* This investigation further demonstrates that

discrete-event drag-modulation trajectory control for planetary entry and aerocapture missions is feasible and exhibits flight performance competitive with state-of-the-art lift-modulation systems. Prototype guidance and targeting algorithms for drag-modulation trajectory control are developed and tested to verify that it is possible for onboard systems to determine and execute the drag profiles necessary to meet mission requirements.

- *Leveraged variational methods and closed-form analytical solutions to provide quantitative, performance-based measures of robustness for planetary entry systems.*

  A quantitative method for comparing bank-to-steer lift-modulation and discrete-event drag-modulation systems to facilitate system selection is developed with the following properties:

  - Quantitative, to provide transparency.
  - Performance-based, to provide a common basis to compare disparate solutions.
  - Includes robustness, to capture off-nominal performance considerations.
  - Applicable early in design process, to facilitate timely decision-making.

  This is accomplished by applying nonlinear variational methods to established closed-form analytical trajectory solutions. This method results in closed-form solutions for variations of arbitrary order due to perturbations in initial state, environment parameters, and vehicle parameters. Lift and drag-modulation systems are shown to exhibit nearly identical responses to model and state perturbations with the exception of aerodynamic perturbations. Drag-modulation systems are not generally susceptible to lift perturbations, as they may be spun to null out the integrated effects of any lift generated. Lift-modulation systems are still subject to uncertainty in drag as well as lift, decreasing their robustness

relative to drag-only systems and requiring them to devote additional control authority to steering out error caused by uncertainty in lift.

- *Developed guidelines for choosing between lift and drag-modulation trajectory control systems for planetary entry.*

  Results of the previous contributions are combined to build a table of guidelines for selecting lift or drag-modulation systems early in the design cycle. This set of guidelines will aid mission and vehicle designers in making intelligent decisions about trajectory control systems for planetary applications.

CHAPTER II

SURVEY OF ANALYTICAL SOLUTIONS FOR PLANETARY ENTRY TRAJECTORIES

Early efforts to understand planetary entry flight dynamics utilized analytical approximations for two reasons: computational resources were limited (although some capability was available) and a desire to gain a thorough understanding of the topic. Eventually, inexpensive and universal access to significant computational resources made numerical integration the approximation method of choice. Today, numerical integration techniques are the standard method for evaluating the equations of motion for planetary entry. However, approximate analytical solutions remain useful for many applications, including onboard real-time Guidance, Navigation, and Control (GNC) algorithms, mission planning, optimization, and first-order conceptual design and architecture studies. The literature contains a plethora of different analytical solutions to the equations of motion for planetary entry; unfortunately, many of these sources are becoming difficult to find, either due to their age or being out of print. A number of texts (see [72], [1],[73], [74], [30], [32], [75]) include overviews of analytical approximations for planetary entry, but none are comprehensive (see Table 1). For example, the Allen-Eggers solution for ballistic entry trajectories is the only analytical solution that is consistently covered.

A survey of analytical methods available in the literature is presented in this chapter. This survey serves to find appropriate analytical solutions for use in this thesis and to document these analytical methods and their sources for posterity. This survey considers only approximate solutions for translational motion. Aerodynamic heating and attitude dynamics are not addressed.

Table 1: Approximations in Selected Flight Dynamics Texts

Author	Publication year	Approximation							
		Allen-Eggers - ballistic	Moe - ballistic	Steep lifting entry	Equilibrium glide	Yarkshevskii	Loh - second-order	Chapman	Vinh - unified
Miele	1962	•	•	•					
Loh	1963	•					•		
Martin	1966	•	•						
Vinh et al.	1980	•				•	•	•	•
Hankey	1988	•			•				
Regan	1993	•		•	•				
Hale	1994	•			•				
Wisel	1997		•			•			
Griffin	2004	•			•		•		
Gallais	2007	•							

2.1 Approximating Trajectory Solutions for Planetary Entry

The equations of motion for planetary entry defy analytical solution unless simplifying assumptions are made. This is due to the highly nonlinear nature of the atmospheric density as a function of altitude. There are two options for solution: apply simplifying assumptions to reach an analytical solution or integrate the equations numerically. Hybrid solutions that utilize a mix of these two methods are also possible. With the exception of Sänger's work in the 1940s, the flight dynamics community began to develop (and publish) approximate solutions for the equations of motion in the early 1950s.

The first planetary entry applications of interest were defense-oriented and were typically associated with the final leg of an IRBM or ICBM trajectory. Civil applications, especially those geared toward crewed vehicles, began to gain interest later as the Space Race between the United States and the Soviet Union started [76].

Planetary entry vehicles are part spacecraft, part aircraft, and part projectile. Planetary entry trajectories exhibit several unique properties that differentiate them

from conventional subsonic and supersonic aircraft and make the analytical approximations for conventional aircraft of limited use. First, planetary entry occurs at extremely high speeds. This requires use of hypersonic aerodynamics and often requires one to account for the curvature of the planet due to the long distances traveled. Second, because planetary entry vehicles are descending from space to the planetary surface, the density variation with altitude must be considered–the steady cruise flight condition often assumed for conventional aircraft simply does not occur. Planetary entry trajectories enable new simplifying assumptions. Vehicle aerodynamic properties may be assumed constant to first order due to Mach number independence in the hypersonic regime. Planetary entry trajectories are also typically unpowered, eliminating the need to account for thrust or changes in vehicle mass. Lastly, planetary entry missions of interest lead to flight scenarios quite different than those experienced by conventional aircraft. Trajectories are often concerned with precision targeting, landing on another planet with a highly uncertain atmosphere, or simply surviving the deceleration and heat pulses during entry.

2.2 Analytical Approximate Solutions

Analytical solutions were developed in the 1950s and 1960s for two reasons: 1) computational resources were extremely limited, if available at all and 2) analytical solutions provided more information than a single, numerically integrated trajectory. The former was especially important, given the newness of planetary entry systems at the time.

In general, analytical solutions apply multiple simplifying assumptions to facilitate solution of the equations of motion. However, these assumptions limit the applicability of any one solution (see Figure 13). The earliest analytical solutions were narrowly focused on a particular class of trajectory. However, by the early 1960s, unified trajectory solutions appeared that were able to treat much broader classes of

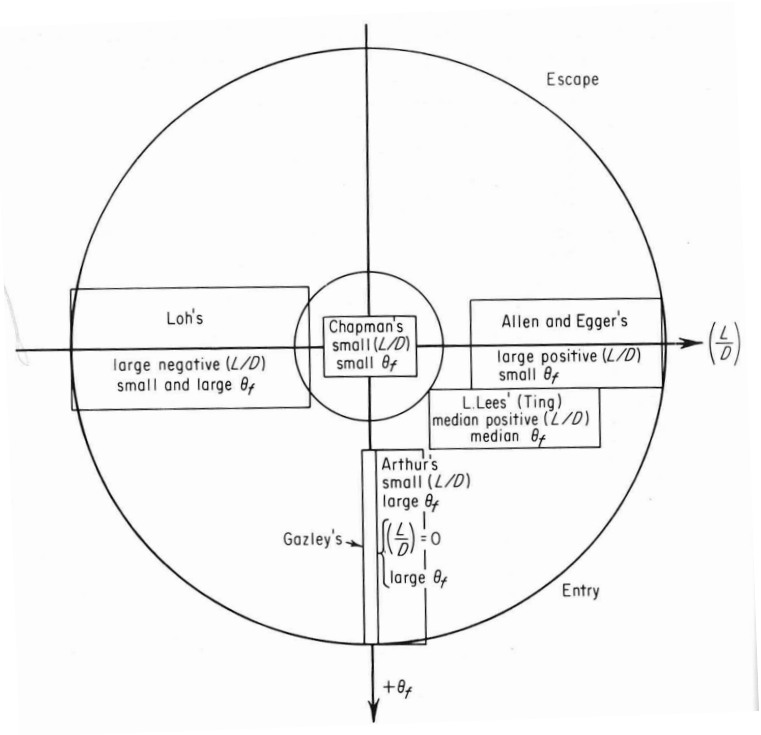

Figure 13: Comparison of the applicability of select first-order methods.[1]

trajectories.

Approximation error varies widely over the analytical solutions available in the literature, as well as within analytical solutions for varying trajectory parameters. It also appears that there was a bit of a rivalry amongst flight dynamicists, at least in the United States: journal articles published on the topic were frequently contested and defended in the same journal shortly after (for example, see Wang and Loh's discussion of Ref. [61] in Refs. [77, 78]).

Solution methods typically apply one or more of the following strategies to simplify the equations of motion such that they are analytically soluble:

- Assume two-degree-of-freedom motion (in-plane motion only)
- Neglect a force (e.g. $D \gg W$, $L = 0$)
- Assume a flat planet (i.e. $\dot{\theta} = 0$ or $R \to \infty$)

- Assume a state or parameter is constant (e.g. γ, H, dV/dt)
- Assume a state or parameter is small (e.g. γ)
- Assume convenient relationships ($\rho = \rho_{reg} \exp(-h/H)$, $D = k\rho V^n$)
- Assume a term is insensitive to integration (see Ref. [61])

2.2.1 Ballistic Entry

Ballistic, or nonlifting, entry is perhaps the simplest scenario in planetary entry. For ballistic entry, $L = 0$ and trajectories are essentially planar. The most significant solutions available in the literature are summarized in Table 2 along with their central assumptions and content.

2.2.1.1 Allen-Eggers and Moe

Amongst all analytical solutions for planetary entry trajectories, the Allen-Eggers solution is the most well-known. It appears in nearly every text on planetary entry flight dynamics, as well as in texts focused on spacecraft design. It's popularity is due to its simplicity.

Harry "Harvey" Julian Allen (Figure 14) and Alfred J. Eggers, working at the Ames Aeronautical Laboratory, first documented their analytical solution for ballistic entry in a classified NACA research memorandum in 1953 [79]. This memorandum was declassified in 1957 [79], and subsequently republished as a NACA report in 1958 [56]. Allen and Eggers developed the analytical solution "to determine means available to the designer for minimizing aerodynamic heating" for missile applications [56]. The Allen-Eggers solution is based on the insight that, for ballistic entry at a sufficiently steep initial flight-path angle, the gravitational force may be neglected relative to the drag force [56]. This yields a closed-form analytical relationship between velocity and altitude:

$$V = V_0 \exp\left[(H\rho_{ref})/(2\beta \sin\gamma_0) \exp\left(-h/H\right)\right] \tag{10}$$

Table 2: Closed-form Ballistic Entry Solutions and Assumptions

Approximation	Year	Assumptions: Exp. atmopshere H constant	g constant	C_D or β constant	C_D or β program	Flat planet	$h << R$	$D >> mg \sin(\gamma)$	$g \sin(\gamma) >> dV/dt$	D, W independent	dV/dt constant	$V \sin(\gamma)$ constant	γ small (shallow)	γ large (steep)	$d\gamma/dt$ small (nonzero)	γ constant	Closed-form relationships: V	h or ρ	S or θ	γ	a	a_{max}	V at a_{max}	h or ρ at a_{max}	γ at a_{max}	t (hypersonic)	t (gravity turn)
Allen-Eggers	1953	•	•	•				•						•		•	$f(h)$				$f(h)$	f	f	f			
Gazley - orbit decay	1957	•	•	•			•		•			•	•				$f(h)$				$f(V)$	f	f	f			
Adler	1958	•		•				•		•							$f^*(V)$										
Turnacliff, Squire	1958	•	•	•												•	$f^*(h)$										
Robinson - const. drag	1960	•	•		•	•		•			•					•	$f(h)$										
Gazley - direct entry	1960	•	•	•				•						•		•	$f^*(\rho)$										$f^*(\rho)$
Moe	1960	•	•	•										•	•		$f(h,\gamma)$			$f^*(h)$							
Warden	1961	•	•	•		•		•						•		•	$f^*(h)$			$f^*(h)$	f^*			$g(h)$			
Ambrosio	1962	•	•	•				•						•		•	$f(\rho)$										$f^*(\rho)$
Loh - "higher-order" theory	1962	•	•	•			•						•	•			$g(\rho,\gamma)$			$g(V,\gamma)$							
Kornreich	1963	•	•	•			•	•						•			$g(\rho,V)$										
Norman - g nonzero	1963	•	•	•			•							•		•	$f^*(\rho)$				f^*			f			
Norman - variable γ	1963	•	•	•			•	•									$f(\rho)$			$f^*(\rho)$							
Cohen	1965				•												$f(\rho,\gamma)$			$g(V,\gamma)$	$f(\rho,V)$			$f(V,\rho,\gamma)$			
Citron-Meir	1965	•	•	•				•									$f^*(V)$			$f^*(V)$							
Barbera - vel. dependent C_D	1981	•						•								•	$f(h)$				$f(V,h)$	f	f	f			
Putnam	2014	•	•	•				•									$f(V)$										

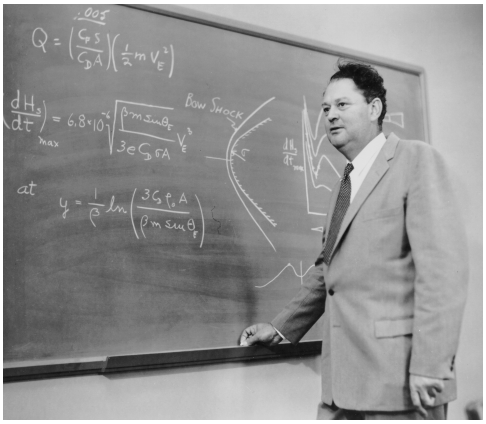

Figure 14: H. Julian Allen with his blunt body theory.[81]

From Eq. (10), Allen and Eggers were able to derive closed-form analytical expressions for deceleration and heating as functions of velocity, including state values at peak conditions of interest. Other assumptions in this solution include constant aerodynamic coefficients, a constant flight-path angle, and planar motion; these assumptions typically have only a small effect on the hypersonic portion of a ballistic entry. However, taken together, these assumptions limit the applicability of the Allen-Eggers solution to initial flight-path angles steeper than -5 to -10 deg [80].

Gazley independently developed the same solution for ballistic entry trajectories: he published his work just before the Allen-Eggers solution was declassified [82]. Gazley not only replicates the Allen-Eggers solution, but extends it to include time of flight for both the hypersonic and gravity-turn portions of an entry trajectory. He also considers application to Mars and Venus entry vehicles, in addition to Earth [83, 84].

Miller developed a closed-form solution for time as a function of altitude as a truncated series in 1961 [85]. This solution requires about six terms of the series. Miller provides no examples or evidence of the efficacy of his solution.

Kornreich developed a truncated-series expression for range as a function of density ratio in 1963 [60]. He argues that the bulk of the range traveled during ballistic entry occurs when the flight-path angle is near its minimum value, allowing it to

be approximated with a series expansion. However, he then proceeds to neglect all higher order terms; this is equivalent to assuming that the flight-path angle is constant over the range integral. Kornreich suggests using the maximum value of the flight-path angle in the range-estimation relationship; this insight produces results that are significantly more accurate than using the initial flight-path angle as proposed by Allen and Eggers. However, Kornreich does not advocate extending this to the rest of the Allen-Eggers approximate solution. Lastly, while Kornreich's range equation is explicit, computation of the maximum flight-path angle requires iteration.

In 1960, Moe was able to include the effects of gravity and a varying flight-path angle in an improved analytical approximate solution for ballistic entry, but still utilized constant aerodynamic coefficients and an exponential atmosphere model [86]. The price of this was an increase in complexity. Moe's solution requires use of the exponential integral, a result that is common for analytical approximate solutions.

$$\cos\gamma = \cos\gamma_0 \left\{1 + 2\ln\left(r/r_0\right) + \left(2gR^2e^{-z_0}\right)/\left(V_0^2 r_0^2/H\right)\left[\mathrm{Ei}(z) - \mathrm{Ei}(z_0)\right]\right\}^{-1/2} \tag{11a}$$

$$V = V_0(\cos\gamma_0/\cos\gamma)(r_0/r)e^{-(z-z_0)/2} \tag{11b}$$

where

$$z = -\left(H\beta\rho_{ref}e^{-h/H}\right)/\sin\gamma \tag{12}$$

Moe's solution reduces to the Allen-Eggers solution in the special case where $g = 0$.

Moe's solution is a more general form of that developed by Munk in 1944 for subsonic vertical dives [87]. Munk states that his work is not valid for high speeds because of Mach-number dependency of aerodynamic coefficients (which he assumes are constant). However, Munk was working in a propeller-driven aircraft world, and does not consider hypersonic speeds. Munk's result is given by:

$$V^2 = 2gHe^{-\beta H\rho}\left[\mathrm{Ei}\left(\beta H\rho\right) - \mathrm{Ei}\left(\beta H\rho_0\right)\right] \tag{13}$$

Eqs. (11b) and (13) are equivalent if $V_0 = 0$, $\gamma = -90$ deg, and one assumes $h \ll r$.

In 1958, prior to the publication of Moe's work, Turnacliff and Hartnett proposed a closed-form solution to velocity as a function of altitude including the effects of gravity for both vertical and "inclined" (nonvertical) flight. This solution utilizes a truncated infinite series and the authors comment that it converges well for low-drag vehicles but not for high-drag vehicles [88]. Squire points out that this solution merely replicates Munk's solution from 1944 with the exponential integral replaced by a particular expansion of its series approximation [89].

In 1962, Blum notes that Moe's approximation does a poor job of predicting performance in the lower atmosphere [90]. Specifically, the gravity turn is not modeled accurately. Blum proposes using a flat-planet approximation to derive a more accurate solution for the gravity turn. The principal result of his work is an expression for the beginning of the gravity turn, assumed to be at the maximum curvature of the trajectory:

$$3g \sin \gamma = -\beta \rho V^2 \tag{14}$$

Blum proposes this condition be utilized to determine whether the Allen-Eggers approximate solution is valid for a given trajectory.

Kumagai developed an expression for trajectory time based in 1964 that is appropriate for use with the Allen-Eggers and Moe solutions [91]. Kumagai's derivation is based on the decay of angular momentum during entry; it approximates an infinite series with the first several terms to achieve a closed-form expression. While Kumagai states that gravity is assumed to have an inverse-square relationship with altitude, this is immaterial, since g divides out in the derivation.

Norman published a comprehensive review of the Allen-Eggers solution and its extensions in 1963 [80]. Norman's stated goal was to improve estimates of peak acceleration for ballistic entry. Norman identifies three central assumptions inherent in the Allen-Eggers solution: neglecting gravity, constant atmospheric scale height, and constant flight-path angle. Norman then identifies solutions for which only two of

these assumptions are enforced. While this results in an excellent review of analytical trajectory solutions for ballistic entry and the relationships between them, Norman presents little new information.

Adler modifies the Allen-Eggers solution to include gravity by assuming drag and gravity effects on velocity are linearly independent.[92] The resulting expression captures vehicle performance where drag and gravity forces are on the same order. A piecewise atmosphere is also used to improve accuracy.

$$V = \left[V_0^2 - (2gR^2)/(R-h_0) + (2gR^2)/(R-h)\right]^{1/2} + V_0 \exp\left[(\rho_{ref}H)/(2\beta \sin\gamma_0)\exp\left(-h/H\right)\right] - V_0 \quad (15)$$

Adler also proposes a modified version of this expression where the inverse scale height varies linearly with altitude.

In 1970 Randall developed a piecewise solution for step changes in ballistic coefficient during entry based on the Allen-Eggers solution [93]. Most recently, in 2014 Putnam and Braun derive equations for range and range-to-go that are consistent with the Allen-Eggers solution [94]. Previous range equations have generally assumed a flat planet, which Allen and Eggers did not. A simpler derivation for range and time-of-flight equations for the Allen-Eggers solution was also proposed, through direct integration of the simplified two-dimensional equations of motion. Most importantly, Putnam and Braun propose an analytical method for determining the constant flight-path angle used in the Allen-Eggers solution. This addresses a long-standing weakness in applying the Allen-Eggers solution to a real problem. Putnam and Braun also attempt to develop hybrid heuristic-analytical bounds on the domain of applicability for the Allen-Eggers solution.

A more detailed discussion of the derivation of the Allen-Eggers solution and relationships is provided in Chapter 3.

2.2.1.2 Loh's Higher-Order Solution

Loh published his higher-order solution for ballistic entry in 1962, where "higher-order" refers to the solution being more accurate than his earlier, more general "second-order" solution (discussed in Sec. 2.2.3.1) [95, 96]. Loh's solution method is to rewrite the two-degree-of-freedom equations of motion in terms of two first-order ordinary differential equations in ρ and $\cos\gamma$. Loh is able to integrate these equations directly by assuming the quantity

$$[H/R][\cos\gamma/\rho][(gR/V^2)-1] \tag{16}$$

is insensitive to integration with respect to ρ or $\cos\gamma$. The result is two equations in V, ρ, and $\cos\gamma$ which, choosing one state as the domain, can be solved for the other two states over that domain.

$$\cos\theta = \cos\theta_f/(1+[1/(\beta R_0)][1/x-1][1-\rho_f/\rho]) \tag{17a}$$

$$\begin{aligned}\left(\frac{x}{x_f}\right) = &\left(\frac{4}{\beta R_0}\right)\left(\frac{1}{x_f}\right)F_1(\theta) \\ &+\left[\left(1-\frac{4}{\beta R_0}\right)\left(\frac{1}{x_f}\right)F_1(\theta_f)\right]\exp\left[\frac{-R_0(C_DA/m)(\theta-\theta_f)\rho}{\cos\theta[(1/x)-1]}\right]\end{aligned} \tag{17b}$$

where

$$x = V^2/(gR_0) = V^2/V_C^2 \tag{18}$$

and

$$\begin{aligned}F_1(\theta) = C_{16}\left[C_1\sin\theta-\cos\theta\right] + C_{16}\left[(1/2)C_1\sin 2\theta-\cos 2\theta\right] \\ - C_{17}\sin^2\theta\left[C_1\sin\theta-3\cos\theta\right]\end{aligned} \tag{19}$$

for steep θ and

$$\begin{aligned}F_1(\theta) \approx &\left[\ln(\theta/2)+C_1\theta+(C_1\theta)^2/4+(C_1\theta)^3/18\right]e^{-C_1\theta} \\ &-\left[\frac{(C_1\theta)^3}{720C_1^4}-\frac{(C_1\theta)^2}{240C_1^4}+\left(\frac{1}{120C_1^4}+\frac{1}{12C_1^2}\right)C_1\theta-\left(\frac{1}{120C_1^4}+\frac{1}{12C_1^2}\right)\right]\end{aligned} \tag{20}$$

for shallow θ. The constants are given by:

$$C_1 = \left[\left(\frac{\cos\theta_m}{\rho_m R_0}\right)\left(\frac{m}{C_D A}\right)\left(\frac{1}{x_m} - 1\right)\right]^{-1} \tag{21a}$$

$$C_{15} = \frac{\frac{1}{\cos\theta_f} + \frac{C_1^2 + 3^2}{\cos^2\theta_f} - \frac{6}{\cos^3\theta_f})}{(2)(C_1^2+1)(C_1^2+3^2)} \tag{21b}$$

$$C_{16} = (1/2)\left[\cos^2\theta_f (C_1^2 + 2^2)\right]^{-1} \tag{21c}$$

$$C_{17} = (1/2)\left[\cos^3\theta_f (C_1^2 + 3^2)\right]^{-1} \tag{21d}$$

The different values of F_1 are based on different approximations made during the derivation of Eqs. 17b.

2.2.1.3 Defined Relationships

Defining a convenient relationship between a particular parameter or state and other parameters or states can aid closed-form solution of the equations of motion. The most common relationship assumed is an exponential atmosphere relationship, such as in Eq. (8).

Robinson and Besonis develop equations of motion for entry in which the drag coefficient varies such that deceleration is constant with altitude [97]. Warden develops an approximate solution in which the ballistic coefficient is defined in terms of a polynomial in altitude of arbitrary order [44]. From this, Warden is able to develop closed-form expressions for velocity, deceleration, maximum deceleration, and the attitude at maximum deceleration. These solutions are relatively complex and require evaluation of the complete and incomplete gamma functions. In 1965, Cohen derived closed-form expressions for ballistic entry when the drag coefficient is assumed to be a specific function of density and flight-path angle [98]. The result is a set of complex closed-form expressions written in terms of the exponential integral.

More recently, Barbera utilized hypersonic drag coefficient data for sphere-cones (available in 1981) to develop a heuristic analytical expression for the inviscid drag

coefficient [99]. This expression applies to both the hypersonic and supersonic regimes when appropriate parameters are used. The expression is a single-term polynomial in V and captures the bulk of the Mach-number variation in the drag coefficient. While this relationship yields simple closed-form solutions, Barbera is forced to break trajectories into four piecewise "zones" to ensure accurate approximation.

2.2.1.4 Others

A variety of other solutions for ballistic entry trajectories are also available in the literature. In addition to co-developing the Allen-Eggers solution, Gazley developed an approximate solution for ballistic decay from orbit that is applicable to entry following de-orbit for small initial flight-path angles (i.e. deorbit $\Delta V \ll V_0$) [84]. In 1962, Ambrosio developed solutions for functions of the form $f = K\rho^i V^j$ that are applicable to a variety of entry trajectory parameters of interest [100]. These solutions involve complicated functions, such as the complete and incomplete gamma functions and the exponential integral.

2.2.2 Lifting Entry

2.2.2.1 Equilibrium Glide

In 1944, Sänger and Bredt published a treatise on suborbital, high-speed flight with specific application to long-range, rocket-powered bombers (see Figure 15) [54]. This publication was translated into English by the U.S. Navy Department Bureau of Aeronautics (BuAer) and released to the public in 1952. Through analytical and numerical calculations, the rocket-powered boost-glide bombers were shown to have near-global reach when skipping trajectories were employed. Sänger and Bredt developed an analytical approximation for computing the portion of high-speed atmospheric flight they refer to as an "equilibrium trajectory," which is now commonly referred to as equilibrium glide.

For equilibrium glide, the flight-path angle is assumed to be small and constant

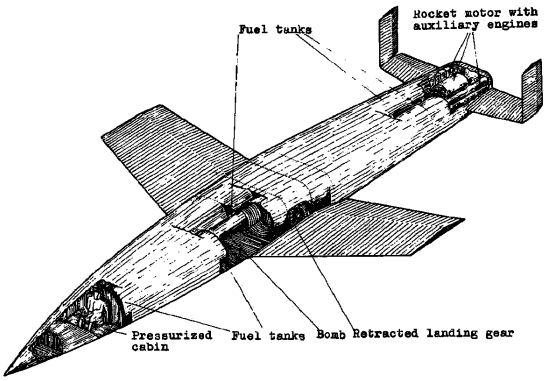

Figure 15: Sänger's and Bredt's rocket bomber.[54]

($d\gamma/dt = 0$). Sänger and Bredt realized that, for sufficiently high velocities, the curvature of the Earth must be taken into account when computing an equilibrium trajectory, instead of just equating the lift to weight as done for conventional aircraft. This may be expressed mathematically as:

$$L + mV^2/r = mg \tag{22}$$

If constant aerodynamic properties are assumed, an expression for velocity as a function of altitude at this flight condition may be derived from Eq. (22). This expression can in turn be used, in conjunction with Eq. (7a) where the gravity term is neglected, to develop expressions for time of flight as a function of velocity and for velocity and range as functions of time:

$$t = \frac{R(L/D)}{2V_C} \ln\left[\frac{(V_C + V_0)\,(V_C - V)}{(V_C - V_0)\,(V_C + V)}\right] \tag{23a}$$

$$V = V_C \frac{(V_C + V_0)\,/\,(V_C - V_0) - \exp\left[(2V_C t)\,/\,(R(L/D))\right]}{(V_C + V_0)\,/\,(V_C - V) + \exp\left[(2V_C t)\,/\,(R(L/D))\right]} \tag{23b}$$

$$s = V_C t + R(L/D) \ln\left[\frac{1 + (V_C + V_0)\,/\,(V_C - V_0)}{\exp\left[(2V_C t)\,/\,(R(L/D))\right] + (V_C + V_0)\,/\,(V_C - V_0)}\right] \tag{23c}$$

where it is assumed that $t_0 = 0$, $s_0 = 0$, and $r = R + h \approx R$. These expressions are derived by Sänger and Bredt. Unfortunately, Sänger and Bredt provide little information on their derivation of these expressions in Ref. [54].

In 1955, Eggers, Allen, and Neice revisited the equilibrium glide solution in a confidential NACA memo [101]. In addition to crediting Sänger and Bredt for the

original development of this theory, they present relations for velocity as a function of range and of density:

$$V = V_C \left[1 - \left(1 - V_f^2/V_C^2\right) \exp\left(\frac{2\theta}{LD}\right)\right]^{1/2} \tag{24a}$$

$$V = V_C \left[1 + \left(\frac{L}{D}\right) \frac{r\rho}{2\beta g} + 1\right]^{-1/2} \tag{24b}$$

These equations are manipulated to determine the maximum range of the vehicle as a function of L/D and final velocity:

$$s_{max} = \frac{R}{2} \left(\frac{L}{D}\right) \ln\left(\frac{1}{1 - V_f^2/V_C^2}\right) \tag{25}$$

This work was re-released in 1957 as a NACA technical note [102] and in 1958 as a full NACA technical report [55], neither of which was considered confidential.

Gazley, apparently unaware of the previous work of Sänger, Bredt, Eggers, Allen, and Neice, derived the equilibrium glide approximation again in 1957 [82]. Gazley recognized that one need only assume a slowly-varying flight-path angle to derive the equilibrium glide equations. Gazley extended the approximation to include expressions for acceleration, flight-path angle, and a simplified equation for range:

$$a = \frac{1}{(L/D) + 1/\left[r\rho\left(L/D\right)/(2\beta g)\right]} \tag{26a}$$

$$\sin\gamma = \frac{2H}{r(L/D)(V/V_0)^2} \tag{26b}$$

$$s = \frac{r}{2} \left(\frac{L}{D}\right) \ln\left[\frac{r}{H}\left(1 - \frac{V^2}{V_0^2}\right)\right] \tag{26c}$$

Eq. (26b) is derived from combining Eq. (26a) with Eq. (7a). While not explicitly stated, Galzey's equilibrium glide formulation assumes $r = R + h \approx R$ and that $V_0 = \sqrt{gr} = V_C$.

Gazley notes that no maximum acceleration occurs during equilibrium glide; the acceleration increases continuously, asymptotically approaching:

$$a_{max} = 1/(L/D) \tag{27}$$

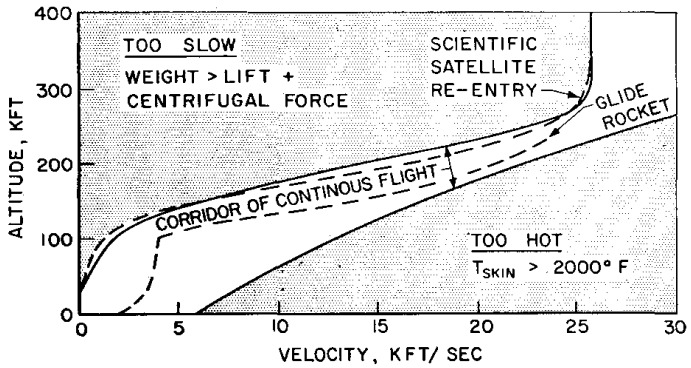

Figure 16: Gazley's lifting entry corridor.[82]

Gazley also presents equations more similar to those developed by Sänger and Bredt tailored for boost-glide trajectories.

Gazley was able to use this work to define a graphical flight corridor for lifting entry vehicles, shown in Figure 16, a corridor remarkably similar to that developed for the Space Shuttle Orbiter nearly 20 years later. A more polished, but limited version of these results was published in 1959 [83]. In 1960 Gazley extended his work to include analyses of corridors and Chapman's method of computing entry trajectories; this is the first time this approximation is referred to as "equilibrium glide" [84].

2.2.2.2 Steep Lifting Entry

In the same set of documents in which they discuss equilibrium glide, Eggers, Allen, and Neice also developed closed-form analytical solutions for lifting skip trajectories where gravity is neglected in both the lift and drag equations [101, 102, 55]. In this solution, gravity is neglected relative to aerodynamic forces in both the drag and lift equations (Eq. (7a) and (7b), respectively). Integrating these equations using an exponential atmosphere results in:

$$\rho - \rho_0 = \frac{2\beta}{H(L/D)} \left(\cos\gamma - \cos\gamma_0\right) \tag{28a}$$

$$V = V_0 \exp\left(\frac{\gamma_0 - \gamma}{L/D}\right) \tag{28b}$$

Eggers et al. developed these equations to model the atmospheric flight portion of a multiple-skip trajectory. From Eq. (28a), Eggers et al. realized that the flight path angles at atmospheric entry and exit must be equal and opposite on a skip trajectory, as the vehicle returns to the same altitude. While large L/D or a steep γ are not explicitly mentioned as assumptions, it is under these conditions that gravity may be neglected. The modern name of steep lifting entry (SLE) derives from this fact.

Lees, Hartwig, and Cohen extended this theory in 1958, developing an expression for acceleration in terms of the flight-path angle [103]:

$$a = \left[\frac{\gamma_0^2 - \gamma^2}{2gH(L/D)} + \frac{\rho_0}{g\beta}\right] V_0^2 \sqrt{1 + \left(\frac{L}{D}\right)^2} \exp\left[\frac{2\left(\gamma - \gamma_0\right)}{L/D}\right] \tag{29}$$

where the flight-path angle is assumed to be small. The flight-path angle at peak acceleration is then:

$$\gamma_{a_{max}} = \frac{2}{2}\left(\frac{L}{D}\right)\left\{\sqrt{1 + \frac{4}{(L/D)^2}\left[\gamma_0^2 + \frac{H(L/D)}{\beta}\right]} - 1\right\} \tag{30}$$

The theory was used to assess discrete-event lift-modulation trajectory control. This report is also available as a journal article, published in 1959 [31].

The work of Lees et al. was in turn extended to greater entry velocities by Wang and Ting in 1960 [57]. Wang and Ting retain the gravity term in the lift equation, resulting in:

$$\gamma = \sqrt{\gamma_0^2 - \frac{H}{\beta}\frac{L}{D}\left(\rho - \rho_0\right) - \left(\frac{2H}{R} - \frac{2gH}{V_0^2}\right)\ln\left(\frac{\rho}{\rho_0}\right)} \tag{31}$$

The key difference between Eq. (31) and Lees et al. is that the velocity from the top of the atmosphere to peak acceleration assumed to be constant.

Braun and Tauber developed an expression for range travelled during steep lifting entry[104], given by:

$$s = H\left(\gamma_0 - \gamma\right) - H\frac{2A}{\sqrt{1 - A^2}}\left(\tanh^{-1}\left[\frac{(A-1)\tan\left(\gamma/2\right)}{\sqrt{1 - A^2}}\right] - \tanh^{-1}\left[\frac{(A-1)\tan\left(\gamma_0/2\right)}{\sqrt{1 - A^2}}\right]\right) \tag{32}$$

where:

$$A = H\rho_0(L/D)/(2\beta) - \cos\gamma_0 \tag{32a}$$

The range traveled during the atmospheric flight segments of a skipping trajectory was neglected by Eggers et al. in Ref. [55]; inclusion of the atmospheric flight range improves total range estimates. Eq. (32) may also be used for direct entries for which the steep-lifting entry assumptions are appropriate, i.e. lifting entry trajectories that exhibit no positive altitude rate. This criterion generally corresponds to entry trajectories that are either steep, have small L/D, or both.

2.2.2.3 Three-Degree-of-Freedom Solutions: Approximating Crossrange

Eggers and Wong review solutions for lifting entry available in 1961 and extend equilibrium glide to the lateral plane, or out-of-plane motion. Their resulting expression for maximum crossrange is

$$l_{max} = \frac{\pi^2}{48} R \left(\frac{L}{D}\right)^2 + \text{H.O.T.} \tag{33}$$

where the bank angle is assumed to be constant at 45 deg.

Nyland and Chen of the RAND Corp. further improved upon extending equilibrium glide to out-of-plane motion. Nyland developed an equation for an equilibrium glide turn at constant L/D and constant bank angle, writing the heading change as [105]:

$$\omega = (L/D)\sin\sigma \ln(V_0/V) \tag{34}$$

Nyland also determines expressions for the time of flight and path length of such a turn, which are nearly identical to those developed by Sänger and Bredt for planar motion, but expressed in terms of velocity and including the bank angle:

$$t = \frac{V_C(L/D)\cos\sigma}{2g} \ln\left[\frac{(1 - V/V_C)(1 + V_0/V_C)}{(1 + V/V_C)(1 - V_0/V_C)}\right] \tag{35a}$$

$$s = \frac{R}{2}\left(\frac{L}{D}\right)\cos\sigma \ln\left(\frac{1 - V^2/V_C^2}{1 - V_0^2/V_C^2}\right) \tag{35b}$$

Expressions for downrange and crossrange are also presented as infinite series that are complicated, but "uniformly convergent in the region of interest."

$$x = \frac{Rg}{\tan\sigma}\left\{\sum_{n=1}^{\infty}\left(V/V_0\right)^{2n}\sin\left[\frac{L}{D}\sin\sigma\ln\frac{V}{V_0}+\tan^{-1}\left(an\right)\right]-\sum_{n=1}^{\infty}\left(V/V_0\right)^{2n}\frac{an}{\sqrt{1+a^2n^2}}\right\} \tag{36a}$$

$$y = \frac{Rg}{\tan\sigma}\left\{\sum_{n=1}^{\infty}\left(V/V_0\right)^{2n}\sin\left[\frac{L}{D}\sin\sigma\ln\frac{V}{V_0}+\tan^{-1}\left(\frac{1}{an}\right)\right]+\sum_{n=1}^{\infty}\left(V/V_0\right)^{2n}\frac{an}{\sqrt{1+a^2n^2}}\right\} \tag{36b}$$

where

$$a = 2\left[\left(L/D\right)\sin\sigma\right]^{-1} \tag{37}$$

Nyland also develops expressions describing flight at bank angles near 90 deg. At this flight condition, there is no lift in the vertical plane, and Nyland arrives at the non-lifting solution of Allen and Eggers.

Chen presents approximate solutions for five different scenarios: equilibrium glide with $\gamma = 0$, equilibrium glide with non-zero flight-path angle, high-altitude constant-speed glide, constant-deceleration glide at constant altitude, and constant-deceleration glide at constant flight-path angle. Chen's coverage of equilibrium glide merely repeats that documented by Nyland. However, Chen extends Nyland's work on equilibrium glide to non-zero flight-path angles, resulting in the following equations to describe a constant-bank, constant-L/D, constant-γ turn:

$$V = V_C\sqrt{1-\frac{2}{\zeta}-\left(1-\frac{2}{\zeta}-u_0^2\right)\exp\left[\zeta\left(\frac{h_0-h}{R+h_0}\right)\right]} \tag{38a}$$

$$\omega = \frac{\tan\sigma}{\gamma\left(\zeta-2\right)}\left[\frac{2}{\zeta}\ln\left(\frac{\zeta V^2-V_C^2\left(\zeta-2\right)}{\zeta V_0^2-V_C^2\left(\zeta-2\right)}\right)+\ln\left(\frac{V_0^2}{V^2}\right)\right] \tag{38b}$$

$$t = \frac{V_0^2(L/D)\cos\sigma}{2gV_C^2}\sqrt{\frac{\zeta}{\zeta-2}}\ln\left[\frac{\left(V\sqrt{\zeta}-V_C\sqrt{\zeta-2}\right)\left(V_0\sqrt{\zeta}+V_C\sqrt{\zeta-2}\right)}{\left(V\sqrt{\zeta}+V_C\sqrt{\zeta-2}\right)\left(V_0\sqrt{\zeta}-V_C\sqrt{\zeta-2}\right)}\right] \tag{38c}$$

$$s = \frac{V_0^2}{g\gamma\zeta}\ln\left[\frac{\zeta V^2-V_C^2\left(\zeta-2\right)}{\zeta V_0^2-V_C^2\left(\zeta-2\right)}\right] \tag{38d}$$

where

$$\zeta = 2/\left[\gamma(L/D)\cos\sigma\right] \tag{39}$$

The associated expressions for crossrange and downrange are integral expressions that must be evaluated numerically. Chen notes that by assuming $\zeta = 0$, the classic equilibrium glide solution is obtained from Eqs. (38).

Chen also provides closed-form expressions for the change in heading for constant-altitude, constant-velocity glide; constant acceleration, constant-altitude glide; and constant-acceleration, constant-flight-path-angle glide:

$$\omega = \omega_0 + \frac{HD_L}{2\sqrt{A_1}} \sin\sigma \left[\exp\left(-\frac{1}{H} \frac{h}{R + h_0} \right) - \exp\left(-\frac{1}{H} \frac{h_0}{R + h_0} \right) \right] \tag{40a}$$

$$\omega = \omega_0 + \frac{g \tan\sigma}{2\bar{a}} \left[\ln\left(\frac{V_0^2}{V^2} \right) + \frac{V^2 - V_0^2}{V_C^2} \right] \tag{40b}$$

$$\omega = \omega_0 - \frac{g \sin\sigma}{2\bar{a}} \left[\ln\left(\frac{V^2}{V_0^2} \right) + \frac{V_0^2 - V^2}{V_C^2} \right] \tag{40c}$$

where $\bar{a}$ is the value of the constant acceleration.

Wang presents closed-form solutions for heading angle, downrange, and crossrange as functions of velocity and density[106, 107]. For a flat planet, with bank angle equal to 90 deg and small crossrange:

$$\psi = (L/D) \ln\left(V_0/V\right) \tag{41a}$$

$$\lambda = \frac{2g\beta}{(L/D)\rho V_C^2} \left(1 - \cos\psi\right) \tag{41b}$$

$$\mu = \frac{2g\beta}{(L/D)\rho V_C^2} \sin\psi \tag{41c}$$

For a spherical planet with σ =90 deg:

$$\cos\psi = \frac{\cos\eta + C^2}{\sqrt{(1 + C^2)^2 - 4C^2 \sin^4\left(\eta/2\right)}} \tag{42a}$$

$$\sin\lambda = C \left(\frac{1 - \cos\psi \sqrt{1 - C^2 \sin^2\psi}}{1 + C^2 \cos^2\psi} \right) \tag{42b}$$

$$\sin\mu = C \sin\psi \tag{42c}$$

where

$$C = \frac{2\beta g}{(L/D)\rho V_C^2} \tag{43a}$$

$$\eta = (L/D)\sqrt{1 + C^2} \ln\left(V/V_0\right) \tag{43b}$$

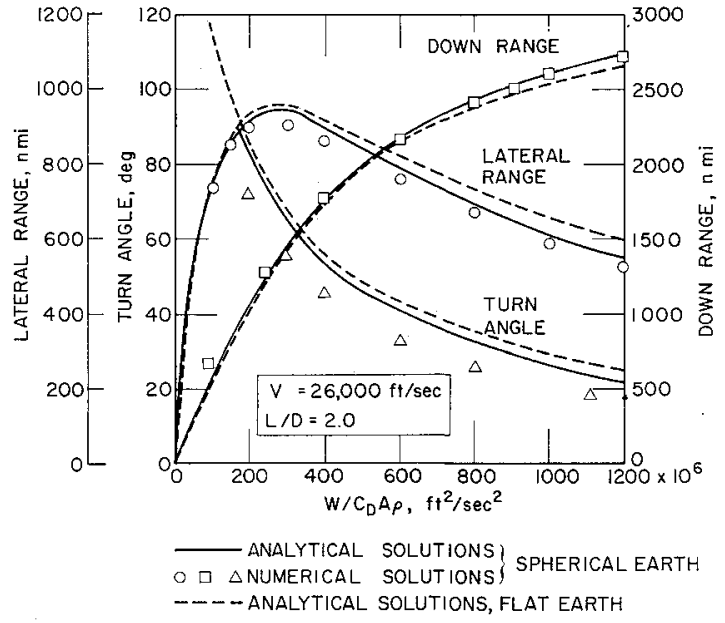

Figure 17: Comparison of analytical and numerical spherical planet solutions with analytical flat planet solutions [107].

Figure 17 shows how these solutions compare to numerical evaluation of the equations of motion.

In 1965, Arthur and Baxter point out that Wang's solution was a special case of a more general approximate solution for a minor-circle turn, where the ratio of the side force to the component of centrifugal force in the vertical direction is maintained at some constant value [108].

2.2.2.4 Defined Relationships

Convenient relationships are often assumed with the goal of simplifying the equations of motion such that analytical solutions may be found. However, these defined relationship solutions are typically more focused on determining a closed-form solution than modeling realistic flight conditions or addressing flight mechanics problems of general interest.

The solutions developed for defined relationships mostly address solutions where ρV^n is assumed to be constant. Loh discusses solutions for n values of 1, 2, 3 [58, 109];

Tikhonravov considers $n = 2$. In general, the different values of n correspond to:

- $n = 1$ Flight at constant Reynold's number[58, 109]
- $n = 2$ Constant aerodynamic load factor, approximately constant acceleration, constant dynamic pressure [58, 109, 110]
- $n = 3$ Constant heat rate, constant equilibrium temperature [58, 109]

These solutions are common because assuming ρV^n constant reduces or eliminates much of the dependence of the solution on the aerodynamic force terms.

Others have defined relationships, or programs, for aerodynamic coefficients. Wang and Chu develop solutions for a lift coefficient represented by $C_L = a - b(c\rho)^n$, where a,b,and c are constants; the drag coefficient is repressed by a parabolic drag polar. The resulting approximate solutions are truncated infinite series solutions and are quite complicated [111].

Cohen develops simpler solutions by assuming L/D is a function of the square of the velocity [98]. This assumption results in a separable differential equation relating V and γ that can be solved analytically.

2.2.2.5 Others

In approximate solutions for planar motion, flight is generally assumed to be in a great-circle plane of the planet. Loh generalized several solutions to flight on minor circles in 1960, specifically flight at positive L/D and small γ (equilibrium glide, although not identified as such) and flight at negative L/D and steep γ [58].

In 1961 Arthur and Karrenberg developed an extension of the Allen-Eggers approximation for small L/D [59]. They assume that small L/D implies small $\dot{\gamma}$ and allowing the flight-path angle to be approximated as $\gamma = \gamma_0 + \delta\gamma$. An integral expression for $\delta\gamma$ is found and integrated to "first order," resulting in the following closed-form "first-order" expressions for density and flight-path angle as functions of

velocity:

$$\gamma = \gamma_0 - \left(\frac{L}{D}\right)\left(\frac{\rho h_0}{2\beta \sin\gamma_0}\right) \tag{44a}$$

$$\rho = \frac{2\beta \sin\gamma_0}{h_0}\left[1 - \frac{L}{D}\frac{\cot\gamma_0}{2}\ln\left(\frac{V}{V_0}\right)\right]\ln\left(\frac{V}{V_0}\right) \tag{44b}$$

Arthur and Karrenberg then proceed to develop expressions for peak acceleration and conditions at peak acceleration in a similar manner as Allen and Eggers. The solution of Allen and Eggers may be recovered from the solution of Arthur and Karrenberg by setting $L/D = 0$.

In 1980, Nachtsheim and Lehman unified the work of Lees[31], Arthur[59], and Chapman[65] with a focus on the effect of lift on peak acceleration [112]. Nachtsheim and Lehman proposed the following improved equation for peak acceleration:

$$a_{max} = -\frac{1}{2Hg}\sin\gamma_{a_{max}} V_0^2 \exp\left[\frac{\gamma_0 - \gamma_{a_{max}}}{(1/2)(L/D)}\right]\sqrt{1 + (L/D)^2} \tag{45}$$

However, this result is restricted to entry velocities near V_C.

2.2.3 General Methods

Experience, and perhaps frustration, with the restricted methods discussed above led to the development of analytical solutions that provide trajectories for both lifting and ballistic entry vehicles. Loh's Second Order implicit solution is perhaps the most well-known of these closed-form analytical solutions. The solution developed by Citron and Meir is less well-known, but provides similar accuracy in an explicit form.

2.2.3.1 Loh's Second-Order Solution

Loh first published his relatively well-known "second-order" solution in 1962 [61]. Loh rewrites the equations of motion in terms of ρ and $\cos\gamma$ and is able to analytically integrate them by assuming $[H/R][\cos\gamma/\rho][(gR/V^2) - 1]$ is insensitive to that integration, and therefore constant. The resulting solution is composed of two closed-form

equations in V, ρ, and $\cos\gamma$:

$$\cos\gamma = \frac{\cos\gamma_0 + \frac{1}{2}\frac{L}{D}\frac{H\rho}{\beta}\left(1 - \frac{\rho_0}{\rho}\right)}{1 + \frac{H}{R}\left(\frac{gR}{V^2} - 1\right)\left(1 - \frac{\rho_0}{\rho}\right)} \tag{46a}$$

$$\frac{H}{\beta}\rho = \frac{\frac{H}{R}\cos\gamma\left(\frac{gR}{V} - 1\right)\ln\left(\frac{V^2}{V_0^2}\right)}{\frac{1}{2}\frac{L}{D}\ln\left(\frac{V^2}{V_0^2}\right) + (\gamma - \gamma_0)} \tag{46b}$$

A trajectory may be approximated by choosing one of the three states as a domain, then solving these implicit equations for the other two at selected points on that domain. While this solution is applicable over a wide range of vehicle and initial state parameters (including both lifting and ballistic entry), the implicit nature of the equations makes application more difficult.

Loh extended his second-order theory to exoatmospheric and endoatmospheric oscillatory (skip) trajectories in 1965 and 1967, respectively [62, 63]. In these extensions, Loh identifies methods for determining whether a trajectory is oscillatory and whether it has exited the atmosphere. Each trajectory oscillation must be computed separately using Eqs. (46); the resulting solution is a piecewise trajectory (see Figure 18). For both types of oscillatory trajectory, Loh proposes useful mathematical shortcuts to reduce the number of required computations. However, the solution is still inherently implicit. These extensions apply only to vehicles with nonzero L/D.

2.2.3.2 The Citron-Meir Solution

In 1965, Citron and Meir published an explicit solution to the equations of motion of the same order of accuracy as Loh's second-order solution [64]. Citron and Meir are able to show that Loh's solution is a special case of their more general solution method. The derivation of the Citron-Meir solution is also more straightforward than Loh's: Loh's apparently arbitrary assumption that certain terms are insensitive to integration is not required. The derivation of this solution is based on approximating

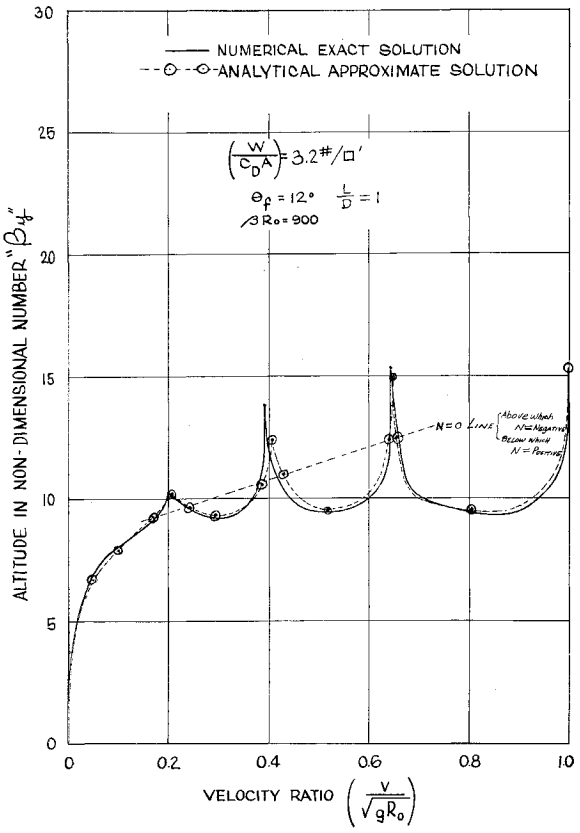

Figure 18: Loh's second-order solution applied to an oscillatory endoatmospheric trajectory ($R/H = 900$) [63]

.

the density as a power series in terms of $\ln V$. Retaining the zeroth and first order terms in this expansion is shown to yield the Allen-Eggers result for ballistic entry; the authors retain up to the second-order term in their solution. The authors also show that Loh's second-order solution may be derived starting from a second-order expansion of density with respect to $\ln V$ and utilizing a series expansion for $\sin\gamma$.

The Citron-Meir solution (Eqs. (47)-(48)), while apparently more complex than Loh's, is simpler to apply because it is explicit in ρ and γ. The solution requires evaluation of the exponential integral once for each trajectory point. Series-expansion estimates for the exponential integral may be used to evaluate this term [113].

$$f' = -f_0' - J\bar{z}/2 + 2F(\bar{z}) \tag{47a}$$

$$f = f_0 - J\bar{z}^2/4 + \bar{z}F(\bar{z}) \tag{47b}$$

where

$$\bar{z} = -\ln(V/V_0)^2 \tag{48a}$$

$$z_c = -\ln(V_C/V_0)^2 \tag{48b}$$

$$f_0 = \rho_0/\rho_{ref} \tag{48c}$$

$$f_0' = -\beta\sin\gamma_0/(H\rho_{ref}) \tag{48d}$$

$$F(\bar{z}) = \left\{ f_0'^2 - f_0' J\bar{z}/2 + (J\bar{z}/4)^2 + I\left[e^{-z_c}\left(\mathrm{Ei}(\bar{z}) - \bar{\gamma} - \ln\bar{z}\right) - \left(1 - e^{-z_c}\right)\ln\left(1 + f_0'\bar{z}/f_0\right)\right]\right\}^{1/2} \tag{48e}$$

$$I = (\beta\cos\gamma_0/\rho_{ref})^2/(RH) \tag{48f}$$

$$J = (1/2)(L/D)(IR/H)^{1/2} \tag{48g}$$

The nomenclature in Eqs. 47 and 48 is the same as that proposed by Eggers et al. in Ref. [114].

In their paper, Citron and Meir provide comparisons of their method, Loh's second-order solution, the Allen-Eggers solution, and numerical integration. Figure 19 shows a comparison between Citron-Meir, Allen-Eggers, Loh, and numerical

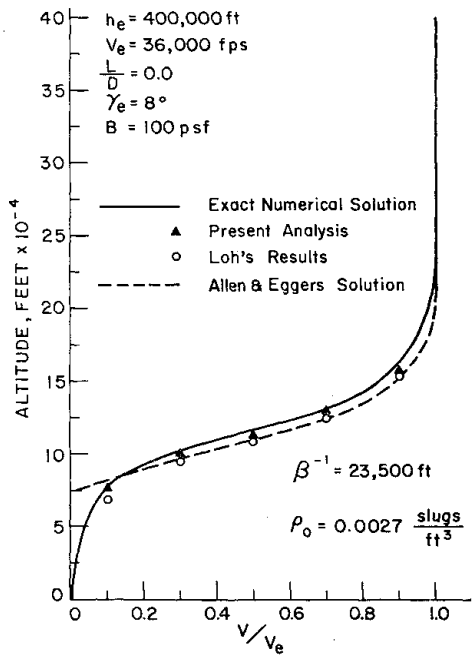

Figure 19: Comparison of Allen-Eggers, Citron-Meir, Loh, and numerical integration ($R/H = 900$).[64]

integration. Citron-Meir and Loh are slightly more accurate than Allen-Eggers and are both able to account for the beginning of the gravity turn. Figures 20 and 21 show Citron-Meir and Loh compared to numerical integration for a variety of trajectory parameters. While results are not identical, both solutions provide similar accuracy. This implies that the chief benefits of the Citron-Meir solution are a more logical derivation and simpler application.

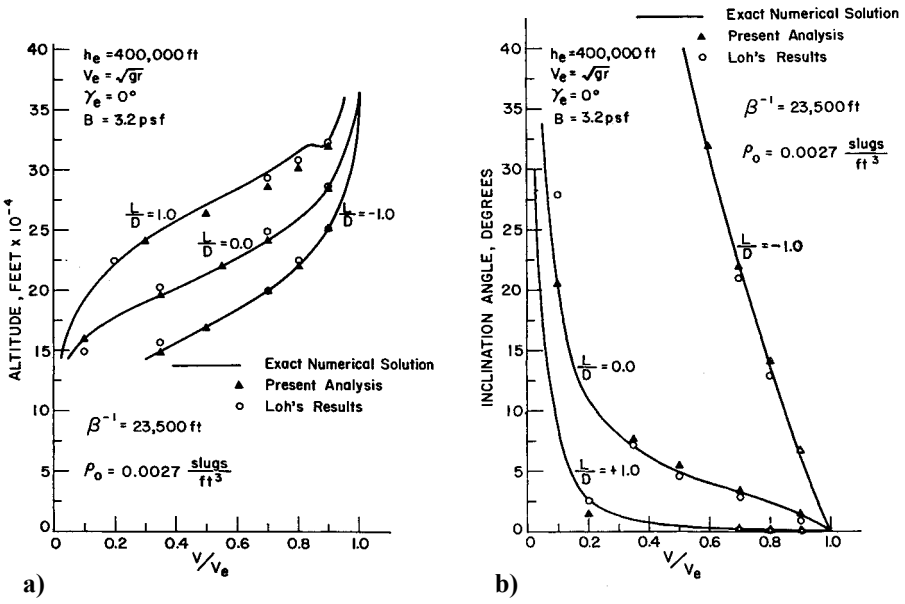

Figure 20: Comparison of Citron-Meir, Loh, and numerical integration for lifting entry: a) altitude and b) flight-path angle versus normalized velocity ($R/H = 900$).[64]

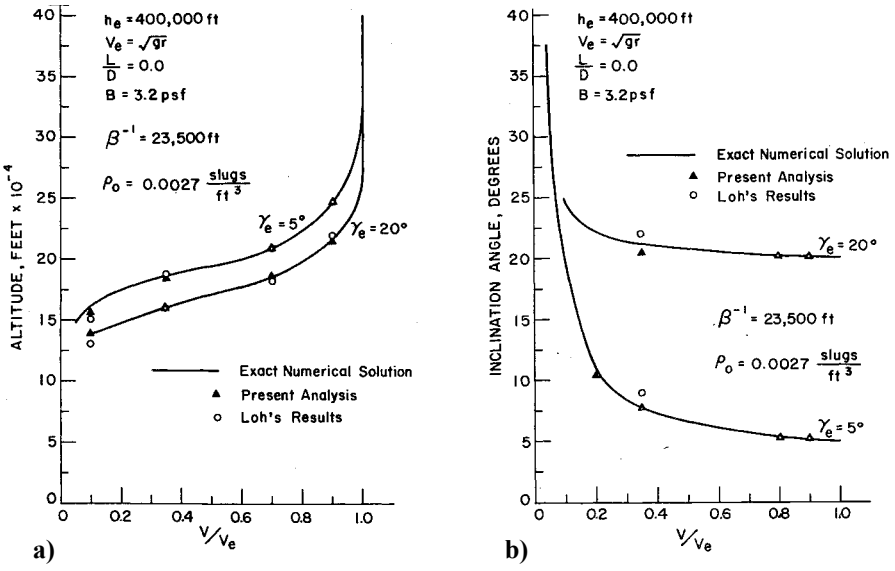

Figure 21: Comparison of Citron-Meir, Loh, and numerical integration for ballistic entry: a) altitude and b) flight-path angle versus normalized velocity ($R/H = 900$).[64]

2.3 Hybrid Analytical-Numerical Approximate Solutions

Hybrid analytical-numerical solutions were proposed alongside fully analytical solutions. These hybrid solutions sought to leverage the limited computer power available. For example, Chapman's solution allowed a single numerical integration of a differential equation of motion to be transformed to compute trajectories for a variety of vehicle and missions. These numerical solutions were tabulated, eliminating the need for others to access a computer to utilize the solution.

2.3.1 Chapman and Vinh

Dean Chapman first published his well-known hybrid analytical-numerical solution in 1959 [65]. By changing variables and manipulating the planar equations of motion, Chapman is able to collapse the equations of motion into a single, second-order equation:

$$\bar{u}\frac{d}{d\bar{u}}\left(\frac{dZ}{d\bar{u}}-\frac{Z}{\bar{u}}\right)-\frac{1-\bar{u}^2}{\bar{u}Z}\cos^4\gamma+\sqrt{Hr}\frac{L}{D}\cos^3\gamma=0 \tag{49}$$

where

$$Z=\frac{\rho_\infty}{2\left(\dfrac{m}{C_D S_{ref}}\right)}\sqrt{\frac{r}{\beta}}\bar{u} \tag{50}$$

and $\bar{u}$ is the horizontal velocity normalized by the circular velocity. Equation (49) is independent of ballistic coefficient (mass, drag coefficient, and reference area) and reference density and acceleration due to gravity. In this manner, tables of Z as a function of the normalized velocity $\bar{u}$ may be created then transformed to whatever trajectory is necessary. Chapman and Kapphahn did precisely this in a NASA technical report in 1961, providing 271 pages of tables of Z-values for a range of initial velocities, L/D, and initial flight-path angles [115]. Chapman utilized this hybrid solution to study entry corridors and other problems of interest to the community [53]. Nonweiler concurrently developed a solution identical to Chapman's, but limited to ballistic entry [116].

In 1960, Levy extended Chapman's solution to include trajectories in which the aerodynamic properties and shape of the vehicle are varied during flight [117]. Gazley proposed a parameter change to improve Chapman's solution, namely introduction of the parameter $\Gamma = Z/\bar{u}$, which Gazley asserts more clearly separates the generalized altitude and velocity in Eq. (49) [84]. Lastly, Boltz further modified Chapman's solution in 1963 by including all terms from the equations of motion as well as rotating atmosphere effects [118].

Vinh's unified theory, originally developed by Buseman, Vinh, and Culp, is based on Chapman's original work, but extends it to three degrees of freedom [119] and the full range of atmospheric entry conditions, from steep entry to orbit contraction from atmospheric drag [66]. The most comprehensive discussion of this solution is provided in Vinh's book, *Hypersonic and Planetary Entry Flight Mechanics* [30], an adaptation of an earlier technical report prepared for NASA [120]. In general, this solution maintains the character of Chapman's solution: the equations of motion are manipulated, primarily through a change of variables, such that their solution is independent of vehicle parameters. This allows a single numerically-integrated trajectory to be utilized for a range of problems. The work of Vinh et al. takes Chapman's equation a step further in that L/D is generalized, in addition to ballistic coefficient. Vinh and his co-authors have continued to publish extensions to this theory to the present day: second-order, closed-form analytic solutions for ballistic, skipping, and equilibrium glide trajectories [121], phugoid motion [67][122], specific ballistic entry trajectories [68], ballute aerocapture [123], and ballistic entry at large flight-path angles [124].

2.3.2 Yaroshevskiy

In 1964, Yaroshevskiy also collapsed the equations of motion for planetary entry into a single, second-order differential equation [125, 126]. For ballistic entry, this equation

is given by:

$$\frac{d^2y}{dx^2} = \frac{e^{2x} - 1}{y} \tag{51}$$

where

$$x = \ln \frac{\sqrt{gR}}{V} \tag{52a}$$

$$y = \frac{1}{2\beta}\sqrt{RH}\rho \tag{52b}$$

In these equations, Yaroshevskiy assumes that aerodynamic parameters are constant, the flight-path angle is small, and $g \sin \gamma$ is small relative to the drag.

Yaroshevskiy used the collapsed differential equation to approximate analytical solutions for specific trajectory cases. This is done using series expansions about intelligently selected solutions for a simplified version of the second-order equation. This work has been revisited and extended several times, including work by Ikawa [127], Gates[123], and Saikia[128].

2.3.3 Matched Asymptotic Solutions

The theory of matched asymptotic solutions was first applied to planetary entry trajectories by Willes et al. in 1967 [129]. The theory of matched asymptotic solutions is fundamentally a perturbation method. For planetary entry, the equations of motion are rewritten in terms of perturbation parameters, then expanded in a linear fashion about those perturbations. The great advantage of matched asymptotic solutions is that approximate solutions for different flight regimes may be easily stitched together, resulting in more general solutions that are applicable across a wider range of conditions (see Figure 22). However, these solutions are algebraically complex and frequently require numerical integration of scalar equations.

The solution of Willes et al. includes three parts: the aerodynamic-dominated regime, the Kepler regime (gravity only), and a middle, "aerogravity," regime, where aerodynamic and gravitational forces are of a similar magnitude. In 1969, Shi and

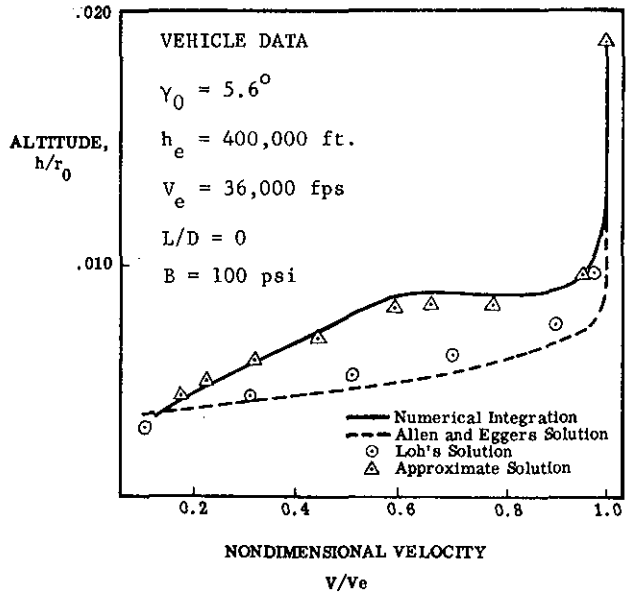

Figure 22: Comparison of solution methods to the matched asymptotic solution [129].

Pottsepp improved on the solution of Willes et al. by eliminating the need for the "aerogravity" flight regime in the solution [130]. Eckstein further extended the work of Shi and Pottsepp to oscillating skip trajectories in 1971 [131], and Shi was able to use the matched asymptotic solution for a study of optimal lifting entry [132]. Lastly, Hough published several extensions to this theory in the early 1980s focusing on ballistic entry: including an inviscid, velocity-dependent drag model[133] and gravity [134].

2.4 Numerical Approximate Solutions and Machine Computation

The rapid development and rise computers is well documented in the literature, including the significant role played by the aerospace industry in driving that development [135, 136]. Many of the analytical approximate solutions discussed earlier in this chapter were developed alongside computers in the 1950s and 1960s. As early as 1955, the presence of numerical solutions (computed by machine) for planetary entry trajectories was assumed [137]. Numerical solutions became common in the

literature around 1960 (see [138],[97],[139],[140]). In 1962 Duncan published an entire textbook that relied extensively on numerical solution of the equations of motion [141]. Researchers also began to utilize numerical solutions to evaluate the accuracy of analytical approximate solutions (see [142], [143]). And by 1962, Blum commented that "it is customary to find the re-entry trajectories of rockets integrated numerically by machine computation" [90].

The maturation of computers and programming languages for them eventually led to the creation of general-purpose programs designed to evaluate trajectories. Examples include the Program to Optimize Simulated Trajectories (POST)[69] and Simulation and Optimization of Rocket Trajectories (SORT)[144]. This has become the dominate method for evaluating planetary entry trajectories. Modern simulations may be quite complex and include detailed models for the environment, entry vehicle, and onboard systems [71].

2.5 Summary

The current literature contains numerous closed-form analytical approximate solutions to the equations of motion for planetary entry. Although most contributions to this body of work were written in the 1950s and 1960s, new contributions have been published at a steady rate since then. These analytical solutions still have value for modern analyses. In particular, they have direct applicability to onboard guidance and targeting systems (e.g. the work of Tannas [145, 146]), optimal control (see Vinh [147]), and first-order performance analyses that support conceptual design and architecture studies.

This thesis seeks to show the feasibility of drag-modulation systems for planetary entry. Of particular interest is the ability of such systems to provide range control during entry. The development of such an expression is the subject of the next chapter.

CHAPTER III

ENHANCEMENT OF THE ALLEN-EGGERS SOLUTION

When planetary entry was first studied in the middle of the twentieth century, analytical approximations were developed to enable vehicle and mission designers to evaluate vehicle trajectories and performance with minimal or no computer usage. Seminal examples of analytical approximations include, in chronological order, Sänger's and Bredt's expressions for lifting entry [54], the Allen-Eggers approximation for ballistic entry [56], Chapman's Z-function [65], Loh's "second-order" approximation [61], and the solutions developed by Vinh et al. [30]. Analytical and hybrid analytical-numerical approximate solutions utilize assumptions to make the nonlinear equations of motion soluble. As a result, they typically only apply to limited classes of entry vehicles and trajectories.

Subsequent advances in computing made high-accuracy approximation via numerical integration of the equations of motion feasible for most applications [135]. Today, vehicle and mission designers have significant computational resources available, enabling relatively rapid, low-cost, and high-fidelity assessment of entry trajectories. However, analytical solutions are still desirable for applications for which simplicity and execution speed are paramount, such as real-time guidance, navigation, and control systems; optimization; and conceptual design. Analytical solutions provide more information about entire families of trajectories, in contrast to the single trajectories generated by numerical methods, and may be manipulated to determine parameter sensitivities and partial derivatives. It is with these identified applications in mind that this study enhances the Allen-Eggers solution for ballistic entry through development of a method for computing the assumed constant flight-path angle, bounds

for the domain of applicability, and closed-form expressions for trajectory range and time.

Harry "Harvey" Julian Allen and Alfred J. Eggers, working at the Ames Aeronautical Laboratory, first documented their approximate solution for ballistic (nonlifting) entry in a classified National Advisory Committee for Aeronuatics (NACA) research memorandum in 1953 [79]. The memorandum was declassified in 1957 [79], and subsequently republished as a NACA report in 1958 [56]. Allen and Eggers developed their approximate analytical solution "to determine means available to the designer for minimizing aerodynamic heating" for missile applications [56]. The Allen-Eggers solution is based on the insight that, for ballistic entry at a sufficiently steep initial flight-path angle, the gravitational force may be neglected because its magnitude is small relative to the magnitude of the drag force [56]. Neglecting gravity yields a closed-form analytical relationship between velocity and altitude from which Allen and Eggers were able to derive closed-form analytical expressions for acceleration and heating as functions of velocity, including state values at peak conditions of interest. The solution is composed of relatively simple explicit, closed-form analytical expressions.

Several extensions to the Allen-Eggers solution have been published, including expressions for range [60] and time of flight [85, 80, 91]. Published extensions typically utilize additional assumptions not present in the original Allen-Eggers solution. Norman provides an excellent discussion and analysis of most early extensions [80]. Unfortunately, many of the references are becoming difficult to locate, due to age or being out of print. While derivations of the Allen-Eggers solution are available in the current literature [32, 148, 75], in-print treatments of the Allen-Eggers approximation are generally incomplete and utilize nomenclature that is inconsistent with current conventions within the entry community. To address this gap, a consistent and complete derivation of the Allen-Eggers approximation is presented and several

extensions are proposed to enhance the approximation. The extensions are compared to the literature where applicable.

3.1 Methods and Assumptions

In this chapter, approximation errors generally are presented as a percentage relative to Eqs. (7). Eqs. (7) are solved numerically using Matlab's intrinsic "ode45" function (based on the Dortmand-Prince method) with absolute and relative error tolerances of 10^{-12} [149]. Error presented as absolute error is the absolute value of the error magnitude.

The relatively short flight times associated with planetary entry, the drag-only trajectories considered in this study, and the unpredictable nature of atmospheric properties make the omission of the planet's rotation and its effects on wind-relative velocity the largest consistent source of error in Eq. (7) relative to higher-fidelity trajectory models. The wind-relative velocity error may be reduced by utilizing the planet-relative velocity in Eqs. (7).

The normalized integrated error is used to compare approximation error across multiple trajectories and is defined by:

$$\varepsilon_X = \frac{1}{\varepsilon_{X,norm}} \sqrt{\sum_{i=1}^{N} \left(\frac{X_{i,approx} - X_{i,EOM}}{X_{i,EOM}} \right)^2} \tag{53}$$

where N is the total number of points computed for the trajectory and X represents the trajectory state of interest. The error is normalized by a reference value. This error metric provides information about the error over an entire trajectory relative to another trajectory (typically associated with the normalization value) in a single number. This allows one to compare error over a range of trajectory parameters. While individual values of this integrated error are physically meaningless, they provide an estimate of the efficacy of an approximate solution relative to a known trajectory.

The Mathematica computer algebra system was used to symbolically evaluate the complicated integrals in this study [150].

Three example ballistic entry trajectories were chosen to illustrate the enhancement of the Allen-Eggers solution: interplanetary robotic sample return, strategic reentry, and low-Earth orbit (LEO) return of crew from the International Space Station. The example trajectories include hyperbolic, orbital, and suborbital entry energies and span several orders of magnitude of ballistic coefficient; they represent current ballistic missions of interest at Earth to the entry community (see Table 3). The sample-return example is based on NASA's Stardust Sample Return Capsule, which successfully landed after a ballistic entry in 2006 [151, 152]. Stardust had the greatest entry velocity of any Earth-return mission. The strategic example features a high ballistic coefficient vehicle on a steep, high-energy suborbital trajectory [153]. The LEO-return example represents ballistic entry of a crewed vehicle and is based on data from the off-nominal ballistic entry of Soyuz TMA-11 [154]. The Soyuz ballistic coefficient is consistent with other blunt-body crewed entry systems and enters the atmosphere at a shallow flight-path angle. A reference nose radius of 1 m is assumed for all three vehicles for simplicity.

All example trajectories occur at Earth, with an equatorial radius $R = 6378$ km and gravitational acceleration $g = 9.81$ m/s. An atmospheric scale height $H = 8.5$ km and reference density $\rho_{ref} = 1.215$ kg/m^3 at reference altitude $h_{ref} = 0$ km are assumed [155]. While the analyses presented in this work are restricted to Earth, Gazley has applied the Allen-Eggers solution to Mars and Venus with good results, indicating applicability at the terrestrial planets with atmospheres [83]. Evaluation of the efficacy of the Allen-Eggers approximate solution at other planetary destinations is left for future investigation.

Table 3: Parameters for example trajectories at Earth

Example	Sample Return	Strategic	LEO Return
Reference	[151, 152]	[153]	[154]
Initial velocity	12.8 km/s	7.2 km/s	7.9 km/s
Initial flight-path angle	-8.2 deg	-30.0 deg	-1.35 deg
Initial altitude	125 km	125 km	100 km
Ballistic coefficient	60 kg/m^2	10000 kg/m^2	450 kg/m^2

3.2 Review of the Allen-Eggers Solution

The Allen-Eggers approximate solution is rederived using modern nomenclature to provide a consistent basis for this study. The results differ slightly from those presented in Ref. [56] due to use of current conventions for the definition of flight-path angle and ballistic coefficient.

3.2.1 Altitude-Velocity Profile

The Allen-Eggers altitude-velocity profile may be derived starting with the planar equations of motion. The planar equations of motion are well-suited to ballistic entries because ballistic trajectories are nearly planar due to the absence of any out-of-plane lift. The key assumption in this derivation is that, for sufficiently steep entries, the drag contribution to the change in velocity is much greater than the gravity contribution. Additionally, the gravity term is multiplied by the sine of the flight-path angle, further reducing its magnitude for more shallow trajectories where the drag magnitude is less.

Starting from Eq. (7a) and neglecting the gravity term relative to the drag term, one may write:

$$\frac{dV}{dt} = -\frac{\rho_{ref}}{2\beta} \exp\left(\frac{h_{ref} - h}{H}\right) V^2 \tag{54}$$

Rearranging Eq. (7c) yields:

$$V = \frac{1}{\sin\gamma} \frac{dh}{dt} \tag{55}$$

Substituting Eq. (55) into Eq. (54) and separating variables gives:

$$\frac{1}{V}\frac{dV}{dt} = -\frac{\rho_{ref}}{2\beta \sin\gamma} \exp\left(\frac{h_{ref} - h}{H}\right)\frac{dh}{dt} \tag{56}$$

Assuming a constant flight-path angle γ^* and eliminating dt, this expression can be integrated from some state 1 to some state 2 and solved for V_2:

$$V_2 = V_1 \exp\left\{\frac{H\rho_{ref}}{2\beta \sin\gamma^*}\left[\exp\left(\frac{h_{ref} - h_2}{H}\right) - \exp\left(\frac{h_{ref} - h_1}{H}\right)\right]\right\} \tag{57}$$

Eq. (57), first derived by Allen and Eggers, determines an altitude-velocity profile (h_2, V_2) as a function of the planetary atmosphere (ρ_{ref}, h_{ref}, H), vehicle properties (β), and a reference vehicle state $(V_1, h_1, \gamma_1 = \gamma^*)$. The altitude-velocity relationship may be expressed in terms of either V_2 or h_2. The constant flight-path angle assumption approximates the flight-path angle history to first order for sufficiently steep ballistic entries and implicitly assumes a nonlifting trajectory for such steep entry trajectories. Allen and Eggers suggest using the initial flight-path angle for γ^* [56]; this approach works well for the steep entry trajectories ($\gamma_0 \ll 0$) that were of interest to Allen and Eggers. Lastly, Eq. (57) assumes that velocity is monotonically decreasing with altitude, limiting application of this approximate solution to trajectories with no positive altitude rate.

3.2.2 Acceleration Magnitude

Combining Eqs. (54) and (57) results in an equation for the acceleration magnitude. The resulting expression, normalized by g, is given by:

$$a_2 = \frac{\rho_{ref}}{2\beta g} V_1^2 \exp\left(\frac{h_{ref} - h_2}{H}\right) \exp\left\{\frac{H\rho_{ref}}{\beta \sin\gamma^*} \times \left[\exp\left(\frac{h_{ref} - h_2}{H}\right) - \exp\left(\frac{h_{ref} - h_1}{H}\right)\right]\right\} \tag{58}$$

Differentiating Eq. (58) with respect to h_2 yields:

$$\frac{da_2}{dh_2} = -\frac{a_2}{H}\left[1 + \frac{H\rho_{ref}}{\beta \sin\gamma^*} \exp\left(\frac{h_{ref} - h_2}{H}\right)\right] \tag{59}$$

Setting $da_2/dh_2 = 0$ and rearranging produces a relatively simple expression for the altitude at peak acceleration:

$$h_{a_{max}} = h_{ref} + H \ln\left(-\frac{H\rho_{ref}}{\beta \sin\gamma^*}\right) \tag{60}$$

Combining Eq. (60) and Eq. (57), the velocity at peak acceleration is:

$$V_{a_{max}} = \frac{V_1}{\sqrt{e}} \exp\left[-\frac{H\rho_{ref}}{2\beta \sin\gamma^*} \exp\left(\frac{h_{ref} - h_1}{H}\right)\right] \tag{61}$$

The maximum acceleration is given by:

$$a_{max} = -\frac{\sin\gamma^*}{2egH} V_1^2 \exp\left[-\frac{H\rho_{ref}}{\beta \sin\gamma^*} \exp\left(\frac{h_{ref} - h_1}{H}\right)\right] \tag{62}$$

If $h_{a_{max}}$ is below the planetary surface, peak acceleration occurs at minimum altitude.

3.2.3 Convective Heat Rate

Allen and Eggers formulated an equation for the convective heat rate at the stagnation point of a blunt-body vehicle [56]:

$$\dot{Q} = k\sqrt{\rho/r_n} V^3 \tag{63}$$

The expression assumes that the vehicle is sufficiently blunt such that a detached bow shock exists ahead of the body. Blunt leading edges for hypersonic vehicles are an innovation developed by Allen as a way to reduce the severity of entry heating on the vehicle [156]. In their original document, Allen and Eggers give a k value of 6.8×10^{-6} without units [56]; dimensional analysis indicates k has units of $\mathrm{kg}^{1/2}\mathrm{m}^{-1}$. The method developed by Sutton and Graves was used to compute a value for k suitable for application at Earth of 1.7623×10^{-4} $\mathrm{kg}^{1/2}/\mathrm{m}$ [157].

Combining Eq. (63) and Eq. (57) results in an expression for heat rate as a function of altitude:

$$\dot{Q}_2 = k\sqrt{\frac{\rho_{ref}}{r_n}} V_1^3 \exp\left(\frac{h_{ref} - h_2}{2H}\right) \exp\left\{\frac{3H\rho_{ref}}{2\beta \sin\gamma^*} \times \left[\exp\left(\frac{h_{ref} - h_2}{H}\right) - \exp\left(\frac{h_{ref} - h_1}{H}\right)\right]\right\} \tag{64}$$

The altitude and velocity at maximum heat rate may be derived in a similar way as maximum acceleration and are given by:

$$h_{\dot{Q}_{max}} = h_{ref} + H \ln\left(-\frac{3H\rho_{ref}}{\beta \sin\gamma^*}\right) \tag{65}$$

$$V_{\dot{Q}_{max}} = \frac{V_1}{e^{1/6}} \exp\left[-\frac{H\rho_{ref}}{2\beta \sin\gamma^*} \exp\left(\frac{h_{ref} - h_1}{H}\right)\right] \tag{66}$$

The maximum heat rate is (for $h_{\dot{Q}_{max}} \geq h_{min}$):

$$\dot{Q}_{max} = k\sqrt{-\frac{\beta \sin\gamma^*}{3eHr_n}} V_1^3 \exp\left[-\frac{3H\rho_{ref}}{2\beta \sin\gamma^*} \exp\left(\frac{h_{ref} - h_1}{H}\right)\right] \tag{67}$$

Otherwise, the maximum heat rate occurs at the minimum altitude.

3.2.4 Simplified Expressions

Setting h_{ref} to 0 m, state 2 to the current state (without subscript), and state 1 to the initial vehicle state near the top of the atmosphere (subscript 0) such that $\exp[-h/H] \gg \exp[-h_0/H]$, a simpler expression for the altitude-velocity profile results:

$$V = V_0 \exp\left[\frac{H\rho_{ref}}{2\beta \sin\gamma^*} \exp\left(-\frac{h}{H}\right)\right] \tag{68}$$

where ρ_{ref} is now the density at zero altitude. The assumptions also simplify the expressions for acceleration and the conditions at maximum acceleration. Eq. (58) becomes:

$$a = \frac{\rho_{ref}}{2\beta g} V_0^2 \exp\left(-\frac{h}{H}\right) \exp\left[\frac{H\rho_{ref}}{\beta \sin\gamma^*} \exp\left(-\frac{h}{H}\right)\right] \tag{69}$$

The conditions at peak acceleration are then given by (for $h_{a_{max}} > h_{min}$):

$$h_{a_{max}} = H \ln\left(-\frac{H\rho_{ref}}{\beta \sin\gamma^*}\right) \tag{70}$$

$$V_{a_{max}} = \frac{V_0}{\sqrt{e}} \approx (0.6065)V_0 \tag{71}$$

$$a_{max} = -\frac{\sin\gamma^*}{2egH} V_0^2 \tag{72}$$

The expression for heat rate becomes:

$$\dot{Q} = k\sqrt{\frac{\rho_{ref}}{r_n}}V_0^3 \exp\left(-\frac{h}{2H}\right) \exp\left[\frac{3H\rho_{ref}}{2\beta \sin\gamma^*} \exp\left(-\frac{h}{H}\right)\right] \tag{73}$$

The conditions at peak heat rate are then (for $h_{\dot{Q}_{max}} > h_{min}$):

$$h_{\dot{Q}_{max}} = H \ln\left(-\frac{3H\rho_{ref}}{\beta \sin\gamma^*}\right) \tag{74}$$

$$V_{\dot{Q}_{max}} = \frac{V_0}{e^{1/6}} \approx (0.8465)V_0 \tag{75}$$

$$\dot{Q}_{max} = k\sqrt{-\frac{\beta \sin\gamma^*}{3eHr_n}}V_0^3 \tag{76}$$

The simplified expressions in Eqs. (68)-(76) are typically presented in texts on atmospheric entry [73, 32, 148, 158, 75], as they readily provide insight into several ballistic entry phenomena. First, the altitudes at which maximum acceleration and heat rate occur are not functions of velocity to first order: they are determined by vehicle parameters, planetary parameters, and the flight-path angle. In contrast, the velocities at maximum acceleration and heat rate are fractions of the initial velocity to first order, and peak heating always occurs prior to peak acceleration. Lastly, maximum acceleration and heat rate are driven primarily by the initial velocity of the vehicle: greater initial kinetic energies result in greater values of acceleration and heat rate.

3.2.5 Application to Example Trajectories

Figure 23 shows the application of the Allen-Eggers solution to the three example trajectories specified in Table 3. The approximate trajectories are co-plotted with numerical solutions to Eqs. (7). Error plots are provided in Fig. 24. The Allen-Eggers solution shows good agreement with the numerically integrated planar equations of motion for the strategic case: vehicle state estimation errors are less than 10% for the bulk of the trajectory. The altitude (Fig. 23a) and heat-rate profiles (Fig. 23d) show small approximation errors for the sample-return case, but the acceleration error is

nearly constant at 30-40%. The Allen-Eggers solution does a poor job approximating the LEO-return case due to its shallow entry.

The assumptions used in the derivation of the Allen-Eggers solution lead to the smallest error during the hypersonic portion of the trajectory. The hypersonic regime encompasses the acceleration and heating pulses, including peak values for these quantities. These quantities and qualities of a planetary entry trajectory typically drive entry vehicle and mission design, making the Allen-Eggers solution a useful tool for conceptual design and analysis. Values of vehicle states at peak acceleration and peak heat rate estimated by the Allen-Eggers approximation are given in Tables 4 and 5, respectively. As before, errors for the strategic example are uniformly low. While estimates of conditions at peak heat rate are within 20% for both the sample-return and LEO-return cases; estimation error for peak acceleration is significantly larger. The limited accuracy reduces the utility of the Allen-Eggers solution for shallow entry trajectories.

The nature of the error in Fig. 24 reveals several weaknesses in the solution. First, while the initial flight-path angle appears to be a good choice for γ^* for the strategic case, this is not true for the other cases. Second, development of bounds on the domain of applicability of the solution would provide greater confidence in the approximation without requiring direct comparison with numerical solutions. Lastly, the Allen-Eggers solution does not provide any information on range or time of flight for entry, both of which are useful quantities for onboard guidance and targeting systems.

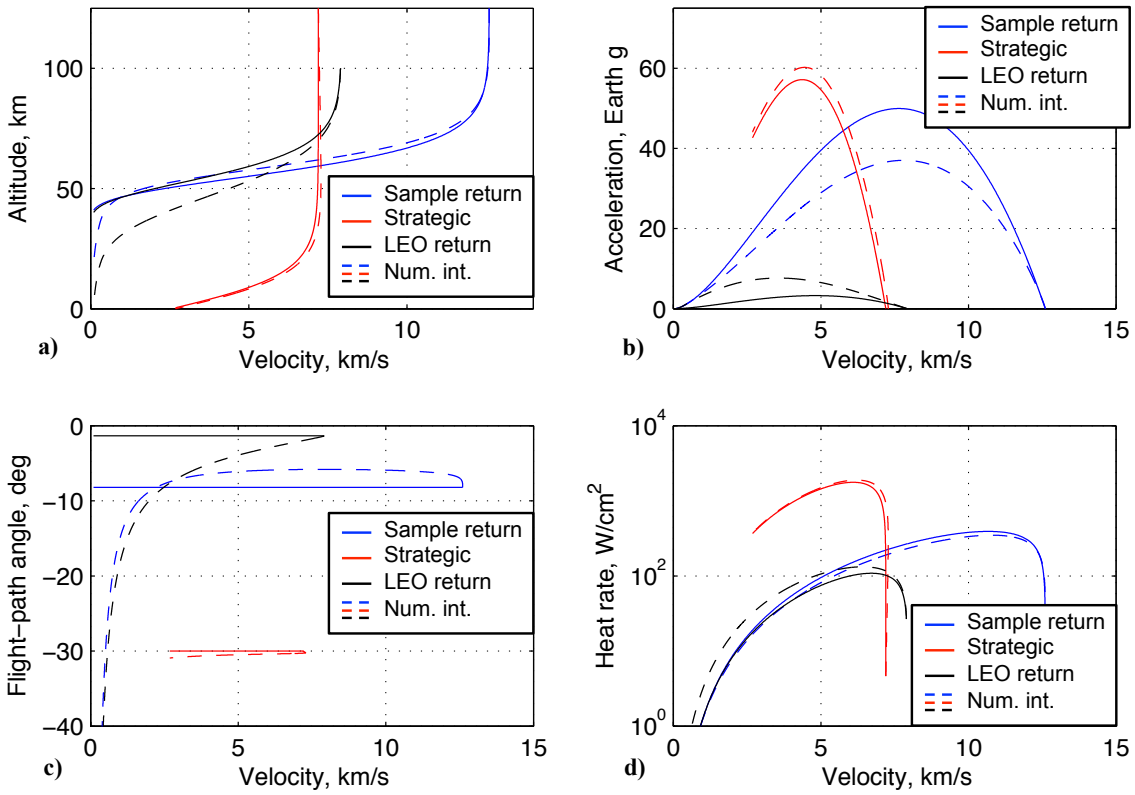

Figure 23: Example application of the Allen-Eggers solution (solid) compared to numerical integration (dashed): a) altitude, b) acceleration, c) flight-path angle, and d) heat rate versus velocity.

Table 4: Vehicle states at peak acceleration

	Acceleration		Velocity		Altitude	
	Earth g	Error, %	km/s	Error, %	km	Error, %
Sample return	50.0	34.9	7.64	-2.1	60.3	-4.6
Strategic	57.2	-5.1	4.37	-1.8	6.2	3.6
LEO return	3.3	-57.3	4.81	34.9	58.5	27.0

Table 5: Vehicle states at peak heat rate

	Heat rate		Velocity		Altitude	
	W/cm^2	Error, %	km/s	Error, %	km	Error, %
Sample return	391.5	12.3	10.67	-1.2	69.7	-3.6
Strategic	1764.3	-6.5	6.09	-1.8	15.5	1.3
LEO return	108.5	-18.0	6.71	4.7	67.8	9.2

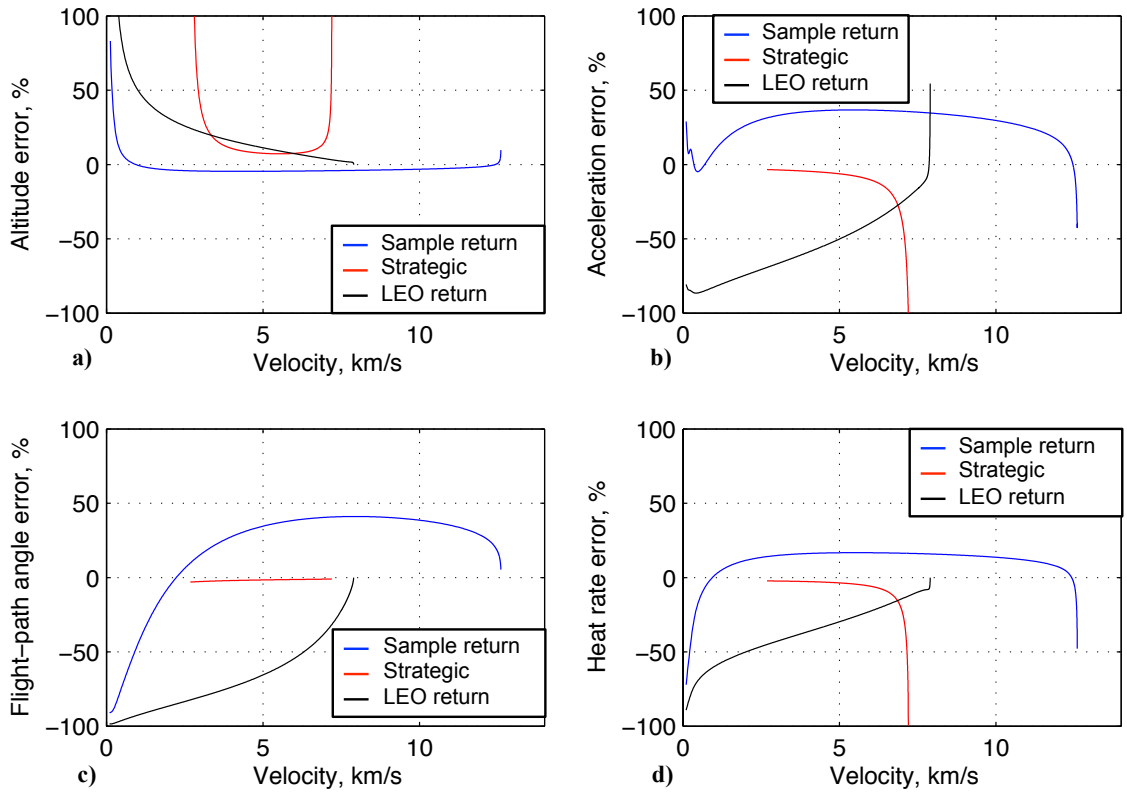

Figure 24: Allen-Eggers approximation error for a) altitude, b) acceleration, c) flight-path angle, and d) heat rate versus velocity.

3.3 Enhancement of the Allen-Eggers Solution

Several enhancements to the Allen-Eggers solution are developed in this section to address implementation weaknesses, provide additional information, and extend applicability of the solution: an analytical method for computing an appropriate constant flight-path angle, bounds on the domain of applicability, and consistent closed-form expressions for range and time. The enhancements obtained result in explicit, analytical expressions that maintain the character and advantages of the Allen-Eggers solution.

3.3.1 Determining the Constant Flight-Path Angle

A singular issue when applying the Allen-Eggers solution is determining a proper value for γ^*, the assumed constant flight-path angle. Steep entries exhibit only a small change in flight-path angle from their initial value in the hypersonic regime, making γ_0 a good approximation of γ^*; shallow trajectories fly at near-constant flight-path angles that are significantly different from the initial value, making γ_0 a relatively poor choice for γ^* (see Fig. 25). The ability to accurately determine more appropriate values for γ^* will extend the domain of applicability of the Allen-Eggers solution to more shallow initial flight-path angles and improve overall accuracy.

It is desirable to develop a method for determining γ^* based on available information that is closed-form, explicit, and does not require numerical integration to preserve the advantages of the Allen-Eggers solution. The solution for flight-path angle as a function of velocity developed by Citron and Meir meets the criteria [64]. Other approximate solutions for flight-path angle were considered: Loh's "Second-order" solution [61], Yaroshevskiy's series approximation [125, 126], and Chapman's Z-function solution [65]. However, none were explicit, analytical, and generally-applicable.

The Citron-Meir expression for flight-path angle is, rederived to be consistent with

nomenclature defined in this study and with $L/D = 0$:

$$\sin\gamma = \sin\gamma_0 \left(2F(V) - 1\right) \tag{77}$$

where

$$F(V) = \left[1 + \frac{H}{R\tan^2\gamma_0}\left\{\frac{V_C^2}{V_0^2}\left[\mathrm{Ei}\left(\ln\frac{V_0^2}{V^2}\right) - \bar{\gamma} - \ln\left(\ln\frac{V_0^2}{V^2}\right)\right] + \left(\frac{V_C^2}{V_0^2} - 1\right)\ln\left(1 - \frac{\beta\sin\gamma_0}{H\rho_0}\ln\frac{V_0^2}{V^2}\right)\right\}\right]^{1/2} \tag{77a}$$

where ρ_0 is the density at V_0 and Ei is the exponential integral, defined by:

$$\mathrm{Ei}(x) = -\int_{-x}^{\infty}\left(e^{-y}/y\right)dy \tag{78}$$

where x is an arbitrary argument. The exponential integral may be approximated using the explicit, analytical method developed by Cody and Thacher [113]. Given an initial state, planetary properties, and ballistic coefficient, Eq. (77) determines the flight-path angle as a function of velocity for most non-skipping entry trajectories [64].

Comparing Fig. 23b and 23c with Fig. 25, the value of the flight-path angle near peak acceleration appears to be a better representation of the constant flight-path angle γ^* than the initial flight-path angle. The velocity at this condition, $V^* = V_{a_{max}}$, can be found using existing relationships in the Allen-Eggers solution; V^* may then be used in Eq. (77) to determine γ^*. Either Allen-Eggers expression for $V_{a_{max}}$ may be used to determine V^*: Eq. (61) or the simplified expression, Eq. (71). Using the simplified expression for $V_{a_{max}}$ yields a more compact expression for γ^*. Substituting Eq. (71) into Eq. (77) gives:

$$\sin\gamma^* = \sin\gamma_0\left(2F^* - 1\right) \tag{79}$$

where

$$F^* = \left[1 + \frac{H}{R\tan^2\gamma_0}\left\{C\frac{V_C^2}{V_0^2} + \left(\frac{V_C^2}{V_0^2} - 1\right)\ln\left(1 - \frac{\beta\sin\gamma_0}{H\rho_0}\right)\right\}\right]^{1/2} \tag{79a}$$

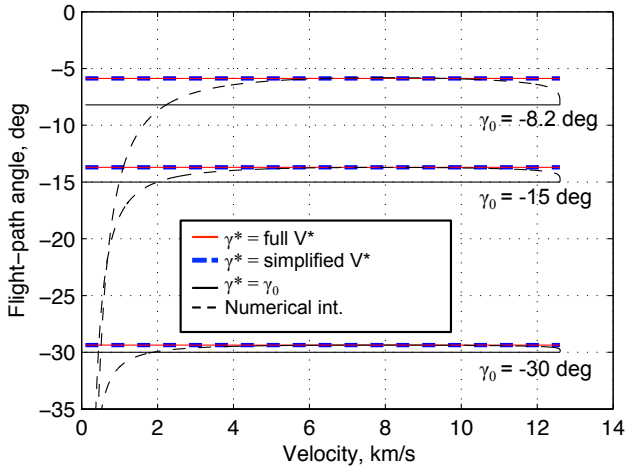

Figure 25: Three methods for computing the Allen-Eggers constant flight-path angle, γ^*, for the sample-return example entering with three different values of γ_0.

and

$$C = \mathrm{Ei}(1) - \bar{\gamma} \approx 1.3179 \tag{79b}$$

The constant C need only be determined once to the desired accuracy. As such, this expression does not require repeated evaluation of the exponential integral.

Figure 25 shows the efficacy of the proposed method for estimating γ^* for the sample-return trajectory at different initial flight-path angles. The resulting values for γ^* more closely approximate numerical solutions of flight-path angle as a function of velocity. The difference between the proposed method and using γ_0 for γ^* increases with more shallow initial flight-path angles, but improvement is present for all initial flight-path angles shown. Both options for computing V^* are shown; the additional complexity of using Eq. (61) with Eq. (77) does not yield results that are appreciably different from those generated by Eq. (79).

The proposed method for determining γ^* improves the accuracy of the Allen-Eggers solution across all three example cases (Fig. 26 and Fig. 27). The improvement is most significant for the sample-return example: acceleration and flight-path angle estimation error is reduced by nearly 40% near mid-trajectory. For the LEO-return case, error is reduced and more balanced about zero, but remains large. Improvements

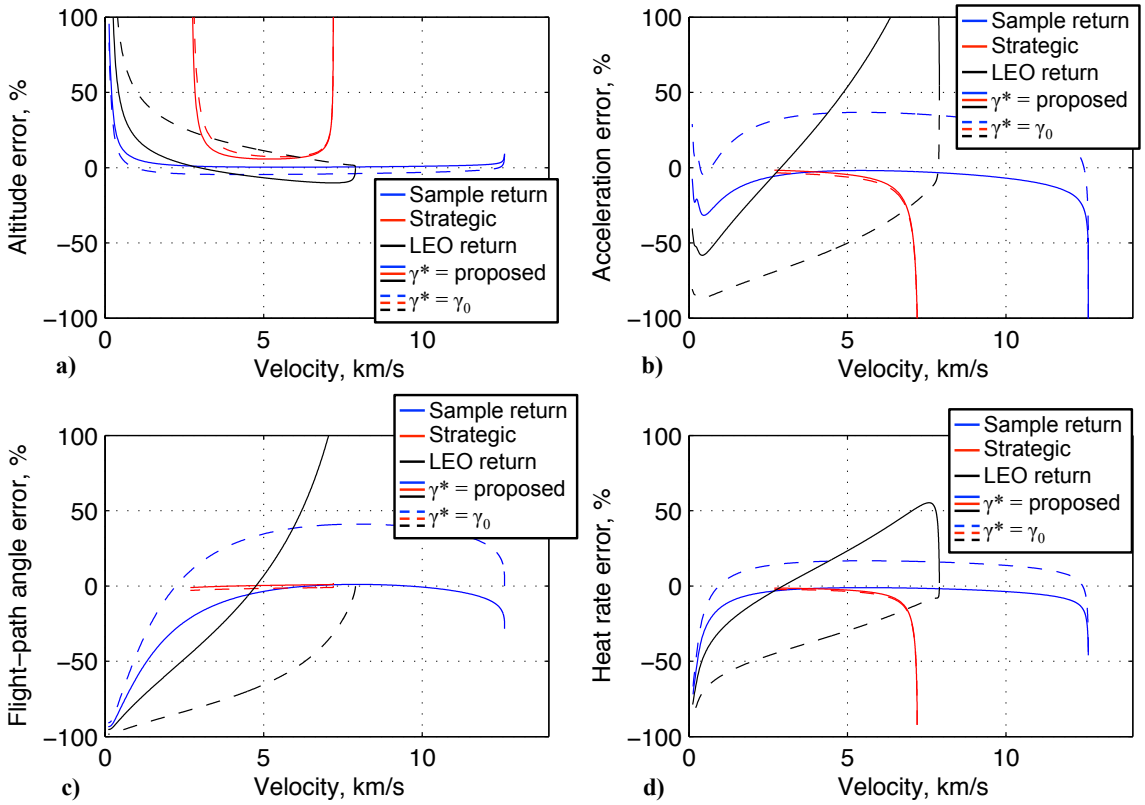

Figure 26: Comparison of the approximation error with $\gamma^* = \gamma_0$ (dashed) and the proposed method for computing γ^* (solid): a) altitude, b) acceleration, c) flight-path angle, and d) heat rate versus velocity.

to the strategic case are small.

As shown in Fig. 27, estimates of vehicle states at peak acceleration and heat rate are improved for all three cases with the exception of the peak heat rate for the LEO-return case. The increase in error is accompanied by an equally large decrease in the error for the estimate of the peak acceleration, as well as smaller reductions in error for estimates of the velocity and altitude at peak conditions.

3.3.2 Bounding the Domain of Applicability

Figure 28 shows the Allen-Eggers altitude-velocity profile relative to the numerical solution to the equations of motion early and late in the trajectory as a function of velocity, normalized by the initial velocity. Early in the trajectory (Fig. 28a) at high altitudes, atmospheric density is low; therefore drag is low and gravity dominates

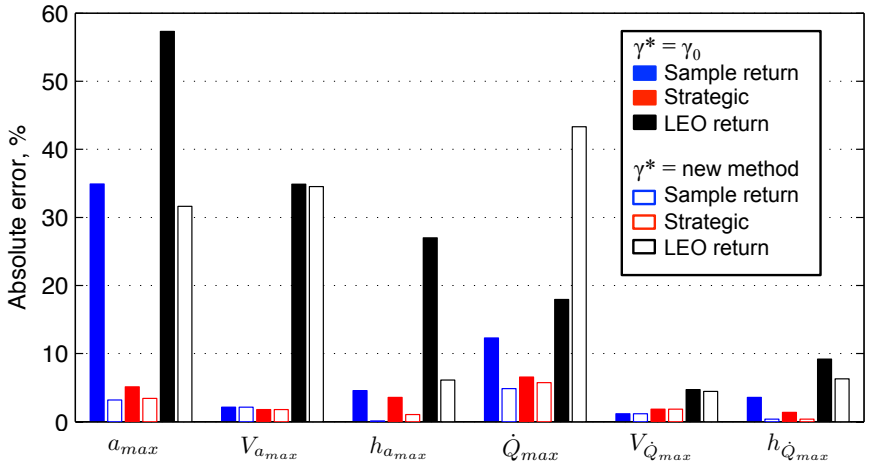

Figure 27: Vehicle state approximation error at peak conditions for $\gamma^* = \gamma_0$ and the proposed method for computing γ^*.

the dynamics, causing the vehicle to accelerate as it descends into the planetary gravity well. As vehicle altitude decreases, atmospheric density builds, causing drag to increase and surpass gravity as the dominant force, causing the vehicle to decelerate. There is a region in which the drag and gravity forces are nearly balanced: above this region, gravity dominates; below, drag dominates. The assumptions inherent in the Allen-Eggers solution are only valid when drag dominates the dynamics.

Late in the trajectory, the Allen-Eggers approximation error becomes large (Fig. 28b). After passing through peak acceleration vehicle velocity continues to decrease, decreasing the dynamic pressure and the drag force. Eventually, the drag force decreases enough that gravity becomes significant again, causing a negative flight-path angle rate known as the gravity turn. In this region of the trajectory, the Allen-Eggers assumptions on gravity and constant flight-path angle are both violated. The strategic case is not depicted because it reaches the surface at a much higher velocity.

While the Allen-Eggers solution shows significant error early and late in the example trajectories where its underlying assumptions are invalid, it is accurate in the middle of the trajectories, encompassing the hypersonic regime. The direct link between the inaccuracies in the Allen-Eggers solution early and late in the trajectory

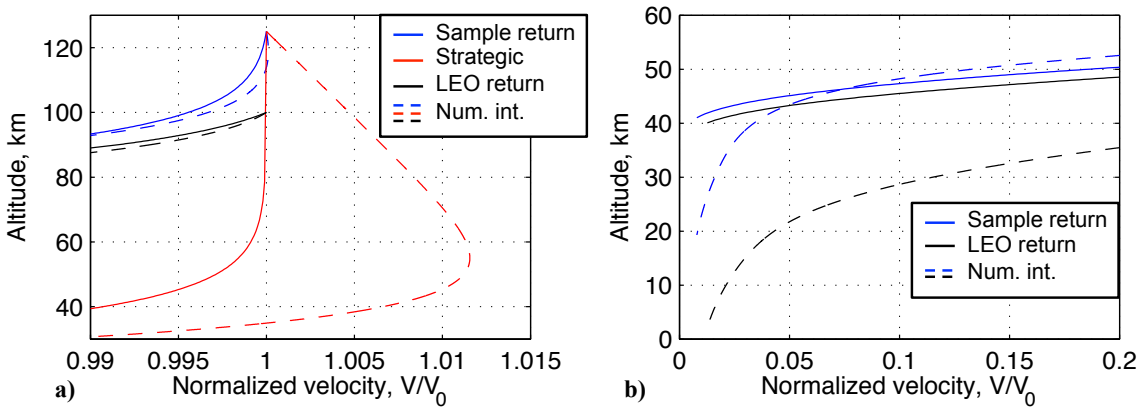

Figure 28: Allen-Eggers approximation error in altitude-velocity profile a) early and b) late in the trajectories.

and the approximation's underlying assumptions suggest that a bounded domain can be identified, based on the equations of motion, over which the Allen-Eggers solution is valid.

3.3.2.1 Bound on Initial Dynamic Pressure

Figure 28a shows that the Allen-Eggers approximation is inaccurate in the region when velocity is increasing under the influence of gravity. The point at which the gravity and drag forces balance occurs when velocity is at a maximum. At this point, from Eq. (7a):

$$\frac{dV}{dt} = 0 = -\frac{\rho}{2\beta}V^2 - g\sin\gamma \tag{80}$$

The Allen-Eggers approximation assumes the gravity force is negligible relative to the drag force, or:

$$\rho V^2/(2\beta) \gg -g\sin\gamma \tag{81}$$

where $\gamma < 0$ for entry, making the right-hand side positive. In terms of dynamic pressure:

$$\bar{q} \gg -g\beta\sin\gamma \tag{82}$$

The limit on the initial dynamic pressure, $\bar{q}_0$, may then be defined in terms of a stand-off factor, δ_q, and the initial flight-path angle such that:

$$\bar{q}_0 = -\delta_q g \beta \sin \gamma_0 \tag{83}$$

Eq. (83) defines a limit on the initial dynamic pressure, and therefore on the acceptable set of (V_0, h_0), as a function of the initial flight-path angle, vehicle properties, planetary properties, and the initial dynamic pressure stand-off factor δ_q. A δ_q value of 1 indicates the dynamic pressure at maximum velocity; a value of 2 or higher is recommended to ensure the vehicle is outside the region in which the gravity and drag magnitudes are similar. Figure 29 shows how this dynamic pressure limit leads to limits on the initial velocity and altitude for several values of δ_q. Conventionally, the initial conditions for entry are defined at an arbitrary altitude; Eq. (83) simply redefines the initial conditions for entry trajectories based on when aerodynamic forces begin to dominate vehicle dynamics.

An appropriate value for δ_q may be chosen by examining the Allen-Eggers state approximation error as a function of δ_q. Figure 30a shows approximation error for the sample-return example at 95% of V_0 as a function of δ_q. The lower velocity is used because there is no approximation error in the altitude at the initial state because it is the initial condition used in the approximation. The percent error in heat rate is not shown; heat rate is small in this region due to high altitude and low density. A δ_q value of 2 is chosen to provide margin relative to the maximum velocity point ($\delta_q = 1$) while limiting the approximation error in acceleration to approximately 10% (see Fig. 30a).

3.3.2.2 Bound on Minimum Velocity

A bound on the terminal state will complete the specification of the domain of applicability for the Allen-Eggers solution. A minimum-velocity bound may be derived

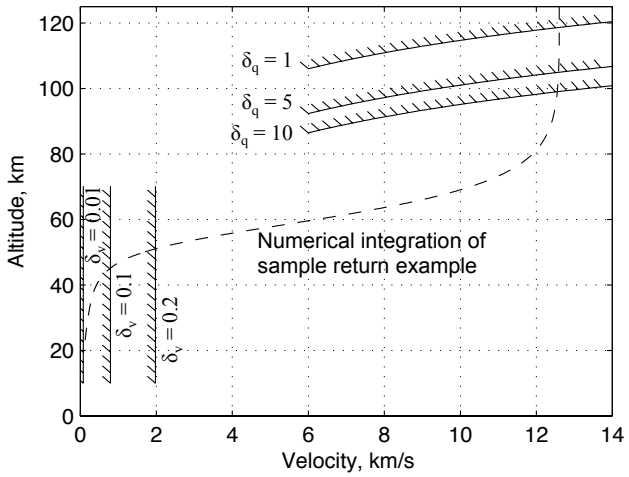

Figure 29: Example bounds on the Allen-Eggers domain of applicability for the sample-return example case.

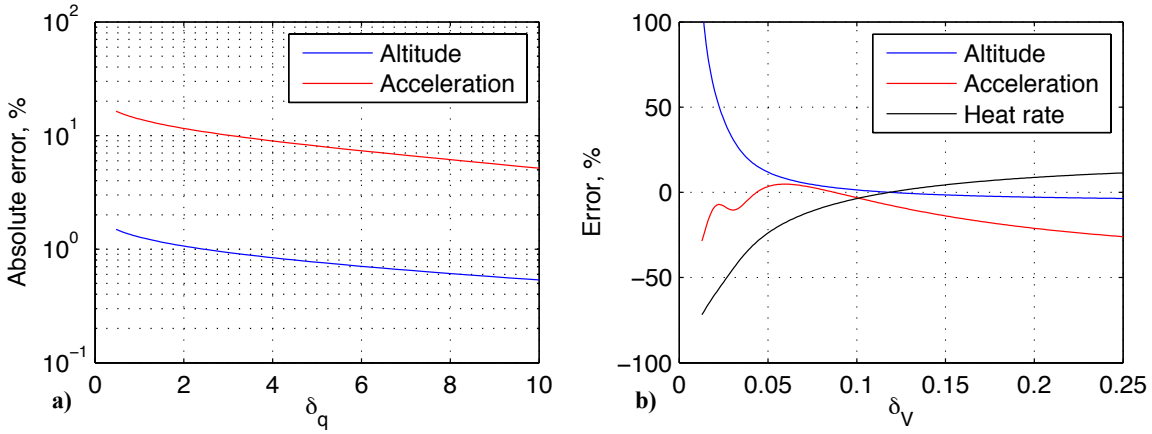

Figure 30: Allen-Eggers approximation error versus a) the initial dynamic pressure stand-off factor and b) the final velocity stand-off factor for the sample-return example case.

by considering Eq. (7b) for ballistic vehicles, rearranged:

$$\frac{d\gamma}{dt} = \left(\frac{V}{R+h} - \frac{g}{V} \right) \cos\gamma \tag{84}$$

As shown in Figs. 23c and 28b, the Allen-Eggers solution becomes inaccurate when the flight-path angle begins to change significantly, indicating a nonzero (and negative) value of $d\gamma/dt$. Since $\cos\gamma$ tends to decrease with increasingly negative γ, any significant increase in the magnitude of $d\gamma/dt$ must be caused by an increase in the magnitude of the other factor. Larger magnitudes of $d\gamma/dt$ occur late in the trajectory and the sign of $d\gamma/dt$ is negative; therefore, a significant $d\gamma/dt$ results when the gravity term, g/V, is larger than the range-angle term, $V/(R+h)$. The Allen-Eggers solution is then valid for velocities where the range-angle term is larger than the gravity term by some factor, $1/\delta^2$:

$$g/V < \left(1/\delta^2\right) V/\left(R+h\right) \tag{85}$$

Neglecting h relative to R (a good assumption at low altitudes near the end of the trajectory) and solving for V determines a lower limit on velocity past which the gravity term exceeds the range-angle term:

$$V > \delta\sqrt{gR} \tag{86}$$

Defining the minimum acceptable final velocity as V_f and designating δ as δ_V, one finds the minimum final velocity is:

$$V_f = \delta_V V_C \tag{87}$$

The minimum velocity bound is a fraction of the circular velocity, the velocity of a notional circular orbit at the planetary surface. The final velocity stand-off factor, δ_V, provides margin beyond the minimum velocity to limit error. Figure 29 shows the minimum velocity bounds for three values of δ_V. Larger values of δ_V imply a more restrictive domain for the Allen-Eggers approximation.

An appropriate value of δ_V may be chosen by examining the Allen-Eggers approximation error as a function of δ_V, as shown in Fig. 30b for the sample-return example trajectory. The figure indicates that a δ_V of 0.05 will limit approximation error in altitude, acceleration, and heat rate to less than approximately 20%. While the flight-path angle error remains large at this value of δ_V, the Allen-Eggers solution does not attempt to estimate the flight-path angle, making this error less significant.

3.3.2.3 Improvements to Approximation Accuracy

Figures 31 and 32 show the decrease in approximation error for the example trajectories with the Allen-Eggers approximation restricted to its domain of applicability by limits on $\bar{q}_0$ and V_f with $\delta_q = 2$ and $\delta_V = 0.05$. Modest improvement in approximation error across all estimated parameters is apparent for the sample-return and strategic examples. No improvement is seen in the LEO-return case because its initial dynamic pressure exceeds that associated with a δ_q of 2.

3.3.3 Closed-Form Expressions for Range

Closed-form, explicit approximations for entry range have generally been restricted to vehicles with nonzero L/D, such as Sänger's and Bredt's equilibrium glide and steep lifting entry [54]. For ballistic entry, approximate trajectory solutions in the literature typically omit range [82] or evaluate range through integrals that must be solved numerically [86, 96]. Kornreich's truncated-series approximation of range during ballistic entry is the only closed-form expression found in the current literature [60]. The dearth of range approximations is likely due to the complexity of analytical solutions for altitude, velocity, and flight-path angle: these complicated state approximations must be combined in an integral expression to compute range. The complexity of the range integrand generally defies analytical solution.

While other solutions for ballistic entry are more accurate, such as those of Moe [86] and Loh [96], the simplicity of the Allen-Eggers solution permits development

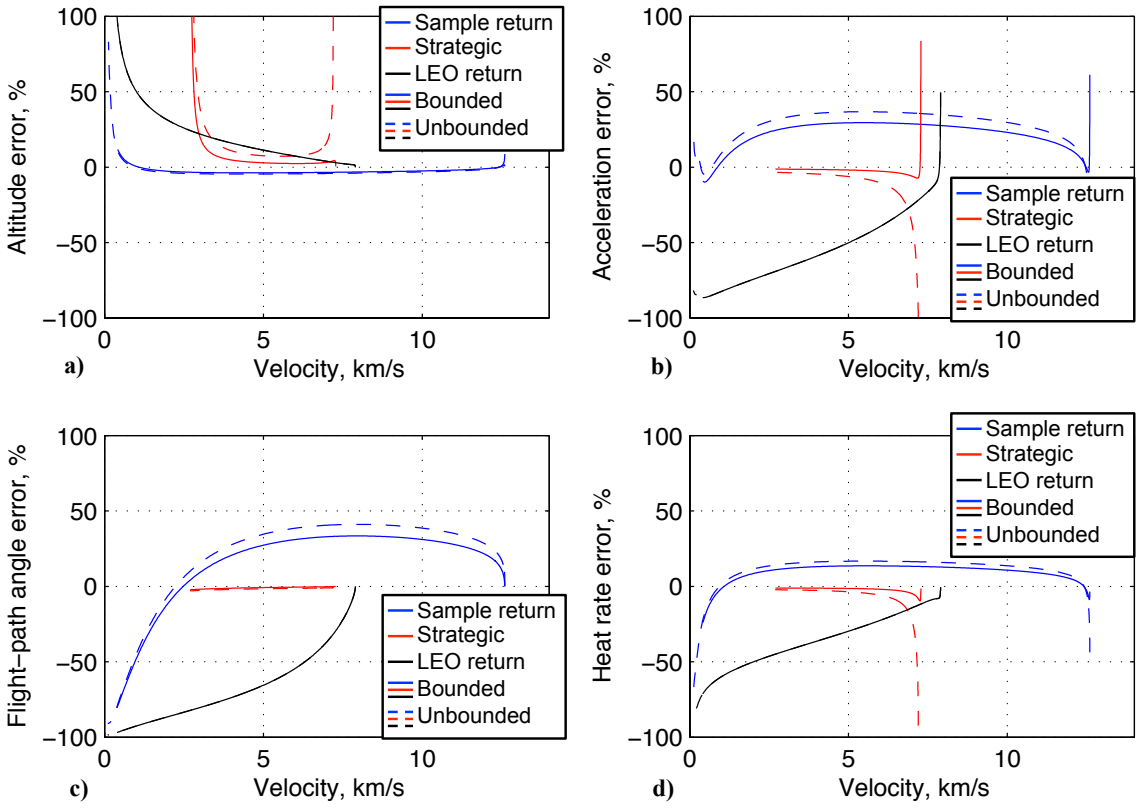

Figure 31: Comparison of the approximation error for bounded (solid, $\delta_V = 0.05$, $\delta_q = 2$) and unbounded (dashed) domains: a) altitude, b) acceleration, c) flight-path angle, and d) heat rate versus velocity.

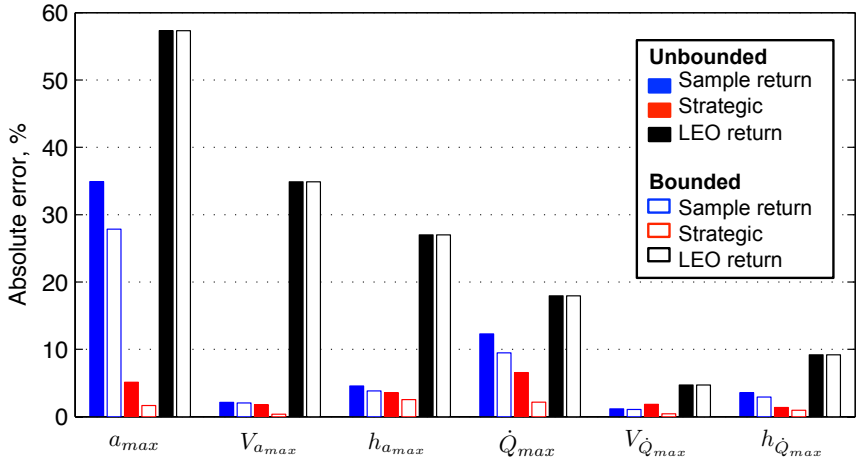

Figure 32: Allen-Eggers approximation error of vehicle states at peak conditions for bounded ($\delta_V = 0.05$, $\delta_q = 2$) and unbounded domains.

of closed-form expression of range and range-to-go as functions of the velocity. The range expressions extend the Allen-Eggers solution to cover all four states in Eqs. (7).

3.3.3.1 Derivation

The energy over weight for an entry vehicle is defined by:

$$E = \left[(1/2)mV^2 + mgh\right] / (mg) = V^2/(2g) + h \tag{88}$$

The derivative of the energy over weight with respect to time is given by, substituting in Eqs. (7a) and (7c):

$$\frac{dE}{dt} = \frac{V}{g}\frac{dV}{dt} + \frac{dh}{dt} = -\frac{\rho}{2g\beta}V^3 \tag{89}$$

The derivative of the subtended range angle with respect to the energy over weight is then:

$$\frac{d\theta}{dE} = \frac{d\theta/dt}{dE/dt} = \frac{-2\beta g\cos\gamma}{\rho V^2(R+h)} \tag{90}$$

Range is the distance traveled over the surface of a spherical planet, as shown in Fig. 33. For a spherical planet, the range is related to the range angle by the arc-length formula. Assuming the initial range s_0 and range angle θ_0 are zero:

$$s = R\theta = R\int_{E_0}^{E} \frac{-2\beta g\cos\gamma}{\rho V^2(R+h)}dE \tag{91}$$

If the final range is s_f, the range-to-go is:

$$s_{togo} = s_f - s = R\int_{E}^{E_f} \frac{-2\beta g\cos\gamma}{\rho V^2(R+h)}dE \tag{92}$$

A differential change in energy over weight may be described by:

$$dE = d(V^2)/(2g) + dh \tag{93}$$

Applying Eq. (93) to Eq. (91) and rearranging yields:

$$s = \int_{V^2}^{V_0^2} \frac{R\beta\cos\gamma}{(R+h)\rho V^2}d(V^2) + \int_{h}^{h_0} \frac{2R\beta g\cos\gamma}{(R+h)\rho V^2}dh \tag{94}$$

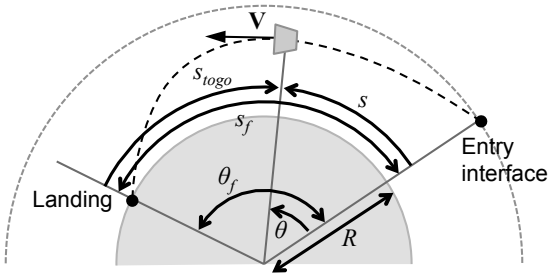

Figure 33: Planetary entry range and range angle.

The integral expression for range in Eq. (94) makes no assumptions relative to Eqs. (7). Analytical solution is possible using the Allen-Eggers assumptions: neglecting gravity eliminates the altitude integral and assuming a constant flight-path angle simplifies the velocity integral. Also, from Eq. (57):

$$\rho = \frac{\beta \sin\gamma^*}{H} \ln\left(\frac{V^2}{V_1^2}\right) + \rho_1 \tag{95a}$$

$$h = h_{ref} - H \ln\left[\frac{\beta \sin\gamma^*}{\rho_{ref} H} \ln\left(\frac{V^2}{V_1^2}\right) + \frac{\rho_1}{\rho_{ref}}\right] \tag{95b}$$

Applying the assumptions, substituting Eqs. (95) for altitude and density, and integrating Eq. (94) from state 2 to the initial state, with state 1 as a reference state:

$$s_2 = R\beta\cos\gamma^* \int_{V_2^2}^{V_0^2} \left\{\left[R + h_{ref} - H\ln\left(\frac{\beta\sin\gamma^*}{\rho_{ref}H}\ln\left(\frac{(V^2)}{V_1^2}\right) + \frac{\rho_1}{\rho_{ref}}\right)\right] \times \left[\frac{\beta\sin\gamma}{H}\ln\left(\frac{(V^2)}{V_1^2}\right) + \rho_1\right](V^2)\right\}^{-1} d(V^2) \tag{96}$$

Evaluating the integral in Eq. (96) using Mathematica's symbolic solver [150] results in a closed-form solution for range as a function of velocity:

$$s_2 = R\cot\gamma^* \left(\ln\left\{H\ln\left[\frac{\rho_1}{\rho_{ref}} + \frac{\beta\sin\gamma^*}{H\rho_{ref}}\ln\left(\frac{V_2^2}{V_1^2}\right)\right] - h_{ref} - R\right\} - \ln\left\{H\ln\left[\frac{\rho_1}{\rho_{ref}} + \frac{\beta\sin\gamma^*}{H\rho_{ref}}\ln\left(\frac{V_0^2}{V_1^2}\right)\right] - h_{ref} - R\right\}\right) \tag{97}$$

Similarly, starting from Eq. (92), the range-to-go at a particular velocity is given by:

$$s_{togo,2} = R\cot\gamma^* \left(\ln\left\{H\ln\left[\frac{\rho_1}{\rho_{ref}} + \frac{\beta\sin\gamma^*}{H\rho_{ref}}\ln\left(\frac{V_f^2}{V_1^2}\right)\right] - h_{ref} - R\right\} - \ln\left\{H\ln\left[\frac{\rho_1}{\rho_{ref}} + \frac{\beta\sin\gamma^*}{H\rho_{ref}}\ln\left(\frac{V_2^2}{V_1^2}\right)\right] - h_{ref} - R\right\}\right) \tag{98}$$

Eqs. (97) and (98) are closed-form, analytical expressions for range as a function of velocity or altitude, vehicle and planetary parameters, initial conditions, and a constant flight-path angle. The constant flight-path angle may be set to the initial flight-path angle, as advocated by Allen and Eggers, or determined with the method outlined in Sec. 3.3.1.

Alternately, solving Eq. (96) assuming $R/(R+h) \approx 1$ and setting $V_1 = V_0$, the range may be reduced to a simple function of altitude:

$$s_2 = \cot\gamma^* \left(h_2 - h_0\right) \tag{99}$$

The additional assumptions made in deriving Eq. (99) make the trajectory a straight path through space; this is not the case for Eqs. (97) and (98). Eq. (99) is equivalent to expressing Kornreich's solution for range as a function of altitude instead of density. Kornreich's range expression is given by:

$$s_2 = H \cot\gamma_0 \ln \rho_2/\rho_0 + \text{ higher order terms} \tag{100}$$

where higher order terms are neglected [60]. Eqs. (99) and (100) reflect the assumption of a flat planet, an assumption not made by Allen and Eggers.

3.3.3.2 Example Application

Figure 34 shows Eqs. (97) and (98) applied to the example trajectories. The approximation is applied over the domain bounded by δ_V and δ_q values of 0.05 and 2, respectively, and γ^* is determined using Eq. (79). Figure 34a uses the Allen-Eggers equations for the vehicle state at peak acceleration for the state-1 reference point; Fig. 34b uses the initial condition for the state-1 reference point. The range and range-to-go estimates are good for the strategic case; estimation of range-to-go appears to result in lower error relative to range for all three cases.

Figure 35 shows the percent and absolute approximation errors for Eq. (97) as well as Kornreich's solution (Eq. (100)), where both utilize Eq. (79) to compute γ^*. Initial

range predictions have near-zero error because the initial range traveled is zero. For all three cases, the error in Eq. (97) quickly climbs to a near-constant value: about 10% for the sample-return case, -2% for the strategic case, and -50% for the LEO-return case. While approximation error is low for the strategic case, the 10% error for the sample-return case corresponds to an absolute error of nearly 80 km. Overall, the errors in Eq. (97) and Kornreich's solution are similar. Both approximations produce nearly identical poor representations of the LEO-return case; Kornreich's solution shows slightly lower error for the strategic case; Eq. (97) shows slightly lower error for the sample-return case.

Eq. (97) includes the altitude variation of $d\theta/dt$; Kornreich's solution does not. Inclusion of the altitude correctly reduces the range rate, and therefore total range, implying that Kornreich's solution should, in general, overestimate the range, as shown for the sample-return case. However, the selection of γ^* also influences the magnitude of $d\theta/dt$. For the strategic example in Fig. 35, the computed γ^* is less than the velocity-averaged flight-path angle; this also reduces the range flown and is an artifact of the choice of V^* at which γ^* is computed. Kornreich's solution's tendency to overestimate the range largely counters this effect. Eq. (97) does not, resulting in a larger error. However, the difference in error signatures is small, with a maximum difference of approximately 300 m. Eq. (97) and Eq. (99) show similar error signatures; the differences in error can be overwhelmed by other factors, such as the choice of V^*. The primary benefit of Eq. (97) over Eq. (99) is that it does not require any additional assumptions beyond those made by Allen and Eggers.

Approximation error for range-to-go (Eq. (98)) is shown in Fig. 36. Percent error is within 2% for the sample-return case and less than 1% for the strategic case. Approximation error is below 3% for even the LEO-return case. The spikes present in Fig. 36b are caused by sign changes in the error. Overall, errors are approximately an order of magnitude less than they are for the range estimate. In addition, because

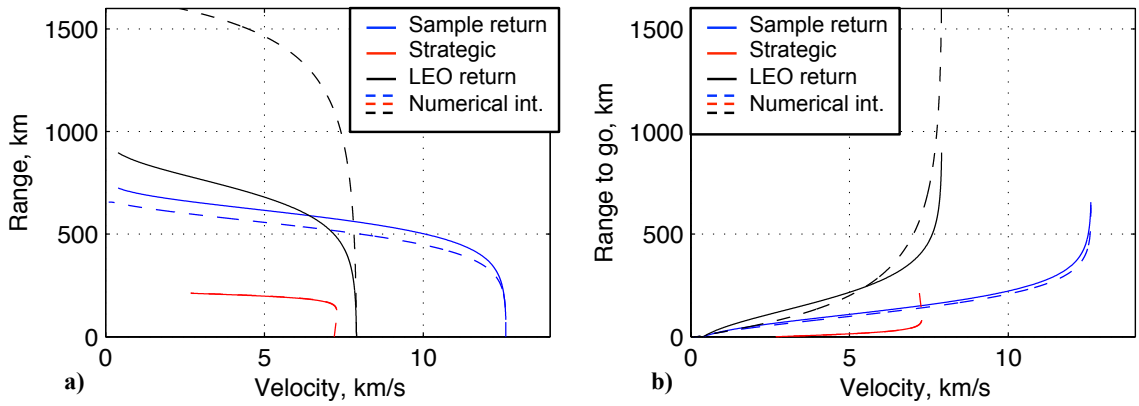

Figure 34: Comparison of numerical integration (dashed) and estimates (solid) of a) range and b) range-to-go.

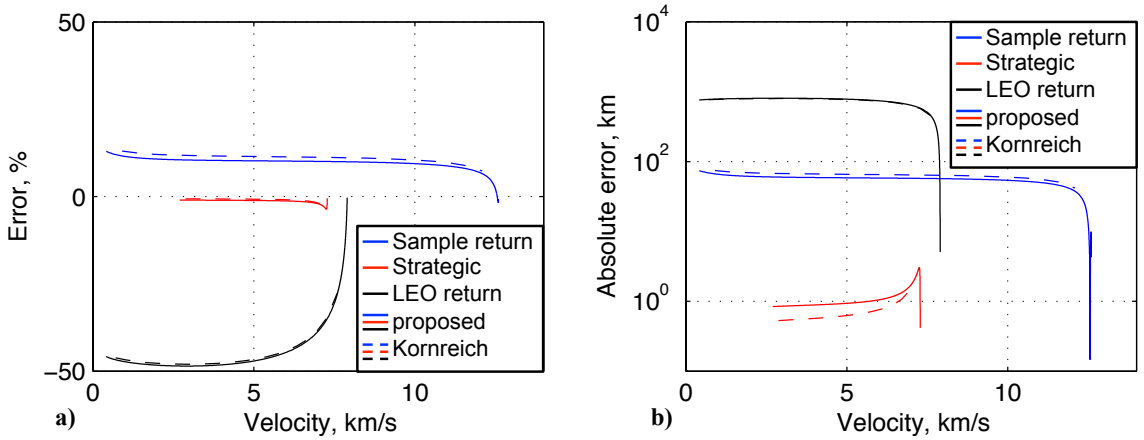

Figure 35: Comparison of range estimation error for Eq. (97) (solid) and Kornreich's expression (dashed) a) percent error with respect to total range and b) absolute error.

range-to-go is always decreasing, the absolute error trends to a near-zero final value.

Results indicate that while Eq. (97) provides a only a rough estimate of the range traveled during entry, the accuracy of Eq. (98) may be sufficient for use in onboard guidance and targeting algorithms for ballistic entry systems, particularly drag-modulation trajectory control systems [159].

3.3.4 Trajectory States as a Function of Time

Three significant assumptions relative to the planar equations of motion (as given in Eqs. (7)) are made in the derivation of the Allen-Eggers solution:

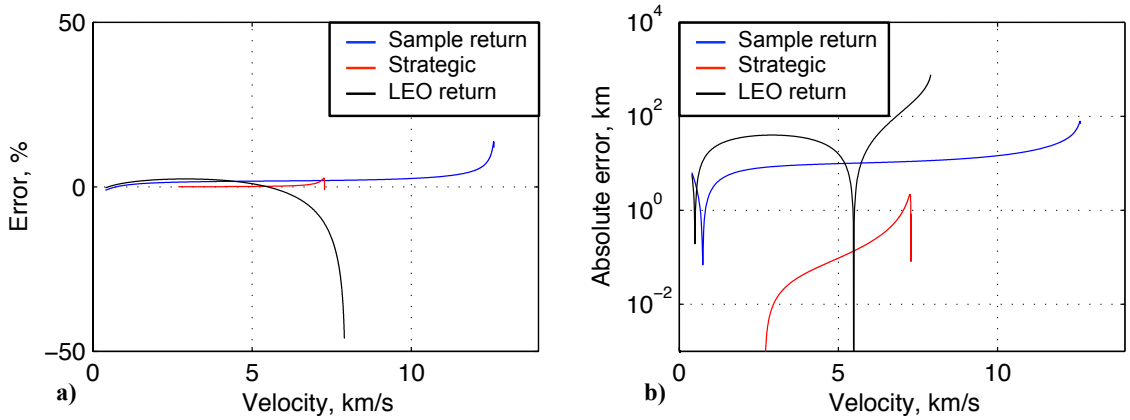

Figure 36: Range-to-go estimation error: a) percent error with respect to total range and b) absolute error.

1. Ballistic entry: $L/D = 0$

2. Constant flight-path angle: $d\gamma/dt = 0$

3. Gravity is negligible relative to drag: $\rho V^2/(2\beta) \gg -g \sin\gamma$

The equations of motion with the above assumptions applied are, reduced from Eqs. (7):

$$\frac{dV}{dt} = -\frac{\rho_{ref}}{2\beta} \exp\left(\frac{h_{ref} - h}{H}\right) V^2 \tag{101a}$$

$$\frac{d\gamma}{dt} = 0 \tag{101b}$$

$$\frac{dh}{dt} = V \sin\gamma^* \tag{101c}$$

$$\frac{d\theta}{dt} = \frac{V \cos\gamma^*}{R + h} \tag{101d}$$

The original Allen-Eggers solution is an exact solution to the reduced equations when t is eliminated by combining Eq. (101a) and (101c). This includes the Allen-Eggers assumption that $\gamma^* = \gamma_0$; as shown previously, more accurate results are obtained when γ^* is computed using the method proposed in Sec. 3.3.1.

Eqs. (101) may be integrated directly with respect to time. Using Mathematica, the resulting solution is [150]:

$$V = C_1 \exp\left[\frac{\rho_{ref} H}{2\beta \sin\gamma^*} \exp\left(\frac{h_{ref} - h}{H}\right)\right] \tag{102a}$$

$$\gamma = \gamma^* \tag{102b}$$

$$-H\mathrm{Ei}\left[-\frac{\rho_{ref} H}{2\beta \sin\gamma^*} \exp\left(\frac{h_{ref} - h}{H}\right)\right] = C_1 \sin\gamma^* t + C_2 \tag{102c}$$

$$\theta = C_3 + \cot\gamma^* \ln(R + h) \tag{102d}$$

If the initial condition is given by V_0, h_0, $\gamma_0 = \gamma^*$, $\theta_0 = 0$, and $t_0 = 0$, the constants of integration are:

$$C_1 = V_0 \exp\left[-\frac{\rho_{ref} H}{2\beta \sin\gamma^*} \exp\left(\frac{h_{ref} - h_0}{H}\right)\right] \tag{103a}$$

$$C_2 = -H\mathrm{Ei}\left[-\frac{\rho_{ref} H}{2\beta \sin\gamma^*} \exp\left(\frac{h_{ref} - h_0}{H}\right)\right] \tag{103b}$$

$$C_3 = -\cot\gamma^* \ln(R + h_0) \tag{103c}$$

Eq. (102a) is similar in structure to the altitude-velocity profile first derived by Allen and Eggers, and is exactly that derived earlier (Eq. (57)) when Eq. (103a) is applied. The range equations, Eqs. (97) and (98), may be derived from Eq. (102d) by multiplying by R to convert from range angle to range and replacing instances of h with V using Eq. (57). Lastly, Eq. (102c) provides a relationship between time and altitude. The time expression was first derived by Norman in 1963 [80]. Miller developed a time expression for ballistic entry in 1961, but failed to recognize that the series approximations in his solution were the exponential integral, causing him to erroneously state that there was no closed-form solution for time [85, 80].

Evaluation of Eqs. (102) is most convenient when altitude is chosen for the domain; this allows time to be found without iterative root finding. Vehicle states computed using Eqs. (102) are compared to numerical integration of Eqs. (7) as a function of time in Fig. 37; acceleration and heating as a function of time are shown

in Fig. 38. Eqs. (102) show good agreement with numerical integration of Eqs. (7) for the strategic case. Agreement for the sample-return case is good for approximately 100 s, which encompasses the acceleration and heat-rate pulses. Agreement for the LEO-return case is poor as in previous examples.

Numerical difficulties may occur when evaluating Eqs. (102) due to the exponential integral in Eq. (102c): for large arguments (greater than 100), the exponential integral is large, i.e. hundreds of orders of magnitude greater than its argument. Large arguments occur at low altitudes for small β and shallow γ^* and correspond to violations of two Allen-Eggers assumptions. First, shallow trajectories (shallow γ^*) are not well-approximated by a constant flight-path angle, as shown by the LEO-return example throughout this study. Second, low-β vehicles decelerate higher in the atmosphere. While small β increases the magnitude of the drag force relative to gravity, it also causes gravity to become significant at higher altitudes, violating the Allen-Eggers negation of gravity. Figure 37c shows an example of this observation for the sample-return trajectory: the analytical solution for time from the Allen-Eggers equations of motion is a good approximation until an altitude of approximately 50 km, at which point the argument of the exponential integral on the left-hand side of Eq. (102c) becomes large causing the left-hand side of the equation to become large, ultimately resulting in large, unrealistic values of t.

Norman's solution for time during entry, given by Eq. (102c), was compared to Kumagai's expression for time of flight for ballistic entry, given by:

$$t = \left[(R+h_0)V_0\left|\sin\gamma_0\right|\right]^{-1}\exp\left(-\frac{H\rho_{ref}}{2\beta\sin\gamma}e^{-h_0/H}\right) \times\left[\frac{(R+h_0)^2-(R+h)^2}{2}+H\sum_{n=1}^{\infty}\frac{e^{-nh/H}}{n(n!)}\left(-\frac{H\rho_{ref}}{2\beta\sin\gamma}\right)^n\left(R+h+\frac{H}{n}\right) -H\sum_{n=1}^{\infty}\frac{e^{-nh_0/H}}{n(n!)}\left(-\frac{H\rho_{ref}}{2\beta\sin\gamma}\right)^n\left(R+h_0+\frac{H}{n}\right)\right] \quad (104)$$

where $t_0 = 0$. Kumagai's solution is based on a representation of the exponential decay of angular momentum during entry and does not neglect gravity nor assume a constant flight-path angle [91]. The similarity between Eq. (104) and Eq. (102c) becomes apparent if one recognizes that the infinite-series expression for the exponential integral is [113]:

$$\mathrm{Ei}(x) = \bar{\gamma} + \ln x + \sum_{n=1}^{\infty} \frac{x^n}{n(n!)} \tag{105}$$

Figure 39 shows that the error curves of Kumagai's solution (utilizing 10 terms in each series approximation and $\gamma = \gamma^*$) and Norman's solution (Eq. (102c)) are nearly identical for the sample-return and LEO-return examples; Eq. (102c) provides a small improvement in accuracy for the strategic case at low altitude. Given the similar accuracy of the two methods, the primary benefits of Eq. (102c) relative to Kumagai's solution are its simpler form and more straightforward derivation as a direct integration of the simplified equations of motion.

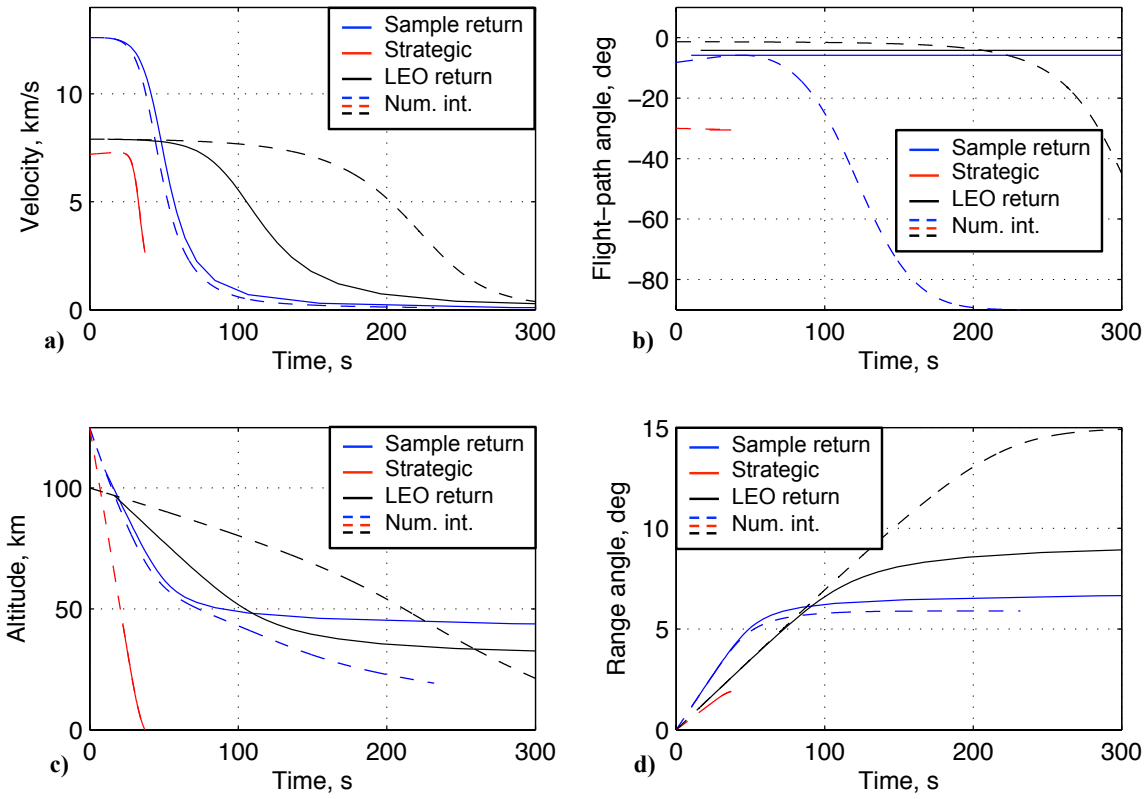

Figure 37: Comparison of states from the time-dependent Allen-Eggers solution (solid) with numerical integration (dashed): a) velocity, b) altitude, c) flight-path angle, and d) range angle versus time.

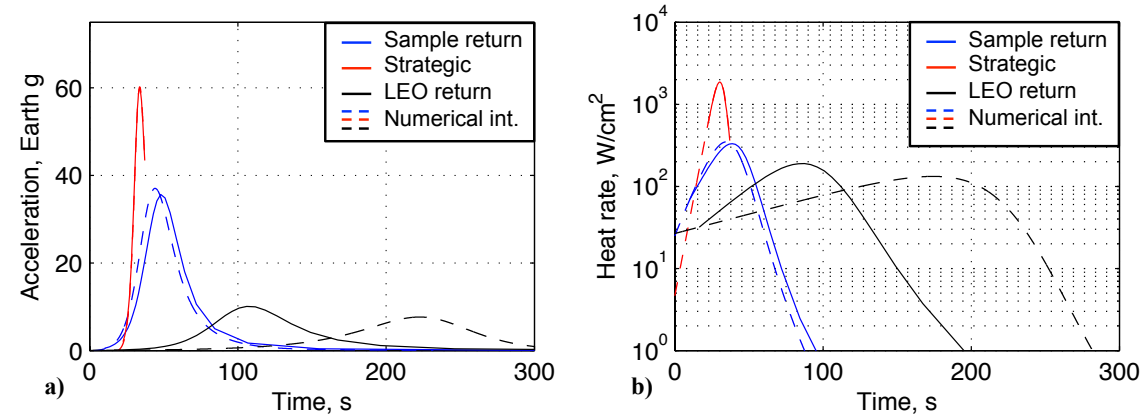

Figure 38: Comparison of states from the time-dependent Allen-Eggers solution (solid) with numerical integration (dashed): a) acceleration and b) heat rate versus time.

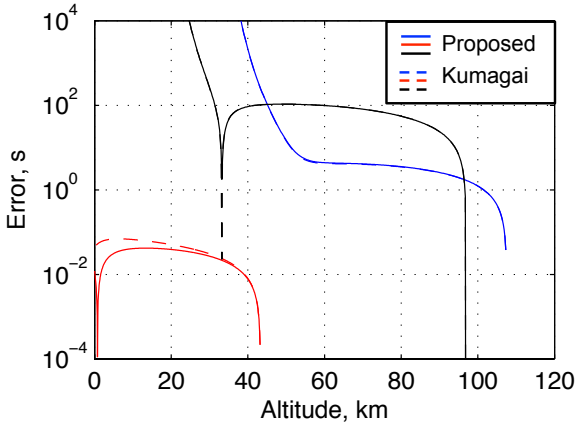

Figure 39: Absolute error in trajectory time estimates for Eq. (102c) (solid) and Kumagai's solution (dashed).

3.4 Assessment of Approximation Error and Applicability

3.4.1 The Extended and Enhanced Allen-Eggers Approximation

Figure 40 shows example applications of the extended and enhanced Allen-Eggers approximation. Application of the original Allen-Eggers approximation is shown in grey. Figure 41 shows the approximation error of the original and extended and enhanced versions. The figures indicate that significant improvements in approximation error were achieved relative to the planar equations of motion. Approximation error for the strategic case is below 5% across Fig. 41, with the exception of altitude at low velocities (Fig. 41a). Approximation error for the sample-return example is below 10% over most of the hypersonic flight regime, typically the most important part of an entry trajectory. The LEO-return example exhibits large, but reduced error that is better centered about zero. A large error magnitude is not unexpected, as the initial flight-path angle for this example is too shallow for the Allen-Eggers negation of gravity to be a good assumption.

Figure 42 shows the approximation error in peak conditions for the extended and enhanced solution relative to the original. Significant improvement is apparent across nearly all parameters, with the exception of the peak heat-rate estimate for the LEO-return case.

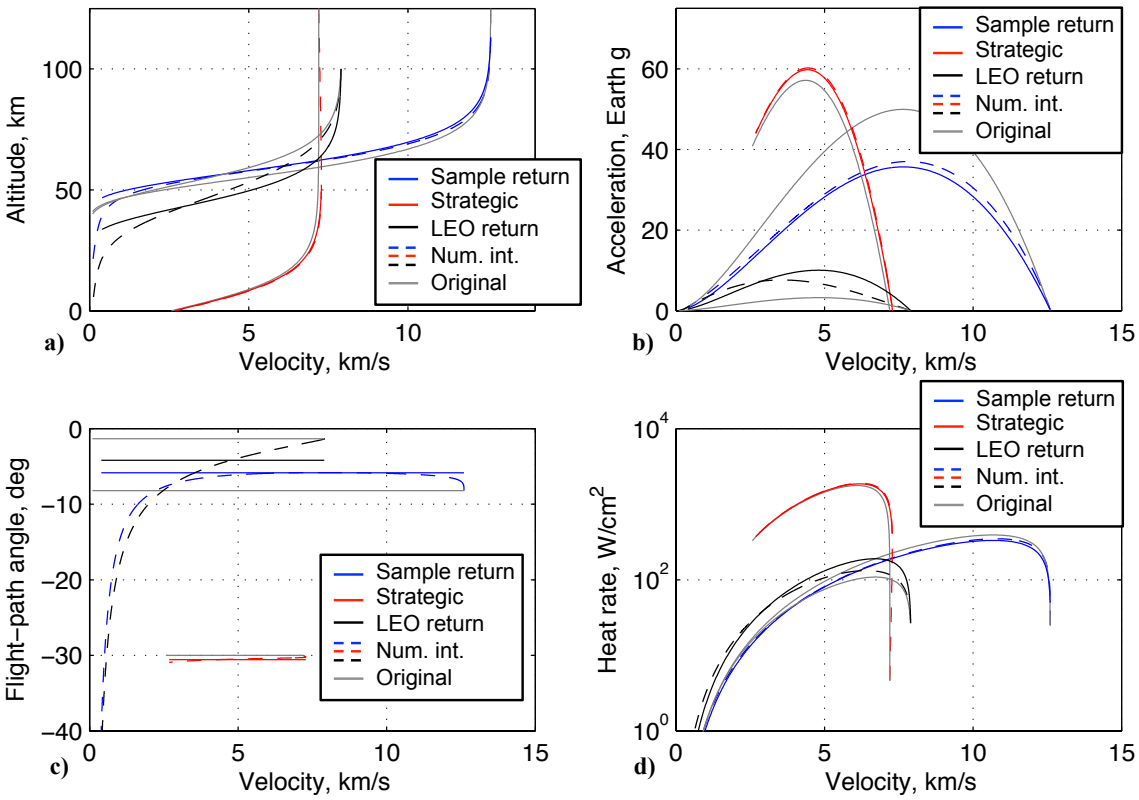

Figure 40: Comparison of the extended and enhanced Allen-Eggers solution (solid), the original Allen-Eggers solution (gray), and numerical integration (dashed): a) altitude, b) acceleration, c) flight-path angle, and d) heat rate versus velocity.

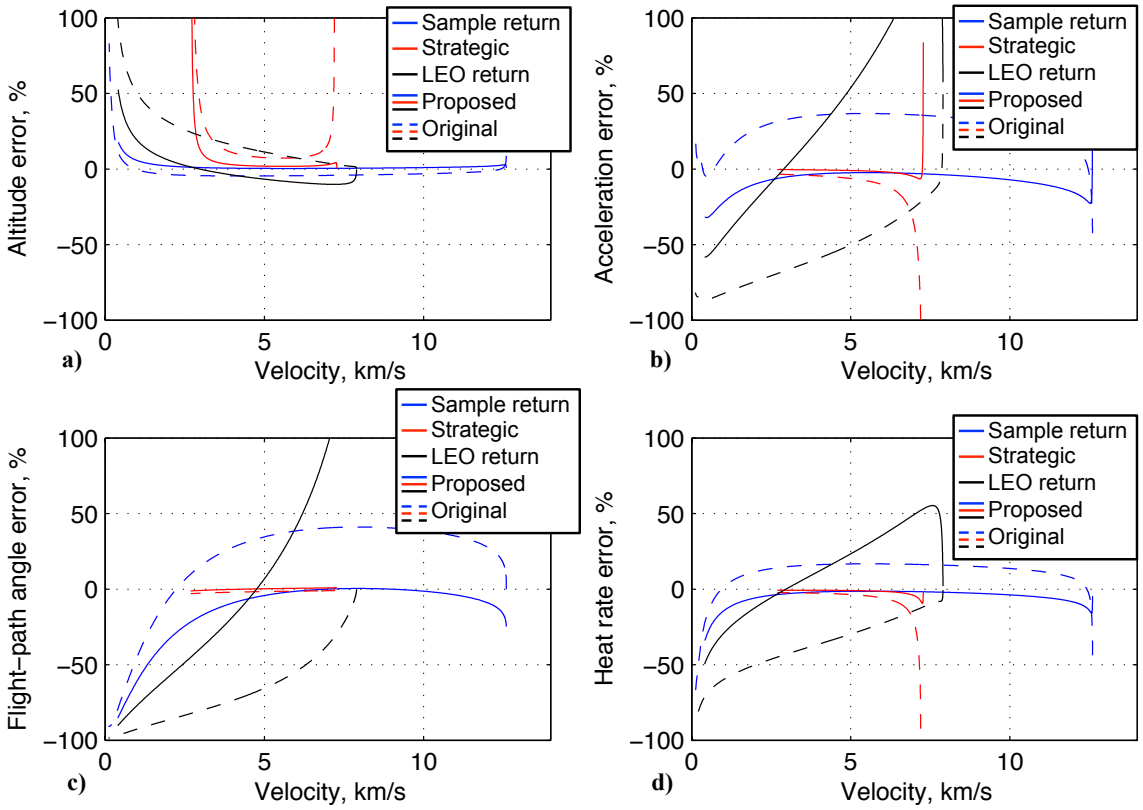

Figure 41: Comparison of approximation error for the extended and enhanced Allen-Eggers solution (solid) and the original Allen-Eggers solution (dashed): a) altitude, b) acceleration, c) flight-path angle, and d) heat rate versus velocity.

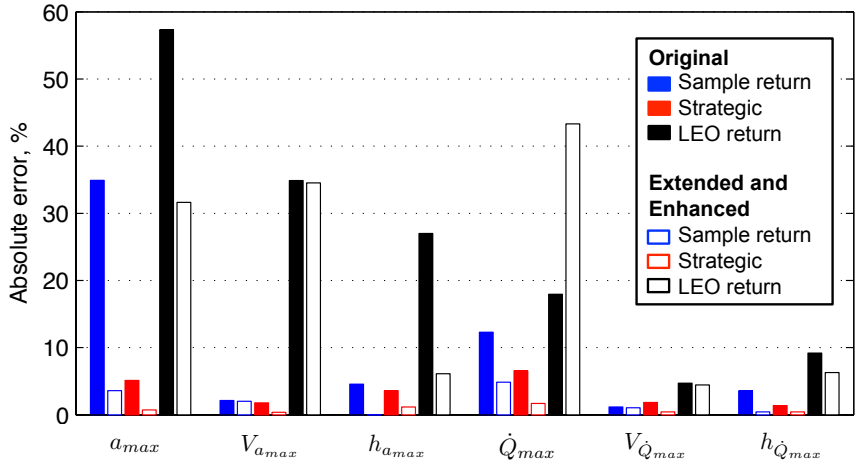

Figure 42: Approximation error for the original and extended and enhanced Allen-Eggers solutions.

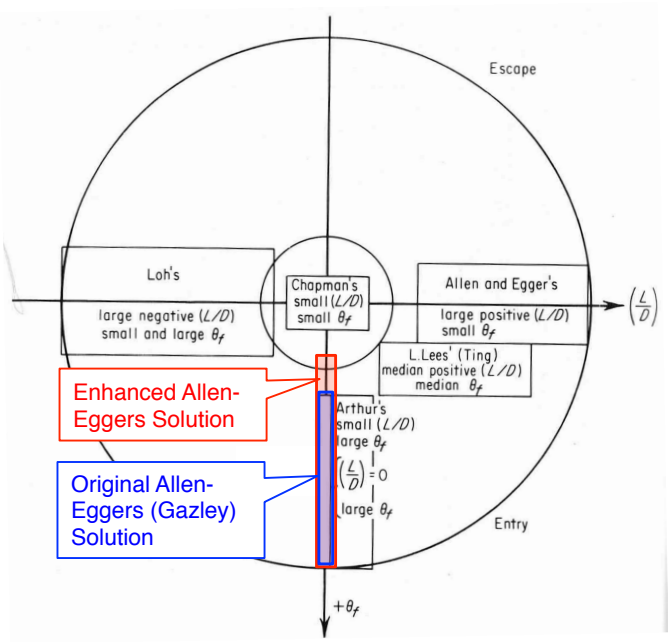

Figure 43: Improvements to the domain of applicability of the Allen-Eggers (Gazley) solution [1].

These improvements have the net effect of improving accuracy of the solution such that it is applicable for more shallow initial flight-path angles than in the original formulation. This may be shown on Loh's chart (see Fig. 43). Loh credits this solution to Gazley (since Allen and Eggers' solution was classified at the time), this work extends the range of the solution as shown by the red box.

3.4.2 Applicability to Other Initial Conditions

Initial velocity and flight-path angle were varied for the three examples used in this study to determine the applicability of the extended Allen-Eggers solution across a broader mission set. The initial flight-path angle and velocity bounds were chosen to cover a wide range of potential entries at Earth. Domains for application of the Allen-Eggers solution to individual trajectories were bound by δ_V and δ_q values of 0.05 and 2, respectively.

3.4.2.1 Normalized Integrated Trajectory Error

Contours of the normalized integrated trajectory approximation error (see Eq. (53)) for acceleration, heat rate, and range-to-go were computed over a range of initial conditions for each example vehicle. Initial conditions resulting in trajectories with any positive altitude rate are not considered; the boundary for these trajectories is marked with a hatched line. The integrated error is normalized by the integrated error for the associated example trajectory, marked on the plot by $\otimes$. For example, in Fig. 44, the black 1 contour represents the locus of initial conditions (and their corresponding trajectories) for which the integrated range-to-go error is equal to that shown in the example sample-return trajectory. Trajectories inside the space bounded by the black 1 contour have lessor integrated range-to-go error; trajectories outside this space have greater integrated range-to-go error.

Figure 44 shows integrated error contours for the sample return vehicle. The error contours for acceleration and heat rate show similar trends above 9 km/s: trajectories with steeper initial flight-path angles have lower integrated error while more shallow initial flight-path angles have greater error. Above 9 km/s, the error contours are also relatively insensitive to the initial velocity. For velocities below 9 km/s, the acceleration and heat-rate error contours no longer track the positive altitude-rate boundary. Additionally, a region of relatively low error appears for steep initial flight-path angles. Overall, accuracy is poor for slower, more shallow initial conditions.

The integrated range-to-go error contours in Fig. 44 follow a different trend: a region with error equal to or less than the example trajectory exists between initial flight-path angles of -5 and -15 deg for velocities greater than 6 km/s. Outside this region, error grows for more steep or shallow initial flight-path angles. However, error growth is slow for steeper initial flight-path angles, with error only rising to twice the example trajectory for initial flight-path angles of -80 deg.

For the strategic vehicle (Fig. 45), acceleration and heat-rate error contours are

mostly coincident over the range of initial conditions assessed, with error decreasing with distance from the positive altitude-rate boundary. The contour values are larger than in the sample-return case because the error is normalized by the relatively low integrated error associated with the strategic case. As in the sample-return case, the range-to-go error contours show a different behavior: integrated range-to-go error is consistently low for flight-path angles steeper than about 10 deg.

The integrated error for the LEO-return vehicle, shown in Fig. 46, is consistent with the LEO-return example trajectory being outside the domain of applicability for the Allen-Eggers solution. Accuracy improves significantly for steeper trajectories, and overall trends are similar to the sample-return example for acceleration, heat-rate, and range-to-go error contours.

Some general trends are apparent across all three figures. First, integrated acceleration and heat-rate error decrease for steeper and faster trajectories. The contours also show that the error in acceleration and heat-rate predictions is relatively low over a broad range of initial conditions. The error increases quickly near the positive altitude rate boundary. The integrated error associated with the range-to-go approximation is larger, with minimum values near -10 deg for velocities over about 6 km/s for the lower β sample-return and LEO-entry vehicles. The region shifts to steeper flight-path angles for the high-β strategic vehicle. The region of low error, and the subsequent increase in error for steeper initial flight-path angles and larger initial velocities, is due to the natures of percent error and estimating range-to-go. Range-to-go is fundamentally tied to the final point of the trajectory; however, unlike the initial point, the final conditions are not specified. This introduces additional error into the range-to-go solution. Additionally, as the flight-path angle steepens, the total range and range-to-go decrease to small values. This can lead to large percent errors that are not necessarily indicative of large absolute error. For example, if $\gamma_0 = -90$ deg, the Allen-Eggers range is identically zero, while numeric integration may arrive

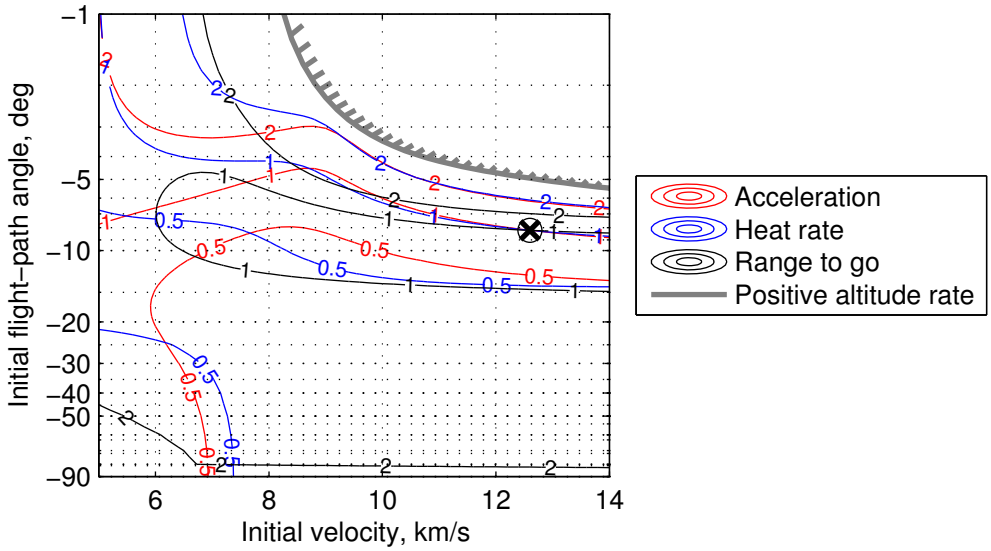

Figure 44: Normalized integrated error in acceleration, heat rate, and range-to-go over a range of initial conditions for the sample-return example vehicle ($\beta = 60$ kg/m^2).

at some small number, resulting in a large percent error. Despite the greater error relative to the acceleration and heat rate, the integrated error for range-to-go remains relatively low over over the velocities considered for trajectories steeper than -7 deg for the sample-return vehicle, steeper than about -10 deg for the strategic vehicle, and steeper than about -8 deg for the LEO-return vehicle.

3.4.2.2 Peak Acceleration and Heat-rate Error

Figure 47 shows contours of the percent error in the Allen-Eggers estimates of the peak acceleration (Fig. 47a) and peak heat rate (Fig. 47b) for all three example vehicles. The different ballistic coefficients of the vehicles result in three vehicle-specific positive altitude-rate boundaries. The trends across all three vehicles are surprisingly consistent, with many contours nearly coincident, implying that the approximation error is nearly independent of the vehicle's ballistic coefficient. For initial flight-path angles steeper than approximately -10 deg, error in the peak acceleration prediction is within 5%; for initial velocities above 8 km/s, error is below 5% for trajectories steeper than -7 deg. For peak heat rate, error is below 5% for all trajectories steeper

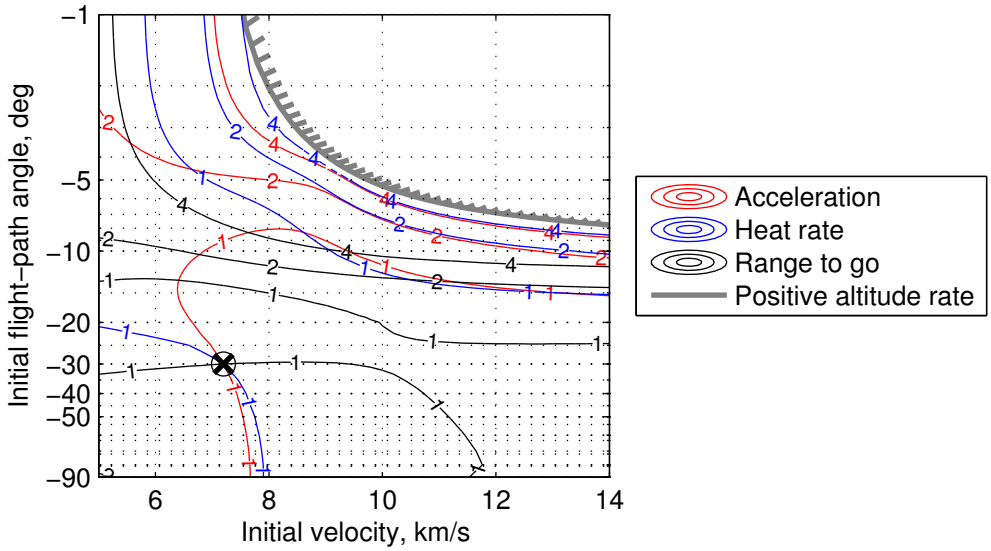

Figure 45: Normalized integrated error in acceleration, heat rate, and range-to-go over a range of initial conditions for the strategic example vehicle ($\beta = 10000$ kg/m^2).

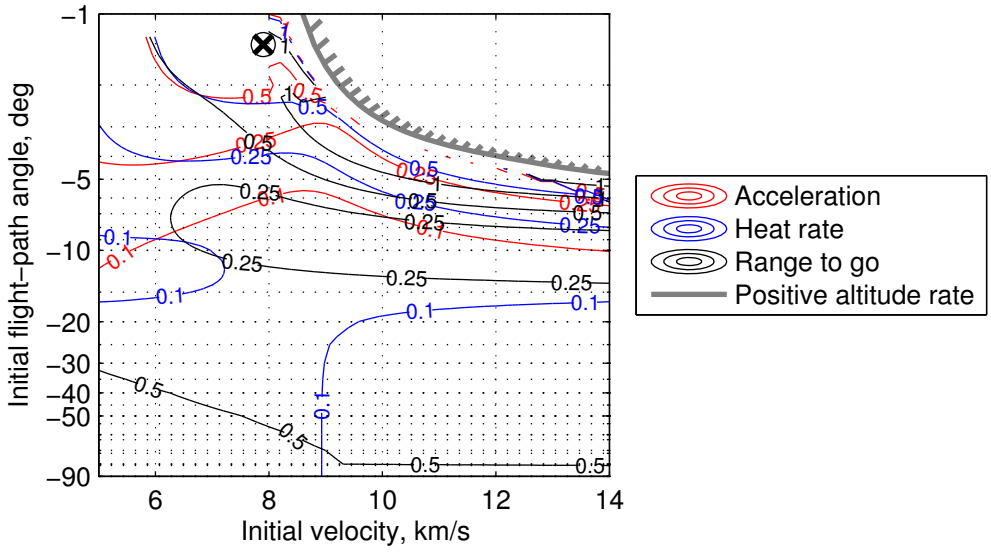

Figure 46: Normalized integrated error in acceleration, heat rate, and range-to-go over a range of initial conditions for the LEO-return example vehicle ($\beta = 450$ kg/m^2).

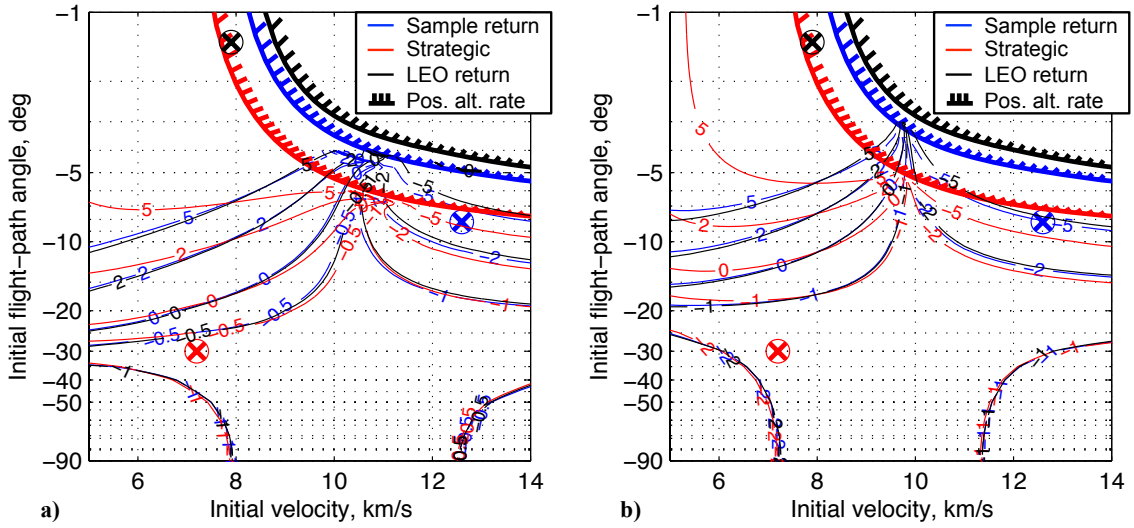

Figure 47: Percent error in a) peak acceleration and b) peak heat rate estimates.

than -8 deg, and for trajectories steeper than -6 deg with initial velocities greater than 8 km/s. Overall, Fig. 47 shows that the Allen-Eggers approximate solutions for peak acceleration and peak heat rate are accurate to 5% for a broad range of initial conditions and ballistic coefficients.

3.5 Summary

The Allen-Eggers approximate solution to the planar equations of motion for ballistic entry has been extended and enhanced. A method has been developed for determining appropriate values for the constant flight-path angle assumed to exist in the Allen-Eggers solution. Determining the constant flight-path angle for use in the Allen-Eggers solution has long been viewed as a practical challenge when applying the approximation to a real-world problem. The proposed method preserves the simplicity and speed inherent in the Allen-Eggers solution and improves approximation accuracy significantly.

The domain of applicability for the Allen-Eggers solution for given trajectory parameters has been bounded by nondimensional initial dynamic pressure and final velocity stand-off factors. Values may be selected for the stand-off factors to ensure

that Allen-Eggers solution approximation error is limited to acceptable magnitudes.

Closed-form, analytical expressions for range and range-to-go have been developed, extending the Allen-Eggers approximation to all four two-dimensional vehicle states in a consistent manner. These expressions adhere to the assumptions made by Allen and Eggers for the rest of the solution.

Lastly, it has been shown that the Allen-Eggers solution may be derived directly, including Norman's expression for time of flight, by applying the Allen-Eggers solution assumptions to the planar equations of motion. The enhancements address key weaknesses in the original solution and are fully consistent with the Allen-Eggers assumptions.

When combined, the enhancements developed in this investigation improve the accuracy of the Allen-Eggers solution relative to the planar equations of motion by up to an order of magnitude. Exploration of approximation error over a range of trajectory parameters shows that the extended and enhanced Allen-Eggers solution provides good accuracy across a range of ballistic coefficients and is generally applicable for ballistic entries at Earth with initial flight-path angles steeper than -7 deg; accuracy for more shallow trajectories may be acceptable depending on specific trajectory parameters.

Lastly, the improved accuracy of the extended and enhanced Allen-Eggers solution and the closed-form expressions for range may form a basis for onboard guidance and targeting algorithms for ballistic entry systems, especially those employing drag-modulation trajectory control. In particular, the Allen-Eggers closed-form analytical expressions may be used to generate vehicle state predictions or be used to supply initial guesses or solution bounds for high-accuracy numerical guidance schemes.

CHAPTER IV

ANALYTICAL ASSESSMENT OF DISCRETE-EVENT DRAG-MODULATION SYSTEMS

4.1 Application of the Enhanced Allen-Eggers Solution

The enhanced Allen-Eggers solution may be used to assess drag-modulation trajectory-control systems for planetary entry. Consider an entry vehicle capable of discrete-event drag-modulation trajectory control that modulates its drag by reducing drag area through a single jettison event at a particular point during entry. The drag-area jettison is assumed to be instantaneous; vehicle properties are constant on either side of the jettison. These properties may be described by the pre-jettison ballistic coefficient, β_1, and post-jettison ballistic coefficient, β_2. Furthermore, we will assume that $\beta_2 > \beta_1$.

An example application is shown in Fig. 48. For this trajectory (parameters given in Table 6), agreement between numerical integration of the equations of motion and the enhanced Allen-Eggers solution (referred to as the Allen-Eggers solution in this chapter) is excellent. The trajectory is constructed using two separate, constant ballistic coefficient segments that join at the jettison point. The first segment starts from the initial condition in Table 6 with $\beta = \beta_1$. The second segment has $\beta = \beta_2$; the jettison point serves as the initial condition for the second trajectory segment, where $V_{0,2} = V_J$, $h_{0,2} = f(V_J)$, and $\gamma_{0,2} = \gamma_1^*$.

The altitude-velocity plot (Fig. 48(a)) shows the corridor-bounding trajectories for this initial state. These trajectories correspond to the cases where no jettison occurs (entry with constant $\beta = \beta_1$) and where jettison occurs at the initial state (entry with constant $\beta = \beta_2$). Figure 48(c) shows the discrete change in acceleration

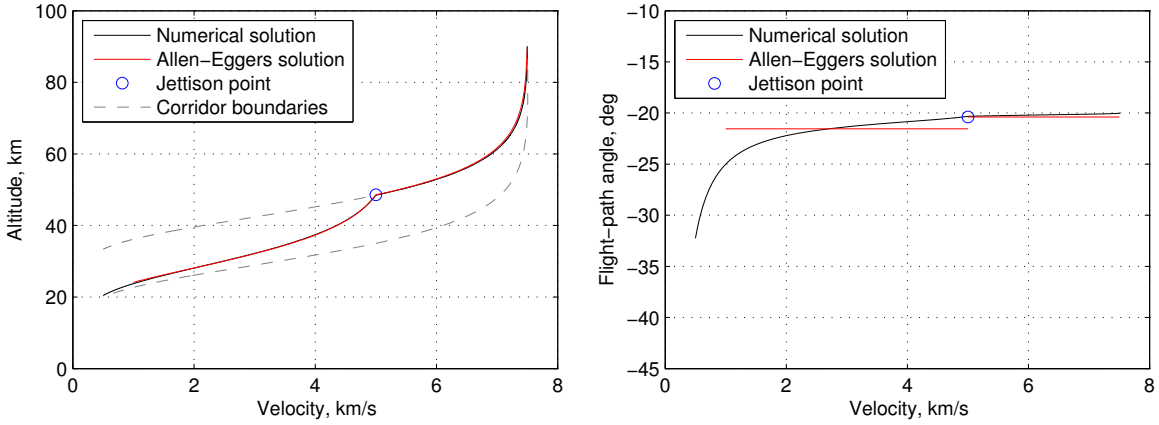

(a) Altitude

(b) Flight-path angle

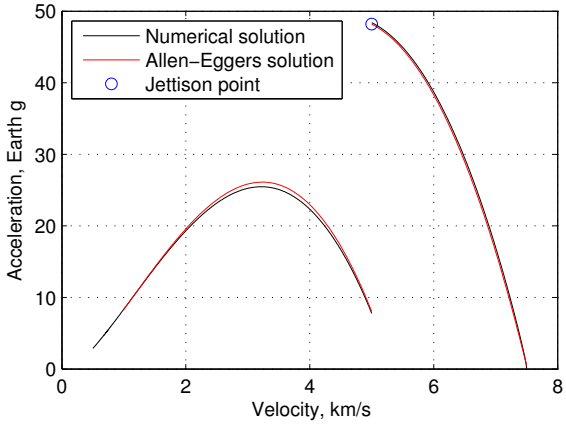

(c) Acceleration

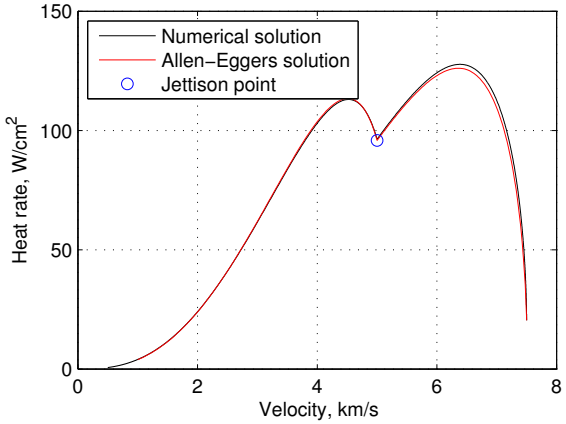

(d) Heat rate

Figure 48: Example application of the Allen-Eggers solution.

at jettison; Figure 48(d) shows the discrete change in the rate of change of the heat rate.

Table 6: Nominal Parameters for Example Trajectory

Parameter	*Value*
Planet	Earth
V_0	7500 m/s
γ_0	-20 deg
h_0	90 km
β_1	50 kg/m^2
β_2	300 kg/m^2
V_J	5000 m/s

4.2 Range Control Authority

The Allen-Eggers approximate solution may be used to show analytically how changes in ballistic coefficient may be used to control range during entry. By varying the jettison velocity, a drag-modulation entry vehicle may control its range (see Fig. 49). The maximum possible range occurs when jettison occurs immediately, resulting in constant-β flight at maximum β, β_2. The minimum possible range occurs when no jettison occurs, resulting in constant-β flight at the minimum β, β_1.

The control authority metric for drag-modulation trajectory control systems is ratio of the maximum to minimum ballistic coefficients, or β_2/β_1. This may be shown analytically, starting with the equation for range-to-go over a flat planet:

$$s_{togo} = \cot\gamma^* \left(h_f - h\right) \tag{106}$$

The divert capability at jettison for a discrete-event drag-modulation system is:

$$\Delta s = \overbrace{\cot\gamma_2^* \left(h_f - h_J\right)}^{\text{max. range}} - \overbrace{\cot\gamma_1^* \left(h_f - h_J\right)}^{\text{min. range}} \tag{107}$$

Altitude may be written as a function of velocity and ballistic coefficient through the Allen-Eggers altitude-velocity profile:

$$h = h_{ref} - H \ln\left[\frac{\beta \sin\gamma^*}{\rho_{ref} H} \ln\left(\frac{V^2}{V_1^2}\right) + \frac{\rho_1}{\rho_{ref}}\right] \tag{108}$$

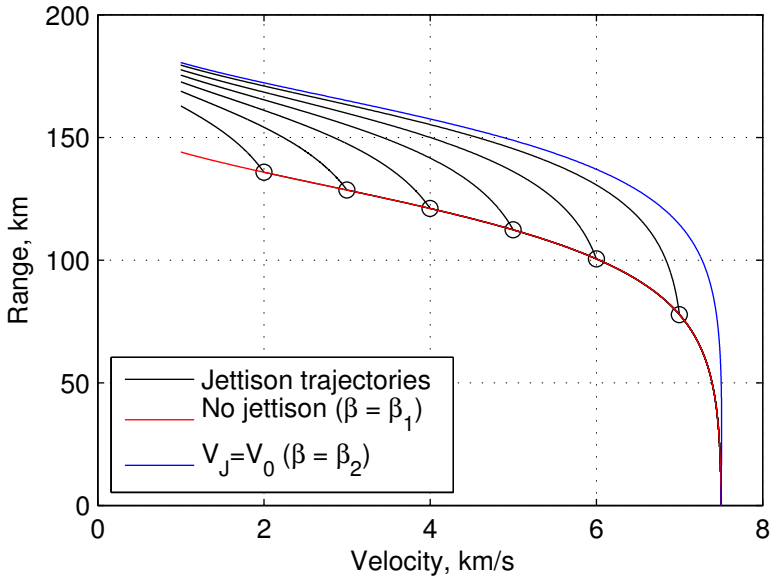

Figure 49: Range profiles for several V_J.

If we choose our reference point (denoted by subscript 1 above) to be the jettison velocity, we find:

$$\Delta s = \cot\gamma_2^* \left(H \ln\left[\frac{\beta_2 \sin\gamma_2^*}{\rho_{ref} H} \ln\left(\frac{V_f^2}{V_J^2}\right) + \frac{\rho_J}{\rho_{ref}} \right] - H \ln\left[\frac{\rho_J}{\rho_{ref}}\right] \right) - \cot\gamma_1^* \left(H \ln\left[\frac{\beta_1 \sin\gamma_1^*}{\rho_{ref} H} \ln\left(\frac{V_f^2}{V_J^2}\right) + \frac{\rho_J}{\rho_{ref}} \right] - H \ln\left[\frac{\rho_J}{\rho_{ref}}\right] \right) \quad (109)$$

Assuming that $\gamma_1^* \approx \gamma_2^*$ for the same γ_0, this equation simplifies to:

$$\Delta s = H \cot\gamma^* \ln\left[\frac{\frac{\beta_2 \sin\gamma^*}{\rho_{ref} H} \ln\left(\frac{V_f^2}{V_J^2}\right) + \frac{\rho_J}{\rho_{ref}}}{\frac{\beta_1 \sin\gamma^*}{\rho_{ref} H} \ln\left(\frac{V_f^2}{V_J^2}\right) + \frac{\rho_J}{\rho_{ref}}} \right] \quad (110)$$

Further,recognizing that ρ_J is given by:

$$\rho_J = \frac{\beta_1 \sin\gamma_1^*}{H} \ln\left(\frac{V_J^2}{V_0^2}\right) + \rho_0 \quad (111)$$

and neglecting ρ_0 relative to ρ_{ref}, we find:

$$\Delta s = H \cot\gamma^* \ln\left[\frac{(\beta_2/\beta_1)\ln\left(V_f^2/V_J^2\right) + \ln\left(V_J^2/V_0^2\right)}{\ln\left(V_f^2/V_0^2\right)} \right] \quad (112)$$

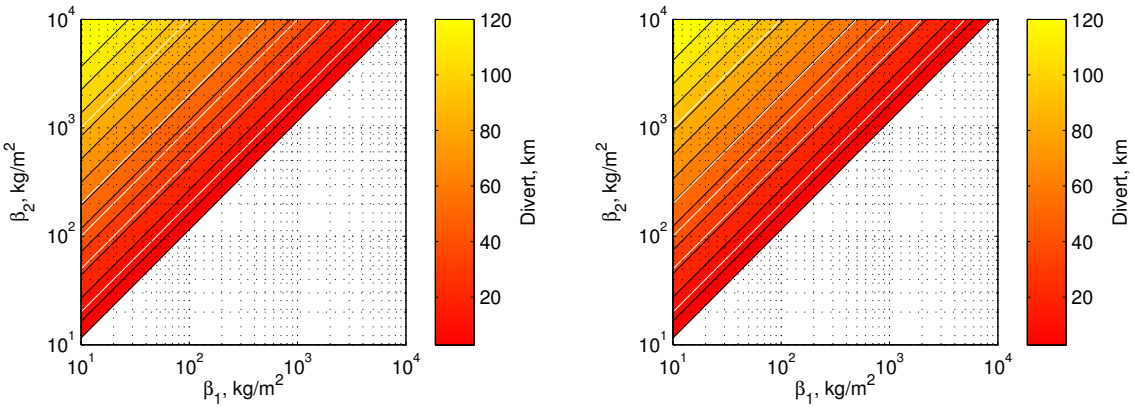

(a) Numerical integration

(b) Allen-Eggers

Figure 50: Divert capability over a range of ballistic coefficients.

This shows the divert capability is a function of the initial and final velocities, the jettison velocity, the ballistic coefficient ratio, and the flight-path angle. The dependence on trajectory parameters is intuitive, but the sole dependence on ballistic coefficient ratio (as opposed to the magnitude of the ballistic coefficients) is not.

The maximum divert capability occurs at the top of the atmosphere. At this state, jettison occurs at a high altitude relative to h_{ref}, the ρ_J/ρ_{ref} term will be small and we can neglect it in Eq. (110). This results in:

$$\Delta s_{max} = H \cot \gamma^* \ln \left(\frac{\beta_2}{\beta_1} \right) \tag{113}$$

This equation shows the relationship between Δs_{max} and β ratio. Increasing the ratio results in a larger maximum divert capability and increased range control authority. The maximum divert range is a weaker function of the magnitude of the ballistic coefficients, which influences the value of γ^*.

Figure 50 shows the maximum divert capability, i.e. Δs at V_0, across a range of values for (β_1, β_2). Numerical integration of the equations of motion is shown in Fig. 50(a); computation using Allen-Eggers is shown in Fig. 50(b). Lines of constant ballistic coefficient ratio are shown in white. The results nearly identical, showing that the Allen-Eggers solution is accurate. Also, it is clear that divert capability

is primarily a function of ballistic coefficient ratio: divert capability increases with increasing β ratio. In this manner, the ballistic coefficient ratio is analogous to the lift-to-drag ratio (L/D) for lift-modulation systems.

4.3 Minimizing Peak Deceleration for Single-Stage Systems

The minimum peak deceleration for single-stage drag-modulation systems occurs when the deceleration at jettison is equal to the peak deceleration in the β_2 trajectory segment. Figure 51 shows the effect of different jettison velocities on the peak deceleration. If the jettison occurs after the β_1 peak deceleration, then the β_2 deceleration pulse is much smaller and does not affect the peak value (black curves). If the jettison occurs early in the trajectory, the opposite occurs: the deceleration pulse for the β_2 trajectory segment is relatively large and dictates the peak deceleration (red curve). From the figure, one can see that some intermediate jettison velocity may yield the minimum peak deceleration for these types of systems (blue curve). Further, the accuracy of the Allen-Eggers solution for the deceleration as a function of velocity indicates it may be used here to determine the jettison velocity associated with the minimum peak deceleration.

Using the Allen-Eggers solution, the deceleration at jettison is:

$$a_{1,J} = \frac{\rho_J}{2\beta g} V_J^2 = \frac{V_J^2}{2\beta_1 g}\left(\frac{\beta_1 \sin\gamma_1^*}{H}\ln\left(\frac{V_J^2}{V_0^2}\right) + \rho_0\right) \tag{114}$$

Where the adjusted constant flight-path angle may be computed via:

$$\sin\gamma_1^* = \sin\gamma_0\,(2F_1^* - 1) \tag{115}$$

where

$$F_1^* = \left[1 + \frac{H}{R\tan^2\gamma_0}\left\{C\frac{V_C^2}{V_0^2} + \left(\frac{V_C^2}{V_0^2} - 1\right)\ln\left(1 - \frac{\beta_1\sin\gamma_0}{H\rho_0}\right)\right\}\right]^{1/2} \tag{115a}$$

The peak deceleration for the β_2 trajectory segment is given by:

$$a_{2,max} = -\frac{\sin\gamma_2^*}{2egH} V_J^2 \exp\left(-\frac{H\rho_J}{\beta_2\sin\gamma_2^*}\right) \tag{116}$$

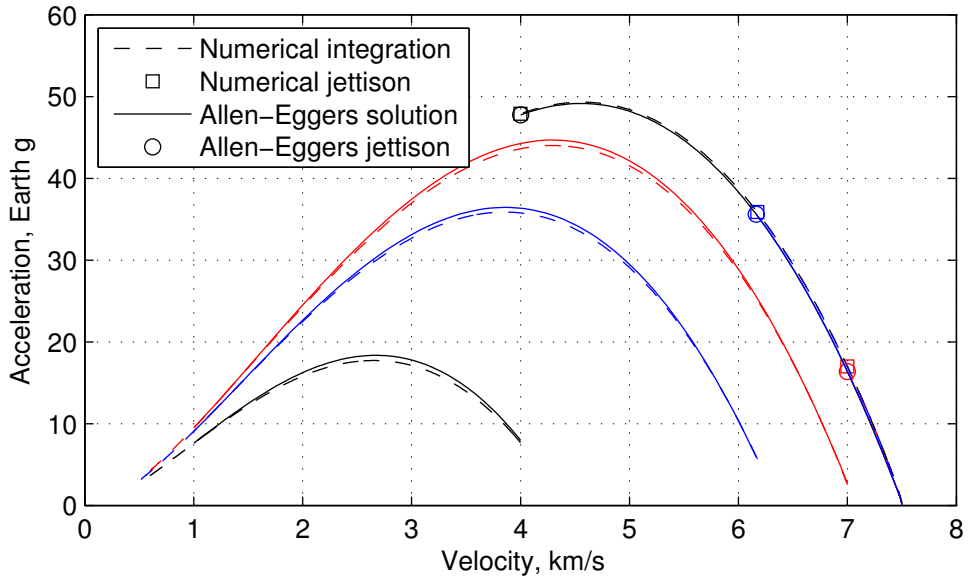

Figure 51: Acceleration profiles for several V_J.

The adjusted constant flight-path angle for this segment may be computed via:

$$\sin\gamma_2^* = \sin\gamma_1^*\left(2F_1^* - 1\right) \tag{117}$$

where

$$F_2^* = \left[1 + \frac{H}{R\tan^2\gamma_1^*}\left\{C\frac{V_C^2}{V_J^2} + \left(\frac{V_C^2}{V_J^2} - 1\right)\ln\left(1 - \frac{\beta_2\sin\gamma_1^*}{H\rho_J}\right)\right\}\right]^{1/2} \tag{117a}$$

Setting Eq. (114) and (116) equal and eliminating common factors, we find:

$$-\frac{\sin\gamma_2^*}{eH}\exp\left(-\frac{H\rho_J}{\beta_2\sin\gamma_2^*}\right) = \frac{\rho_J}{\beta_1} \tag{118}$$

The density at jettison is given by Eq. (111). If we assume ρ_0 is small relative to the other term in Eq. (111) and substitute for ρ_J in Eq. (118), we find:

$$-\frac{\sin\gamma_2^*}{e}\exp\left(-\frac{\beta_1\sin\gamma_1^*\ln\left(V_J^2/V_0^2\right)}{\beta_2\sin\gamma_2^*}\right) = \sin\gamma_1^*\ln\left(\frac{V_J^2}{V_0^2}\right) \tag{119}$$

Taking the natural logarithm of both sides yields:

$$\ln\left(-\frac{\sin\gamma_2^*}{e}\right) - \frac{\beta_1}{\beta_2}\frac{\sin\gamma_1^*}{\sin\gamma_2^*}\ln\left(\frac{V_J^2}{V_0^2}\right) = \ln\left[\sin\gamma_1^*\ln\left(\frac{V_J^2}{V_0^2}\right)\right] \tag{120}$$

Rearranging, one finds:

$$-\frac{\beta_1}{\beta_2}\frac{\sin\gamma_1^*}{\sin\gamma_2^*}\ln\left(\frac{V_J^2}{V_0^2}\right) = \ln\left[\frac{\sin\gamma_1^*}{\sin\gamma_2^*}\ln\left(\frac{V_J^2}{V_0^2}\right)\right] + 1 \tag{121}$$

If we further assume that $\sin\gamma_1^*/\sin\gamma_2^* \approx 1$ and rearrange in terms of the ballistic coefficient ratio, we find:

$$\frac{\beta_2}{\beta_1} = \frac{\ln\left(V_0^2/V_J^2\right)}{\ln\left[\ln\left(V_0^2/V_J^2\right)\right]+1} \tag{122}$$

This relationship gives the jettison velocity for minimum peak deceleration for a particular β ratio. Beyond the Allen-Eggers assumptions, this relationship only assumes that the initial density at the top of the atmosphere is negligible and that the corrected constant flight path angles are of similar magnitudes. While this relationship is unfortunately transcendental in V_J, it does show that the jettison velocity for minimum a_{max} (as a fraction of V_0) is only a function of the ballistic coefficient ratio, not the magnitude of the ballistic coefficients, planetary parameters, or the initial flight-path angle.

To test the validity of this equation, we will compare it to two other solution methods: 1. numerical minimization coupled with numerical integration of the equations of motion and 2. direct solution of Eq. (118) via numerical root-finding. Figure 52 shows the jettison velocity associated with minimum a_{max} over a range of different ballistic-coefficient pairs evaluated using the two different methods. Lines of constant ballistic-coefficient ratio are shown in white. The lower right half of the figure represents β ratios less than one, or $\beta_1 > \beta_2$. This case is not considered, since it violates the assumed deceleration profile. Also, the jettison velocity is not defined for a β ratio of one, since $\beta_1 = \beta_2$. The figure shows that jettison velocity for minimum a_{max} appears to be a function of ballistic coefficient only. The velocity decreases with decreasing β ratio, but is relatively constant for a large range of β ratios (those above about 5). Agreement between the a) numerical solution and b) Allen-Eggers solution appears to be good in both trend and overall magnitude.

Figure 53 shows the minimum a_{max} associated with the jettison velocities in Figure 52. Again, agreement is good between the two methods and a similar trend is seen where a_{max} is only a function of ballistic-coefficient ratio. The peak deceleration

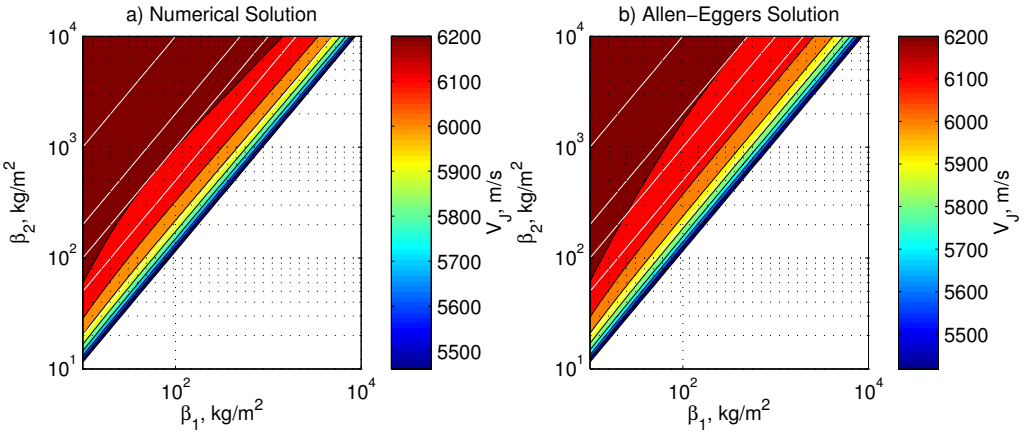

Figure 52: Jettison velocity for minimum a_{max} as a function of (β_1, β_2).

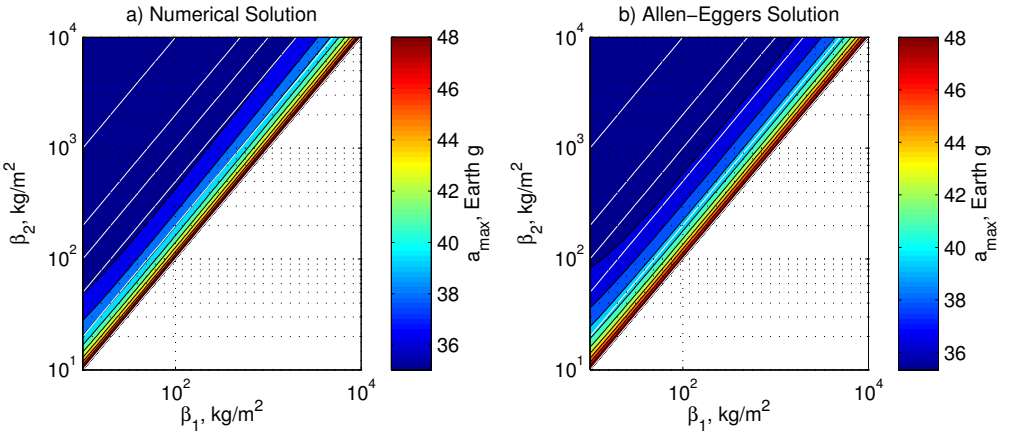

Figure 53: Minimum a_{max} as a function of (β_1, β_2).

increases with decreasing ballistic coefficient ratio, but is relatively flat for ballistic coefficient ratios above about 5. The maximum peak deceleration shown is 48 g, which corresponds to the case where $\beta_1 = \beta_2$. This is the deceleration for this particular trajectory for a vehicle with a constant ballistic coefficient. The lower values of a_{max} shown in the figure show the ability of a drag-modulation system to reduce peak acceleration.

To compare the two methods shown in Figures 52 and 53, as well as the relationship proposed in Eq. (122), the data points for these figures are plotted as a function of ballistic coefficient ratio in Figure 54 and Figure 55. Figure 54 shows that there is excellent agreement between the numerical solution and the Allen-Eggers solution. It

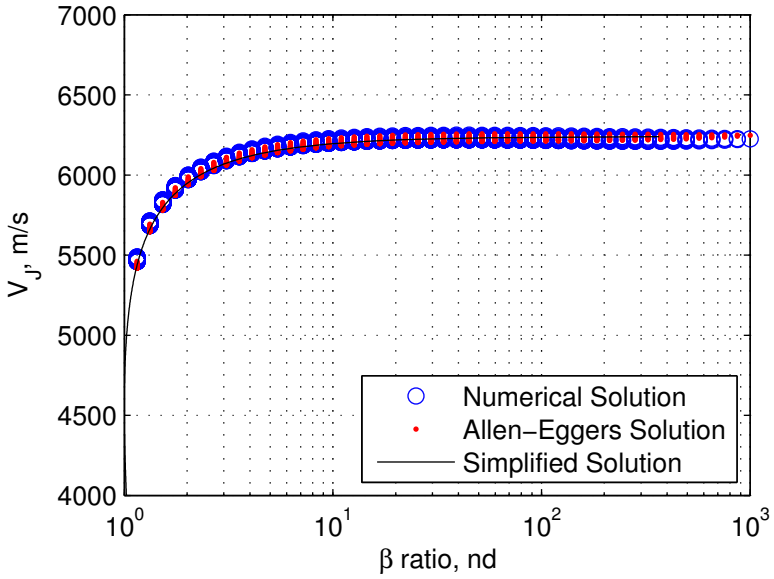

Figure 54: Jettison velocity for minimum a_{max} as a function of ballistic coefficient ratio.

also shows that Eq. (122) effectively predicts the trend in jettison velocity. The agreement in Figure 55 is also good: the Allen-Eggers prediction of the peak deceleration is within 3% of the numerical solution.

The reduction in peak deceleration can be quantified as the drag-modulation a_{max} over the a_{max} associated with a constant-β_1 trajectory. It turns out to be (again, neglecting ρ_0 relative to ρ_J):

$$\frac{a_{DM}}{a_{max}} = e\frac{V_J^2}{V_0^2}\ln\left(\frac{V_0^2}{V_J^2}\right) \tag{123}$$

This expression shows that the reduction in peak deceleration is only a function of V_J as a fraction of V_0, which in turn is only a function of ballistic-coefficient ratio (see Eq. (122)).

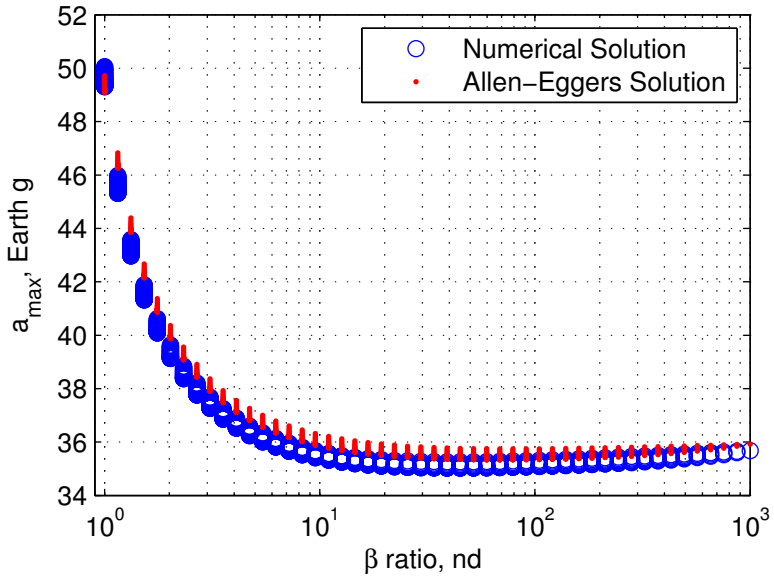

Figure 55: Minimum a_{max} as a function of ballistic coefficient ratio.

4.4 Minimizing Stagnation-Point Heat Rate

Larger ballistic coefficients imply flight at lower altitude (and correspondingly higher density) and smaller effective nose radii, increasing in heat rate. With this in mind, it becomes apparent that the best way to minimize peak heat rate during entry is to maintain a low ballistic coefficient through peak heating. After the initial heat pulse, changing to a higher ballistic coefficient may still cause the heat rate to rise above the previous peak if the jettison velocity is too close to the velocity at the first peak (see Fig. 56). An expression may be derived for a limit on the jettison velocity such that the peak of the initial heat-rate pulse is not exceeded.

To determine the jettison velocities that minimize peak heat rate, we start by enforcing the condition:

$$\dot{Q}_{max,1} > \dot{Q}_{max,2} \tag{124}$$

We can use the Allen-Eggers solution to write expressions for these peak heat rates in terms of known trajectory parameters:

$$k\sqrt{-\frac{\beta_1 \sin\gamma_1^*}{3eHr_{n,1}}}V_0^3 \exp\left(-\frac{3H\rho_0}{2\beta_1 \sin\gamma_1^*}\right) > k\sqrt{-\frac{\beta_2 \sin\gamma_2^*}{3eHr_{n,2}}}V_J^3 \exp\left(-\frac{3H\rho_J}{2\beta_2 \sin\gamma_2^*}\right) \tag{125}$$

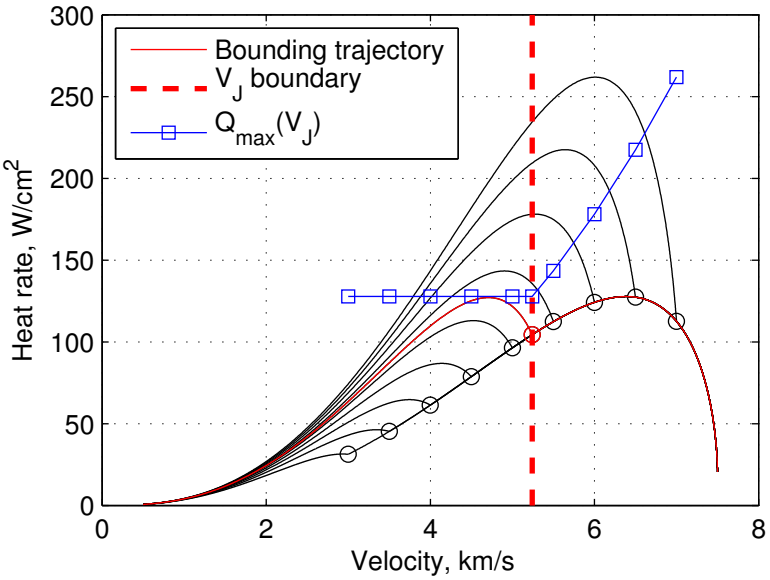

Figure 56: Heat rate as a function of velocity for several V_J.

Substituting Eq. (111) for ρ_J and neglecting ρ_0 because it is small relative to other densities, we find:

$$k\sqrt{-\frac{\beta_1 \sin\gamma_1^*}{3eHr_{n,1}}}V_0^3 > k\sqrt{-\frac{\beta_2 \sin\gamma_2^*}{3eHr_{n,2}}}V_J^3 \exp\left(-\frac{3H}{2\beta_2 \sin\gamma_2^*}\frac{\beta_1 \sin\gamma_1^*}{H}\ln\frac{V_J^2}{V_0^2}\right) \tag{126}$$

Simplifying leads to:

$$\sqrt{\frac{\beta_1}{\beta_2}\frac{\sin\gamma_1^*}{\sin\gamma_2^*}\frac{r_{n,2}}{r_{n,1}}}V_0^3 > V_J^3 \exp\left(-\frac{3}{2}\frac{\beta_1 \sin\gamma_1^*}{\beta_2 \sin\gamma_2^*}\ln\frac{V_J^2}{V_0^2}\right) \tag{127}$$

Taking the natural logarithm to map the multiplication above to addition yields:

$$\frac{1}{2}\ln\left(\frac{\beta_1}{\beta_2}\frac{\sin\gamma_1^*}{\sin\gamma_2^*}\frac{r_{n,2}}{r_{n,1}}\right) + 3\ln V_0 > 3\ln V_J - 3\frac{\beta_1}{\beta_2}\frac{\sin\gamma_1^*}{\sin\gamma_2^*}(\ln V_J - \ln V_0) \tag{128}$$

Grouping like terms and solving for V_J leads to a condition on V_J for minimizing the peak heat rate:

$$V_J < V_0 \exp\left[\frac{\ln\left(\frac{\beta_1}{\beta_2}\frac{\sin\gamma_1^*}{\sin\gamma_2^*}\frac{r_{n,2}}{r_{n,1}}\right)}{6\left(1-\frac{\beta_1}{\beta_2}\frac{\sin\gamma_1^*}{\sin\gamma_2^*}\right)}\right] \tag{129}$$

If one assumes that $\sin\gamma_1^* \approx \sin\gamma_2^*$ and that the effective nose radius does not change across the jettison event, this inequality reduces to:

$$V_J < V_0 \exp\left[\frac{\ln(\beta_1/\beta_2)}{6(1-\beta_1/\beta_2)}\right] \tag{130}$$

Figure 56 shows the effect of varying jettison time on the heat rate (trajectory parameters are given in Table 6), the proposed V_J limit in Eq. (130), and the peak heat rate as a function of V_J for the example trajectory (see Table 6). The proposed limit on the jettison velocity to limit the peak heat rate appears to be correct–at this jettison velocity, the two peaks of the heat pulse are nearly equal. The trajectory data in this figure were generated using numerical integration, but it agrees well with the proposed analytical condition on V_J.

4.5 Summary

In this chapter, the enhanced Allen-Eggers solution for ballistic entry was applied to discrete-event drag-modulation systems. The Allen-Eggers solution was shown to accurately reproduce trajectories relative to numerical solutions to the equations of motion for discrete-event drag-modulation systems. Analytical relationships were developed that show ballistic coefficient ratio is the control authority metric for drag-modulation systems. Ballistic coefficient ratio governs range control authority, peak deceleration reduction capability, and the jettison velocity associated with minimum peak heat rate. Relationships for constraining the jettison velocity for single-stage systems were also developed to limit peak deceleration and peak heat rate. These relationships may be of significant benefit in the development of efficient onboard guidance and targeting systems.

CHAPTER V

APPLICATION OF DRAG-MODULATION TRAJECTORY CONTROL TO AEROASSIST SYSTEMS: NUMERICAL FEASIBILITY

State-of-the-art numerical techniques were used to evaluate the feasibility of a notional drag-modulation trajectory control systems, for precision landing at Mars and for planetary aerocapture at Venus, Mars, and Titan. While work-intensive, numerical techniques allow one to model all aspects of planetary entry, including complex nonlinearities, such as parachute deployment. This level of modeling detail allows one to address nuanced feasibility questions, such as the ability of an onboard real-time system to target a specific landing site target using drag-modulation trajectory control. Numerical evaluation of the equations of motion also allows one to conduct uncertainty analysis via Monte Carlo simulation from which statistics about flight performance can be determined, such as landed accuracy. These types of analysis also facilitate development of prototype guidance and targeting algorithms for use with drag-modulation trajectory control systems. However, such analyses are limited in the sense that they apply only to the single point design examined, and not necessarily to broader classes of planetary entry vehicles and architectures.

5.1 Precision Landing at Mars Using Discrete-Event Drag-Modulation

Over the past several decades, NASA has compiled an impressive record of successful missions to the surface of Mars. However, landing payloads of useful size at scientifically interesting locations on the surface of Mars remains a significant challenge

[14]. For example, the Mars Science Laboratory (MSL) mission required a complex entry, descent, and landing (EDL) system to meet modest landed accuracy and altitude requirements for a payload of approximately one metric ton [6]. The MSL EDL system utilized a lifting aeroshell, RCS, and a bank-to-steer guidance, navigation, and control system to achieve the required terminal accuracy and maintain altitude margin for terminal descent. MSL was the first demonstration of such a system at Mars. Bank-to-steer systems provide good terminal accuracy, but add significant complexity, mass, and cost to an EDL system. All bank-to-steer systems to date have required an RCS with its associated thrusters, propellant, tanks, and plumbing; an off-centerline center of gravity (c.g.) position to produce the required lift; and an onboard guidance, navigation, and control system. In addition to the cost, mass, and complexity of these systems, including design, manufacture, and test, bank-to-steer subsystems may also impact other EDL subsystems. For MSL, these subsystem impacts required the use of two sets of ballast masses and their associated jettison events to control c.g. position during the mission [6] and extensive study of aerothermodynamic jet-interaction effects in the hypersonic flow regime around the vehicle [160].

A simple EDL architecture for precision landing on the surface of Mars is presented in this chapter: discrete-event drag-modulation trajectory control, achieved through a one-time jettison of a rigid, annular forebody heatshield skirt. The jettison event instantly changes the vehicle's ballistic coefficient, β, defined by Eq. (1), and may be thought of as adjusting the ratio of inertial to aerodynamic forces such that the desired range is flown. The one-time jettison event instantaneously reduces the drag area, raises β, and lowers the sensed deceleration. Using measurements from the inertial measurement unit, the onboard guidance algorithm selects the jettison point in real time to achieve the desired range; crossrange errors are not controlled. No lift is required for this architecture, so no c.g. offset is necessary and the vehicle c.g. may

remain on centerline through all mission phases. This architecture does not require any vehicle attitude maneuvers during EDL, eliminating the need for an RCS on the entry vehicle. Lastly, the jettisonable drag area may be rigid and deployed prior to launch; the maximum diameter of the drag skirt is restricted to maintain compatibility with current launch vehicle payload fairing diameters. This EDL architecture utilizes existing designs and technologies to minimize development and flight risk, allowing the architecture to facilitate significant scientific investigation while also serving as a low-risk technology demonstration for drag-modulation trajectory control.

A more detailed discussion of this work is presented in Ref. [159].

5.1.1 System Concept

5.1.1.1 Vehicle Configuration

The proposed EDL architecture is comprised of four major parts: a Mars Exploration Rover (MER) class aeroshell, a rigid annular heatshield extension, a 14-m diameter MER-class supersonic disk-gap-band (DGB) parachute [14], and an airbag landing system. The MER-class aeroshell is a 2.65-m diameter 70-deg sphere cone with a nose radius of 0.66 m [161]. The rigid heatshield extension, or drag skirt, is shaped to maintain the 70-deg sphere cone geometry while increasing the outer diameter from 2.65 m to 4.5 m. This outer diameter allows the vehicle to fit within current 5-m diameter launch fairings in its entry configuration (see Fig. 57), eliminating the need for in-space deployment events prior to atmospheric entry at Mars. The total vehicle entry mass is 950 kg, composed of a 830-kg MER entry vehicle and a 150-kg drag skirt. The mass of the drag skirt was approximated using the areal mass of the MER heatshield. This drag skirt mass estimate is likely conservative, because the skirt is not part of the primary structure or load path and because expected heat rates are significantly lower for this EDL architecture relative to MER. Jettison of the drag skirt, in three segments, is accomplished by three sets of redundant pyrotechnic separation bolts. The MER-sized aeroshell β is significantly higher than the three

expended drag skirt segments, aiding in performance of a reliable separation and decreasing re-contact risk.

Drag skirt jettison and parachute deploy are commanded by the onboard guidance, navigation, and control system. The navigation system is anticipated to be a strap-down inertial system, with a state update provided immediately prior to entry by the Deep Space Network using standard high-accuracy state determination techniques, such as delta-differenced one-way range measurements [162].

The entry sequence for the system concept is shown in Fig. 58. Prior to EI, a final navigation state update is received and the interplanetary cruise stage is jettisoned. The vehicle then enters the atmosphere and begins the low-β deceleration phase. The onboard guidance algorithm determines when to jettison the rigid drag skirt based on onboard inertial measurement unit data. Peak heating and peak deceleration may occur either before or after jettison depending on the target range and day-of-flight dispersions. At jettison, vehicle β immediately rises and the vehicle continues to decelerate in the high-β phase to the proper parachute deploy conditions. The supersonic parachute is then deployed and the vehicle descends to terminal descent initiation and touchdown.

5.1.1.2 Real-time Guidance and Targeting Algorithm

During atmospheric entry, the onboard guidance algorithm uses data from the navigation system to determine, in real time, when to jettison the drag skirt and deploy the parachute based on day-of-flight conditions. Performance assessment of this algorithm will provide information on the feasibility of selecting jettison conditions in a rate-limited, real-time system.

Three different operational modes of the guidance algorithm were evaluated (see Fig. 59). Mode 1 targets the parachute deploy point. Mode 2 models the parachute descent phase, enabling the algorithm to target the touchdown point. For modes 1

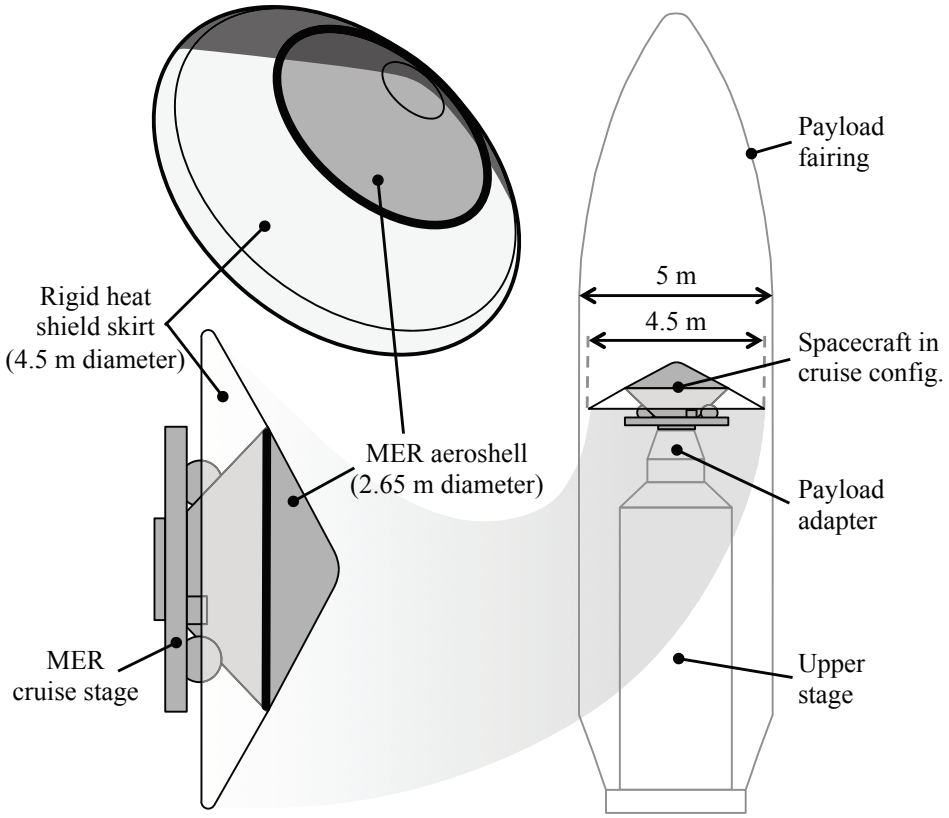

Figure 57: Discrete-event drag-modulation vehicle concept.

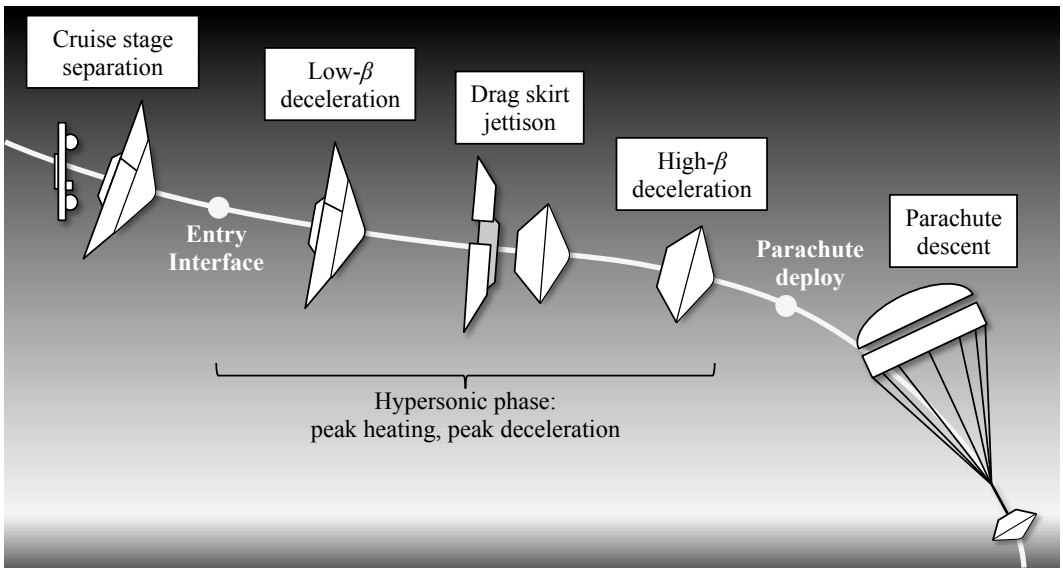

Figure 58: Discrete-event drag-modulation trajectory control concept EDL sequence.

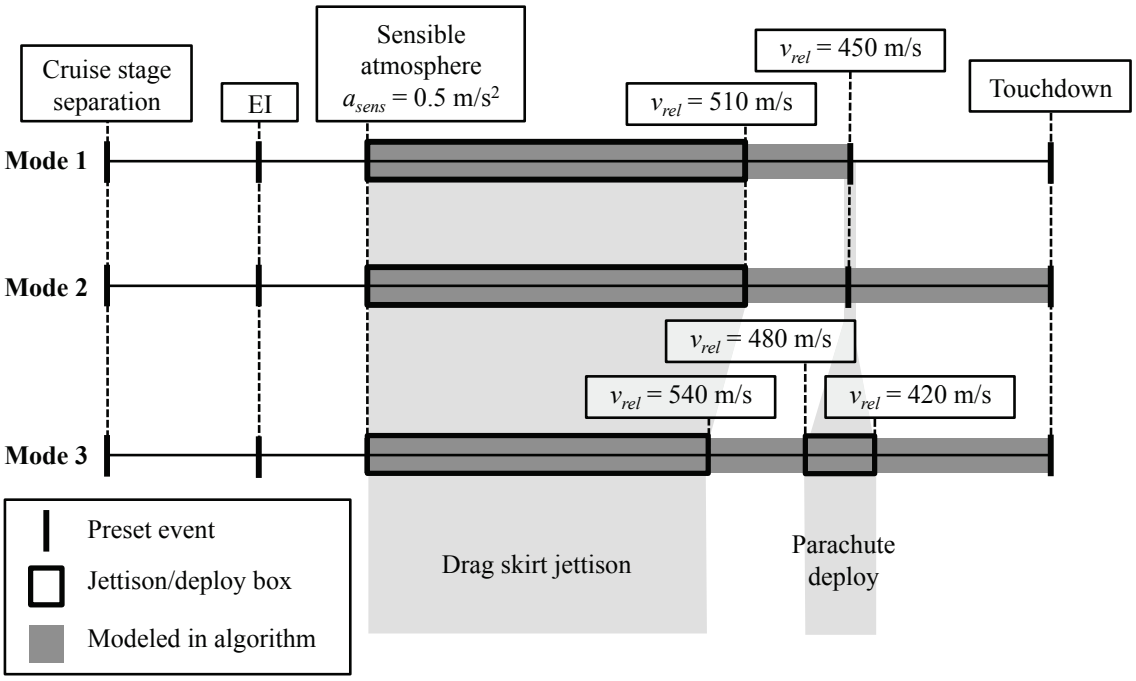

Figure 59: Guidance and targeting modes.

and 2, the parachute is deployed at a preset velocity. Mode 3 uses a range-based parachute deploy trigger to reduce range error at touchdown, effectively creating a two-stage drag-modulation system.

After EI, the guidance algorithm begins targeting computations once the sensible atmosphere has been reached, defined by sensed accelerations greater than 0.5 m/s^2. Targeting is performed with a numerical predictor-corrector (NPC). The NPC determines the drag skirt jettison time that nulls the terminal range error, subject to a minimum velocity jettison limit. This minimum jettison velocity is chosen to provide at least 60 m/s between jettison and parachute deploy. Guidance execution terminates after parachute deploy.

The guidance target is input as a set of geodetic latitude-longitude coordinates. At initialization, these coordinates are transformed into a planet-centered inertial position vector. Current target position is then estimated based on the initial target position, the estimated time of flight computed by the predictor, and the planet rotation rate.

The guidance predictor models Mars as an oblate spheroid with inverse-square gravity including J_2 oblateness effects and a nominal altitude-density atmosphere table. The vehicle is modeled as a point mass that generates only drag. Vehicle and parachute drag are modeled with constant C_D values. The predictor integrates the three-degree-of-freedom equations of motion using a 4th-order Runge-Kutta method. While the bulk of the integration is performed with a constant time step of 1 s, the step sizes immediately adjacent to the jettison event are adjusted such that the jettison occurs at a major integration step. This method enhances the accuracy and stability of the prediction without significantly increasing computational resource requirements, i.e. the predictor may utilize a relatively large step size while allowing accurate modeling of more precise jettison times. Protection is provided for off-nominal cases through an integration time limit (2000 s) and minimum and maximum altitude bounds (-1.5 and 130 km, respectively). For mode 1, prediction is terminated at parachute deploy. For modes 2 and 3, the predictor models the parachute descent phase assuming a preset parachute deploy velocity and prediction is terminated at touchdown. For mode 3, after drag skirt jettison, the predictor continues to run, terminating at touchdown, but the parachute is now deployed at a velocity determined by the corrector.

In all three algorithm modes, the corrector utilizes the terminal states computed by the predictor to determine when the drag skirt should be jettisoned to satisfy the terminal range error tolerance. First, the corrector computes the terminal range error from the estimated target position and the predicted terminal vehicle position. If the computed range error is less than the tolerance, the jettison time and corresponding range error are stored and the NPC terminates. If the range error is greater than the tolerance and no previous (jettison time, range error) prediction pairs exist, the corrector adjusts the jettison time in the direction of decreasing range error and recomputes the range error with the updated jettison time estimate. If the range error

is greater than the tolerance, and a previous prediction pair exists, the corrector uses a linear fit of the two available points to update the jettison time estimate. The linear curve fit computation includes divide-by-zero protection. The predictor is then re-run with the updated jettison time. This process repeats until either the range error tolerance is satisfied (0.1 km) or the NPC iteration limit is reached (5 iterations). For mode 3, a similar corrector algorithm is used after drag skirt jettison to determine the parachute deploy velocity that nulls the range error at touchdown.

The guidance algorithm estimates a constant-bias atmospheric density correction factor at the start of each guidance cycle. This estimation accounts for day-of-flight variability in the Mars atmosphere and is required to achieve accurate terminal state predictions. The correction factor is computed from navigated acceleration and velocity and an onboard table look-up atmosphere model. The current estimate of the density is determined from Eq. (131) as done in the PredGuid algorithm developed by Bairstow and Barton [36]. Since a_{axial} and V_W are not available directly in the absence of a flush air data system, they are approximated with the sensed acceleration magnitude and the planet-relative velocity magnitude, respectively.

$$\rho_{est} = \frac{2ma_{axial}}{V_W^2 S_{ref} C_A} \approx \frac{2ma_{sens}}{V_{rel}^2 S_{ref} C_A} \tag{131}$$

Using a correction factor allows the predictor to update the onboard atmosphere model by multiplying it by a constant parameter. To improve the estimate, the factor is limited to minimum and maximum values and filtered with previous values using a discrete-time low-pass filter. A filter gain of 0.05 provides a balance between reducing noise and capturing short-period changes in the atmosphere relative to the onboard model. The bounded, filtered estimate is then stored for use by the predictor.

Two different parachute deploy triggers were evaluated: a velocity trigger (modes 1 and 2) and a range-based trigger (mode 3). The velocity trigger deploys the parachute at a pre-set planet-relative velocity of 450 m/s. This type of trigger was used on

the Phoenix and MSL missions [163]. The deploy velocity was selected to ensure compliance with the MER DGB parachute deployment box [164]. The range-based trigger utilizes the drag skirt jettison predictor-corrector to determine the parachute deploy velocity which minimizes the range error at touchdown. The range-based trigger deploy velocity is restricted to planet-relative velocity values between 420 and 480 m/s. The lower velocity bound was selected to ensure at least 70 s were available for terminal descent, similar to Mars Pathfinder [165, 166]. The upper velocity bound was selected to limit Mach number and dynamic pressure at deploy to the MER parachute deployment box [164].

The guidance algorithm is run at 0.5 Hz to balance call rate with computational load on the flight computer, and is consistent with previous entry guidance algorithms [11, 36]. Guidance parameters may be adjusted to reduce the computational resource requirements of the algorithm as required, including the call rate, internal iteration limit, the nominal prediction time step, and the size of the onboard atmosphere table. Future design studies should examine trade-offs with respect to these settings between improved performance at higher rates and fidelities and reduced computational load at lower rates and fidelities, but the relatively high-performance system selected is more appropriate for determining feasibility of determining the jettison point in real time.

5.1.2 Numerical Analysis Methods and Assumptions

A three-degree-of-freedom trajectory simulation was used to evaluate flight performance of the proposed EDL system concept. The simulation is written in Matlab and is auto-coded to C and compiled to improve execution speed. A constant time step 4th-order Runge-Kutta technique is used to integrate the equations of motion at 100 Hz.

Table 7: Mars Properties

Property	Value
Equatorial radius	3396.2 km
Polar radius	3376.2 km
Gravitational parameter	4.283×10^{13} m^3/s^2
J_2 perturbation	1.9605×10^{-3}
Mars-GRAM date, time	6 August 2012, 5:17 UTC
Mars-GRAM dusttau	0.3
Ratio of specific heats	1.2941
Sutton-Graves coefficient	1.898×10^{-4} kg$^{0.5}$/m

Table 7 summarizes the relevant parameters used to characterize the Mars environment. The Mars atmosphere is modeled using Mars-GRAM 2010 [167]. Atmospheric data is generated as a function of altitude at the equator for the same day MSL landed using default Mars-GRAM settings. The surface of Mars is modeled as an oblate spheroid. Gravity is modeled as an inverse-square relation with J_2 oblateness effects. Convective stagnation point heat rates are estimated using the Sutton-Graves relation [157]. Radiative heating is assumed to be negligible for the entry velocities and energies considered in this study [168].

The vehicle is modeled as a point mass. The drag skirt jettison event is accompanied by a step change in the vehicle mass and aerodynamic reference area. Tables of aerodynamic coefficients were generated for a 70-deg sphere cone as a function of Mach number and angle-of-attack using CBAero, a modified-Newtonian panel code [169]. The aerodynamic coefficients are assumed to be constant across the jettison event, since the overall shape of the vehicle remains a 70-deg sphere cone, although aerodynamic force magnitudes change drastically due to the reduction in aerodynamic reference area. The vehicle is given a constant 2 RPM bank rate to mitigate the integrated effects from lift generated by potential off-centerline c.g. positions. The MER aeroshell nose radius of 0.66 m is used to compute stagnation point heating rates [161]. The parachute drag coefficient is computed as a function of Mach

number using data from the MSL program [170]. Parachute inflation is not modeled; parachute deployment is considered to be instantaneous. Terminal descent and impact attenuation systems are not modeled.

The jettisoned drag skirt segments are modeled as point masses with C_D equal to 0.85 and C_L equal to 0. These values represents the average hypersonic C_D and C_L for a flat plate over all possible angles of attack using modified Newtonian aerodynamics and provides a first-order approximation of the drag generated by a tumbling drag skirt segment.

The vehicle flight computer is modeled as collection of rate-differentiated processes. Navigation is run at 40 Hz; the navigation model computes vehicle state information used by guidance and flight control. Guidance runs at 0.5 Hz; it determines the time at which drag skirt jettison and parachute deployment should occur. Flight control runs at 20 Hz; it continuously checks drag skirt jettison, and then parachute deploy, criteria and issues the jettison and deploy commands when the criteria are satisfied.

The navigation system is modeled as a Markov process. The model generates navigation errors that would be observed if the navigation system performed according to a given set of navigation accuracy requirements. The Markov-process random variable is given by Eq. (132), where Δt is the time between measurements; τ is the time constant, set to 3600 seconds for this model; and η_i is the noise magnitude at a given time step.

$$x_{i+1} = e^{\left(\frac{-\Delta t}{\tau}\right)} x_i + \eta_i \tag{132}$$

The incremental error at a given time step, $\mathbf{e}_i$, is then given by Eq. (133), where $\mathbf{P}_{SS}$ is the steady-state error covariance matrix, defined by the required navigation system performance and $\mathbf{x}_i$ is a vector of Markov-process random variables.

$$\mathbf{e}_i = \mathbf{P}_{SS}\mathbf{x}_i \tag{133}$$

Defining η_i as shown in Eq. (134) ensures that the knowledge error in the navigation system does not exceed that defined by $\mathbf{P}_{SS}$.

$$\eta_i = 1 - e^{\left(\frac{-2\Delta t}{\tau}\right)} \tag{134}$$

The incremental errors are then applied to the inertial position, velocity, and acceleration truth state vectors generated from the equations of motion to determine the current navigated vehicle state, as shown in Eq. (135). This navigated vehicle state is then used to compute state quantities required for the guidance algorithm.

$$\begin{bmatrix} \mathbf{r} \\ \mathbf{V} \\ \mathbf{a} \end{bmatrix}_{nav,i} = \mathbf{e}_i + \begin{bmatrix} \mathbf{r} \\ \mathbf{V} \\ \mathbf{a} \end{bmatrix}_{truth,i} \tag{135}$$

Monte Carlo simulation techniques were used to evaluate system performance in the presence of day-of-flight dispersions, including state, vehicle, and environmental uncertainties. Table 8 summarizes the uncertainty models and their parameters used for Monte Carlo simulation.

Both delivery and knowledge errors were modeled. Correlated delivery error was modeled using a covariance matrix generated from MSL navigation data [162]. State knowledge error was modeled during entry using a Markov-process navigation error model. Vehicle aerodynamic properties were varied based on vehicle configuration and flight regime. Uncertainties in aeroshell aerodynamics in the supersonic and hypersonic regimes were modeled with correlated normal distributions [171]. Uncertainty in aeroshell aerodynamics in the subsonic regime was not modeled, as the subsonic aerodynamics are dominated by the parachute. Parachute drag coefficient uncertainty was modeled as a function of Mach number and a uniformly-distributed factor [170]. In addition to aerodynamic coefficients, vehicle angle of attack was dispersed about a nominal of zero degrees and the initial bank angle was dispersed with a uniform

distribution over 360 degrees to account for off-centerline c.g. positions. A constant bank rate was used to mitigate the effects of nonzero angles of attack; the constant bank rate was dispersed about its nominal of 2 RPM with a normal distribution. Vehicle mass uncertainty was modeled with a normal distribution. Dispersed atmospheric data were generated using Mars-GRAM 2010 [167]. The required number of dispersed atmosphere tables were generated offline and stored for use in the Monte Carlo simulation.

Downrange and crossrange at the landing site were determined relative to a reference azimuth. The reference azimuth was defined to be the planet-relative azimuth angle of a nominal trajectory at parachute deploy. The reference azimuth and the target landing site position vector define a plane; downrange is then the in-plane distance traveled over the surface of Mars during EDL and crossrange is the out-of-plane distance, both relative to the target position. Range over the surface of Mars is calculated using Vincenty's algorithm for computing geodesics [172]. Accuracy was determined by the total range error, the distance between the vehicle's position and the target landing site.

5.1.3 Corridor Definition and Divert Capability

The feasibility of utilizing a discrete-event drag-modulation trajectory control system for trajectory control during entry at Mars was assessed using simplified models for the Mars environment: an exponential atmosphere and a spherical planet. Entry trajectories shown in this section are eastbound equatorial. The MER-B entry interface state is used: EI inertial velocity of 5.5 km/s and EI inertial flight-path angle of -11.47 deg [14].

The EI flight-path angle corridor for a drag-modulation trajectory control system is defined by two trajectories: the minimum-β trajectory, which carries the drag skirt all the way to the surface, and the maximum-β trajectory, which jettisons the drag

Table 8: Monte Carlo Simulation Uncertainty Models and Parameters

Parameter	Dispersion min/max or 3σ	Notes
Atmosphere	model	Mars-GRAM, default settings for 6 AUG 2012, 5:17 UTC
Hypersonic C_A	3%	Correlated with supersonic C_A [171]
Supersonic C_A	10%	Correlated with hypersonic C_A [171]
Hypersonic C_N	5%	Correlated with supersonic C_N [171]
Supersonic C_N	8%	Correlated with hypersonic C_N [171]
Parachute C_D factor	± 1	MSL DGB parachute [170]
Trim angle of attack	2 deg	Accounts for off-centerline c.g. positions
Initial bank angle	± 180 deg	Covers all possible c.g. offset orientations
Bank angle rate	5%	
Vehicle mass	2 kg	Ref. [171]
EI velocity	0.65 m/s	Correlated delivery error [162]
EI flight-path	0.018 deg	Correlated delivery error [162]
EI azimuth	0.006 deg	Correlated delivery error [162]
EI latitude	0.013 deg	Correlated delivery error [162]
EI longitude	0.017 deg	Correlated delivery error [162]
EI altitude	1.17 km	Correlated delivery error [162]
State knowledge	model	Markov-process with MSL knowledge error estimate

skirt at EI. For a given entry range, the most shallow EI flight-path angle possible is achieved by the minimum-β trajectory, while the steepest possible EI flight-path angle possible is achieved by the maximum-β trajectory. Figure 60 shows example corridor-bounding trajectories at Mars. In Fig. 60, the maximum-β is that of MER and the minimum-β corresponds to the MER entry mass with a 4.5-m diameter forebody heatshield. The maximum-β trajectory utilizes the MER-B EI flight-path angle of -11.47 deg. The minimum-β trajectory decelerates higher in the atmosphere (Fig. 60a) and requires a more shallow EI flight-path angle (-10.41 deg) to achieve the same range as the maximum-β trajectory, approximately 738 km (Fig. 60b). This results in a flight-path angle corridor width of approximately 1 deg; this is well within current approach navigation capabilities at Mars [162].

From a given EI state, the maximum-β trajectory will have the longest possible entry range and the minimum-β trajectory will have the shortest possible entry range. The difference between these ranges is the total divert capability of the vehicle; jettisoning the drag skirt at different points during the trajectory will result in intermediate ranges. Figure 61a shows total entry range as a function of drag skirt jettison time and planet-relative velocity for the MER-B EI state. Early jettisons result in a range of approximately 738 km and late jettisons result in a range of approximately 634 km, resulting in a divert capability of over 100 km. Figure 61b shows that the change in entry range with vehicle velocity at jettison is nearly linear. While not explored in this study, this relationship may provide an avenue for future development of a simple guidance law. The slope of the jettison time versus range curve shown in Fig. 61a, Δ(range)/Δ(jettison time), is plotted in Fig 62. This slope is the range control sensitivity with respect to jettison time. Peak control sensitivity roughly corresponds to peak deceleration for the minimum-β entry and has a value of approximately -1.1 km/s. This peak occurs near the middle of the flight, indicating that jettison must be acceptable both before and after peak deceleration (and

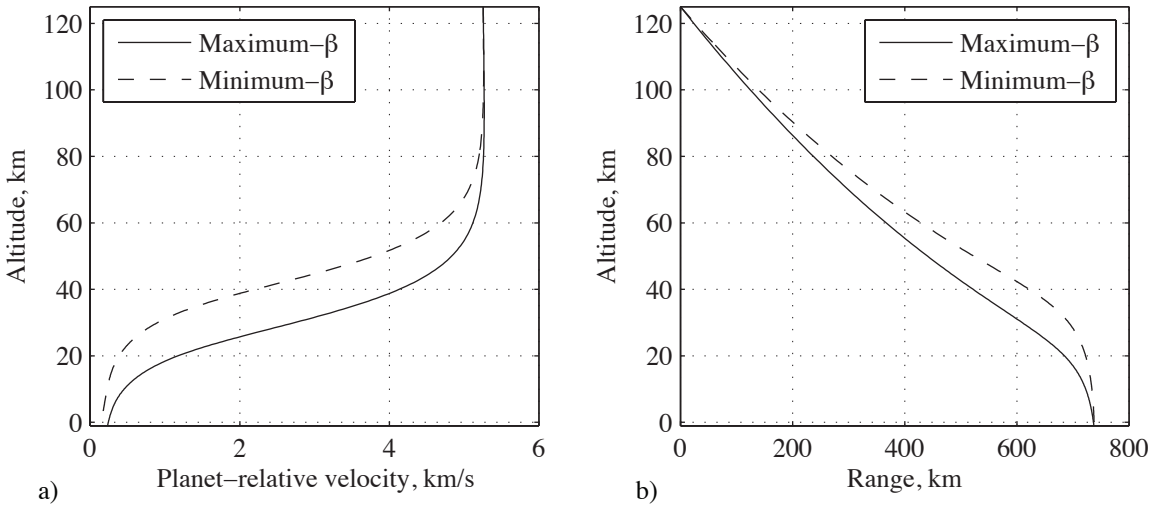

Figure 60: Example corridor-bounding entry trajectories for a drag-modulation trajectory control system at Mars.

peak heating) to capitalize fully on the available range control authority. However, the data also indicate that the vehicle must be able to calculate the jettison time to within less than 1 s to achieve precision landing.

Figure 63 shows bounding minimum- and maximum-β trajectories (maximum-β is that of MER, minimum-β corresponds to the MER entry mass with a 4.5-m diameter forebody heatshield) for the MER-B EI state for three atmospheric density biases: -30% (dashed), nominal (black), and $+30\%$ (grey). These represent first-order estimates of the bounding cases for dispersed entry performance: atmospheric uncertainty typically dominates flight dispersions. Each of these sets of trajectories shows that the vehicle is capable of range diverts over 100 km. More significantly, there exists a nearly 50 km range "window" between the minimum-β, low-density trajectory and the maximum-β, high-density trajectory (the two central dashed and grey trajectories, respectively). This provides an estimate of the remaining range control authority available under off-nominal atmospheric conditions, and indicates that discrete-event drag-modulation trajectory control may be feasible for entry at Mars when drag skirt diameters are limited to 4.5 m.

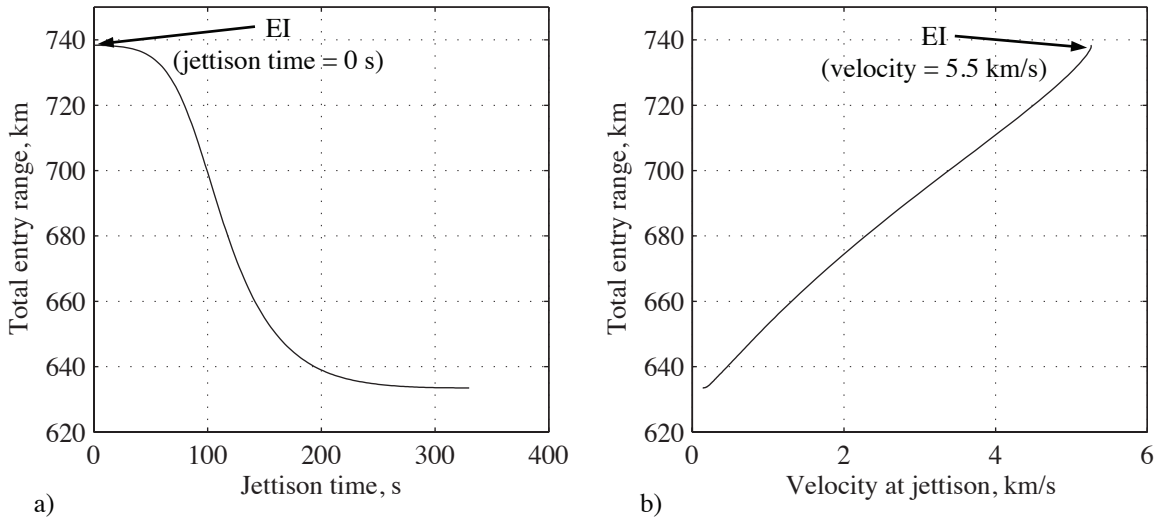

Figure 61: Total entry range as a function of a) drag skirt jettison time and b) planet-relative velocity at jettison.

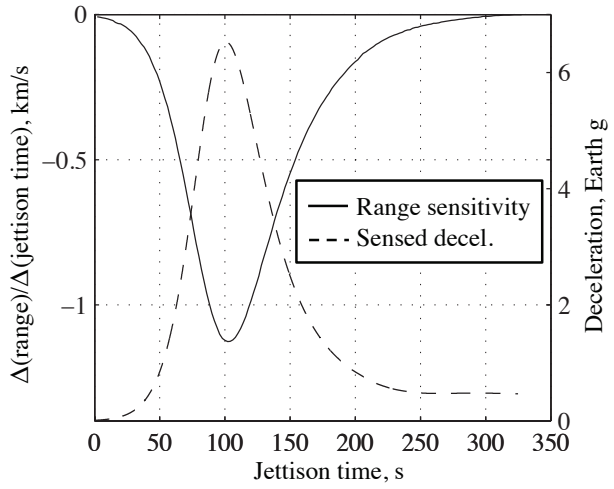

Figure 62: Change in total entry range and nominal g-load as a function of drag skirt jettison time.

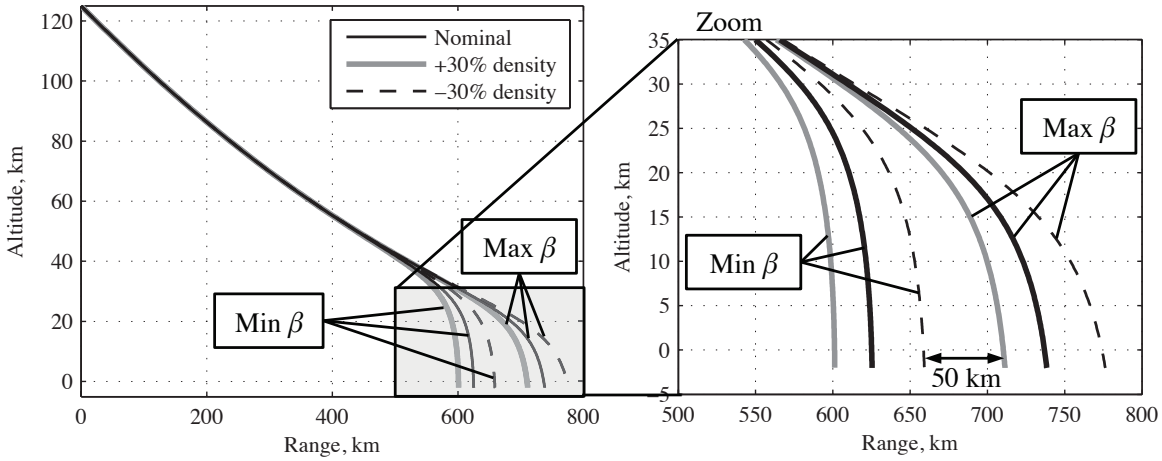

Figure 63: Altitude versus downrange for corridor-bounding trajectories over three different density profiles.

5.1.4 Entry, Descent, and Landing Flight Performance

5.1.4.1 Mission Design

The nominal EI state and target landing site used for the rest of this study are given in Table 9. The landing site corresponds to Gale Crater, MSL's landing site. The nominal EI state was selected to match the inertial velocity of the MER-B entry. The EI flight-path angle was selected to be more shallow than MER-B's value of -11.47 deg to accommodate the lower initial β of the proposed EDL architecture. The EI latitude and longitude were selected to line up the EI point with the target landing site while maintaining an initial azimuth of 45 deg. For this EI-target pair, the flight range is approximately 900 km.

The selection of the initial position is critical and places a constraint on interplanetary navigation performance, since drag-modulation trajectory control systems have no out-of-plane (crossrange) control authority. The EI state error can be tailored to reduce specific initial state errors [173]; this strategy should be used to minimize initial crossrange and azimuth errors for drag-modulation EDL systems to minimize the effect of their lack of out-of-plane control authority on terminal accuracy.

Table 9: Nominal Trajectory Parameters

Item	Parameter	Nominal value
EI state	Altitude	125 km
	Geodetic latitude	-16.258 deg N
	Longitude	127.165 deg E
	Inertial velocity magnitude	5.5 km/s
	Inertial flight-path angle	-11.0 deg
	Inertial azimuth	45 deg
Target	Altitude	-1.5 km
	Latitude	-5.4 deg
	Longitude	137.7 deg

5.1.4.2 Nominal Flight Performance

The nominal guided entry performance of the proposed EDL architecture was assessed through numerical simulation using mode 1 of the algorithm (parachute deploy target). Figure 64 shows the simulated nominal trajectory, including the trajectory of a single piece of the jettisoned drag skirt. The jettison event occurs near 175 s and the parachute is deployed at 450 m/s. After drag-skirt jettison, the vehicle's higher β immediately reduces the sensed deceleration (Fig. 64b) and causes the altitude-velocity curve to steepen (Fig. 64a). The hypersonic peak deceleration is approximately 6 g; while parachute opening loads reach 9 g, parachute inflation is not modeled, so this number may be inaccurate. Range error is approximately 300 m at parachute deploy, increasing to 4.7 km at touchdown. This increase in range error during parachute descent is due to the relatively shallow flight-path angle of -27 deg at parachute deploy: the vehicle still has significant horizontal velocity well into the parachute descent (Fig. 64c).

Post-jettison, the vehicle has a β of approximately 90 kg/m^2 and each skirt segment has a β of 17.0 kg/m^2. This difference in β between the vehicle and jettisoned skirt segments provides a favorable jettison scenario where re-contact is unlikely. Figure 64d shows that re-contact does not appear to be an issue for this trajectory.

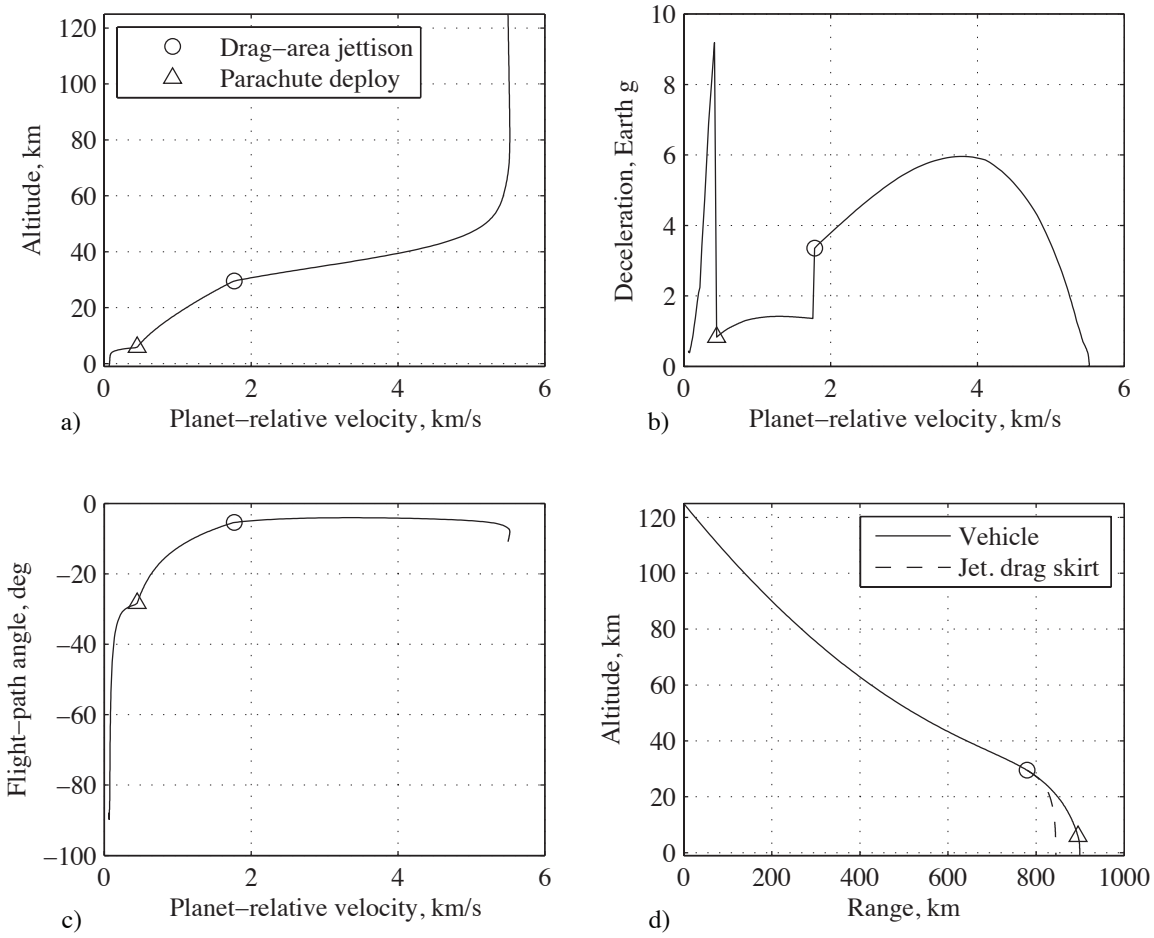

Figure 64: Nominal entry trajectory for guidance mode 1.

5.1.4.3 Dispersed Flight Performance

Monte Carlo simulation was used to assess the performance of the proposed EDL architecture in the presence of day-of-flight uncertainties for all three guidance modes about the nominal trajectory described in Table 9. A sample size of 1000 was used for each Monte Carlo simulation. Results are summarized in Table 10; uncertainty inputs are given in Table 8.

Figure 65 shows the nominal and dispersed entry trajectories for guidance mode 1. Figure 65a shows that, while the range of expected conditions is relatively small prior to drag skirt jettison, the range of drag skirt jettison times lead to a much wider range of conditions post-jettison. Figure 65b highlights the range of conditions over which the drag skirt is jettisoned. However, similar trends emerge across all trajectories. For this EI-target pair, all jettisons occur after hypersonic peak deceleration (and peak heating). This is due to intentional bias of the jettison point towards the end of the trajectory to improve terminal accuracy; the bias is created by choosing a relatively short target range that forces the vehicle to retain the drag skirt for more of the trajectory. This strategy also reduces peak heat rate and integrated heat load, because the vehicle retains its minimum β through peak heating at approximately 4.8 km/s (Fig. 65c). This results in a more benign heating environment than that estimated for the MER entries. Specifically, the mean-plus-3σ heat rate for this system is over 30% lower than the estimated MER value; the mean-plus-3σ integrated heat load is nearly 20% lower [164]. These low heat rates indicate that the heritage SLA561V forebody heatshield material may be used with considerable margin in this EDL architecture. Peak deceleration is similar to that of MER: the reduction in peak deceleration from the more shallow EI flight-path angle used for this trajectory, relative to MER, is largely countered by the increase in peak deceleration associated with the decrease in the initial β of the vehicle [164]. Lastly, the step change in sensed deceleration at drag skirt jettison becomes much smaller as jettison time increases.

Figure 66 shows trajectories for a single drag skirt segment for the mode 1 Monte Carlo simulation data. The range of drag skirt jettison times leads to a relatively large drag skirt impact footprint (Fig. 66a). However, Fig. 66b shows that the minimum separation distance at vehicle touchdown is over 14 km, with an average separation distance near 65 km. Additionally, the separation after 3 s is found to be above 100 m, which compares favorably to the MER requirement for heatshield separation of 21 m in 3 s[174].

Overall, hypersonic flight performance and drag skirt jettison results were similar for all three guidance modes, as shown in Table 10. All three modes exhibit a more benign heating environment relative to the MER EDL system and preserve at least 70 s of parachute descent time. However, significant differences are present in the parachute deploy conditions and in terminal accuracy.

Significantly, terminal accuracy is competitive with the MSL requirement (within 10 km of the target landing site), even for mode 1. While mode 1 does not satisfy the requirement at touchdown, its mean-plus-3σ range error at parachute deploy is only 6.35 km. The mode 1 touchdown range error is larger due to the unaccounted-for bias incurred during parachute descent, which raises the total error to 11.28 km. Modeling the parachute descent, as done in mode 2, effectively removes this bias, reducing the total range error (mean-plus-3σ) to 5.54 km, well within the MSL accuracy requirement. The addition of the range-based parachute trigger in mode 3 further improves landed accuracy, with a mean-plus-3σ range error of only 3.11 km and a maximum below 5 km. Figure 67a shows that modeling the parachute descent phase (mode 2) removes the touchdown range bias, but without changing the overall shape of the distribution of range error relative to mode 1. In contrast, adding the range-based parachute trigger (mode 3) reduces the variability of the range error by shrinking the standard deviation. Figure 67b shows that crossrange error is approximately constant, with a constant bias of about 0.5 km, regardless of guidance mode. This is the

expected behavior, as the vehicle does not possess any out-of-plane control authority. Lastly, Fig. 67c shows the total touchdown range error cumulative density functions for all three modes, and highlights the improvements in performance from modeling the parachute descent and including a range-based parachute trigger. Interestingly, the larger improvement comes from modeling the parachute descent. These results indicate that the proposed discrete-event drag-modulation EDL system is capable of achieving MSL-class landed accuracy without thrusters, propellant, tanks, or the complexity of lift modulation, a significant improvement relative to the MER EDL system.

Figure 68 shows the parachute deploy conditions for all three guidance modes. The margined MER parachute deploy criteria are represented by the dashed line, with a dynamic pressure limit of 810 N/m^2. The dotted line represents the MER parachute design limits, with a dynamic pressure limit of 900 N/m^2 [164]. Lines of constant velocity are shown in grey in 10 m/s increments; the parachute deploy velocity (modes 1 and 2) and box (mode 3) are shown as black lines. For modes 1 and 2 (Fig. 68a), the parachute deploy conditions are similar. The margined MER deploy box is exceeded, but the peak dynamic pressure at deploy remains below 850 N/m^2 for both modes, satisfying the MER design limits. Most trajectories deploy slightly below the trigger velocity of 450 m/s because of latency in the control system. The segmentation into two groups of the deploy conditions is also due to control system latency and is reflective of the control rate of 20 Hz. This latency is the primary cause of error in the deploy velocity; navigation system error is present, but is a small contributor to the error. Figure 68b shows the range of parachute deploy conditions for the range-based trigger. Trajectories are grouped near the deploy box boundaries (also in two groups at each boundary, due to latency). The deploy box velocity boundaries were chosen to satisfy the MER design limit criteria, and while those criteria are satisfied, little margin exists at the top of the deploy box

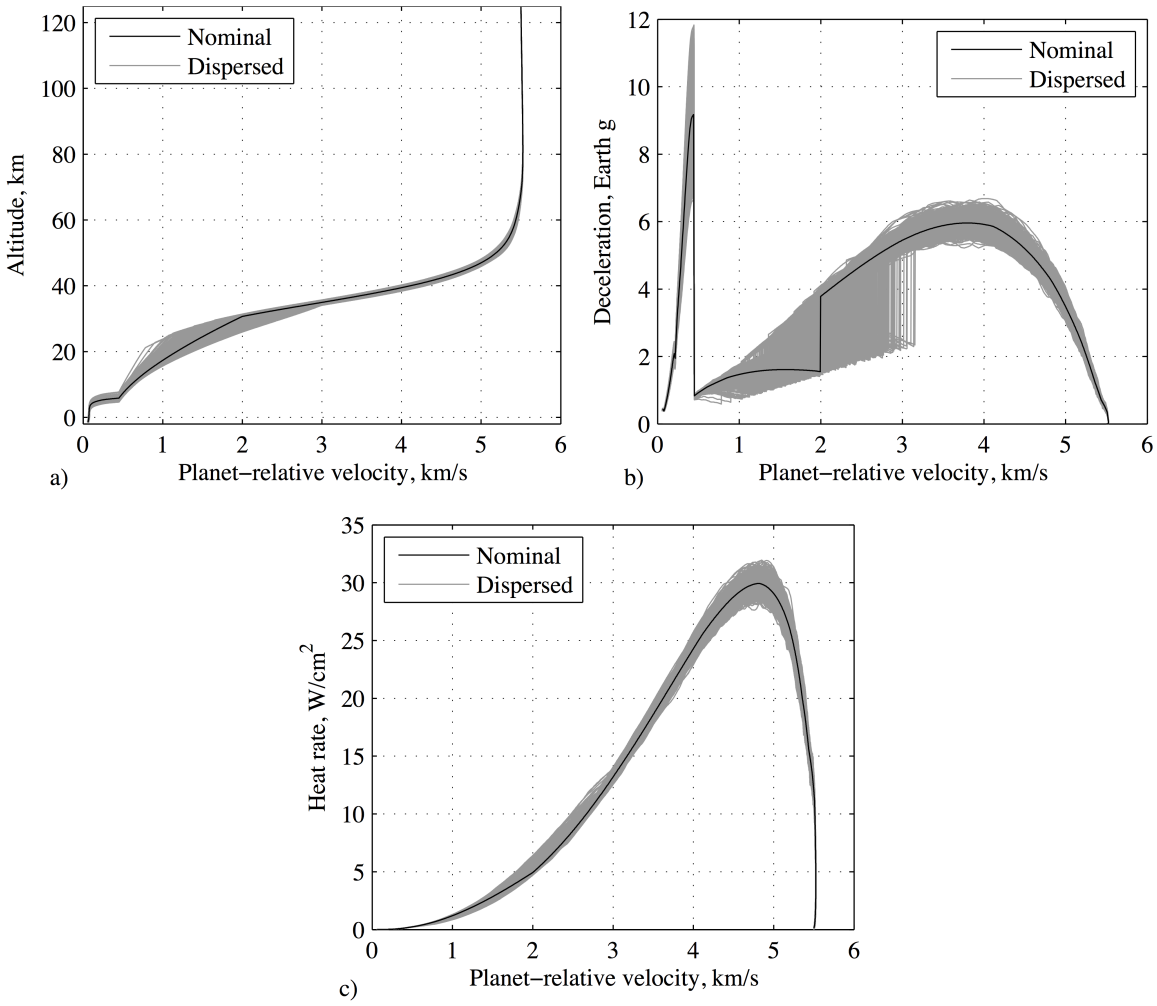

Figure 65: Dispersed entry trajectories for guidance mode 1.

in either Mach or dynamic pressure. However, small excursions from the accepted DGB flight qualification envelope may be acceptable: the MSL program successfully enlarged its DGB parachute and increased the maximum deployment Mach number [163]. Alternately, a reduction in the size of the velocity deploy box will decrease the range of parachute deploy conditions that must be accommodated at the expense of increasing terminal range error.

5.1.5 Summary

Numerical analysis techniques were used to develop and evaluate a point-design discrete-event drag-modulation trajectory control EDL architecture for an assumed

Table 10: Monte Carlo Simulation Results

Parameter	Mean	σ	Mean-3σ	Mean$+3\sigma$	Min.	Max.
Guidance Mode 1: Parachute Deploy Target						
Drag skirt jettison Mach	10.23	2.06	4.04	16.42	3.72	16.45
Parachute deploy altitude, km	5.89	0.41	4.67	7.12	4.63	7.71
Parachute deploy velocity, m/s	447.49	2.27	440.69	454.29	443.97	450.18
Parachute deploy dynamic pressure, N/m^2	760.44	26.16	681.96	838.92	657.33	848.56
Parachute deploy Mach	1.98	0.01	1.95	2.01	1.95	2.01
Parachute deploy range error, km	2.12	1.41	--	6.35	0.07	8.77
Parachute descent time, s	95.24	6.18	76.70	113.78	76.52	115.22
Touchdown range error, km	5.17	2.04	--	11.28	0.82	12.48
Peak deceleration (hypersonic), Earth g	6.06	0.19	5.48	6.64	5.42	6.68
Peak heat rate, W/cm^2	30.16	0.58	28.41	31.91	28.58	31.95
Integrated heat load, J/cm^2	2276	47.7	2133	2419	2180	2466
Guidance Mode 2: Touchdown Target						
Drag skirt jettison Mach	9.24	2.03	3.14	15.34	3.07	15.35
Parachute deploy altitude, km	5.94	0.44	4.61	7.27	4.64	9.02
Parachute deploy velocity, m/s	447.65	2.24	440.94	454.37	443.89	450.25
Parachute deploy dynamic pressure, N/m^2	758.06	28.31	673.14	842.98	574.20	848.37
Parachute deploy Mach	1.98	0.01	1.95	2.01	1.95	2.01
Parachute deploy range error, km	--	--	--	--	--	--
Parachute descent time, s	95.42	6.37	76.30	114.54	76.00	125.88
Touchdown range error, km	1.85	1.23	--	5.54	0.03	7.92
Peak deceleration (hypersonic), Earth g	6.06	0.19	5.48	6.64	5.42	6.68
Peak heat rate, W/cm^2	30.16	0.58	28.41	31.91	28.58	31.95
Integrated heat load, J/cm^2	2251	40.8	2128	2373	2169	2411
Guidance Mode 3: Range-based Parachute Deploy Trigger						
Drag skirt jettison Mach	8.92	2.03	2.83	15.00	2.80	15.00
Parachute deploy altitude, km	5.84	0.65	3.88	7.80	4.20	8.05
Parachute deploy velocity, m/s	445.36	23.80	373.95	516.78	413.73	480.10
Parachute deploy dynamic pressure, N/m^2	755.47	48.29	610.60	900.33	556.50	875.94
Parachute deploy Mach	1.97	0.11	1.64	2.30	1.82	2.14
Parachute deploy range error, km	--	--	--	--	--	--
Parachute descent time, s	93.98	8.91	67.25	120.71	72.65	120.87
Touchdown range error, km	1.10	0.67	--	3.11	0.04	4.96
Peak deceleration (hypersonic), Earth g	6.06	0.19	5.48	6.64	5.42	6.68
Peak heat rate, W/cm^2	30.16	0.58	28.41	31.91	28.58	31.95
Integrated heat load, J/cm^2	2243	38.5	2128	2359	2165	2393

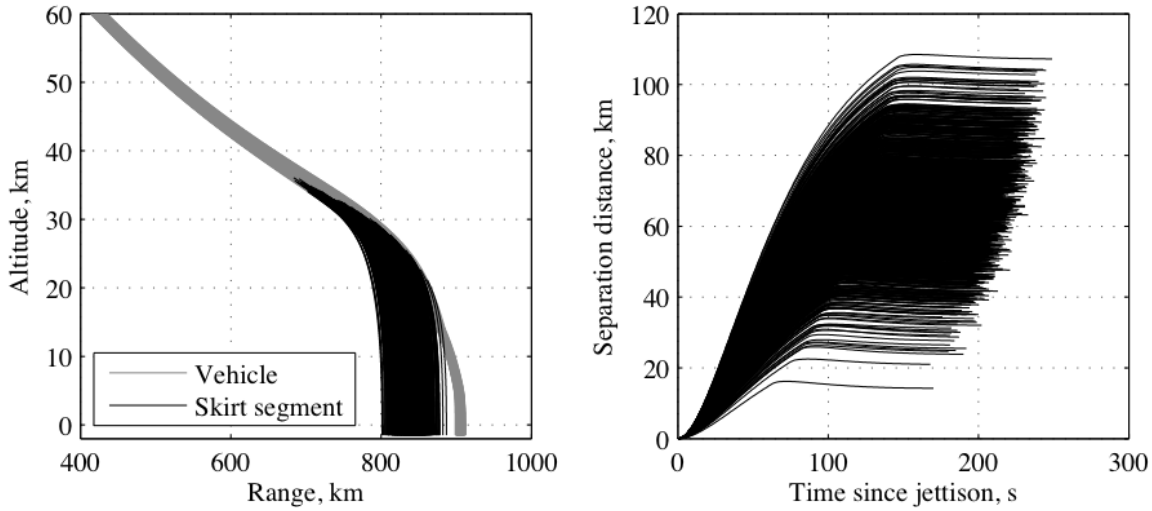

Figure 66: Post-jettison drag skirt segment trajectories for guidance mode 1.

Mars exploration mission. The proposed EDL architecture is a feasible option for delivering an MER-class payload to the surface of Mars with MSL-class accuracy. The proposed EDL architecture offers significant benefits over traditional bank-to-steer lift-modulation systems in terms of cost and complexity. Relative to MSL, the proposed architecture reduces the number of jettison events and eliminates the need for an off-centerline c.g. and RCS (including propellent, tanks, and jets) on the aeroshell. Relative to MER, the proposed architecture has a more benign aerothermal environment and superior landed accuracy. The proposed system architecture is largely enabled by advances in approach navigation at Mars and onboard computing capabilities. Precise approach navigation reliably provides a narrow range of in-plane EI states and reduces the need for out-of-plane trajectory control. Modern flight computers are capable of running advanced NPC algorithms, which can take advantage of real-time parameter estimation to provide precision guidance and targeting for discrete-event trajectory control systems.

This precision-landing architecture is easily extensible to the low-β vehicles utilizing HIADs currently being considered by NASA for future high-mass Mars missions

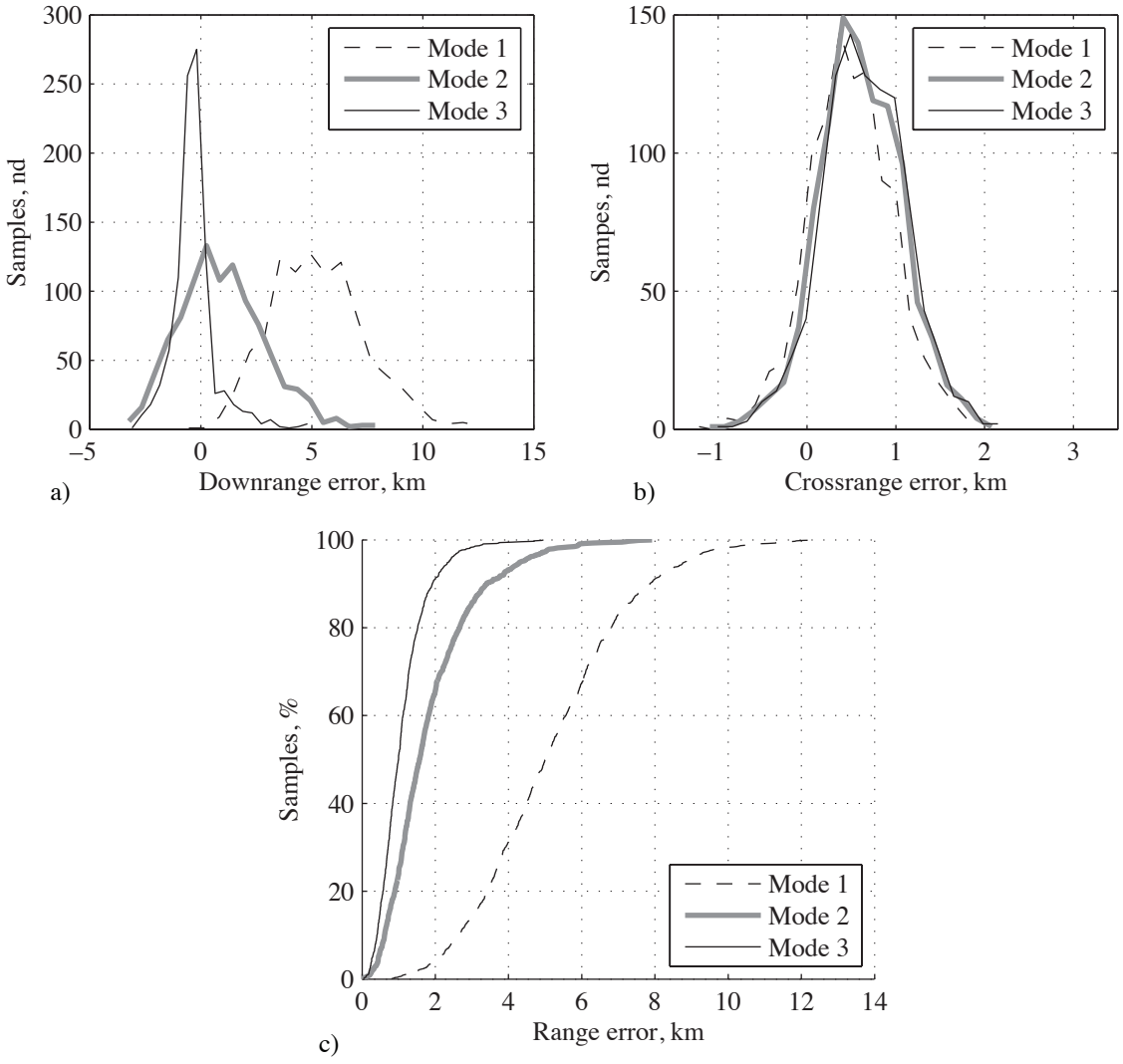

Figure 67: Terminal a) downrange, b) crossrange, and c) total range error for all three guidance modes.

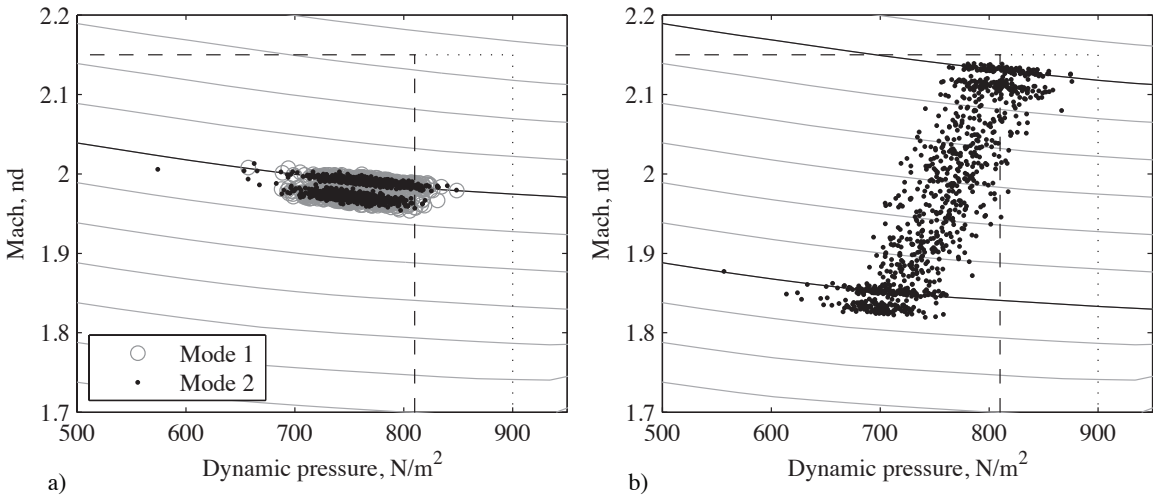

Figure 68: Parachute deploy conditions for a) pre-set velocity trigger and b) range-based trigger.

[22]. To support the development of this capability, the proposed EDL architecture may be used as a low-risk technology demonstrator for more ambitious drag-modulation systems while still landing useful payload on surface of Mars. The use of a jettisonable drag area deployed prior to launch significantly reduces risk and allows a technology demonstration mission to focus on entry flight performance of the system concept. Further, the simplicity of this EDL architecture may lend itself to Discovery-class, low-cost exploration missions that require accurate landing for targeted science investigation but cannot afford or accommodate the complexity of a lift-modulation system and its associated system-level impacts.

The detailed numerical analysis and conceptual design of the proposed discrete-event drag-modulation EDL architecture also revealed new challenges. First, the drag skirt jettison must be accommodated over wide range of Mach numbers while ensuring that drag skirt segment re-contact risk is minimized. While Mach number independence in the hypersonic regime mitigates this risk, verification and validation approaches have yet to be developed. Second, the proposed drag-modulation trajectory control concept has less divert capability available to recover from large, unexpected delivery errors. Given that the presence of such large errors can also

overwhelm a traditional bank-to-steer lift-modulation system, this is likely a small increase in overall mission risk relative to a bank-to-steer system.

5.2 Drag-Modulation System Options for Planetary Aerocapture

Only a small number of studies on using drag modulation for aerocapture missions is available in the literature. Vinh et al. proposed an explicit analytical guidance algorithm for aeroassisted orbit transfer assuming drag could be continuously varied during atmospheric flight.[45] Discrete-event drag modulation has been studied for planetary aerocapture missions at the conceptual level, but few studies address realistic guided system performance.[47, 51, 50] Miller et al. present a real-time predictive algorithm for single-stage jettison aerocapture at Titan using a trailing toroidal ballute but provide only limited information on flight performance.[18] Johnson and Lyons use a heuristic trigger based on curve fits of the aerocapture vehicle dynamics to perform single-stage jettison aerocapture at Titan but results show that this technique results in a significant number of failures when uncertainty is applied.[52]

Recent work has shown that drag modulation may be possible for a specific set of aerocapture missions at Earth and Mars.[175] The goal of this study is to expand upon those results by determining the feasibility and relative performance of different drag modulation flight control system options for planetary aerocapture at Venus, Mars, and Titan. Three drag modulation flight control system options will be considered: single-stage jettison, two-stage jettison, and continuously-variable drag modulation systems. This study improves upon existing results in the literature by utilizing flight-realistic real-time guidance and targeting algorithms coupled with uncertainty analysis to provide a realistic assessment of feasibility and flight performance.

A more detailed discussion of this work is presented in Ref. [176].

5.2.1 Drag Modulation Flight Control Concepts

5.2.1.1 Single-stage Jettison Systems

Single-stage jettison systems, shown in Fig. 69, provide the simplest means of drag modulation flight control for aerocapture. The vehicle deploys a large drag skirt prior to atmospheric interface (AI) to lower the vehicle's β to its minimum value, β_1. Alternately, the vehicle may launch in its β_1 configuration if the maximum diameter fits within the launch vehicle payload fairing. During the atmospheric pass, the flight computer uses available navigation data to determine when the drag skirt should be jettisoned such that the proper amount of energy is dissipated prior to atmospheric exit to achieve the desired transfer orbit properties. Once the drag skirt is jettisoned, β immediately rises to its maximum value, β_2, and the spacecraft coasts to atmospheric exit.

While simple, single-stage jettison systems are vulnerable to day-of-flight dispersions since they have only a single control event. After the jettison, no control authority is available to correct for unforeseen dispersions. Mission designers may bias the nominal jettison point towards the end of the atmospheric pass to reduce the effect of post-jettison uncertainty, but this strategy requires additional control authority and increases the likelihood of a skip-out trajectory.

5.2.1.2 Two-stage Jettison Systems

In some circumstances, two-stage jettison systems provide performance benefits over a single-stage systems by reducing vulnerability to day-of-flight dispersions. A two-stage system splits the drag skirt into two concentric pieces, allowing the spacecraft to perform a "clean-up" jettison later in the trajectory. This drag modulation strategy trades additional system complexity for reduced susceptibility to unforeseen late-trajectory dispersions.

Figure 70 shows a notional aerocapture maneuver using a two-stage jettison drag

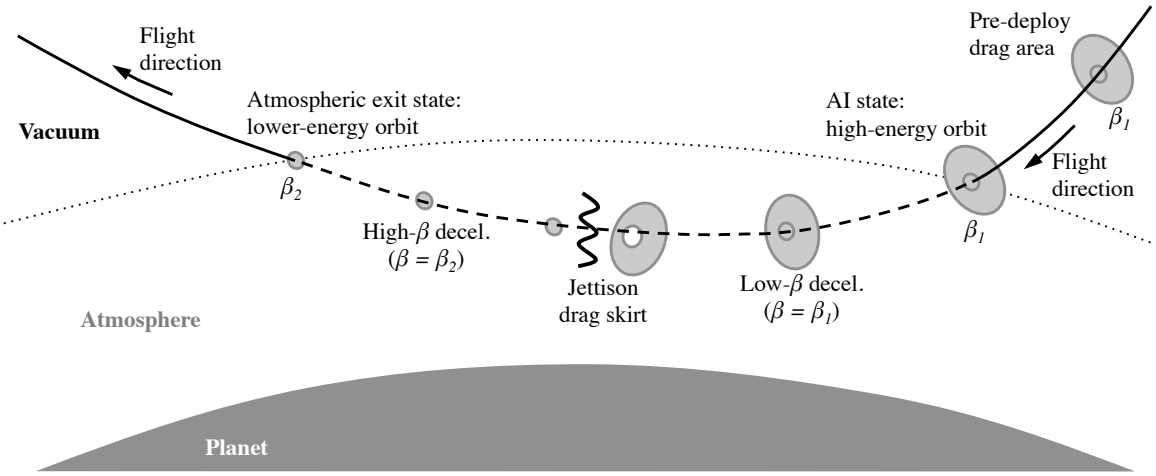

Figure 69: Single-stage jettison drag modulation aerocapture system.

modulation system. As in the single-stage system, the drag skirts are deployed prior to AI and the vehicle enters the atmosphere with $\beta = \beta_1$. The outer drag skirt is jettisoned first, such that the final apoapsis error is minimized while assuming a pre-set inner skirt jettison time. The outer skirt jettison changes β to an intermediate value, $\beta_{1.5}$. The inner drag skirt jettison time is then adjusted to null the final transfer orbit apoapsis altitude error. When the inner drag skirt is jettisoned, β rises to β_2 and the spacecraft coasts to atmospheric exit. This strategy allows the flight computer to solve two one-dimensional searches in series, reducing flight software complexity and limiting computational resource requirements. The pre-set inner skirt jettison time is selected to be later than the expected range of outer skirt jettison times to force the guidance algorithm to hold some control authority in reserve until later in the trajectory.

5.2.1.3 Continuously-variable Systems

As the number of jettison stages becomes large, a staged-jettison vehicle may be approximated by a one-directional continuously-variable drag modulation system. However, it is likely that such a system would be capable of both decreasing and increasing β. This continuously-variable (CV) drag modulation system uses a drag

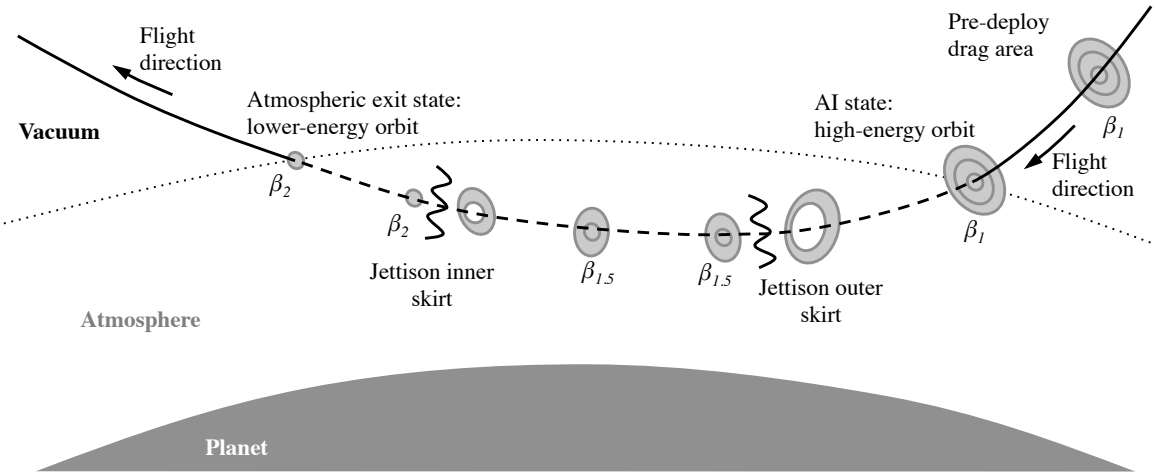

Figure 70: Two-stage jettison drag modulation aerocapture system.

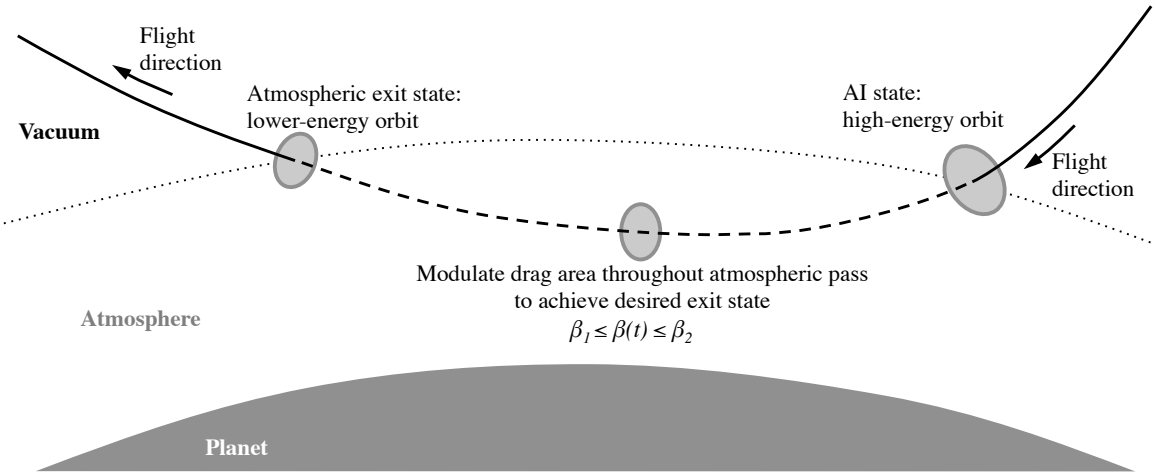

Figure 71: Continuously-variable drag modulation aerocapture system.

skirt that can be deployed and retracted during the atmospheric pass. While this in-flight reconfiguration capability requires significant technology development, current technology programs indicate that such a system may be feasible.[17]

The CV drag modulation system concept analyzed in this study is shown in Fig. 71. The vehicle enters the atmosphere with its drag skirt deployed. During the atmospheric pass, the vehicle determines the constant drag area that minimizes the final apoapsis altitude error, subject to limits β_1 and β_2. This type of system retains a measure of control authority throughout the atmospheric pass, but requires a more mechanically complex system relative to staged-jettison systems.

5.2.2 Real-time Guidance

During the atmospheric pass, a real-time guidance algorithm is used to determine drag skirt jettison times and drag area commands using data from the navigation system. This strategy allows the vehicle to select a drag profile based on day-of-flight conditions such that the desired transfer orbit is achieved. A similar algorithm is used for all three drag modulation system options.

The guidance algorithm is organized into three functional phases. The first phase is the pre-AI attitude hold phase. During this phase, the guidance algorithm checks whether the sensible atmosphere has been reached. The sensible atmosphere is defined by sensed accelerations greater than 0.5 m/s^2. The second phase is the numerical predictor-corrector (NPC) targeting phase. During this phase, the algorithm adjusts the jettison time or drag area command to minimize the final apoapsis altitude error. The third and final phase is the exit phase: no additional commands are issued when the sensed acceleration drops below 0.5 m/s^2.

The predictor integrates the three-degree-of-freedom equations of motion to determine the vehicle state at atmospheric exit. While the motion of drag modulation vehicles is nearly planar, the full three-degree-of-freedom equations allow the predictor to account for a rotating planetary atmosphere and provide a flexible platform for increasing environment model fidelity.

The predictor models the planetary body of interest as a sphere with inverse-square gravity and a nominal altitude-density atmosphere table. The vehicle is modeled as a point mass that generates only drag; vehicle drag is modeled with a constant C_D. While the majority of the integration is performed with a constant time step of 2 s, the time steps immediately adjacent to jettison events are adjusted such that the jettisons occur at a major time step. This strategy enhances the accuracy and stability of the prediction without significantly increasing the computation time. Nominally, prediction terminates at atmospheric exit, defined by a maximum altitude. Protection is

provided within the predictor against off-nominal cases through limits on integration time and minimum altitude.

The corrector utilizes the terminal states computed by the predictor to perform a one-dimensional search for the jettison time or drag area command, for staged-jettison or CV systems, respectively, that results in acceptable apoapsis altitude error. First, the corrector computes the properties of the transfer orbit from the estimated terminal vehicle position and velocity vectors at atmospheric exit. Next, if the jettison time or drag area command solution is bounded, the corrector uses a bisection algorithm to null the transfer orbit apoapsis error. Bisection reduces the error until either the specified error tolerance is reached or the maximum number of iterations is exceeded. The bisection algorithm was selected over algorithms with faster convergence properties because of its simplicity and the nonlinearity of the apoapse altitude as a function of jettison time or drag area command near the solution.

If the solution is not bounded, the corrector marches the jettison time or drag area commands by constant amounts to determine bounding values. This typically occurs during the first guidance pass. For example, if the predicted transfer orbit semi-major axis is negative, indicating a hyperbolic escape trajectory, the corrector increases the jettison time or increases the drag area command by a fixed amount to reduce the energy of the transfer orbit. The predictor is then re-run and new terminal orbit properties are computed. The jettison time or drag area commands are marched in this direction until the corrector finds a captured transfer orbit (positive semi-major axis). The jettison time or drag area command associated with this transfer orbit bounds the solution on the high-energy side. The low-energy boundary is found in a similar manner, and is defined to be any trajectory with an apoapsis altitude below the target altitude, including trajectories that impact the planet's surface.

The guidance algorithm estimates a constant bias atmospheric density correction factor to account for day-of-flight uncertainty in the atmosphere and improve the

accuracy of terminal state predictions.

5.2.3 Methodology

The same three-degree-of-freedom simulation was used to generate aerocapture trajectories. Planetary atmosphere data for Mars, Venus, and Titan were generated using the Global Reference Atmosphere Models (GRAM) for each planetary body. [177] Stagnation-point convective heat rates are estimated using the Sutton-Graves relation for a 1 m reference nose radius [157]. Radiative contributions to total heat rate are significant at Venus and Titan, but are not modeled. A summary of planetary model parameters is given in Table 11. Two-body orbital mechanics are used to compute the ΔV required for periapsis raise and apoapsis correction maneuvers. All numerical simulations begin at AI altitude, defined to be 150 km altitude for Mars and Venus and 1000 km altitude for Titan.

Table 11: Planetary Model Parameters

Parameter	Mars	Titan	Venus
Gravitational parameter, m^3/s^2	4.283×10^{13}	8.9797×10^{12}	3.249×10^{14}
Volumetric mean radius , m	3.3895×10^{6}	2.575×10^{6}	6.0518×10^{6}
Atmosphere model	Mars-GRAM	Titan-GRAM	Venus-GRAM
Sutton-Graves coefficient, $kg^{0.5}/m$	1.898×10^{-4}	1.7407×10^{-4}	1.986×10^{-4}

Aerocapture vehicles were assumed to have constant mass. A 70-deg spherecone shape was assumed for Mars and Titan missions and a 60-deg spherecone shape was assumed for Venus missions. Mach-dependent aerodynamics data were generated for these shapes using CBAero.[169] For all three drag modulation system options, drag modulation is accomplished through changes in S_{ref}; aerodynamic coefficients were assumed to be constant across all S_{ref} changes. The nominal vehicle center of gravity (c.g.) position is along the vehicle axis of symmetry. The vehicles are spun about their axis of symmetry at 2 RPM to reduce the effect of lift generated by off-nominal c.g. positions.

Table 12: Monte Carlo Simulation Input for Mars Trajectories

Parameter	Dispersion min/max or 3σ	Notes
Atmospheric density and wind	Mars-GRAM	Default settings for 5 August 2012
Hypersonic C_A	3%	70 deg sphere-cone[171]
Hypersonic C_N	5%	70 deg sphere-cone[171]
Trim angle of attack	2 deg	Accounts for off-centerline c.g.
Initial bank angle	$\pm$180 deg	Covers all possible c.g. offset orientations
Bank angle rate	5%	
Vehicle mass	3 kg	
AI velocity	0.49 m/s	Correlated MSL error[162]
AI flight-path	0.013 deg	Correlated MSL error[162]
AI azimuth	0.0075 deg	Correlated MSL error[162]
AI latitude	0.017 deg	Correlated MSL error[162]
AI longitude	0.012 deg	Correlated MSL error[162]
AI altitude	0.74 km	Correlated MSL error[162]

The flight computer was modeled with two rate groups: a low-rate group for guidance (the predictor-corrector targeting algorithm) running at 0.25 for Titan and 0.5 Hz for Venus and Mars and a high-rate group for jettison and drag area adjustment logic, running at 25 for Titan and 50 Hz for Venus and Mars. The truth dynamics are integrated at 50 Hz at Titan and 100 Hz at Venus and Mars. These rates reflect differences in flight times at Venus, Mars, and Titan. The difference between the high- and low-rate groups reduces the computational load of guidance while allowing precision drag area jettisons with respect to time or quick adjustments to the drag area. The onboard inertial navigation system was assumed to have perfect knowledge of the vehicle dynamics.

Monte Carlo simulation was used to evaluate aerocapture system performance at Mars in the the presence of day-of-flight uncertainties, including state, vehicle, and environmental uncertainties. Monte Carlo simulation uncertainty inputs are given in Table 12. Correlated state errors are generated based on 3σ 1.5 km position and 1 m/s velocity errors, corresponding to Mars Science Laboratory (MSL) approach navigation performance.[162] Correlated atmospheric density and wind uncertainties were generated using Mars-GRAM.

5.2.4 Corridor and Feasibility

For aerocapture drag modulation flight control systems, the aerodynamic corridor is bounded by the minimum-β (β_1) and maximum-β (β_2) trajectories. These bounding trajectories represent the most shallow and most steep trajectories, respectively, that may be flown while reaching a given transfer orbit, regardless of the type of drag modulation system employed. For single-stage systems, these trajectories represent either retaining the drag skirt to atmospheric exit (maximum drag area throughout the atmospheric pass) or jettisoning it at AI (minimum drag area throughout the atmospheric pass). For CV systems, these trajectories represent flight at a constant β of β_1 or β_2 throughout the atmospheric pass. The set of AI flight-path angles bounded by the AI flight-path angles of these trajectories is the aerodynamic flight-path angle corridor. For a given AI velocity, with perfect state knowledge, a drag modulation aerocapture vehicle that can vary β between β_1 and β_2 should be able to reach the desired transfer orbit as long as the AI flight-path angle lies within the corridor.

Figure 72 shows example bounding trajectories for aerocapture at Mars at an inertial AI velocity of 6 km/s with a 400 km apoapsis altitude transfer orbit target for a vehicle with $\beta_1 = 10$ kg/m^2 and $\beta_2 = 100$ kg/m^2. AI is denoted by squares and atmospheric exit by triangles. Figure 72(a) shows that the β_2 trajectory decelerates about 20 km lower in the atmosphere. The β_2 trajectory must enter the atmosphere at a steeper flight-path angle, and exists with a slightly less shallow flight-path angle, as shown in Fig. 72(b). Figure 72(c) shows the deceleration pulses are similar for both cases. The ΔV required for the periapsis raise maneuver is similar for both cases: 97.9 and 97.7 m/s for the β_1 and β_2 trajectories, respectively.

Corridor trends were evaluated at Mars with respect to vehicle and mission design quantities; similar trends emerge for aerocapture at Titan and Venus. Figure 73 shows how the aerodynamic corridor changes with respect to AI velocity for several values of

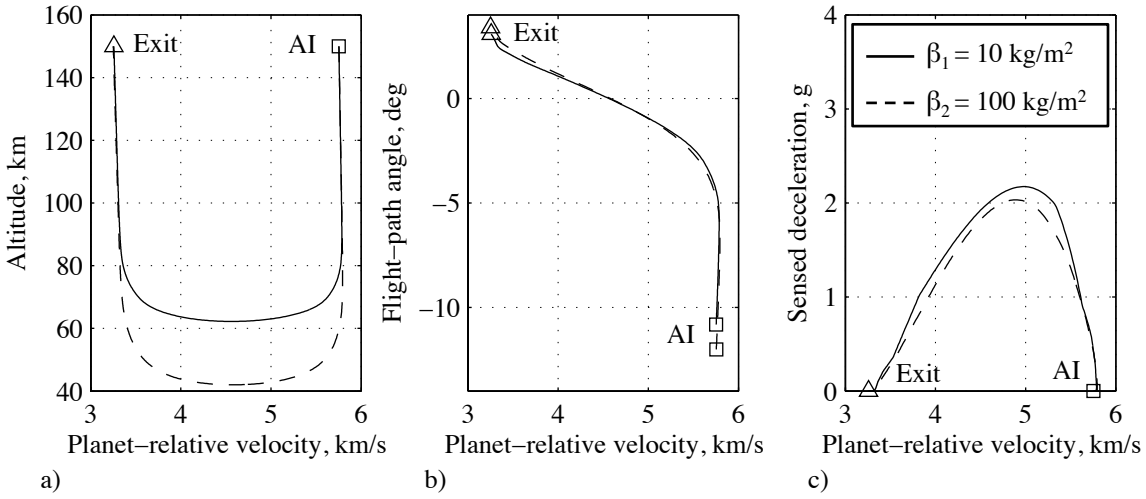

Figure 72: Example bounding trajectories for aerocapture aerodynamic corridor at Mars: a) altitude, b) flight-path angle, and c) sensed deceleration versus planet-relative velocity.

β. The corridor width for a given drag modulation system corresponds to the distance between the two curves corresponding to the β_1 and β_2 for that vehicle. Similar to atmospheric entry, the corridor steepens and widens as AI velocity increases, but at high velocities, trajectory constraints on deceleration or heat rate may reduce the width of the corridor. Figure 74 shows the aerodynamic flight-path angle corridor width as a function of β-ratio for four AI velocities, where β-ratio is the ratio of β_2 to β_1. β-ratio is a measure of the gross control authority of a drag modulation system.[175] A β-ratio of 1 results in a zero-width corridor, since $\beta_1 = \beta_2$. Increasing the β-ratio or AI velocity increases the width of the corridor with diminishing returns.

Figure 75 shows the variation in aerodynamic corridor width with respect to β_1, for an AI velocity of 6 km/s . For all but the smallest values of β_1, corridor width is constant with respect to β_1 and determined by β-ratio. This implies that only the relative change in β of a given vehicle is important for determining corridor width, not the values of β_1 or β_2.

Aerodynamic flight-path angle corridor width was evaluated as a function of AI velocity for aerocapture at Mars, Titan, and Venus. The AI velocity range for Mars

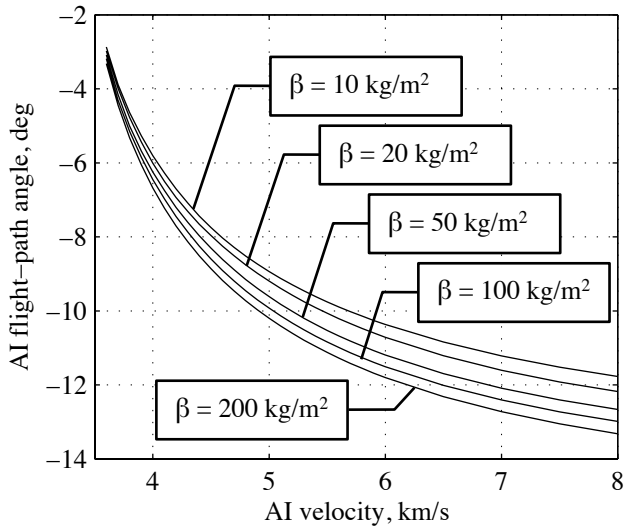

Figure 73: Aerocapture corridor bounding AI flight-path angles versus AI velocity for several β at Mars.

was selected to capture a range of launch opportunities from Earth, consistent with the efficient trajectories used for robotic missions.[178] The Titan AI velocity range spans Titan escape velocity to 10 km/s, the upper bound on approach velocities assumed by Lockwood.[179] Venus AI velocities were selected to correspond to existing literature.[180] The transfer orbit apoapsis altitude target of 400 km is used at Venus and Mars and an apoapsis altitude target of 1700 km is used at Titan. The results presented in Fig. 76 show that, for a given β-ratio, corridor width at Mars is approximately double that at Venus, and corridor width at Titan is nearly two and a half times that at Mars. With identical approach navigation precision, aerocapture at Venus would require twice as much control authority as aerocapture at Mars. However, approach navigation at Venus is likely less precise, requiring even more control authority relative to Mars. This translates to a larger required initial drag area for a given spacecraft mass. At Titan, less control authority is required for a given approach navigation precision. However, approach navigation at Titan is significantly less precise than at Mars, reducing the impact of this advantage. As discussed in the previous section, Fig. 76 shows that β-ratio is the primary factor determining corridor

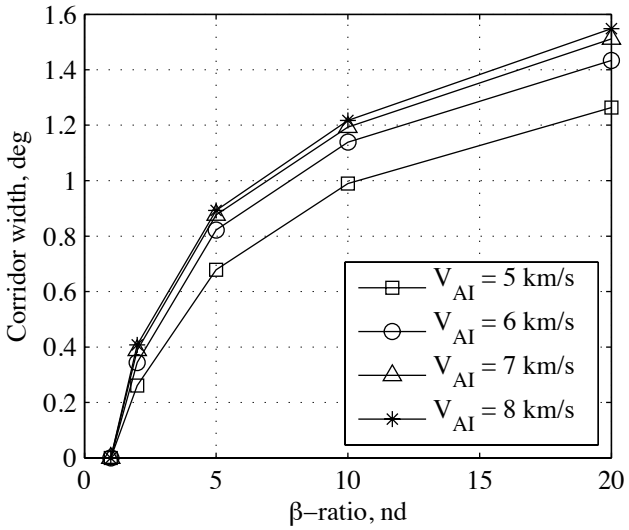

Figure 74: Aerodynamic corridor width as a function of β for several AI velocities at Mars.

width, corridor width increases a modest amount with increasing AI velocity, and β_1 has only a small effect on the corridor width.

Figure 77 shows peak stagnation-point convective heating rates for aerocapture trajectories for β values of 1, 10, and 100 kg/m^2; radiative heating effects are not included. For a spacecraft mass of 1500 kg, these β values correspond to diameters of approximately 33.5, 10.6, and 3.4 m, respectively. The data in Fig. 77 represent bounding peak heat rates over potential aerocapture corridors. For example, aerocapture at Mars with an AI velocity of 6 km/s, a β_1 of 10 kg/m^2, and a β-ratio of 10 may experience peak convective peak heat rates between 10 and 30 W/cm^2. A 400 km transfer orbit apoapsis altitude target was used for Mars and Venus and 1700 km was used for Titan. While heat rate limits for insulating thermal protection systems (TPS) are material specific, typical limits are well below 100 W/cm^2 for current flexible insulating TPS suitable for inflatable decelerator systems. Therefore, 100 W/cm^2 was adopted as a conservative upper bound on the capabilities of flexible insulating TPS. Higher heat rates require an ablative TPS, which may require a rigid heat shield. Therefore, the insulating TPS heat rate limit may be seen as a delimiter

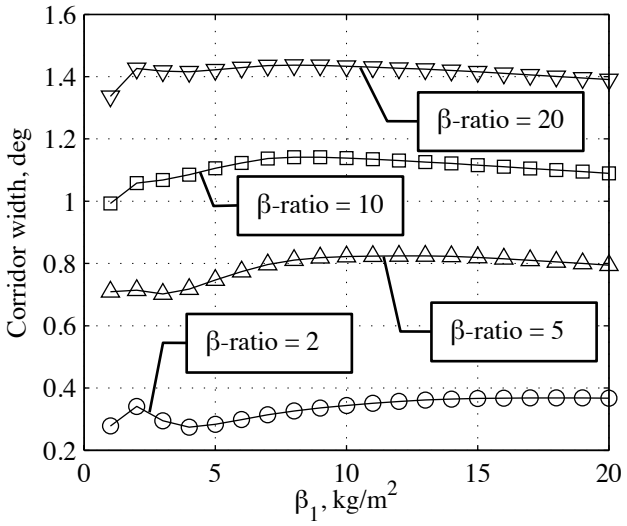

Figure 75: Aerodynamic corridor width as a function of β_1 for several β-ratios at Mars for AI velocity of 6 km/s.

between currently available inflatable decelerators and traditional rigid aeroshells.

The peak heat rates in Fig. 77 indicate that aerocapture at Venus requires a low β to limit the peak heat rate if current inflatable decelerators are to be used. Additionally, at the high velocities associated with Venus aerocapture, the radiative contribution to total heat rate may be equal to or greater than the convective contribution, increasing the peak heat rate the TPS must accommodate. For Mars, the radiative component of heating is typically small or negligible,[168] indicating that inflatable decelerators may be used for aerocapture. Radiative heating may also be significant at Titan and may lead to a requirement for a low β or ablative TPS.[179]

These results allow one to draw preliminary conclusions on the feasibility of using drag-only flight control for aerocapture. For Mars missions, adequate flight-path corridor width to accommodate uncertainties is provided by current approach navigation precision and β-ratios of less than 10.[171] Additionally, low heat rates at Mars make the use of lightweight HIAD drag skirts possible. Together, these make Mars an attractive target for drag modulation aerocapture systems. At Venus, expected peak heat rates require large diameter drag skirts to lower β to limit peak heat rates

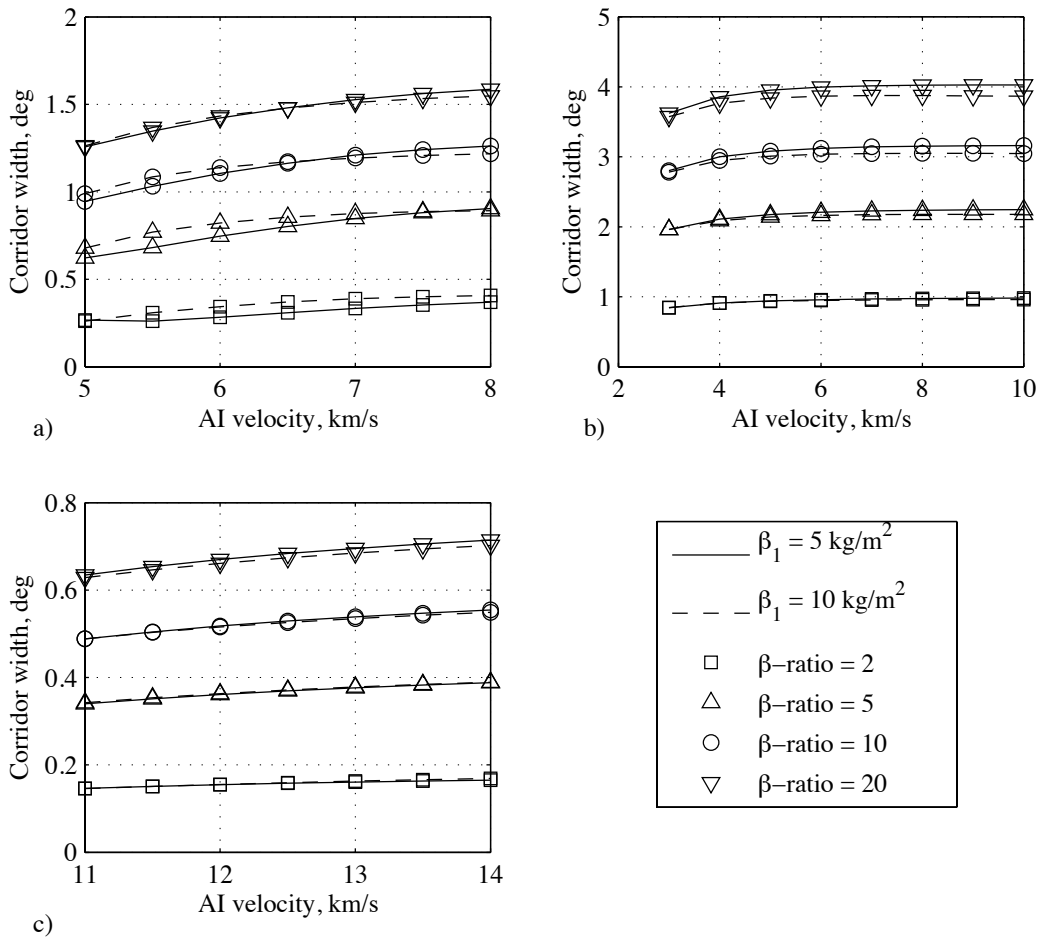

Figure 76: Aerocapture aerodynamic corridor widths at a) Mars, b) Titan, and c) Venus for two values of β_1 and several β-ratios.

such that current inflatable TPS technology may be used. Smaller drag skirts may be used, but will require ablative TPS. However, aerocapture at Venus still requires β-ratios near 10 to provide adequate corridor width, independent of the specific drag modulation system selected. The requirement for either a large drag skirt using existing flexible TPS or ablative TPS for a moderately large drag skirt create a system that is likely not mass competitive with traditional lift modulation systems. This makes Venus an unattractive target for drag modulation aerocapture. Conclusions about drag modulation aerocapture at Titan are less clear: while large flight-path angle corridor widths are available for reasonable β-ratios, distance from Earth and limited flight experience make approach navigation less precise at Titan than in the

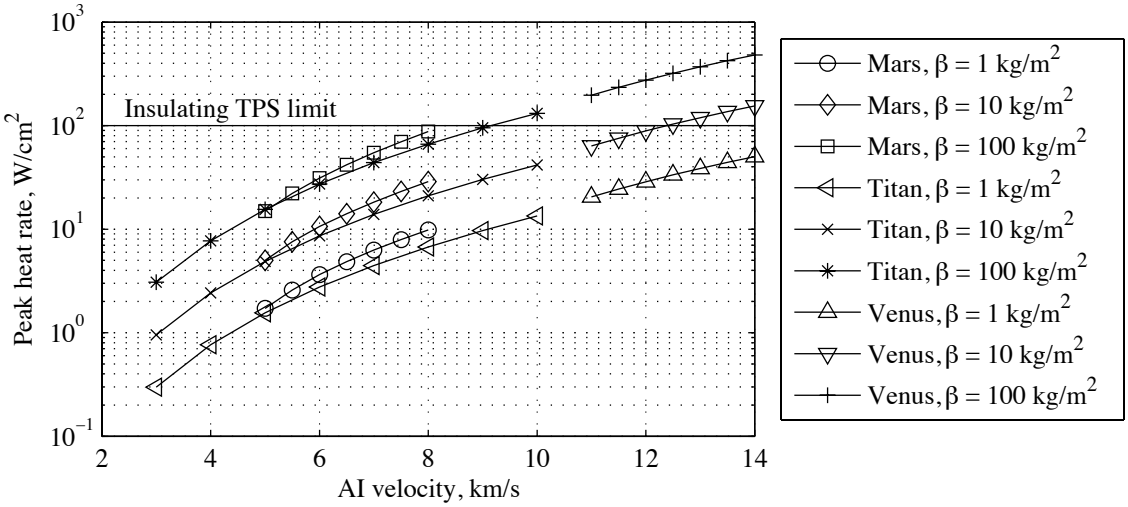

Figure 77: Peak stagnation-point convective heat rates for several β.

inner Solar System. Also, while convective heat rates are below the insulating TPS limit for AI velocities below 9 km/s, radiative heating is expected to contribute significantly to total heating at Titan.[179] Therefore, drag modulation aerocapture at Titan may be attractive if the AI velocity or β are sufficiently low for use of insulating flexible TPS, if flexible ablative TPS is developed, or if navigation precision is sufficient to allow a low β-ratio rigid drag skirt with an ablative TPS to be used. For these reasons, the remainder of this study focuses on drag modulation flight control aerocapture missions to Mars and Titan.

5.2.5 Case Study: Aerocapture at Mars

A Mars science orbiter concept vehicle is used to evaluate three drag modulation system options for aerocapture. The spacecraft mass is nominally 1500 kg, corresponding to the Mars Reconnaissance Orbiter (MRO), less the propellent required for a Mars orbit insertion burn.[181] The spacecraft is packaged behind a 4 m diameter lightweight heat shield, producing a β_2 value of 70.2 kg/m^2. This diameter provides space for a MRO-sized 3 m diameter high-gain antenna. An eastbound equatorial trajectory is used, with a nominal AI inertial velocity of 6 km/s and a nominal AI inertial flight-path angle of -11.11 deg. The AI flight-path angle was selected to

center the apoapsis altitude target within the vehicle's capability. The target orbit is a 400 km circular orbit.

The single-stage system utilizes a HIAD drag skirt, which is deployed prior to AI to increase vehicle drag area. The inflation pressure is assumed to be sufficient to maintain a 70-deg spherecone shape throughout the atmospheric pass. The skirt has an outer diameter of 12.65 m, resulting in a β_1 of 7.02 kg/m^2 and a β-ratio of 10.

Results are provided in Fig. 78 and Table 13 for a 1000-sample Monte Carlo simulation. Sufficient apoapsis altitude accuracy is achieved to limit the mean+3σ total ΔV required to 110.7 m/s. Additionally, apoapsis error is roughly centered about the target, indicating good guidance algorithm performance. For all samples, peak deceleration is below 4 g and peak heat rates are below 15 W/cm^2, low enough to allow use of currently available insulating flexible TPS. Out-of-plane errors are minimal, with final transfer orbit inclinations near zero. Jettison times selected by the guidance algorithm range from about 160 s to 230 s (Fig. 78(a)). Maximum apoapsis errors are generally associated with the earliest jettison times: when the drag area must be jettisoned early in the trajectory, the vehicle is unable to account for dispersions encountered during the bulk of the atmospheric pass, leading to larger apoapsis altitude errors. As expected, Fig. 78(b) shows the magnitude of the periapsis raise ΔV does not vary significantly with apoapsis error, although lower energy cases with negative apoapsis errors require greater ΔV. The magnitude of the apoapsis correction ΔV is a strong function of apoapsis error, although most cases require less than 40 m/s of ΔV (Fig. 78(c)). While the accuracy of the single-stage system does not lead to large ΔV requirements, apoapsis error may be an issue for extreme cases, potentially causing reentry into the Mars atmosphere.

The two-stage jettison system was designed such that the first jettison event has a β-ratio of 5, while the second jettison even has a β-ratio of 2, resulting in a β_3 of 35.10 kg/m^2 and an inner skirt maximum diameter of 5.66 m; β_1 was retained

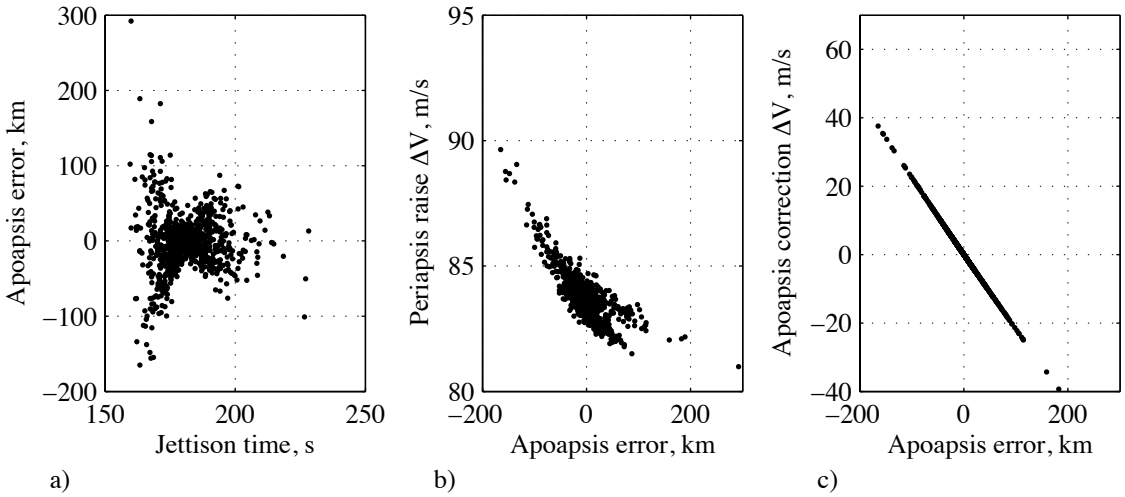

Figure 78: Monte Carlo results for single-stage system at Mars: a) apoapsis error versus jettison time and b) periapsis raise ΔV and c) apoapsis correction ΔV versus apoapsis error.

Table 13: Monte Carlo Simulation Results for Single-stage System at Mars

Parameter	Mean	σ	Mean-3σ	Mean$+3\sigma$	Min.	Max.
Single-stage system						
Apoapsis error, km	-3.923	37.197	-115.515	107.669	-164.918	292.231
Final inclination, deg	0.225	0.050	0.075	0.374	0.076	0.393
Periapsis raise ΔV, m/s	83.751	0.900	81.053	86.450	80.992	89.643
Apoapsis correction ΔV, m/s	0.921	8.233	-23.779	25.621	-61.839	37.601
Total ΔV, m/s	89.417	6.400	70.216	108.618	82.841	142.831
Peak deceleration, g	3.419	0.235	2.714	4.123	2.618	4.090
Peak conv. heat rate, W/cm^2	11.377	0.378	10.245	12.510	10.146	12.494
Integrated heat load, kJ/cm^2	1.819	0.100	1.519	2.120	1.415	2.089

from the single stage case. This split creates a course-fine control scheme, where the initial jettison event has more control authority to remove delivery error and predicted biases in aerodynamics and atmospheric properties and the second jettison event's lesser control authority is adequate to clean up any remaining error resulting from unforeseen biases or noise during the β_3 portion of the atmospheric pass.

Results for the two-stage system are given in Fig. 79 and Table 14. Using a second stage improves apoapsis accuracy and reduces the required propulsive ΔV, mostly through reducing the standard deviation of the apoapsis correction ΔV (Fig. 79(c)). Figure 79(a) shows the relationship between the first- and second-stage jettison times. The grey line denotes equal jettison times; the two circled cases jettison both stages

at the same time to reduce their energy depletion rate early in the trajectory. Figures 79(b) and (c) also indicate a bias towards positive apoapsis error and the resulting retrograde apoapsis correction ΔV. Other performance metrics, including peak deceleration, peak heating, and heat load are similar to the single-stage system.

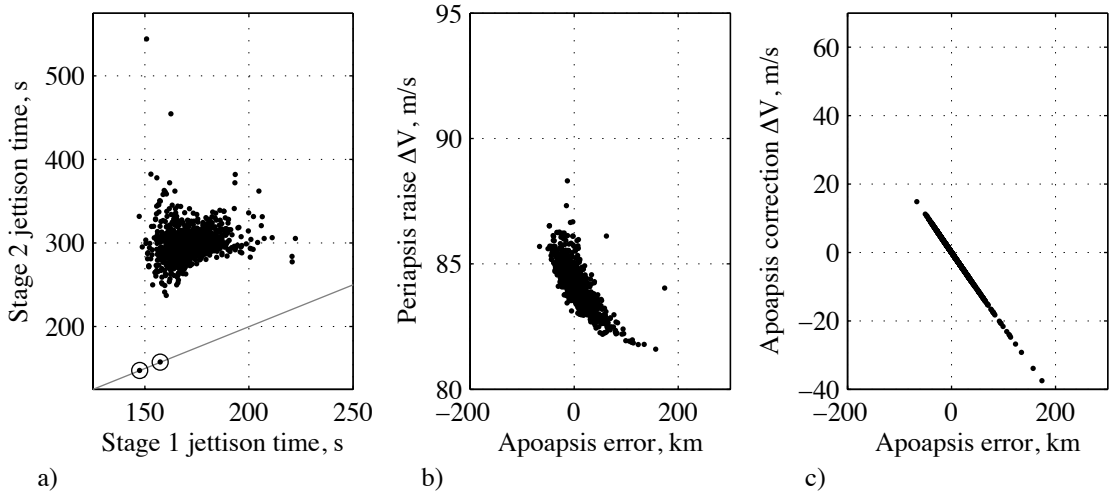

Figure 79: Monte Carlo results for two-stage system at Mars: a) stage 2 versus stage 1 jettison time and b) periapsis raise ΔV and c) apoapsis correction ΔV versus apoapsis error.

Table 14: Monte Carlo Simulation Results for Two-stage System at Mars

Parameter	Mean	σ	Mean-3σ	Mean$+3\sigma$	Min.	Max.
Apoapsis error, km	5.567	27.109	-75.761	86.894	-66.423	173.939
Final inclination, deg	0.222	0.051	0.070	0.375	0.072	0.392
Periapsis raise ΔV, m/s	84.126	0.847	81.586	86.667	81.602	88.306
Apoapsis correction ΔV, m/s	-1.207	5.970	-19.116	16.702	-37.503	14.895
Total ΔV, m/s	88.604	3.886	76.946	100.262	83.698	121.538
Peak deceleration, g	3.419	0.235	2.714	4.123	2.618	4.090
Peak conv. heat rate, W/cm^2	11.377	0.378	10.245	12.510	10.146	12.494
Integrated heat load, kJ/cm^2	1.746	0.079	1.508	1.984	1.409	1.951

Results for a CV system with the same β_1 and β_2 (diameters of 12.65 and 4 m, respectively) as the staged-jettison cases are given in Fig. 80 and Table 15. Results indicate good aerocapture performance, with lower peak deceleration, better apoapsis altitude accuracy, and a lower total ΔV requirement relative to the staged-jettison systems. However, while the CV system has a lower total ΔV requirement, it also has a higher periapsis raise ΔV requirement. The CV system exits the atmosphere

with a low β, relative to the staged-jettison systems, which results in a steeper flight-path angle and lower energy at atmospheric exit for the same transfer orbit apoapsis altitude. This energy must then be replaced with a larger periapsis raise ΔV when circularizing. The accumulated out-of-plane error and aerothermal environments remain similar to the staged-jettison systems. Figure 80(a) shows that a significant amount of jitter is present in the area command signal for some cases. This jitter is caused by Monte Carlo dispersions in the atmosphere that the constant-bias density estimator is unable to account for. However, for the nominal case, in black, the area command is nearly constant, validating the guidance algorithm's constant-area solution method.

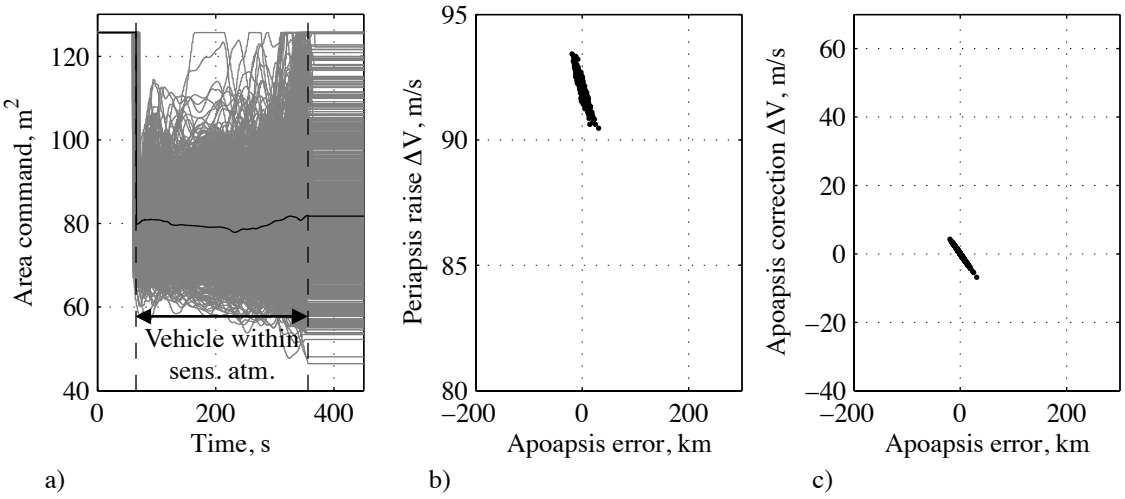

Figure 80: Monte Carlo results for CV system at Mars: a) area command versus time (black curve denotes nominal) and b) periapsis raise ΔV and c) apoapsis correction ΔV versus apoapsis error.

Table 15: Monte Carlo Simulation Results for Continuously-variable System at Mars

Parameter	Mean	σ	Mean-3σ	Mean$+3\sigma$	Min.	Max.
Apoapsis error, km	0.807	6.870	-19.804	21.418	-19.154	30.989
Final inclination, deg	0.177	0.048	0.034	0.321	0.042	0.336
Periapsis raise ΔV, m/s	92.015	0.470	90.606	93.425	90.465	93.426
Apoapsis correction ΔV, m/s	-0.177	1.523	-4.747	4.393	-6.838	4.262
Total ΔV, m/s	93.238	0.999	90.239	96.236	91.849	97.687
Peak deceleration, g	2.508	0.093	2.229	2.787	2.276	2.859
Peak conv. heat rate, W/cm^2	12.895	0.579	11.159	14.632	10.985	14.785
Integrated heat load, kJ/cm^2	1.586	0.066	1.386	1.785	1.348	1.775

The results presented indicate that single-stage, two-stage, and continuously-variable drag modulation systems are all feasible for aerocapture at Mars for the selected β-ratio of 10. However, a clear trend emerges in accuracy with the single-stage system being the least accurate and the CV system being the most accurate. The disparity in accuracy is highlighted in Fig. 81, which shows the high and low mean+3σ apoapsis errors. However, Fig. 81 also shows that, while better accuracy reduces the total ΔV required to circularize into a 400 km orbit, the difference in total ΔV between the three drag modulation system concepts is small. The CV system saves less than 15 m/s of ΔV which translates to a propellant mass savings of only about 10 kg for a 1500 kg spacecraft. However, the two-stage and CV systems provide additional robustness to uncertainty and design issues over the single-stage system, where atmospheric reentry may be more likely. Other trajectory metrics of interest are similar across all three systems, with the exception of peak deceleration, which is lower for the CV system.

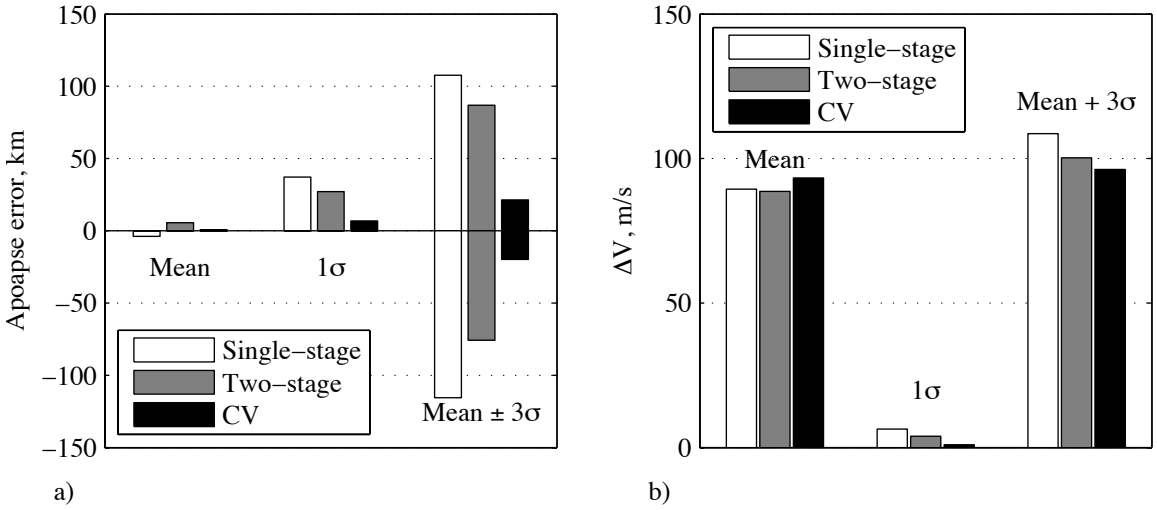

Figure 81: Comparison of drag modulation aerocapture system options for Mars: a) apoapse error and b) total ΔV.

5.2.6 Summary

Results indicate that drag modulation flight control presents an attractive option for aerocapture systems at Mars where low heat rates enable the use of large, lightweight, inflatable drag areas. The use of HIADs enables large β-ratios which provide a high degree of robustness to day-of-flight uncertainties, even for single-stage jettison systems. Although not discussed in this chapter, drag modulation at Titan is found to require advanced non-ablative thermal protection systems for inflatable decelerators to withstand peak heat rates during the atmospheric pass or large drag areas to limit peak heat rates to current non-ablative thermal protection system limits. Results indicate that a two-stage system with inflatable drag skirts provides acceptable orbital insertion performance with a potentially lower system complexity than comparable lift modulation systems. The large gravity well and high heat rates experienced during aerocapture at Venus make drag modulation flight control unattractive when combined with a non-ablative thermal protection system. Significantly larger drag areas or advances in fabric-based material thermal properties are required to improve feasibility at Venus.

5.3 Conclusions

Overall, drag modulation flight control is largely enabled by three technologies: precise approach navigation, modern flight computers, and, for more massive payloads, deployable hypersonic decelerators. Current deep space navigation precision results in minimal delivery and knowledge errors at the top of the atmosphere, making out-of-plane control optional in the absence of plane-change or crossrange requirements. Modern flight computers provide enough throughput to allow the use of onboard parameter estimation techniques coupled with numerical predictor-corrector algorithms, resulting in accurate terminal state predictions and steering commands. Deployable

hypersonic decelerators provide a mass-efficient solution to lower the ballistic coefficient and achieve the required ballistic coefficient ratio and control authority.

Drag-modulation trajectory control has been shown to be feasible for the developed concepts for both entry and aerocapture and appears to be extensible to other classes of missions, the full range of applicability for drag-modulation trajectory control has not been determined. Determining feasibility for point designs is possible, as as shown in this chapter, but no general method has been identified for determining whether lift or drag-modulation is best, with respect to some relevant objective function, for a particular mission. The development of such method is proposed in the following chapter.

CHAPTER VI

COMPARISON OF LIFT AND DRAG-MODULATION SYSTEMS USING NONLINEAR VARIATIONAL METHODS

6.1 Introduction

Comparing lift and drag-modulation trajectory control systems for planetary entry applications presents a challenge. Current industry practice would likely utilize Monte Carlo analysis techniques to assess flight performance and robustness for particular vehicle design and mission sets. This strategy is both resource-intensive, requiring significant computational resources and engineering analysis, and limited, as its results will apply only to the narrow, mission-specific parameters considered. During design, this type of analysis typically requires more information about the system than is available at the time a decision must be made about which type of control system to select. Therefore, these analyses either will not be conducted for lack of information or resources, or if conducted, will be tainted by overly detailed assumptions necessary to populate numerical models.

High-accuracy analytical approximate solutions to the equations of motion allow one to evaluate the robustness of lift and drag-modulation systems in a more general, more conclusive manner. Specifically, nonlinear variational methods may be used to generate expressions for variations in flight-performance parameters of interest with respect to perturbations in vehicle, mission design, and environment parameters. A particular system's response to such perturbations is indicative of that system's robustness to such perturbations. A smaller change in a performance parameter of interest relative to a perturbation implies greater inherent system robustness than a

larger change.

6.2 Nonlinear Variational Methods

Consider a nonlinear system defined by:

$$\dot{\mathbf{x}}(t) = \mathbf{f}\left(t, \mathbf{x}(t), \mathbf{p}\right) \tag{136}$$

where $\mathbf{x}$ is the state vector and $\mathbf{p}$ is a vector of static parameters. The solution to this nonlinear system of equations is:

$$\mathbf{x}(t) = \mathbf{x}(t_0) + \int_{t_0}^{t} \mathbf{f}\left(\tau, \mathbf{x}(\tau), \mathbf{p}\right) d\tau = \phi(t_0, t, \mathbf{x}_0, \mathbf{p}) \tag{137}$$

Using a Taylor Series expansion, one can write the variation in final state (at time t_f) due to initial state perturbations (at time t_0) and static parameter perturbations as:

$$\mathbf{x}_f + \delta\mathbf{x}_f = \phi(t_0, t_f, \mathbf{x}_0, \mathbf{p}) + \frac{\partial\phi(t_0, t_f, \mathbf{x}_0, \mathbf{p})}{\partial\mathbf{x}_0}\delta\mathbf{x}_0 + \frac{\partial\phi(t_0, t_f, \mathbf{x}_0, \mathbf{p})}{\partial\mathbf{p}}\delta\mathbf{p} + \text{H.O.T.} \tag{138}$$

Or:

$$\delta\mathbf{x}_f = \frac{\partial\phi(t_0, t_f, \mathbf{x}_0, \mathbf{p})}{\partial\mathbf{x}_0}\delta\mathbf{x}_0 + \frac{\partial\phi(t_0, t_f, \mathbf{x}_0, \mathbf{p})}{\partial\mathbf{p}}\delta\mathbf{p} + \text{H.O.T.} \tag{139}$$

Where the subscript f denotes the value at the final time, t_f. This relation is typically written in terms of the state transition matrix, $\Phi(t_0, t_f)$, and the parameter sensitivity matrix, $\Psi(t_0, t_f)$:

$$\delta\mathbf{x}_f = \Phi(t_0, t_f)\delta\mathbf{x}_0 + \Psi(t_0, t_f)\delta\mathbf{p} + \text{H.O.T.}$$

Φ and Ψ contain the first-order information for the series expansion about some reference trajectory, $\mathbf{x}(t)$. The above vector equations represent multiple scalar equations. For example, if one changes the domain from t to V and wishes to determine the change in final range with respect to changes in initial altitude, then, to first order:

$$\delta s_f = \left.\frac{\partial s(V)}{\partial h_0}\right|_f \delta h_0 \tag{140}$$

Table 16: Parameters in the Allen-Eggers Solution

Category	Parameter	Description
Environment	ρ_{ref}	Reference density
	h_{ref}	Reference altitude
	H	Scale height
	g	Acceleration due to gravity
	R	Planetary radius
Initial state	V_0	Initial velocity
	γ_0	Initial flight-path angle
	h_0	Initial altitude
	θ_0	Initial range angle
Vehicle	β	Ballistic coefficient
	L/D	Lift-to-drag ratio

These expressions typically require numerical approximation and evaluation for non-linear functions, such as the equations of motion. However, if closed-form analytical solutions are available, the variations may be written in closed form as a function of perturbations, provided the appropriate partial derivatives exist. Closed-form solutions typically are a function of the environmental, initial state, and vehicle parameters given in Table 16.

Computational symbolic manipulation software, such as *Mathematica*, may be used to retain higher-order terms, potentially generating more accurate expressions for state variations. The Taylor series for a scalar function of several variables is, for an expansion about some point $\mathbf{a} = (a_1, ..., a_d)$:

$$\begin{aligned} f\left(a_1 + x_1, ..., a_d + x_d\right) &\approx T\left(x_1, ..., x_d\right) \\ &= \sum_{n_1=0}^{\infty} \cdots \sum_{n_d=0}^{\infty} \frac{\left(x_1 - a_1\right)^{n_1} \cdots \left(x_d - a_d\right)^{n_d}}{n_1! \cdots n_d!} \left(\frac{\partial^{n_1 + \cdots + n_d} f}{\partial^{n_1} x_1 \cdots \partial^{n_d} x_d} \right) \left(a_1, ..., a_d\right) \end{aligned} \quad (141)$$

where $\mathbf{x} = (x_1, ..., x_d)$ is the deviation from point $\mathbf{a}$. If only the linear terms are retained:

$$T\left(x_1, ..., x_d\right) = f\left(a_1, ..., a_d\right) + \sum_{j=1}^{d} \frac{\partial f\left(a_1, ..., a_d\right)}{\partial x_j} \left(x_j - a_j\right) + \text{H.O.T.} \quad (142)$$

If the squared terms are retained:

$$T\left(x_1,...,x_d\right) = f\left(a_1,...,a_d\right) + \sum_{j=1}^{d} \frac{\partial f\left(a_1,...,a_d\right)}{\partial x_j}\left(x_j - a_j\right) + \frac{1}{2}\sum_{j=1}^{d}\sum_{k=1}^{d} \frac{\partial^2 f\left(a_1,...,a_d\right)}{\partial x_j \partial x_k}\left(x_j - a_j\right)\left(x_k - a_k\right) + \text{H.O.T.} \quad (143)$$

If the cubic terms are retained:

$$T\left(x_1,...,x_d\right) = f\left(a_1,...,a_d\right) + \sum_{j=1}^{d} \frac{\partial f\left(a_1,...,a_d\right)}{\partial x_j}\left(x_j - a_j\right) + \frac{1}{2}\sum_{j=1}^{d}\sum_{k=1}^{d} \frac{\partial^2 f\left(a_1,...,a_d\right)}{\partial x_j \partial x_k}\left(x_j - a_j\right)\left(x_k - a_k\right) + \frac{1}{6}\sum_{j=1}^{d}\sum_{k=1}^{d}\sum_{l=1}^{d} \frac{\partial^3 f\left(a_1,...,a_d\right)}{\partial x_j \partial x_k \partial x_l}\left(x_j - a_j\right)\left(x_k - a_k\right)\left(x_l - a_l\right) + \text{H.O.T.} \quad (144)$$

However, for the purpose of evaluating only the change in the function of interest, letting $\mathbf{x} - \mathbf{a} = \delta\mathbf{x}$, we can write the somewhat simpler result using vector notation:

$$\delta\mathbf{f} = \mathbf{T}(\delta\mathbf{x}) \quad (145)$$

6.3 Application to Ballistic Entry Using the Allen-Eggers Solution

Applying nonlinear variational methods to the Allen-Eggers solution for ballistic entry trajectories results in closed-form expressions for variations in trajectory and performance parameters of interest.

The Allen-Eggers solution allows us to analytically compute $\delta\mathbf{x}_f$. Writing the state as a function of V, we have

$$\mathbf{x}(V) = \begin{bmatrix} V \\ \gamma^* \\ h(V) \\ \theta(V) \end{bmatrix} \quad (146)$$

Where $h(V)$ and $\theta(V)$ are given by the Allen-Eggers solution. Since we have the solution for the states, we can always determine $\mathbf{x}$ based on some assumed $\mathbf{x}_0$. This means we can write the change in the final state as:

$$\delta\mathbf{x}_f = \frac{\partial}{\partial\mathbf{x}}\phi\left(V_f, \mathbf{x}, \mathbf{p}\right)\delta\mathbf{x} + \frac{\partial}{\partial\mathbf{p}}\phi\left(V_f, \mathbf{x}, \mathbf{p}\right)\delta\mathbf{p} \tag{147}$$

Where $\delta\mathbf{x}_f$ is variation in the state associated with V_f and changes in V_f have been neglected. V may still be included in $\mathbf{x}$ if desired. Separately, there is no need for $\mathbf{x}_0$ to be at the top of the atmosphere; a closed-form solution for the equations of motion allows one to use any point on the trajectory as the initial point.

6.3.1 Robustness to Atmospheric Parameters

The sensitivity of various ballistic entry performance parameters to changes in the atmosphere model was evaluated. If an exponential atmospheric density model is used, the density as a function of altitude is governed by three parameters: ρ_{ref}, h_{ref}, and H. In particular, we might like to know what the sensitivity of the total entry range is relative to some change in ρ_{ref}. To first order, we may write this as:

$$\delta s_f = \frac{\partial s_f}{\partial \rho_{ref}}\delta\rho_{ref} \tag{148}$$

where s_f is the range s evaluated at the terminal velocity V_f. Using the Allen-Eggers approximate solution, we can determine δs_f as a function of $\delta\rho_{ref}$. A computer algebra system is used to compute this partial; the result is complicated, and is provided in Figure 82 for illustrative purposes only.

Figure 83 shows the effect of reference density perturbations on final range; Figure 84 shows this relationship for several ballistic coefficients for a steep entry at Earth. Trajectory parameters are given in Table 17.

Figure 83(a) shows the change in final range for different percent changes in ρ_{ref}. As one might expect, range increases with decreasing density (the vehicle decelerates more slowly in a thinner atmosphere) and decreases with increasing density.

Figure 82: Closed form solution for $\partial s_f / \partial \rho_{ref}$ using the Allen-Eggers solution.

Table 17: Ballistic Entry Trajectory Parameters

Parameter	*Value*
Planet	Earth
V_0	7500 m/s
γ_0	-20 deg
h_0	90 km
V_f	500 m/s
β	100 kg/m^2
R	6378 km
g	9.81 m/s^2
ρ_{ref}	1.215 kg/m^3
H	7500 m
h_{ref}	0 m

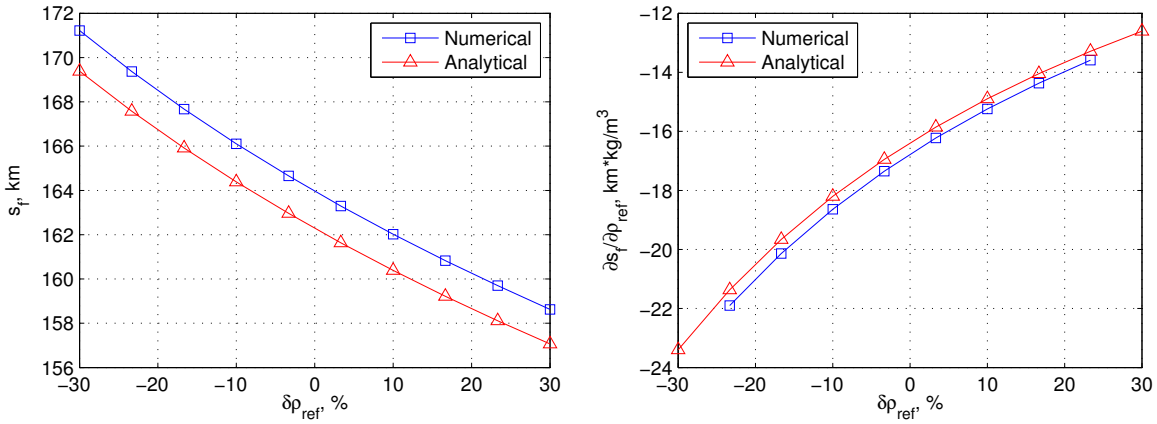

(a)

(b)

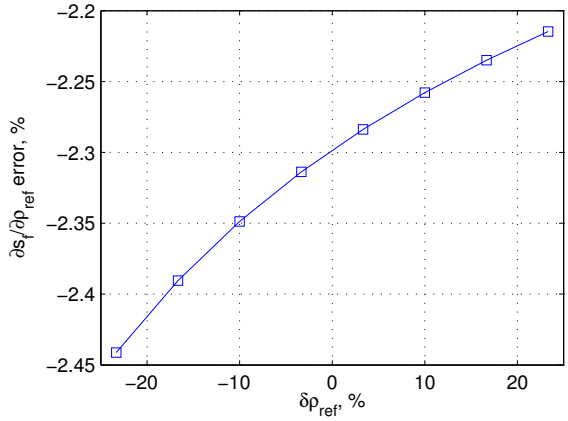

(c)

Figure 83: Effect of reference density perturbations on final range.

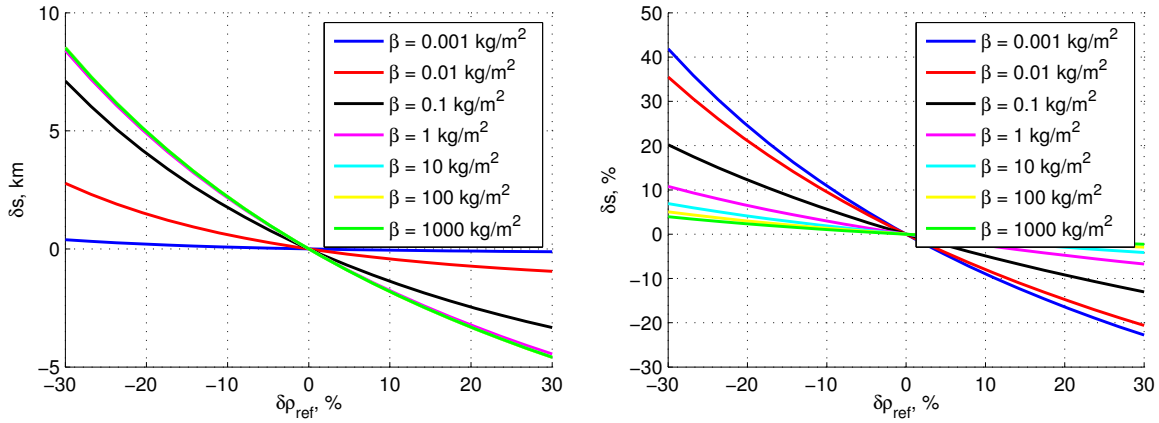

(a) Change in magnitude.

(b) Percent change.

Figure 84: Change in final range for various β values, analytical solution.

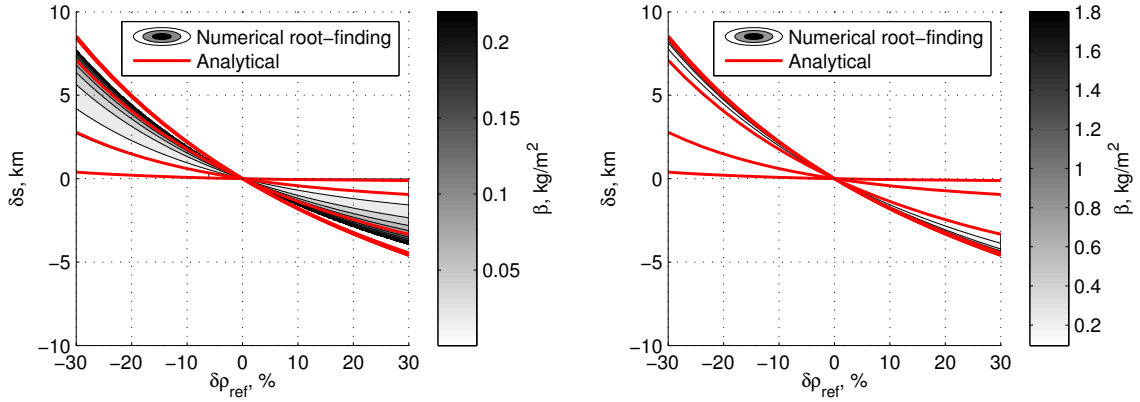

(a) Initial guess of 0.1 kg/m^2

(b) Initial guess of 1 kg/m^2

Figure 85: Change in final range for various β values, numerical root-finding computation.

The Allen-Eggers analytical solution provides a good estimate of the total range, with error in the range of 1-2 km. Figure 83(b) show the partial of final range with respect to changes in ρ_{ref}. The numerical (computed using a central difference approximation) and analytical (computed using analytic differentiation) solutions show excellent agreement. The curve is nonlinear, and shows that decreases in ρ_{ref} have a larger effect on the total range than increases do. Lastly, Figure 83(c) shows that the analytical partial derivative is within 3% of the numerical solution.

One application of the analytical solution is to look at the sensitivity of the final

range to reference density perturbations for a range of β, as shown in Figure 84. As β becomes larger, the magnitude of the change in range becomes insensitive to ballistic coefficient (see Fig. 84(a)). This is true for ballistic coefficients over about 1 kg/m^2, which essentially tells us that the change in range magnitude with respect to constant biases in density is not a function of ballistic coefficient for realistic systems. This result shows that estimating a change in range based on a constant-bias density correction computed during flight is valid for the full range of ballistic coefficients a vehicle might exhibit during atmospheric flight. However, the percent change in range due to perturbation in reference density does change with ballistic coefficient (see Fig. 84(b)). As ballistic coefficient increases, the vehicle becomes relatively less sensitive to changes in reference density, with the percent change in range approaching zero as ballistic coefficient becomes large.

This type of plot may also be constructed using numerical methods. One can use root-finding to determine the ballistic coefficient that satisfies a particular $(\delta s, \delta\rho_{ref})$. This is a computationally intensive process (it requires 3-4 orders of magnitude more time than the analytical solution), and like most numerical solutions, requires some knowledge of the problem to find an acceptable answer. For example, Figure 85 shows two numerical solutions. Figure 85(a) uses an initial guess of 0.1 kg/m^2 for β; Fig. 85(b) uses an initial guess of 1 kg/m^2. These two initial guesses result in drastically different results, neither of which clearly show the collapsing feature that is shown by the analytical solution in Fig. 84(a). This highlights the ease with which these trends may be studied using analytical solutions; analytical solutions reduce the need for initial guesses and other information that may be difficult to discern *a priori*. Lastly, one can easily see that the accuracy of the analytical solutions remains good across different β.

The same equations may be used to determine the effect of reference density perturbations on a ballistic entry vehicle's divert capability. Figure 86 below shows

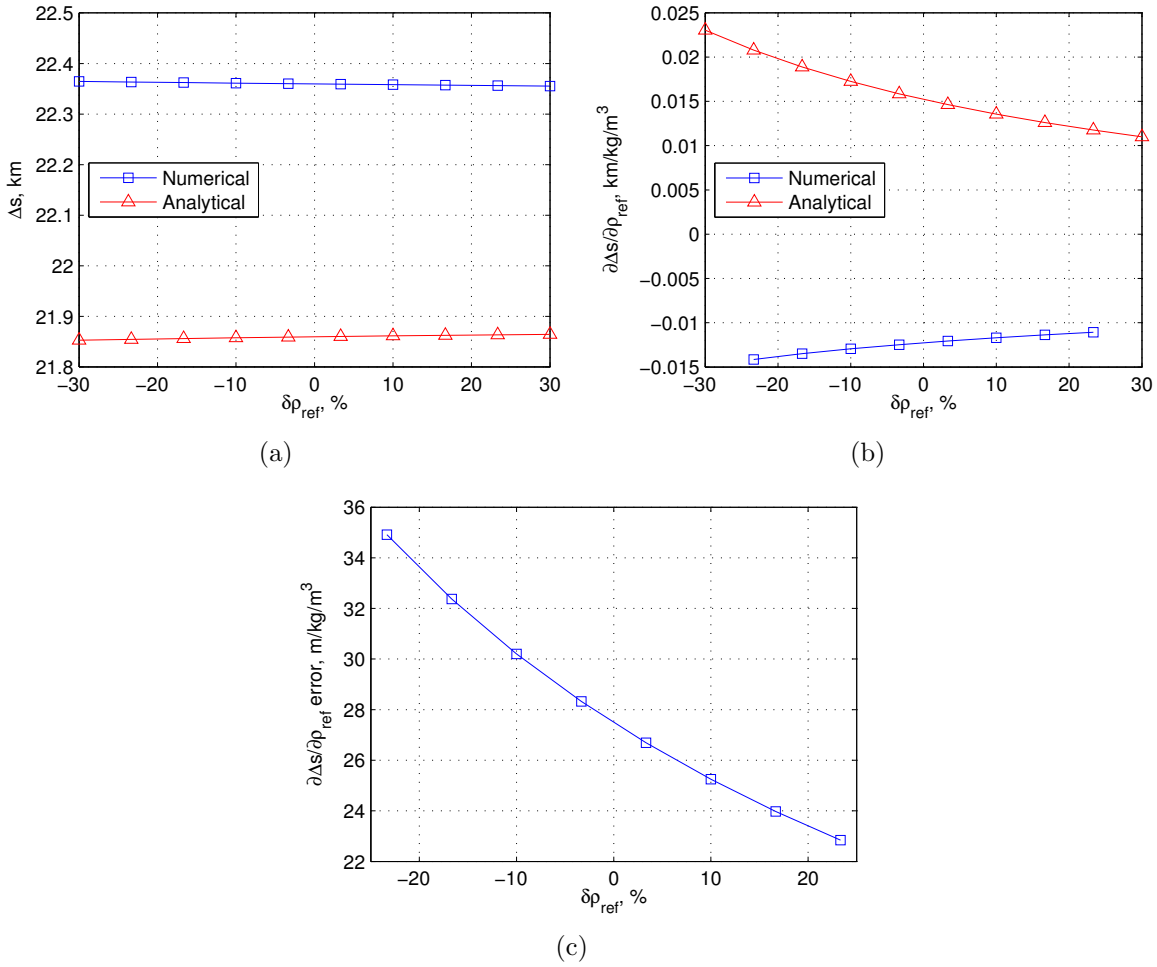

Figure 86: Effect of reference density perturbations on range divert capability.

the effects for a vehicle with $\beta_1 = 100$ kg/m^2 and $\beta_2 = 300$ kg/m^2. As expected, Δs is insensitive to changes in reference density: because changes in s are independent of ballistic coefficient, subtracting s_2 (at β_2) from s_1 (at β_1) produces little change. The error is shown to be low for the analytical solution; Figure 86(c) shows the error in m/kg/m^3 instead of km/kg/m^3–error is in the 10s of meters per unit change in density.

We can apply a similar methodology to look at sensitivity to changes in scale height. Figure 87 shows the change in range with respect to changes in scale height, the partial of range with respect to change in scale height, and the percent error of the analytical solution relative to the numerical solution. As with the previous analysis,

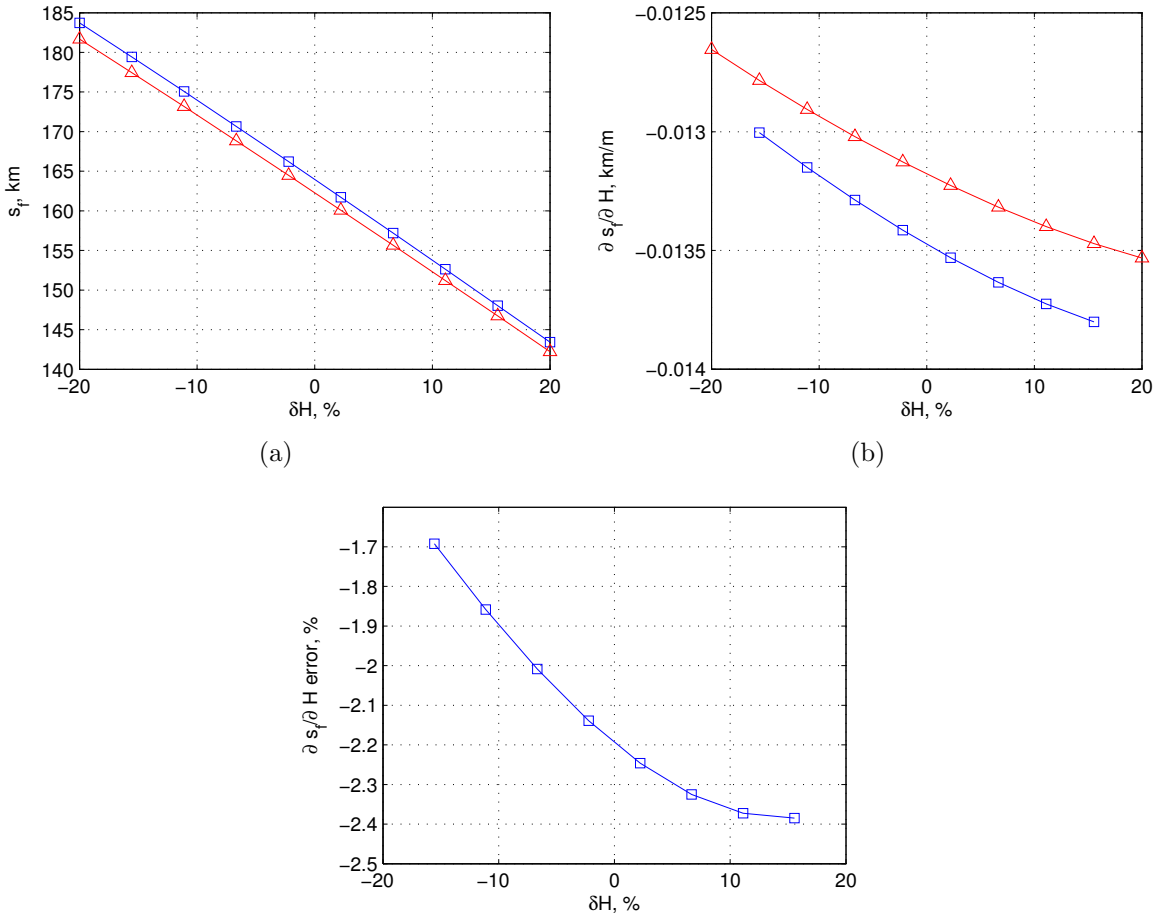

Figure 87: Effect of scale height perturbations on final range.

the error is within 3%. The expected trend with respect to range is also shown: larger scale heights correspond to density increasing more quickly with changes in altitude.

Looking at how the final range changes with respect to changes in δH for different β is enlightening (see Figure 88): one can a see that there is a β, near 10^4 kg/m^2, that minimizes the effect of changes in scale height on range. For ballistic coefficients greater than this, the sign of the partial of range with respect to changes in scale height changes such that larger scale height increases range. Unlike changes in final range due to perturbations in ρ_{ref}, changes in final range due to H perturbations are a function of ballistic coefficient. As before, numerical methods may be used to develop similar results, but the numerical results are highly dependent on the initial guess

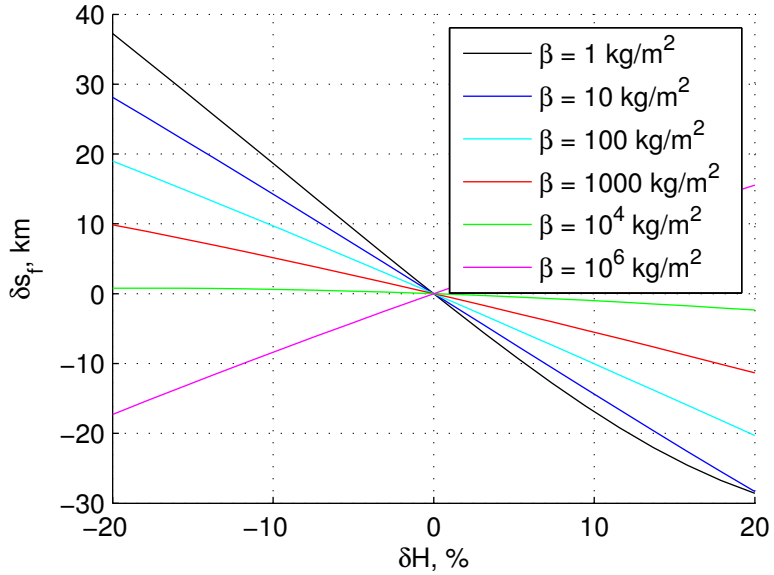

Figure 88: Change in final range with respect to changes in scale height for various β values, analytical solution.

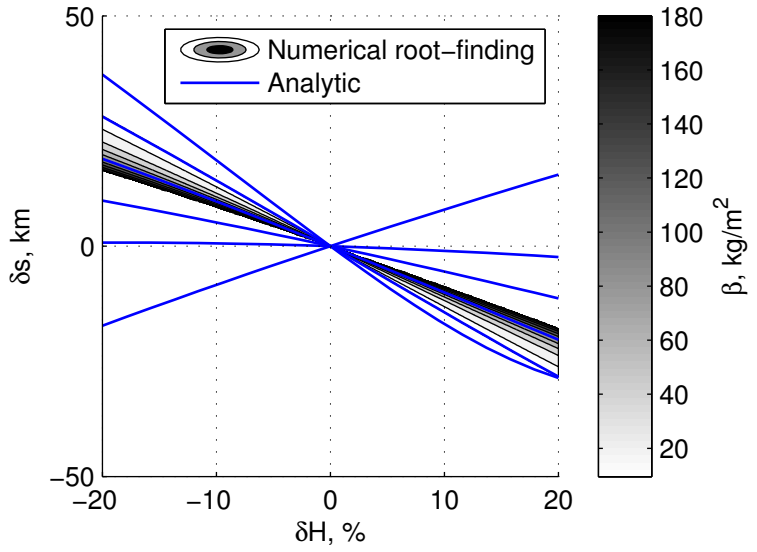

Figure 89: Change in final range with respect to changes in scale height for various β values, numerical solution with analytical solution superimposed in blue.

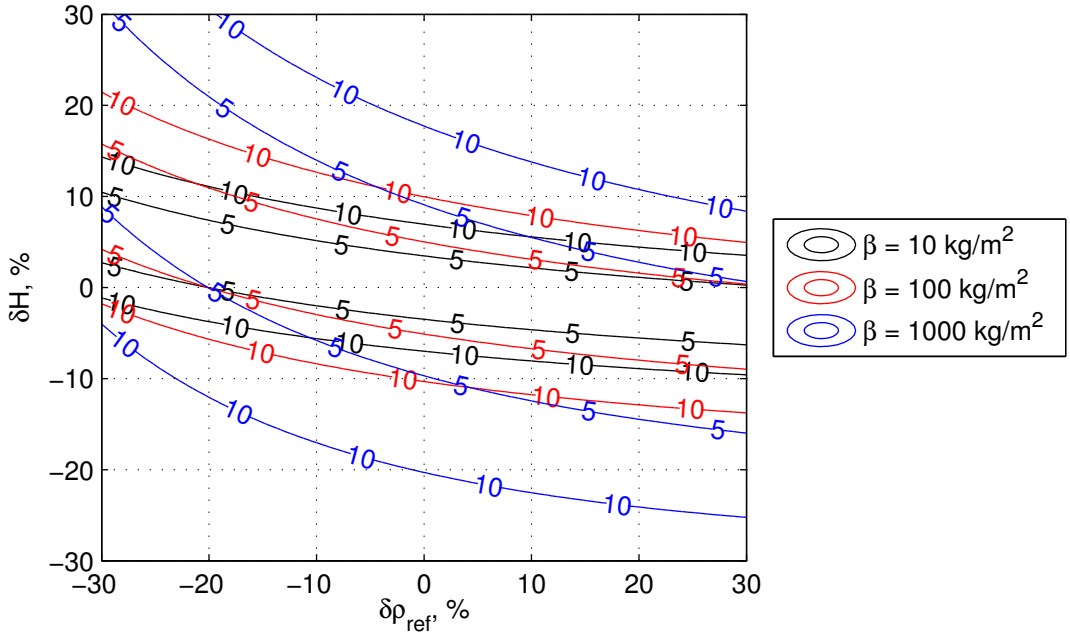

Figure 90: First-order change in final range in km for various β with respect to perturbations in H and ρ_{ref}.

provided. Figure 89 shows the numerical solution for an initial guess of 100 kg/m^2 and the analytical solutions from Fig. 88 superimposed in blue. The numerical and analytical solutions match up well, exhibiting the same trends.

Figure 90 show how total range changes when subject to perturbations in both scale height and reference density. The change in range is given by the first-order approximation:

$$\delta s(V_f) = \frac{\partial s(V_f)}{\partial \rho_{ref}} \delta \rho_{ref} + \frac{\partial s(V_f)}{\partial H} \delta H \tag{149}$$

The figure shows that the trends observed when a single perturbation is applied remain consistent. First, increasing ballistic coefficient reduces the change in final range due to a change in scale height (a much larger perturbation is required in H to cause a 10 km change in range for $\beta = 1000$ kg/m^2 than for 1 kg/m^2). Second, percent changes in H have a relatively greater impact on δs than equivalent percent changes in ρ_{ref}. Lastly, changes in δs due to $\delta \rho_{ref}$ are relatively insensitive to the magnitude of β.

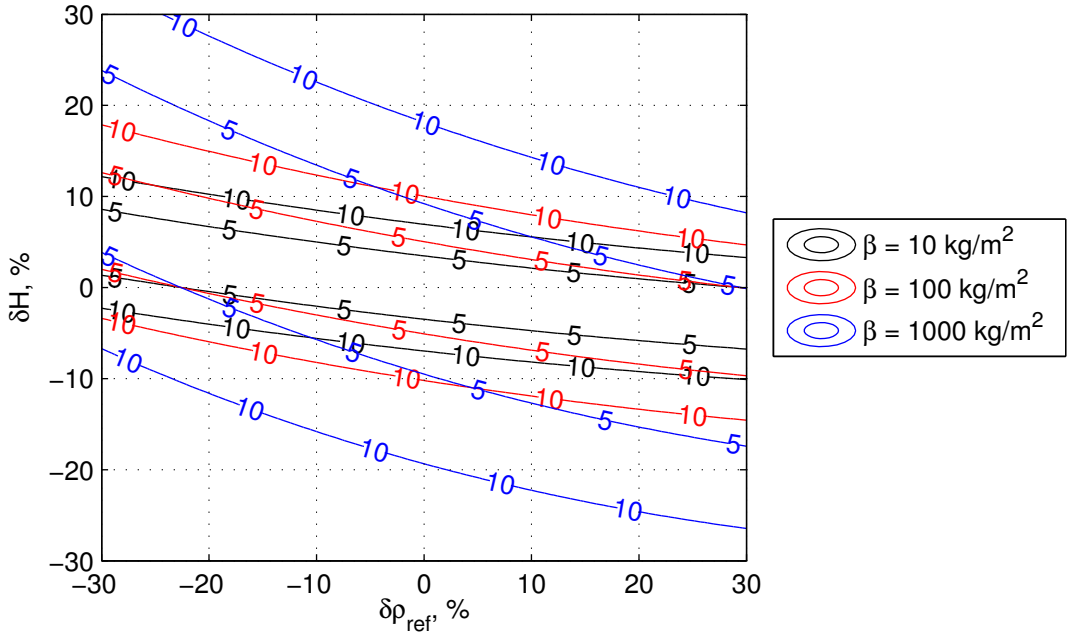

Figure 91: Combined first and second-order change in final range in km for various β with respect to perturbations in H and ρ_{ref}.

One can easily include the second-order terms in the expression for the variation of range with respect to changes in scale height and reference density:

$$\delta s(V_f) = \frac{1}{2}\frac{\partial^2 s(V_f)}{\partial \rho_{ref}^2}\delta\rho_{ref}^2 + \frac{\partial s(V_f)}{\partial \rho_{ref}}\delta\rho_{ref} + \frac{\partial^2 s(V_f)}{\partial \rho_{ref}\partial H}\delta\rho_{ref}\delta H + \frac{\partial s(V_f)}{\partial H}\delta H + \frac{1}{2}\frac{\partial^2 s(V_f)}{\partial H^2}\delta H^2 \tag{150}$$

One can combine the mixed partial derivatives above because both are continuous on some open interval. This allows one to account for any interaction effects from simultaneous perturbations in H and ρ_{ref}. Figure 91 shows that the results are similar, but not identical, to those presented in Figure 90. Overall trends remain the same, but responses are more linear, especially for larger ballistic coefficients.

Overall, one can see that higher-β vehicles are less susceptible to atmospheric perturbations. This is perhaps intuitively obvious, since β appears in the denominator of the aerodynamic force terms in the equations of motion. However, it does help explain why single-event drag-modulation systems work so well: while the vehicle no longer has any control authority after the jettison event, it is also less susceptible to

uncertainty since its ballistic coefficient has risen significantly.

6.4 Comparison of Lift and Drag-Modulation Systems for Steep Entry Trajectories

Comparisons of flight performance and robustness for steep entry between lift and drag-modulation vehicles may be accomplished through application of nonlinear variational methods to closed-form trajectory solutions. This section illustrates the method using the steep lifting entry and Allen-Eggers solutions with a focus on changes in final range. These solutions are applicable to the same types of trajectories, allowing use of identical initial conditions and vehicle properties for comparison purposes. While these solutions assume constant vehicle properties, they provide trajectory solutions that may represent nominal flight. For example, the Apollo guidance Final Phase algorithm is based around a reference trajectory, flown at a constant, reference L/D.

While the steep-lifting entry approximation requires a small L/D (or steep γ_0), these results are applicable to vehicles with larger L/D. Lifting vehicles cannot fly at maximum L/D. Doing so saturates the trajectory control system. Again, while the Apollo Command Module had a maximum hypersonic lift-to-drag ratio of approximately 0.3, the Apollo Final Phase reference trajectory was designed about a constant L/D of 0.18, or 60% lift up ($\sigma \approx 53.13$ deg).

6.4.1 Atmospheric Parameters

Figure 92 shows a comparison of the range response of lifting and ballistic entry vehicles to single, first-order atmospheric model parameter perturbations. Trajectory parameters are given in Table 17; the lifting vehicle has a lift-to-drag ratio of 0.1. Figure 92 shows that the lifting and ballistic vehicles exhibit nearly identical responses to these perturbations. The one small difference is that lifting systems appear to be slightly less susceptible to H perturbations. This is likely due to the fact that lifting

systems achieve more shallow flight-path angles during entry than a ballistic system for a given initial flight-path angle. This renders any difference in the way density changes with altitude less significant.

Lastly, responses to perturbations in reference density (Figure 92(a)) and reference altitude (Figure 92(c)) are similar; this is as one might expect, given the coupled nature of these parameters. For example, a higher-than-expected density at 0 km altitude could be caused by a larger ρ_{ref} or a lower value of h_{ref}.

Figure 92 shows both analytical and numerical solutions. Accuracy is quite good for both lifting and ballistic entry cases, to the extent that the analytical solutions correctly model the small difference in response to scale height perturbations.

6.4.2 Initial State Parameters

Figure 93 shows numerical and analytical solutions for the change in range due to first-order, single-parameter perturbations in initial state for the same lifting and ballistic vehicles. Performance is similar for perturbations in initial altitude (Figure 93(c)). The ballistic vehicle is slightly more robust to initial flight-path angle perturbations (Figure 93(b)).

However, responses are quite different for changes in initial velocity (Figure 93(a)). First, the accuracy of the analytical solutions is poor for this case because changing V_0 directly changes the domain over which the analytical solutions are derived and applied. Second, the numerical evaluation shows that ballistic entry vehicles are slightly more robust to changes in initial velocity.

6.4.3 Vehicle Aerodynamic Parameters

Figure 94 shows the effect on final range due to perturbations in β and L/D. Once again, results are similar for lifting and ballistic vehicles for perturbations in β (see Figure 94(a)). Results are markedly different for L/D perturbations. Specifically, ballistic entry vehicles are not subject to uncertainty in L/D. While ballistic vehicles

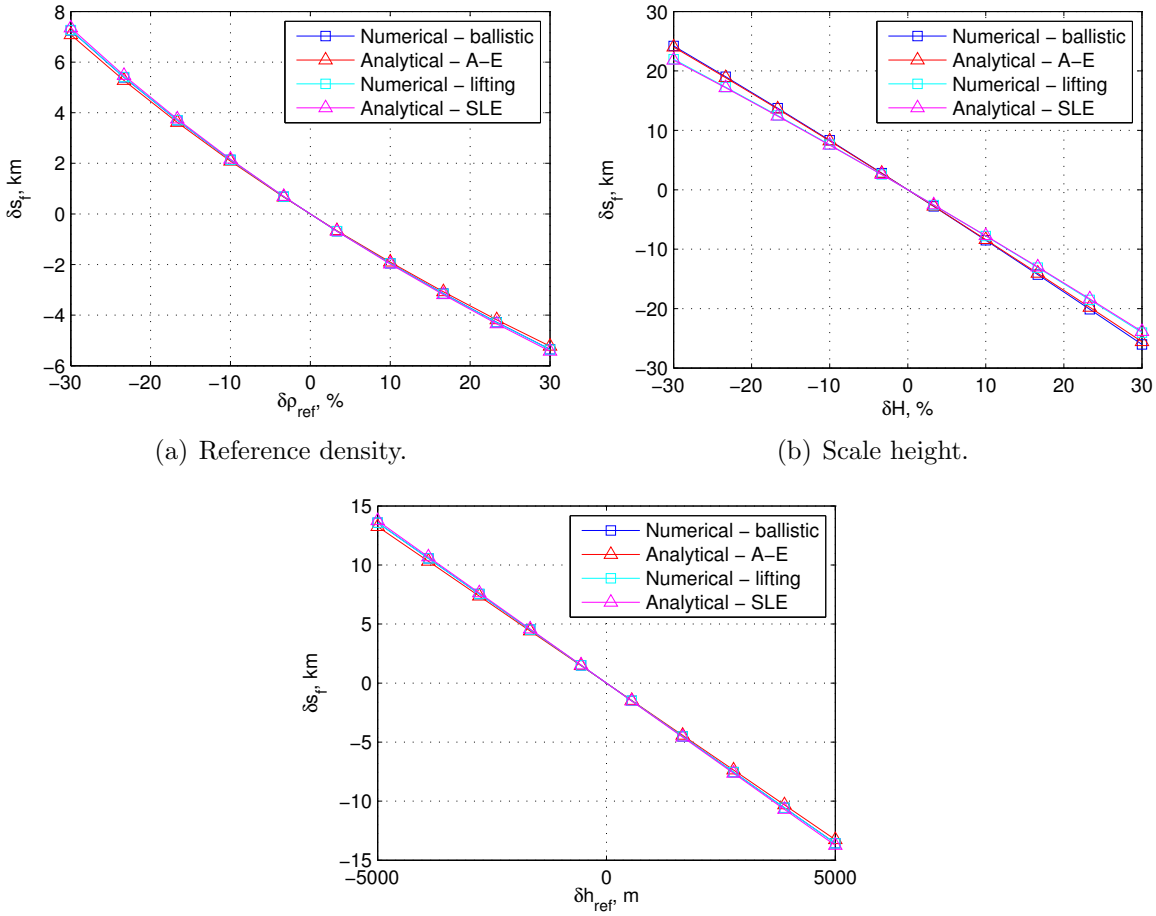

(a) Reference density.

(b) Scale height.

(c) Reference altitude.

Figure 92: Comparison of perturbations in final range relative to atmospheric parameter perturbations for lift and drag-modulation systems.

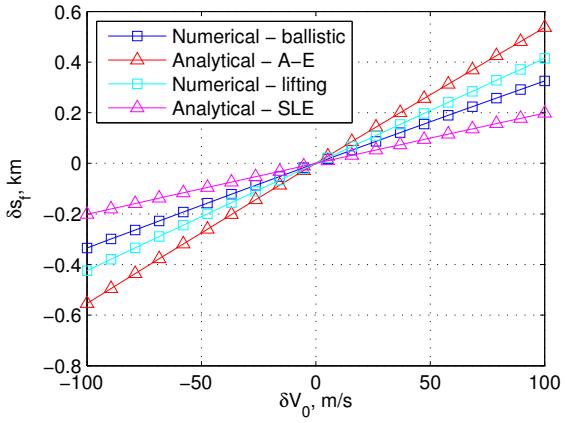

(a) Velocity.

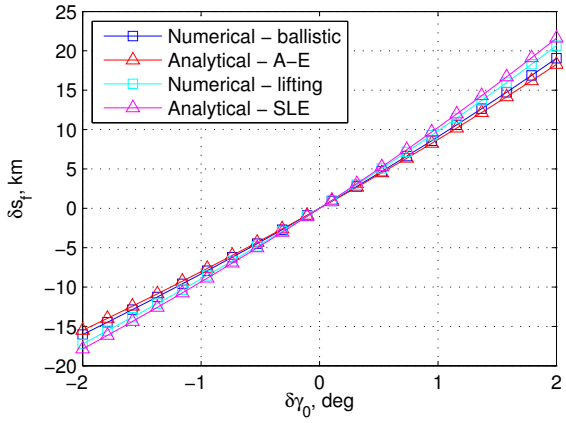

(b) Flight-path angle.

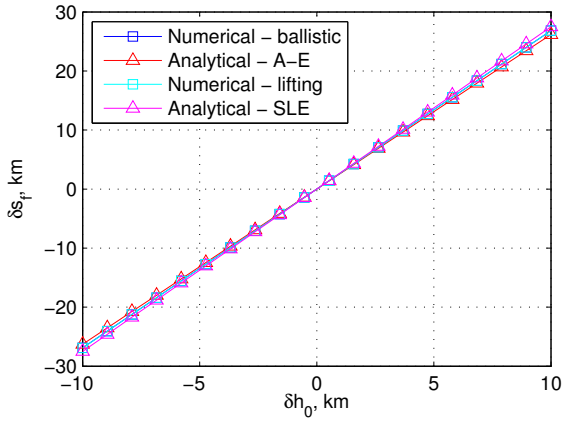

(c) Altitude.

Figure 93: Comparison of perturbations in final range relative to initial state perturbations for lift and drag-modulation systems.

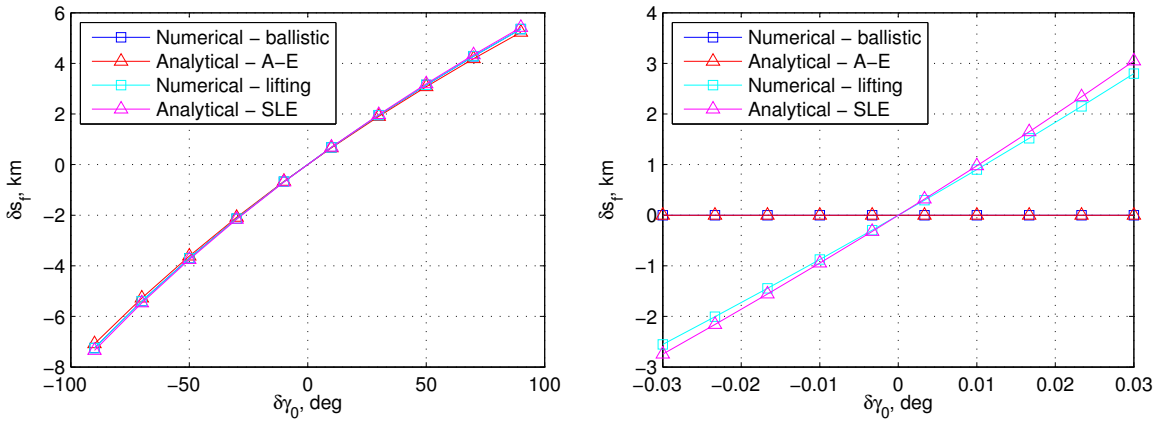

(a) Ballistic coefficient.

(b) Lift-to-drag ratio.

Figure 94: Comparison of perturbations in final range relative to vehicle parameter perturbations for lift and drag-modulation systems.

may generate small amounts of lift due to shape and c.g. position uncertainties, ballistic vehicles are typically spun at a small rate to null out the integrated effects of any lift generated. So, while ballistic vehicles are not sensitive to perturbations in lift, lifting vehicles are still subject to perturbations in β: lifting vehicles still have mass and generate drag.

One can develop a second-order solution to perturbations in final range relative to perturbations in aerodynamic parameters, including interaction effects between β and L/D perturbations. Results are shown for the same ballistic and lifting vehicles in Figure 95. Changes in final range are as expected: greater β and greater L/D produce greater positive changes in final range.

To show the value of a plot such as that shown in Figure 95, an example is shown below for an MSL-class vehicle entering the Mars atmosphere. Trajectory parameters for this example are provided in Table 18. Results are shown in Figure 96. The lifting vehicle has an L/D of 0.144, equivalent to 60% of the maximum L/D of MSL; this roughly corresponds to a nominal lifting trajectory for a guided vehicle. The ballistic coefficient is 145 kg/m^2 for both vehicles, the same as MSL. Just as before, the figure shows that lifting vehicles are less robust to atmospheric perturbations. For

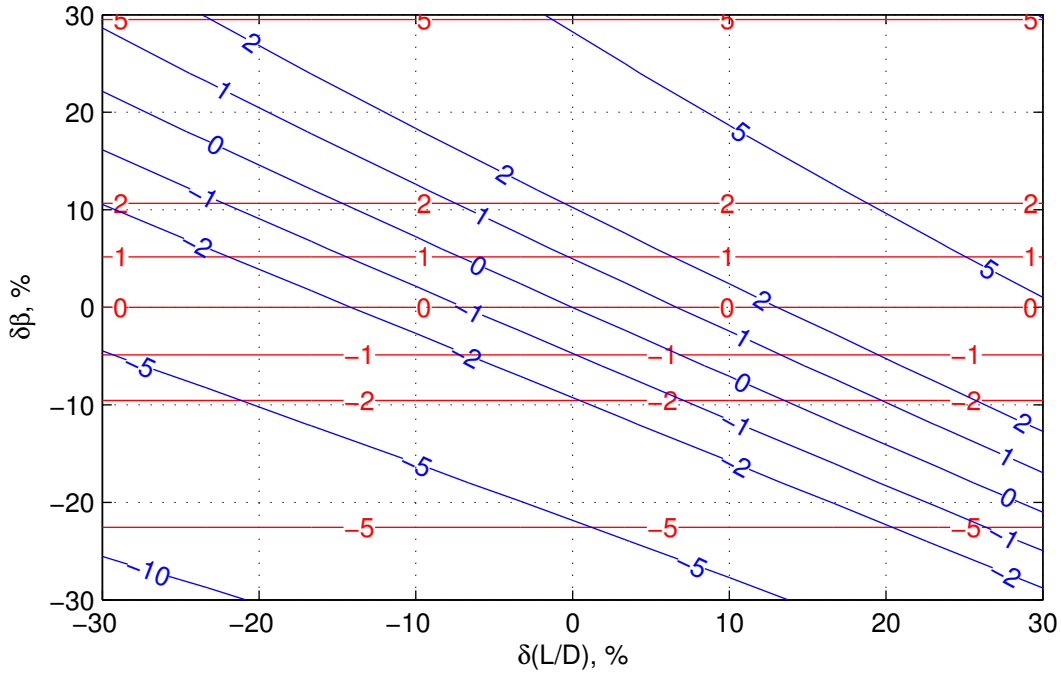

Figure 95: Change in final range in km due to perturbations in β and L/D for ballistic systems (red) and lifting systems (blue, $L/D = 0.1$) at Earth.

example, the black box in Figure 96 shows the approximate preflight uncertainty in MSL's aerodynamics [171]. For the lifting system, the maximum change in final range due to aerodynamic perturbations within this box is roughly ±7 km; for the ballistic system, it is only ±2 km. This extra effect on final range must be flown out by the lifting control system during entry, reducing the control authority available for other trajectory goals, such as maintaining altitude, limiting deceleration, or out-of-plane maneuvers.

Table 18: MSL-Class Vehicle Entry Trajectory Parameters

Parameter	*Value*
Planet	Mars
V_0	5900 m/s
γ_0	-12 deg
h_0	50 km
V_f	1000 m/s
β	145 kg/m^2
R	3389.5 km
g	3.71 m/s^2
ρ_{ref}	0.02 kg/m^3
H	11000 m
h_{ref}	0 m

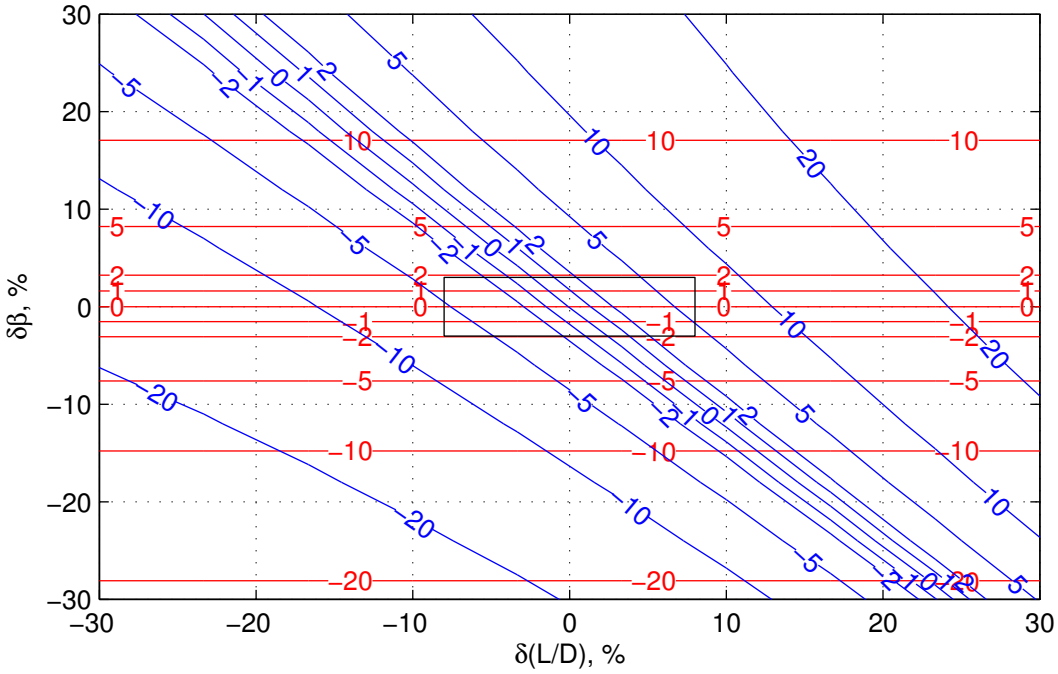

Figure 96: Change in final range in km due to perturbations in β and L/D for ballistic systems (red) and lifting systems (blue, $L/D \approx 0.24$). Black box shows approximate uncertainty in MSL aerodynamics.

6.5 Integrated Results

The results presented in this thesis may be combined to build a set of guidelines for selecting lift or drag-modulation systems early in the design cycle for planetary entry missions. Table 19 shows example compiled results for an MSL-class vehicle landing on Mars. This set of guidelines may help mission and vehicle designers make more intelligent decisions about trajectory control systems. For example, if crossrange is required, a lifting system must be used. However, in the absence of crossrange requirements, a drag-modulation system is preferable if peak deceleration limits are not strict.

Table 19: Lift Versus Drag Modulation for an MSL-Class Vehicle

Metric	*Lift Modulation*	*Drag Modulation*
Landed crossrange	Capable	No capability
Limit peak deceleration	More capable	Less capable
Limit peak heat rate	Less capable	More capable
Landed accuracy	Similar	
Range sensitivity to atmospheric perturbations	Similar	
Range sensitivity to initial state perturbations	Similar	
Range sensitivity to aerodynamic perturbations	Larger (±7 km)	Smaller (±2 km)

6.6 Conclusions

Nonlinear variational methods have been applied to closed-form analytical solutions to the equations of motion to analyze planetary entry systems. This approach allows one to evaluate the robustness of planetary entry systems relative to one another in a quantitative fashion.

While it is possible to compute many of the curves and quantities shown in this chapter numerically, there are distinct advantages to analytical solutions. First, the analytical solutions execute quickly. Second, the analytical solutions represent exact solutions to the equations of motion under certain assumptions; the partial derivatives and other expressions shown in this chapter are also exact, and do not include numerical computation error. Third, analytical expressions for variations in state parameters of interest have direct application to onboard guidance and targeting algorithms. For example, the Apollo Final Phase reference trajectory is pre-generated and includes range, altitude rate, and drag as a function of velocity, in addition to control gains which are simply partial derivatives. Because the trajectory is generated prior to flight, it is only capable of accounting for error in the states carried. However, one could easily carry analytical solutions onboard that could account for

any number of perturbations experienced during flight. This would allow inclusion of correction parameters for L/D or atmospheric density estimated by the navigation system. This type of algorithm would also preserve much of the simplicity that is the hallmark of the Apollo Final Phase algorithm.

CHAPTER VII

CONCLUSIONS AND FUTURE WORK

7.1 Research Contributions

This thesis advances the state of the art in several ares of interest to the aeroassist and design methods community.

The closed-form analytical solution to the equations of motion for ballistic entry developed by Allen and Eggers is enhanced. A method of choosing an appropriate constant flight-path angle was identified, a closed-form expression for range to go was developed, and limits based on the equations of motion and acceptable approximation error were proposed to bound the domain of applicability of the solution. These extensions address key weaknesses in the original solution and a gap in the current literature: existing analytical solutions for ballistic entry in the literature did not provide closed-form expressions for flight range. A comprehensive survey of analytical methods for the solution of planetary entry trajectories was completed to place the extended Allen-Eggers solution in proper context. This survey is especially important as many of the sources that document such solutions in the literature are becoming more difficult to find due to their age.

The extended and enhanced Allen-Eggers solution was utilized to develop closed-form analytical relationships for discrete-event drag modulation systems. Analytical boundaries on jettison conditions were developed to limit peak deceleration and peak heating. The ratio of the maximum to minimum ballistic coefficient was shown analytically to be the control authority metric for drag-modulation systems, analogous to L/D for lift-modulation systems.

The feasibility of drag-modulation trajectory control for planetary entry and aerocapture missions was demonstrated for several missions of interest to the community. Flight performance was shown to be competitive with state-of-the-art lift-modulation systems. Prototype guidance and targeting algorithms for drag-modulation trajectory control were developed and tested to verify that onboard systems could determine and execute the drag profiles necessary to meet mission requirements.

Variational methods were applied to closed-form analytical solutions for planetary entry trajectories to provide quantitative, performance-based measures of robustness to compare lift and drag-modulation systems. This technique results in closed-form solutions for variations of arbitrary order due to perturbations in initial state, environment parameters, and vehicle parameters. Lift and drag-modulation systems are shown to exhibit nearly identical responses to model and state perturbations with the exception of aerodynamic perturbations. Drag-modulation systems are not generally susceptible to lift perturbations, as they may be spun to null out the integrated effects of any lift generated. Lift-modulation systems are still subject to uncertainty in drag as well as lift, decreasing their robustness relative to drag-only systems and requiring them to devote additional control authority to steering out error caused by uncertainty in lift.

7.2 Future Work

The results presented in this thesis point to several areas in which additional contributions to the current literature may be made.

The analytical solutions developed and surveyed have direct application to real-time onboard guidance and targeting algorithms. Specifically,

- Analytical partials may be used to speed the convergence of other algorithms
- Analytical solutions may be used to provide better initial guesses for numerical algorithms

- Analytical relationships may provide useful bounds on solutions
- Fully-analytical algorithms may be developed

For example, the Apollo Final Phase algorithm utilizes a table of trajectory states and partials as a function of velocity to generate bank angle commands during entry. It may be possible to completely replace the table with closed-form analytical relationships for the trajectory states and partials. This would eliminate the need to maintain ground-support software and checkout for reference trajectories for the algorithm.

While there is some discussion of analytical approximate solutions for grazing or skip trajectories in the literature, there are not solutions which are generally appropriate for aerocapture. This is largely because most analytical solutions predate the concept of aerocapture. Existing solutions for entry trajectories point towards possible closed-form aerocapture solutions. Such solutions would have applicability to first-order engineering analysis and real-time guidance and targeting algorithms.

Closed-form solutions to the equations of motion may also have application to a wide range of engineering problems of interest beyond real-time algorithms, including closed-form first-order uncertainty analysis using covariance methods and rapid trajectory optimization.

This thesis has shown that drag-modulation trajectory-control systems are feasible from a guidance, navigation, and control standpoint. However, significant efforts are required to mature the concept before an aerocapture or entry flight test. First, higher-fidelity, six-degree-of-freedom numerical simulations should be conducted to determine stability characteristics of drag-modulation vehicles. These simulations may also be used, in conjunction with computational fluid dynamics, to assess hypersonic separation dynamics for discrete-event systems. Computational fluid dynamics, in conjunction with shock-tube and wind-tunnel tests, may be used to assess aerodynamic properties of the vehicle over changes in drag area. System-level studies

are also needed to provide more detailed data for comparison among potential drag-modulation mechanisms, including mass, power, and volume requirements. The scalability of drag-modulation trajectory-control systems to higher-mass vehicles should be evaluated; this is especially important to determine the feasibility of utilizing drag modulation in support of future human missions to Mars. Lastly, hybrid lift and drag-modulation systems should be explored.

REFERENCES

[1] Loh, W. T., *Dynamics and Thermodynamics of Planetary Entry*, Prentice-Hall International Series in Space Technology, Prentice-Hall, Englewood Cliffs, NJ, 1963.

[2] Becker, J. V., "Re-entry from Space," *Scientific American*, Vol. 204, No. 1, Jan. 1961, pp. 49–57.

[3] Hall, J. L., Noca, M. A., and Bailey, R. W., "Cost-Benefit Analysis of the Aerocapture Mission Set," *Journal of Spacecraft and Rockets*, Vol. 42, No. 2, March 2005, pp. 309–320.

[4] "The Corona Story," Tech. Rep. BYE 140001-88, Dec. 1988.

[5] Larson, W. J. and Pranke, L. K., editors, *Human Spaceflight: Mission Analysis and Design*, Space Technology Series, McGraw-Hill, New York, NY, 1999.

[6] Prakash, R., Burkhard, P. D., Chen, A., Comeaux, K. A., Guernsey, C. S., Kipp, D. M., Lorenzoni, L. V., Mendeck, G. F., Powell, R. W., Rivellini, T. P., Sansom, R., Sell, S. W., Steltzner, A. D., and Way, D. W., "Mars Science Laboratory Entry, Descent, and Landing System Overview," *2008 IEEE Aerospace Conference*, Big Sky, MT, March 2008, pp. 1–18.

[7] Broome, J. and Johnson, W., "Orion Entry, Descent and Landing Performance and Mission Design," *AIAA Guidance, Navigation, and Control Conference and Exhibit*, NASA Johnson Space Center, American Institute of Aeronautics and Astronautics, Hilton Head, SC, Aug. 2007.

[8] Vozoff, M. and Couluris, J., "SpaceX Products-Advancing the Use of Space," *AIAA Space 2008 Conference & Exposition*, American Institute of Aeronautics and Astronautics, San Diego, CA, Sept. 2008.

[9] Gamble, J. D., Cerimele, C. J., Moore, T. E., and Higgins, J., "Atmospheric Guidance Concepts for an Aeroassist Flight Experiment," *Journal of the Astronautical Sciences*, Vol. 36, No. 1/2, Jan. 1988, pp. 45–71.

[10] Hall, J. L., "An Overview of the ST-7 Aerocapture Flight Test Experiment," *AIAA Atmospheric Flight Mechanics Conference and Exhibit*, Monterey, CA, Aug. 2002.

[11] Morth, R., "Reentry Guidance for Apollo," Tech. Rep. R-532, MIT Instrumentation Laboratory, Jan. 1966.

[12] Walberg, G. D., "A Survey of Aeroassisted Orbit Transfer," *Journal of Spacecraft and Rockets*, Vol. 22, No. 1, Jan. 1985, pp. 3–18.

[13] Heppenheimer, T. A., *Development of the Space Shuttle*, Smithsonian Institution, Washington, DC, May 2002.

[14] Braun, R. D. and Manning, R. M., "Mars Exploration Entry, Descent, and Landing Challenges," *Journal of Spacecraft and Rockets*, Vol. 44, No. 2, March 2007, pp. 310–323.

[15] Adler, M., "Draft Entry, Descent, and Landing Roadmap," Tech. rep., NASA, Washington, DC, Nov. 2010.

[16] Hughes, S. J., Dillman, R. A., Starr, B. R., Stephan, R. A., Lindell, M. C., Player, C. J., and Cheatwood, F. M., "Inflatable Reentry Vehicle Experiment (IRVE) Design Overview," *18th AIAA Aerodynamic Decelerator Systems Technology Conference*, NASA Langley Research Center, Munich, Germany, May 2005.

[17] Venkatapathy, E., Arnold, J., Fernandez, I., Hamm, K. R., Kinney, D., Laub, B., Makino, A., McGuire, M. K., Peterson, K., Prabhu, D., Empey, D., Dupzyk, I., Huynh, L., Hajela, P., Gage, P., Howard, A. R., and Andrews, D., "Adaptive Deployable Entry and Placement Technology (ADEPT): A Feasibility Study for Human Missions to Mars," *21st AIAA Aerodynamic Decelerator Systems Technology Conference and Seminar*, American Institute of Aeronautics and Astronautics, Reston, Virigina, Nov. 2012.

[18] Miller, K. L., Gulick, D., Lewis, J., Trochman, B., Stein, J., Lyons, D. T., and Wilmoth, R. G., "Trailing Ballute Aerocapture: Concept and Feasibility Assessment," *39th AIAA/ASME/SAE/ASEE Joint Propulsion Conference and Exhibit*, Huntsville, AL, July 2003.

[19] Rohrschneider, R. R. and Braun, R. D., "Survey of Ballute Technology for Aerocapture," *Journal of Spacecraft and Rockets*, Vol. 44, No. 1, Jan. 2007, pp. 10–23.

[20] Cassell, A., Swanson, G., Johnson, R., Hughes, S., and Cheatwood, F., "Overview of Hypersonic Inflatable Aerodynamic Decelerator Large Article Ground Test Campaign," *21st AIAA Aerodynamic Decelerator Systems Technology Conference and Seminar*, American Institute of Aeronautics and Astronautics, Reston, Virigina, Nov. 2012.

[21] Olds, A., Beck, R., Bose, D. M., White, J., Edquist, K. T., Hollis, B. R., Lindell, M., Cheatwood, F. M., Gsell, V., and Bowden, E. L., "IRVE-3 Post-Flight Reconstruction," *AIAA Aerodynamic Decelerator Systems (ADS) Conference*, American Institute of Aeronautics and Astronautics, Reston, Virginia, March 2013.

[22] Cianciolo, A. M. D., Davis, J. L., Komar, D. R., Munk, M. M., Samareh, J. A., Powell, R. W., Shidner, J. D., Stanley, D. O., Wilhite, A. W., Kinney, D., McGuire, M. K., Arnold, J. O., Howard, A. R., Sostaric, R. R., Studak, J., Zumwalt, C. H., Llama, E. G., Casoliva, J., Ivanov, M. C., Clark, I. G., and Sengupta, A., "Entry, Descent and Landing Systems Analysis Study," Tech. Rep. NASA TM-2010-216720, July 2010.

[23] Cianciolo, A. M. D., Davis, J. L., Engelund, W. C., Komar, D. R., Queen, E. M., Samareh, J. A., Way, D. W., Zang, T. A., Murch, J. G., Krizan, S. A., Olds, A. D., Powell, R. W., Shidner, J. D., Kinney, D., McGuire, M. K., Arnold, J. O., Covington, M. A., Sostaric, R. R., Zumwalt, C. H., and Llama, E. G., "Entry, Descent and Landing Systems Analysis Study," Tech. Rep. NASA TM-2011-217055, Feb. 2011.

[24] Rohrschneider, R. R., Masciarelli, J. P., and Miller, K. L., "A Comparison of Inflatable and Semi-rigid Deployable Aerodynamic Decelerators for Future Aeroacapture and Entry Missions," *8th International Planetary Probe Workshop*, Hampton, VA, July 2011.

[25] Dutta, S., Smith, B., Prabhu, D., and Venkatapathy, E., "Mission Sizing and Trade Studies for Low Ballistic Coefficient Entry Systems to Venus," *2012 IEEE Aerospace Conference*, Big Sky, MT, March 2012.

[26] Clark, I. G. and Braun, R. D., "Ballute Entry Systems for Lunar Return and Low-Earth-Orbit Return Missions," *Journal of Spacecraft and Rockets*, Vol. 45, No. 3, May 2008, pp. 619–630.

[27] Meginnis, I. M., Putnam, Z. R., Clark, I. G., Braun, R. D., and Barton, G. H., "Guided Entry Performance of Low Ballistic Coefficient Vehicles at Mars," *Journal of Spacecraft and Rockets*, Vol. 50, No. 5, Sept. 2013, pp. 1047–1059.

[28] Bose, D. M., Shidner, J., Winski, R., Zumwalt, C., Cheatwood, F. M., and Hughes, S. J., "The Hypersonic Inflatable Aerodynamic Decelerator (HIAD) Mission Applications Study," *AIAA Aerodynamic Decelerator Systems (ADS) Conference*, American Institute of Aeronautics and Astronautics, Reston, Virginia, March 2013.

[29] D.H. Platus, "Ballistic Re-entry Vehicle Flight Dynamics," *Journal of Guidance, Control, and Dynamics*, Vol. 5, No. 1, Jan. 1982, pp. 4–16.

[30] Vinh, N. X., Busemann, A., and Culp, R. D., *Hypersonic and Planetary Entry Flight Mechanics*, University of Michigan Press, Ann Arbor, MI, 1980.

[31] Lees, L., Hartwig, F. W., and Cohen, C. B., "Use of Aerodynamic Lift During Entry Into the Earth's Atmosphere," *ARS Journal*, Vol. 29, No. 9, Sept. 1959.

[32] Regan, F. J. and Anandakrishnan, S. M., *Dynamics of Atmospheric Re-Entry*, AIAA Education Series, American Institute of Aeronautics and Astronautics, Reston, VA, 1993.

[33] Anderson, J. D., *Hypersonic and High Temperature Gas Dynamics*, American Institute of Aeronautics and Astronautics, Reston, VA, 2000.

[34] Sepahban, S. and Williams, R., "The Soyuz Assured Crew Return Vehicle operations concept," *Space Programs and Technologies Conference and Exhibit*, American Institute of Aeronautics and Astronautics, Reston, Virigina, Sept. 1993.

[35] Mendeck, G. F. and Craig, L. E., "Entry Guidance for the 2011 Mars Science Laboratory Mission," *AIAA Atmospheric Flight Mechanics Conference and Exhibit*, Portland, Oregon, Aug. 2011, pp. 1–22.

[36] Bairstow, S. H. and Barton, G. H., "Orion Reentry Guidance with Extended Range Capability Using PredGuid," *AIAA Guidance, Navigation, and Control Conference*, Hilton Head, South Carolina, Aug. 2007, pp. 1–17.

[37] Harpold, J. C. and Graves, C. A., "Shuttle Entry Guidance," Tech. Rep. NASA-TM-79949, NASA, Houston, Texas, Feb. 1979.

[38] Powell, R. W., "Six-Degree-of-Freedom Guidance and Control-Entry Analysis of the HL-20," *Journal of Spacecraft and Rockets*, Vol. 30, No. 5, Sept. 1993, pp. 537–542.

[39] Howard, R. D., Krevor, Z. C., Mosher, T., Scott, K. P., Voss, J. S., Sanchez, M. J., and Curry, J. M., "Dream Chaser Commercial Crewed Spacecraft Overview," *17th AIAA International Space Planes and Hypersonic Systems and Technologies Conference*, April 2011.

[40] Putnam, Z. R., Neave, M. D., and Barton, G. H., "PredGuid entry guidance for Orion return from low Earth orbit," *Aerospace Conference, 2010 IEEE*, Big Sky, MT, 2010.

[41] Putnam, Z. R., Braun, R. D., Rohrschneider, R. R., and Dec, J. A., "Entry System Options for Human Return from the Moon and Mars," *Journal of Spacecraft and Rockets*, Vol. 44, No. 1, Jan. 2007, pp. 194–202.

[42] Levy, L. L., "The Use of Drag Modulation to Limit the Rate at Which Deceleration Increases During Nonlifting Entry," Tech. Rep. NASA TN D-1037, Ames Research Center, Washington, DC, Sept. 1961.

[43] Rose, P. H. and Hayes, J. E., "Drag Modulation and Celestial Mechanics," *7th Annual Meeting of the American Astronautical Society*, Dallas, TX, Jan. 1961.

[44] Warden, R. V., "Ballistic Re-Entries With a Varying W/CD A," *ARS Journal*, Vol. 31, No. 2, Feb. 1961, pp. 208–213.

[45] Vinh, N. X., Johannesen, J. R., Mease, K. D., and Hanson, J. M., "Explicit guidance of drag-modulated aeroassisted transfer between elliptical orbits," *Journal of Guidance, Control, and Dynamics*, Vol. 9, No. 3, May 1986, pp. 274–280.

[46] Kuo, Z.-S., Liu, K.-C., and Chang, Y.-S., "Explicit Guidance of Ballistic Entry Using Improved Matched Asymptotic Expansions," *Transactions of the Japan Society for Aeronautical and Space Sciences*, Vol. 50, No. 168, Jan. 2007, pp. 121–127.

[47] McRonald, A. D., "A Lightweight Inflatable Hypersonic Drag Device for Planetary Entry," *Association Aeronautique de France Conference*, Arcachon, France, March 1999.

[48] McRonald, A. D., "A Light-weight Inflatable Hypersonic Drag Device for Venus Entry," *AAS/AIAA Astrodynamics Specialist Conference*, Girdwood, AK, Aug. 1999, pp. 1–12.

[49] McRonald, A. D., "A Light-weight Hypersonic Inflatable Drag Device for a Neptune Orbiter," *AAS/AIAA Space Flight Mechanics Meeting*, Clearwater, FL, Jan. 2000.

[50] Hall, J. L. and Le, A. K., "Aerocapture Trajectories for Spacecraft with Large Towed Ballutes," *AAS/AIAA Space Flight Mechanics Meeting*, Santa Barbara, CA, Feb. 2001.

[51] Westhelle, C. H. and Masciarelli, J. P., "Assessment of Aerocapture Flight at Titan Using a Drag-only Device," *AIAA Atmospheric Flight Mechanics Conference and Exhibit*, Austin, TX, Aug. 2003, pp. 1–7.

[52] Johnson, W. R. and Lyons, D. T., "Titan Ballute Aerocapture Using a Perturbed TitanGRAM Model," *AIAA Atmospheric Flight Mechanics Conference and Exhibit*, Providence, RI, Aug. 2004.

[53] Chapman, D. R., "An Analysis of the Corridor and Guidance Requirements for Supercircular Entry into Planetary Atmospheres," Tech. Rep. NASA TR R-55, NASA, Nov. 2013.

[54] Sänger, E. and Bredt, J., "A Rocket Drive for Long Range Bombers," Tech. Rep. CGD-32, Aug. 1944.

[55] Eggers, A. J., Allen, H. J., and Neice, S. E., "A Comparative Analysis of the Performance of Long-Range Hypervelocity Vehicles," Tech. Rep. R-1382, Ames Aeronautical Laboratory, Washington, DC, 1958.

[56] Allen, H. J. and Eggers, A. J., "A Study of the Motion and Aerodynamic Heating of Ballistic Missiles Entering the Earth's Atmosphere at High Supersonic Speeds," Tech. Rep. NACA-TR-1381, Ames Aeronautical Laboratory, Washington, DC, 1958.

[57] Wang, K. and Ting, L., "An Approximate Analytic Solution of Re-Entry Trajectory with Aerodynamic Forces," *ARS Journal*, Vol. 30, No. 6, June 1960.

[58] Loh, W. T., "Dynamics and Thermodynamics of Re-Entry," *Journal of Aerospace Sciences*, Vol. 27, No. 10, 1960, pp. 748–762.

[59] Arthur, P. D. and Karrenberg, H. K., "Atmospheric Entry With Small L/D," *Journal of the Aerospace Sciences*, Vol. 28, No. 4, April 1961, pp. 351–352.

[60] Kornreich, T. R., "Approximate Solutions for the Range of a Nonlifting Re-Entry Trajectory," *AIAA Journal*, Vol. 1, No. 8, Aug. 1963, pp. 1925–1926.

[61] Loh, W. T., "A Second-Order Theory of Entry Mechanics Into a Planetary Atmosphere," *Journal of Aerospace Sciences*, Vol. 29, No. 10, 1962, pp. 1210–1221.

[62] Loh, W. T., "Extension of second-order theory of entry mechanics to oscillatory entry solutions," *AIAA Journal*, Vol. 3, No. 9, Sept. 1965, pp. 1688–1691.

[63] Loh, W. T., "Extension of the second-order theory of entry mechanics to nearly exact solutions." *AIAA Journal*, Vol. 5, No. 10, Oct. 1967, pp. 1823–1827.

[64] Citron, S. J. and Meir, T. C., "An analytic solution for entry into planetary atmospheres," *AIAA Journal*, Vol. 3, No. 3, March 1965, pp. 470–475.

[65] Chapman, D. R., "An Approximate Analytical Method for Studying Entry Into Planetary Atmospheres," Tech. Rep. R-11, Ames Research Center, 1959.

[66] Longuski, J. M. and Vinh, N. X., "Analytic Theory of Orbit Contraction and Ballistic Entry Into Planetary Atmospheres," Tech. Rep. JPL Publication 80-58, NASA CR-163627, Sept. 1980.

[67] Vinh, N. X., Coppola, V. T., and de Olive Ferreira, L., "Phugoid motion for grazing-entry trajectories at near-circular speeds," *Journal of Spacecraft and Rockets*, Vol. 33, No. 2, March 1996, pp. 206–213.

[68] de Olivé Ferreira, L., , Vinh, N. X., and Greenwood, D. T., "Critical Cases of Ballistic Entry: New, Guidance-Oriented, Higher-Order Analytic Solutions," *Journal of Spacecraft and Rockets*, Vol. 37, No. 5, Sept. 2000, pp. 630–637.

[69] Brauer, G. L., Cormick, D. E., and Stevenson, R., "Capabilities and Applications of the Program to Optimize Simulated Trajectories (POST)," Tech. Rep. NASA CR-2770, Feb. 1977.

[70] Cameron, J., Balaram, J., Jain, A., Kuo, C., Lim, C., and Myint, S., "Next Generation Simulation Framework for Robotic and Human Space Missions," *AIAA SPACE 2012 Conference & Exposition*, American Institute of Aeronautics and Astronautics, Reston, Virigina, Sept. 2012.

[71] Hoelscher, B., "Orion Entry, Descent and Landing Simulation," *AIAA Guidance, Navigation, and Control Conference and Exhibit*, American Institute of Aeronautics and Astronautics, Reston, Virigina, Aug. 2007.

[72] Miele, A., *Flight Mechanics*, Vol. 1, Addison-Wesley, Reading, MA, 1962.

[73] Martin, J. J., *Atmospheric Reentry*, Prentice-Hall, Englewood Cliffs, NJ, 1966.

[74] Loh, W. T., editor, *Re-entry and Planetary Entry Physics and Technology*, Vol. 1, Springer-Verlag, New York, NY, 1968.

[75] Gallais, P., *Atmospheric Re-Entry Vehicle Mechanics*, Springer, Berlin, 2007.

[76] Launius, R. D. and Jenkins, D. R., *Coming Home: Reentry and Recovery from Space*, NASA, Washington, DC, 2011.

[77] Wang, K. N., "Comment on "A Second-Order Theory of Entry Mechanics into a Planetary Atmosphere"," *AIAA Journal*, Vol. 1, No. 4, April 1963, pp. 0977b–0977b.

[78] Loh, W. T., "Author's Reply to Comment by Kenneth Wang," *AIAA Journal*, Vol. 1, No. 4, April 1963, pp. 0978a–0978a.

[79] Allen, H. J. and Eggers, A. J., "A Study of the Motion and Aerodynamic Heating of Missiles Entering the Earth's Atmosphere at High Supersonic Speeds," Tech. Rep. NACA RM A53D28, Washington, DC, Aug. 1953.

[80] Norman, W. S., "Improvements to the Allen and Eggers Solution for Ballistic Re-Entry," *Air Force Science and Engineering Symposium*, edited by J. Seiden and J. O. Hamlet, Colorado Springs, CO, Oct. 1963, pp. M–1 to M–48.

[81] "H. Julian Allen with Blunt Body Theory," NASA Ames Research Center, Dec. 1957.

[82] Gazley, C., "Deceleration and Heating of a Body Entering a Planetary Atmosphere from Space," Tech. Rep. P-955, Feb. 1957.

[83] Gazley, C., "The Penetration of Planetary Atmospheres," *Journal of Heat Transfer*, Vol. 81, No. Series C, Nov. 1959, pp. 315–322.

[84] Gazley, C., "Atmospheric Entry," Tech. Rep. P-2052, RAND Corp., Santa Monica, CA, July 1960.

[85] Miller, B. P., "Approximate Velocity, Position and Time Relationship for Ballistic Re-Entry," *ARS Journal*, Vol. 31, No. 3, March 1961, pp. 437–438.

[86] Moe, M. M., "An Approximation to the Re-Entry Trajectory," *ARS Journal*, Vol. 30, No. 1, Jan. 1960, pp. 50–53.

[87] Munk, M. M., "Mathematical Analysis of the Vertical Dive," *Aero Digest*, Vol. 44, Feb. 1944, pp. 114–213.

[88] Turnacliff, R. D. and Hartnett, J. P., "Generalized Trajectories for Free-Falling Bodies of High Drag," *Jet Propulsion*, Vol. 28, No. 4, April 1958, pp. 263–266.

[89] Squire, W., "Some Comments on Generalized Trajectories for Free Falling Bodies of High Drag," *Jet Propulsion*, Vol. 28, No. 12, Dec. 1958, pp. 838–839.

[90] Blum, R., "Re-Entry Trajectories: Flat Earth Approximation," *ARS Journal*, Vol. 32, No. 4, April 1962, pp. 616–620.

[91] Kumagai, T. T., "Approximation of time of ballistic entry," *Journal of Spacecraft and Rockets*, Vol. 1, No. 6, Nov. 1964, pp. 675–676.

[92] Adler, A. A., "Calculation of Re-Entry Velocity Profile," *Jet Propulsion*, Vol. 28, No. 12, Dec. 1958, pp. 827–828.

[93] Randall, D. E., "Influence of staging on re-entry trajectory characteristics," *Journal of Spacecraft and Rockets*, Vol. 7, No. 3, March 1970, pp. 370–372.

[94] Putnam, Z. R. and Braun, R. D., "Extension and Enhancement of the Allen-Eggers Solution for Ballistic Entry Trajectories," *Journal of Guidance, Control, and Dynamics*, Jan. 2015.

[95] Loh, W. H. T., "A Higher Order Theory of Ballistic Entry," *American Astronautical Society Eighth Annual Meeting*, American Astronautical Society 8th Annual Meeting, Washington, DC, Jan. 1962, pp. 529–540.

[96] Loh, W. H. T., "Ballistic Re-Entry at Small Angles of Inclination," *ARS Journal*, Vol. 32, No. 5, 1962, pp. 718–721.

[97] Robinson, A. and Besonie, A., "On the Problems of Re-Entry into the Earth's Atmosphere," *Journal of the Astronautical Sciences*, Vol. 7, No. 1, April 1960, pp. 7–21.

[98] Cohen, M. J., "Some closed form solutions to the problem of re-entry of lifting andnon-lifting vehicles," *2nd Aerospace Sciences Meeting*, Northhampton College of Advanced Technology, American Institute of Aeronautics and Astronautics, New York, NY, Jan. 1965.

[99] Barbera, F. J., "Closed-Form Solution for Ballistic Vehicle Motion," *Journal of Spacecraft and Rockets*, Vol. 18, No. 1, Jan. 1981, pp. 52–57.

[100] Ambrosio, A., "A General Atmospheric Entry Function and Its Characteristics," *ARS Jounral*, Vol. 32, No. 6, June 1962, pp. 906–910.

[101] Eggers, A. J., Allen, H. J., and Neice, S. E., "A Comparative Analysis of the Performance of Long-Range Hypervelocity Vehicles," Tech. Rep. NACA RM A54L10, NACA - Ames Aeronautical Laboratory, Washington, DC, March 1955.

[102] Eggers, A. J., Allen, H. J., and Neice, S. E., "A Comparative Analysis of the Performance of Hypervelocity Vehicles," Tech. Rep. Technical Note 4046, Washington, DC, Oct. 1957.

[103] Lees, L., Hartwig, F. W., and Cohen, C. B., "The Use of Aerodynamic Lift During Entry Into the Earth's Atmosphere," Tech. Rep. GM-TR-0165-00519, Nov. 1958.

[104] Braun, R. D. and tauber, M. E., "Planetary Entry," *Georgia Tech*, Atlanta, GA, 2005.

[105] Nyland, F. S., "Hypersonic Turning With Constant Bank Angle Control," Tech. Rep. RM-4483-PR, RAND Corp., March 1965.

[106] Wang, H. E., "Approximate Solutions of the Lateral Motion of Re-Entry Vehicles During Constant Altitude Glide," Tech. Rep. TDR 169 (3560-10) TN-1, Aerospace Corp., El Segundo, CA, Feb. 1963.

[107] Wang, H. E., "Motion of re-entry vehicles during constant-altitude glide," *AIAA Journal*, Vol. 3, No. 7, July 1965, pp. 1346–1348.

[108] Arthur, P. D. and Baxter, B. E., "Approximate Atmospheric Entry Trajectories on a Cylindrical Planet," *AIAA Journal*, Vol. 4, No. 8, Aug. 1966, pp. 1436–1437.

[109] Loh, W. T., "Some Exact Analytical Solutions of Planetary Entry," *AIAA Journal*, Vol. 1, No. 4, April 1963, pp. 836–842.

[110] Tikhonravov, M. K., Iatsunskii, I. M., Maksimov, G. I., Bazhinov, I. K., and Gurko, O. V., *Principles of the Theory of Flight and Elements of Projections of Artificial Earth Satellites*, Mashinostroenie, Moscow, 1967.

[111] Wang, H. E. and Chu, S. T., "Variable-Lift Re-Entry at Superorbital and Orbital Speeds," *AIAA Journal*, Vol. 1, No. 5, May 1963, pp. 1047–1055.

[112] Nachtsheim, P. R. and Lehman, L., "Unified Treatment of Lifting Atmospheric Entry," *Journal of Spacecraft and Rockets*, Vol. 17, No. 2, March 1980, pp. 119–122.

[113] Cody, W. J. and Thacher, H. C., "Rational Chebyshev Approximations for the Exponential Integral $E_1(x)$," *Mathematics of Computation*, Vol. 22, No. 103, July 1968, pp. 641–649.

[114] Eggers, A. J. and Wong, T. J., "Motion and Heating of Lifting Vehicles During Atmosphere Entry," *ARS Journal*, Vol. 31, No. 10, Oct. 1961, pp. 1364–1375.

[115] Chapman, D. R. and Kapphahn, A. K., "Tables of Z Functions for Atmosphere Entry Analyses," Tech. Rep. NASA TR R-106, Washington, DC, 1961.

[116] Nonweiler, T., "The Motion of an Earth Satellite on Re-entry to the Atmosphere," *Astronautica Acta*, Vol. 5, No. 1, 1959, pp. 40–62.

[117] Levy, L. L., "An Approximate Analytical Method for Studying Atmosphere Entry of Vehicles With Modulated Aerodynamic Forces," Tech. Rep. TN D-319, Ames Research Center, Washington, DC, Oct. 1960.

[118] Boltz, F. W., "Z-Function Solutions for the Motion and Heating During Atmosphere Entry from Equatorial Orbits of a Rotating Planet," Tech. Rep. TN D-1555, Ames Research Center, Washington, DC, Feb. 1963.

[119] Busemann, A., Vinh, N. X., and Culp, R. D., "Optimum Three-Dimensional Atmospheric Entry from the Analytical Solution of Chapman's Exact Equations," Tech. Rep. CR-132571, 1974.

[120] Busemann, A., Vinh, N. X., and Culp, R. D., "Hypersonic Flight Mechanics," Tech. Rep. NASA CR-149170, Washington, DC, Sept. 1976.

[121] Vinh, N. X., Kim, E.-K., and Greenwood, D. T., "Second-order Analytic Solutions for Re-entry Trajectories," *AIAA Guidance, Navigation, and Control Conference*, University of Michigan, Monterrey, CA, Aug. 1993.

[122] Vinh, N. X., Ferreira, L. d.-O., Kim, E.-K., and Greenwood, D. T., "Higher-order Analytic Solutions for Critical Cases of Ballistic Entry," *AIAA Atmospheric Flight Mechanics Conference*, San Diego, CA, July 1996.

[123] Gates, K. L., Ayoubi, M. A., Longuski, J. M., and Lyons, D. T., "Analytic Solutions for Aerocapture, Descent, and Landing Trajectories for Dual-Use Ballute Systems," *AIAA/AAS Astrodynamics Specialist Conference and Exhibit*, Keystone, CO, Aug. 2006, pp. 1–25.

[124] Longuski, J. M. and Saikia, S. J., "Analytical Theory for Ballistic Entry at Circular Speed for Various Flight Path Angles," 2013.

[125] Yaroshevskiy, V. A., "Approximate Calculation of Trajectory for Entry Into Atmosphere I," *Kosmicheskiye Issledovaniya (Cosmic Research)*, Vol. 2, No. 4, 1964.

[126] Yaroshevskiy, V. A., "Approximate Calculation of Trajectory for Entry Into Atmosphere II," *Kosmicheskiye Issledovaniya (Cosmic Research)*, Vol. 2, No. 5, 1964.

[127] Ikawa, H., "A Methodology for Aerodecelerating Entry Trajectory Analysis," *AIAA Atmospheric Flight Mechanics Conference*, Rockwell International, Gatlinburg, TN, Aug. 1983.

[128] Saikia, Sarag J., L. J. M. and Rhoads, J. F., "Solution of Yaroshevksii's Planetary Entry Equation Via a Perturbative Method," 2013.

[129] WIlles, R. E., Francisco, M. C., Reid, J. G., and Lim, W. K., "An application of matched asymptotic expansions to hypervelocity flight mechanics," *AIAA Guidance, Control, and Flight Dynamics Conference*, American Institute of Aeronautics and Astronautics, Huntsville, AL, Aug. 1967.

[130] Shi, Y.-Y. and Pottsepp, L., "Asymptotic expansion of a hypervelocity atmospheric entry problem." *AIAA Journal*, Vol. 7, No. 2, Feb. 1969, pp. 353–355.

[131] Eckstein, M. C., Pottsepp, L., and Shi, Y.-Y., "A Matched Asymptotic Solution for Skipping Entry Into Planetary Atmosphere," *AIAA Journal*, Vol. 9, No. 4, April 1971, pp. 736–738.

[132] Shi, Y.-Y., "Matched Asymptotic Solutions for Optimum Lift Controlled Atmospheric Entry," *AIAA Journal*, Vol. 9, No. 11, Nov. 1971, pp. 2229–2238.

[133] Hough, M., "Ballistic Entry Motion Using a Generic Inviscid Drag Model," *AIAA/AAS Astrodynamics Conference*, American Institute of Aeronautics and Astronautics, San Diego, CA, Aug. 1982.

[134] Hough, M. E., "Ballistic Entry Motion, Including Gravity - Constant Drag Coefficient Case," *Journal of Guidance, Control, and Dynamics*, Vol. 5, No. 6, Nov. 1982, pp. 553–557.

[135] Ceruzzi, P. E., *Beyond the Limits: Flight Enters the Computer Age*, MIT Press, Cambridge, MA, 1989.

[136] Ceruzzi, P. E., *A History of Modern Computing*, MIT Press, Cambridge, MA, 2nd ed., 2003.

[137] Friedrich, H. R. and Dore, F. J., "The Dynamic Motion of A Missile Descending Through the Atmosphere," *Journal of the Aeronautical Sciences*, Vol. 22, No. 9, Sept. 1955, pp. 628–632.

[138] Grant, F. C., "Importance of the Variation of Drag With Lift in Minimization of Satellite Entry Acceleration," Tech. Rep. TN D-120, Langley Research Center, Washington, DC, Oct. 1959.

[139] Lichtenstein, J. H., "Analytical Investigation of the Dynamic Behavior of a Nonlifting Manned Reentry Vehicle," Tech. Rep. TN D-416, Washington, DC, Sept. 1960.

[140] Cheatham, D. C., Young, J. W., and Eggleston, J. M., "The Variation and Control of Range Traveled in the Atmosphere by a High-Drag Variable-Lift Entry Vehicle," Tech. Rep. NASA TN D-230, Washington, DC, March 1960.

[141] Duncan, R. C., *Dynamics of Atmospheric Entry*, McGraw-Hill Series in Missile and Space Technology, McGraw-Hill, New York, 1962.

[142] Loh, W. H. T., "Numerical and Approximate Solutions of Re-Entry at Large Angles of Inclination," *Journal of the Aerospace Sciences*, Vol. 28, Dec. 1961, pp. 982–983.

[143] Loh, W. H. T., "On Exact Numerical and Approximate Analytical Solution for Ballistic Re-Entry at Nearly-Zero-Degree Angle of Inclination," *Journal of the Aerospace Sciences*, Vol. 29, No. 4, 1962, pp. 495–496.

[144] Wahbah, M. M., Berning, M. J., and Choy, T. S., "Simulation of Airplane and Rocket Trajectories," Tech. Rep. MSC-20933, Houston, TX, July 1987.

[145] Tannas, L. E., "Manual Entry Guidance," *Journal of Spacecraft and Rockets*, Vol. 3, No. 2, Feb. 1966, pp. 175–181.

[146] Tannas, L. E., "Re-entry Guidance Through Closed-form Equations." *AIAA Journal*, Vol. 5, No. 6, June 1967, pp. 1102–1109.

[147] Vinh, N. X., Chern, J. S., and Lin, C. F., "Phugoid oscillations in optimal reentry trajectories," *Acta Astronautica*, Vol. 8, 1981, pp. 311–324.

[148] Hale, F. J., *Introduction to Space Flight*, Prentice-Hall, 1994.

[149] *Matlab R2013b*, The Mathworks, Natick, MA, 2013.

[150] *Mathematica 10*, Wolfram Research, Champaign, IL, 2014.

[151] Desai, P. N. and Qualls, G. D., "Stardust Entry Reconstruction," *Journal of Spacecraft and Rockets*, Vol. 47, No. 5, Sept. 2010, pp. 736–740.

[152] Kontinos, D. A. and Wright, M. J., "Introduction: Atmospheric Entry of the Stardust Sample Return Capsule," *Journal of Spacecraft and Rockets*, Vol. 47, No. 6, Nov. 2010, pp. 865–867.

[153] King, H. H., "Ballistic missile re-entry dispersion," *Journal of Spacecraft and Rockets*, Vol. 17, No. 3, May 1980, pp. 240–247.

[154] Oberg, J., "Internal NASA Document Gives Clues to Scary Soyuz Return Flight," *IEEE Spectrum*, May 2008.

[155] Fegley, B., "Properties and Composition of the Terrestrial Oceans and of the Atmosphere of the Earth and Other Planets," *Global Earth Physics: A Handbook of Physical Constants*, American Geophysical Union, Washington, DC, 1995, pp. 320–345.

[156] *Memorial Tributes*, Vol. 1, National Academy of Engineering, Washington, DC, 1979.

[157] Sutton, K. and Graves, R. A., "A General Stagnation-point Convective-heating Equation for Arbitrary Gas Mixtures," Tech. Rep. NASA TR R-376, NASA, Washington, DC, Nov. 1971.

[158] Griffin, M. D. and French, J. R., *Space Vehicle Design*, AIAA, Reston, VA, second edition ed., 2004.

[159] Putnam, Z. R. and Braun, R. D., "Precision Landing at Mars Using Discrete-Event Drag Modulation," *Journal of Spacecraft and Rockets*, Vol. 51, No. 1, Feb. 2014, pp. 128–138.

[160] Schoenenberger, M., Dyakonov, A., Buning, P., Scallion, W., and Van Norman, J., "Aerodynamic Challenges for the Mars Science Laboratory Entry, Descent and Landing," *41st AIAA Thermophysics Conference*, San Antonio, Texas, June 2009, pp. 1–29.

[161] McDaniel, R. D., Wright, M. J., and Songer, J. T., "Aeroheating Predictions for Phoenix Entry Vehicle," *AIAA Aerospace Sciences Meeting*, Reno, Nevada, Jan. 2008, pp. 1–25.

[162] Martin-Mur, T. J., Kruizinga, G. L., and Wong, M. C., "Mars Science Laboratory Interplanetary Navigation Analysis," *21st International Symposium in Space Flight Dynamics*, San Jose dos Campos, Brazil, Jan. 2011, pp. 1–15.

[163] Way, D. W., "On the Use of a Range Trigger for the Mars Science Laboratory Entry, Descent, and Landing," *IEEE Aerospace Conference*, Big Sky, Montanta, March 2011, pp. 1–8.

[164] Desai, P. N., Schoenenberger, M., and Cheatwood, F. M., "Mars Exploration Rover Six-Degree-of-Freedom Entry Trajectory Analysis," *Journal of Spacecraft and Rockets*, Vol. 43, No. 5, Sept. 2006, pp. 1019–1025.

[165] Braun, R. D., Powell, R. W., Engelund, W. C., Gnoffo, P. A., Weilmuenster, K. J., and Mitcheltree, R. A., "Mars Pathfinder Six-Degree-of-Freedom Entry Analysis," *Journal of Spacecraft and Rockets*, Vol. 32, No. 6, Nov. 1995, pp. 993–1000.

[166] Spencer, D. A. and Braun, R. D., "Mars Pathfinder Atmospheric Entry: Trajectory DesignandDispersion Analysis," *Journal of Spacecraft and Rockets*, Vol. 33, No. 5, Sept. 1996, pp. 670–676.

[167] Justh, H. L. and Ramey, H. S., "Mars-GRAM 2010: Improving the Precision of Mars-GRAM," *4th International Workshop on the Mars Atmosphere: Modelling and Observations*, Feb. 2011, pp. 1–4.

[168] Tauber, M. E. and Sutton, K., "Stagnation-point Radiative Heating Relations for Earth and Mars Entries," *Journal of Spacecraft and Rockets*, Vol. 28, No. 1, June 1991, pp. 40–42.

[169] Kinney, D., "Aero-Thermodynamics for Conceptual Design," *42nd AIAA Aerospace Sciences Meeting and Exhibit*, Reno, Nevada, Jan. 2004, pp. 1–11.

[170] Cruz, J. R., Way, D. W., Shidner, J. D., Davis, J. L., and Kipp, D. M., "Mars Science Laboratory: Description of the Parachute Models Used in the POST End-to-end Simulation," Tech. rep., NASA Langley Research Center, Hampton, VA, July 2012.

[171] Striepe, S. A., Way, D. W., and Dwyer, A. M., "Mars Science Laboratory Simulations for Entry, Descent, and Landing," *Journal of Spacecraft and Rockets*, Vol. 43, No. 2, March 2006, pp. 311–323.

[172] Vincenty, T., "Direct and Inverse Solutions of Geodesics on the Ellipsoid with Application of Nested Equations," *Survey Review*, Vol. XXII, No. 176, April 1975, pp. 88–93.

[173] Mase, R. A., Spencer, D. A., Smith, J. C., and Braun, R. D., "Navigation Stragtegy for the Mars 2001 Lander Mission," *AAS/AIAA Astrodynamics Specialist Conference*, Girdwood, AK, 1999.

[174] Raiszadeh, B., Desai, P. N., and Michelltriee, R., "Mars Exploration Rover Heat Shield Recontact Analysis," *21st AIAA Aerodynamic Decelerator Systems Technology Conference and Seminar*, Dublin, Ireland, May 2011.

[175] Putnam, Z. R., Clark, I. G., and Braun, R. D., "Drag modulation flight control for aerocapture," *Aerospace Conference, 2012 IEEE*, 2012, pp. 1–10.

[176] Putnam, Z. R. and Braun, R. D., "Drag-Modulation Flight-Control System Options for Planetary Aerocapture," *Journal of Spacecraft and Rockets*, Aug. 2013, pp. 1–12.

[177] Duvall, A. L., Justus, C. G., and Keller, V. W., "Global Reference Atmospheric Model (GRAM) Series for Aeroassist Applications," *43rd AIAA Aerospace Sciences Meeting and Exhibit*, Reno, NV, Jan. 2005.

[178] Wooster, P. D., Braun, R. D., Ahn, J., and Putnam, Z. R., "Mission design options for human Mars missions," *MARS*, Vol. 3, 2007, pp. 12–28.

[179] Lockwood, Mary Kae, "Titan Aerocapture Systems Analysis," *39th AIAA/ASME/SAE/ASEE Joint Propulsion Conference and Exhibit*, Huntsville, AL, July 2003.

[180] Craig, S. and Lyne, J. E., "Parametric Study of Aerocapture for Missions to Venus," *Journal of Spacecraft and Rockets*, Vol. 42, No. 6, Nov. 2005, pp. 1035–1038.

[181] Graf, J. E., Johnston, M. D., Zurek, R. W., De Paula, R. P., Eisen, H. J., and Jai, B., "The Mars Reconnaissance Orbiter Mission," *54th International Astronautical Congress*, Bremen, Germany, Oct. 2003.